Pt(II) complexes as scaffolds in supramolecular assemblies

Stephan Sinn

UNIVERSITÉ DE STRASBOURG

ÉCOLE DOCTORALE DES SCIENCES CHIMIQUES

Institut de Science et d'Ingénierie Supramoléculaires (ISIS)

THÈSE présentée par :

Stephan SINN

soutenue le : **31 mars 2017**

pour obtenir le grade de : **Docteur de l'université de Strasbourg**

Discipline/ Spécialité : CHIMIE

Complexes de platine (II) comme ossatures dans les assemblages supramoléculaires

THÈSE dirigée par :

Mme DE COLA Luisa	Professeur, Université de Strasbourg
Mr LEHN Jean-Marie	Professeur, Université de Strasbourg

RAPPORTEURS :

Mr SCHMUCK Carsten	Professeur, Universität Duisburg-Essen
Mr BRUCE Duncan	Professeur, University of York

AUTRES MEMBRES DU JURY :

Mr BRAUNSTEIN Pierre	Professeur, Université de Strasbourg
Mme DE COLA Luisa	Professeur, Université de Strasbourg

Dissertation

Pt(II)-Complexes as Scaffolds in Supramolecular Assemblies

Stephan Sinn

Wo auch immer man hinschaut,

es gibt immer etwas zu sehen.

This work is dedicated to my family.

My wife Elisabeth, my son Tristan,

my brother Bastian and my parents Doris and Michael Sinn.

Table of contents

Résumé Complexes de platine (II) comme ossatures dans les assemblages supramoléculaires I

Introduction I
But de la thèse IV
Résultats et discussions IV
Un complexe éther couronne dinucléaire de Pt(II) IV
Détection différentielle d'aza-hétérocycles VII
Architectures supramoléculaires polygonales XI
Particules luminescentes pseudo-virales XIV
Conclusion XVII
Références XIX

Chapter I General Introduction 1

Abstract 1
Light-matter interactions 1
Transition metal complexes 8
Ligand-field theory 9
Photophysics of Pt(II)-complexes 12
N-metallacycles 15
Self-assembly 17
Self-assembly of Pt(II)-complexes 19
Cowpea Chlorotic Mottle Virus (CCMV) 22
Coat proteins 24
Platinum(II)-complex-protein interactions 25
Supramolecular Sensing 27
Single analyte sensing 28
Differential sensing 29
Scope of the thesis 30
References 31

Chapter II A Ratiometric Luminescent Switch Based on Platinum Complexes Tethered to a Crown-Ether Scaffold 39

Abstract 39
Introduction 40
Sensing metal cations by crown ethers 40
Transition metal complexes as phosphorescent reporters 41
Neutral Pt(II)-complexes with pronounced supramolecular features 42
Results and discussion 42
Defined conformation of the crown ether scaffolds 43
Pt(II)-complex installation onto the scaffold 45

Photophysical analysis in solution and solid state 45
Sensing of potassium 48
Determination of the binding constants 50
Reversible switching of the luminescence 52
Conclusion 55
Experimental part 56
Synthesis of CF_3-tzH_2 (L-2H) 56
Synthesis of Pt$DMSO_2Cl_2$ 57
Synthesis of L-Pt-PyA 57
Synthesis of L-Pt_2-18C4 58
Synthesis of L-Pt_2-18C6 59
References 60

Chapter III Differential Sensing of Aza-heterocyclic Drugs and Toxins in Water by Specific Emission Colors of Platinum Complexes 65

Abstract 65
Introduction 66
Metal complexes as luminescent labels 66
Results and discussion 68
L-Pt-DMSO as reactive luminescent probe for aza-heterocycles 72
Enhanced robustness by the use of surfactants 73
Analyte discrimination by their unique emission spectra 79
Mathematical models for analyte differentiation 100
L-Pt-DMSO as reactive luminescent tag for aza-heterocycles 108
Conclusion 110
Experimental part 112
Synthesis of L-Pt-DMSO 112
Synthesis of L-Pt-1 112
References 113

Chapter IV Discrete Polygonal Supramolecular Architectures of Isocytosine-Based Pt(II)-complexes at the Solution/Graphite Interface 117

Abstract 117
Introduction 117
Results and discussion 119
Design and synthesis of the H-bond scaffolds 119
Photophysical investigations on L-Pt-Py-iCyt 120
Self-assembly of 4-isoCytosinyl-pyridine (Py-iCyt) 122
Self-assembly of L-Pt-Py-iCyt 124
Re-arrangement energies 131
Conclusion 133

Computational details 133
Experimental part 135
Synthesis of 4-isoCytosinyl-pyridine (Py-iCyt) 135
Synthesis of L-Pt-Py-iCyt 136
References 137

Chapter V Highly Luminescent Virus Like Particles (VLPs) Through the Encapsulation of Pt(II)-Amphiphiles 140

Abstract 140
Results and discussion 145
Synthesis of the Pt(II)-amphiphiles 145
Photophysics of the Pt-R in organic solvent and the solid state 148
Photophysics of the Pt(II)-amphiphiles in organic and aqueous solution 151
Material characterization of the Pt(II)-complexes 160
Encapsulation into CCMV capsids 165
Material characterization of VLPs 165
Photophysics of the VLPs 170
Induced Shape Change 173
Conclusion 175
Experimental part 176
Synthesis of Ts-O-TEG-O-Me 176
Synthesis of HO-TEG-O-Bnz 176
Synthesis of Ts-O-TEG-O-Bnz 177
Synthesis of Py-Alkyl-Br 177
Synthesis of PA-2xOMe 178
Synthesis of PA-3xOMe 178
Synthesis of P-Alkyl-2 179
Synthesis of P-2 180
Synthesis of P-3 180
Synthesis of AR 181
Synthesis of PA-2 181
Synthesis of PA-3 182
Synthesis of A-2xOMe 182
Synthesis of A-3xOMe 183
Synthesis of A-2xOH 184
Synthesis of A-3xOH 184
Synthesis of A-2xSO_4 185
Synthesis of A-3xSO_4 186
Synthesis of A-Alkyl-2xSO_4 186
Synthesis of L-Pt-2xOMe 187
Synthesis of L-Pt-3xOMe 188

Synthesis of L-Pt-2xOH 188
Synthesis of L-Pt-3xOH 189
Synthesis of L-Pt-2xSO_4 190
Synthesis of L-Pt-3xSO_4 191
Synthesis of L-Pt-Alkyl-2xSO_4 191
Synthesis of L-Pt-R 192
References 194

Instrumentation 198

Electronic absorption spectroscopy 201
Fluorescence spectroscopy 202
Time correlated single photon counting 204
Photoluminescence quantum yield 206
Dynamic light scattering 208
Scanning tunneling microscopy 209
References 211

Appendix 215

Curriculum Vitae 221

Acknowledgment 225

Abbreviations

sh	shoulder
CT	charge transfer
MLCT	metal-to-ligand charge transfer
MMLCT	metal-metal-to-ligand charge transfer
LC	ligand-centered
MP-LC	metal perturbed - ligand-centered
MeOH	methanol
EtOH	ethanol
DCM	dichloromethane
MeCN	acetonitrile
THF	tetrahydrofuran
NaOAc	sodium acetate
TRIS	tris(hydroxymethyl)aminomethane
DTT	dithiothreitol
Laser	light amplification by stimulated emission of radiation
NMR	nuclear magnetic resonance
MS	mass spectrometry
ToF	time of flight
ESI	electrospray ionization
STM	scanning tunneling microscopy
TEM	transmission electron microscopy
STEM	scanning transmission electron microscopy
HAADF	high-angle annular dark-field
TCSPC	time-correlated single photon counting

FPLC	fast-protein liquid chromatography
TLC	thin-layer chromatography
HPLC	high-pressure liquid chromatography
©	copyright
FLIM	fluorescence lifetime imaging
PLIM	phosphorescence lifetime imaging
$[Ru(bpy)_3]^{2+}$	ruthenium-tris(2,2'-bipyridyl)

Résumé

Complexes de platine (II) comme ossatures dans les assemblages supramoléculaires

Introduction

Les architectures supramoléculaires permettent de construire des matières complexes dans une approche ascendante en utilisant des blocs moléculaires bien définis.[1, 2] Etant définie comme la chimie au-delà de la liaison covalente,[3] la chimie supramoléculaire met en œuvre des forces intermoléculaires entraînent la formation d'assemblages présentant des propriétés non présentes dans les molécules elles-mêmes. Par conséquent, les motifs supramoléculaires permettent le contrôle de l'agrégation de la matière. Bien que chaque liaison supramoléculaire soit faible par rapport à une liaison covalente,[4, 5] l'addition des plusieurs forces peut résulter en des structures stables composées de liaisons intermoléculaires. Néanmoins, la faible énergie de dissociation pour chaque liaison permet de déclencher le désassemblage des agrégats par *stimuli* externes. La compréhension et la conception rationnelle des motifs supramoléculaires rendent donc la formation de structures complexes réactives vis-à-vis de *stimuli*. Ce comportement *stimuli*-réactif fournit des informations, de l'environnement aux structures complexes. Par exemple, des changements chimiques peuvent conduire à une altération de la structure complexe, accompagnée de variations de ses propriétés photophysiques. Les phénomènes observés, à leur tour, peuvent être utilisés pour certaines applications, telles que des matériaux réactifs aux stimuli et / ou photoniques, des outils de bioimagerie ou des matériaux fonctionnels hybrides.

Les matériaux luminescents tels que les fluorophores sont très intéressants pour la recherche fondamentale et l'industrie, puisqu'ils sont les composants clés de la luminescence et des étiquettes pour la bio-imagerie. En raison de la relaxation émissive permise par le spin depuis le premier état excité du singulet vers l'état fondamental singulet, les fluorophores organiques possèdent habituellement une courte durée de vie à l'état excité, de quelques nanosecondes, et un petit déplacement de Stokes, de quelques nanomètres. Ces caractéristiques photophysiques des fluorophores organiques sont indésirables pour de nombreuses applications. Inversement, les complexes de métaux de transition utilisant par exemple Ru(II),[6-12] Os(II),[13] Ir(III),[14-16] Pt(II)[17] montrent un croisement intersystème efficace vers un état excité triplet en raison d'un fort couplage spin-orbite induit par l'atome lourd. En vertu de la règle de conservation de spin, la durée de vie de l'état excité de ces luminophores sera fortement prolongée (jusqu'à quelques secondes), ce qui entraînera une désintégration radiative changeante de spin, à savoir une phosphorescence qui s'accompagne d'un grand déplacement de Stokes.

En général, les luminophores souffrent souvent d'une auto-extinction à des concentrations plus élevées, appelée extinction induite par l'agrégation (ACQ, aggregation-caused quenching), ce qui entraîne une diminution importante des rendements quantiques (φ). Les complexes Pt(II), à géométrie plane carrée, neutres et phosphorescents, convenablement décorés de ligands chromophores, présentent la condition géométrique nécessaire pour surmonter ce problème. Dans la forme monomère, nous observons une bande d'émission structurée dans la région bleue du spectre électromagnétique avec une courte durée de vie à l'état excité ($\tau \sim 2$ ns) et un faible rendement quantique ($\varphi < 1\%$). A l'état agrégé, cependant, nous observons une luminescence décalée à effet bathochromique et une bande large, présentant une durée de vie à l'état excité prolongé ($\tau \sim 450$ ns) et un rendement quantique fortement augmenté ($\varphi \sim 65\%$).

Lors de l'agrégation, les complexes Pt(II) carrés plans possèdent une forte tendance à un empilement z-directionnel (où z désigne l'axe Pt-Pt), du fait des interactions hydrophobes, π-π, dipôle-dipôle et dispersifs. Lorsque deux ions Pt(II) sont suffisamment proches l'un de l'autre, (3,5 Å, à savoir le rayon de Van der Waals du platine), les orbitales complexes sont affectées d'une manière telle que les orbitales dz^2 sont fortement déstabilisées en raison d'une interaction répulsive de ces orbitales remplies, de sorte qu'elles forment la plus haute orbitale moléculaire occupée (HOMO) du dimère. De plus,

l'orbitale moléculaire inoccupée la plus basse (LUMO), qui consiste principalement en orbitales π, est légèrement stabilisée par des interactions π-π attractives. Le Schéma 1 illustre les effets d'agrégation simplifiés sur l'exemple d'une formation de dimères, révélant ainsi le rétrécissement de l'intervalle d'énergie entre les orbitales frontières. Dans l'état monomère, l'émission du complexe Pt(II) se produit principalement à partir d'un état centré sur le ligand (^{3}LC), alors que dans la forme agrégée se produisent de nouvelles transitions sur les interactions électroniques, à savoir le transfert de charges métal-métal-ligand (MMLCT) conduisant à une émission ^{3}MMLCT.

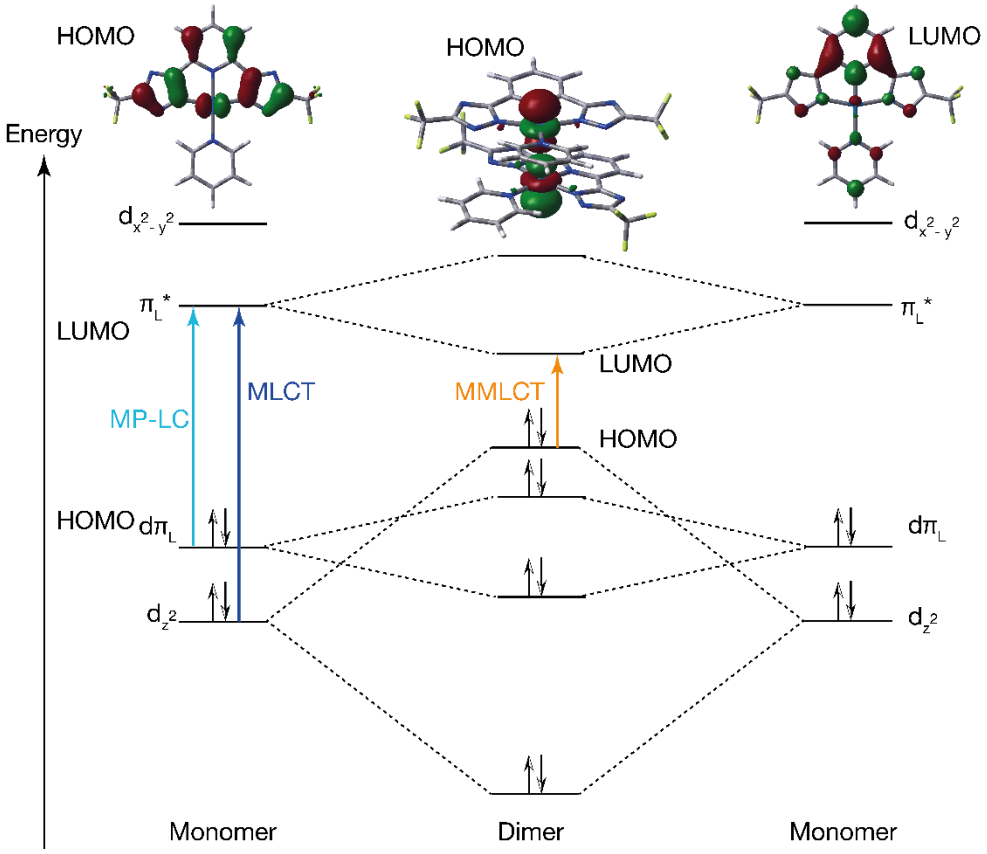

Schéma 1: Diagramme d'orbitale moléculaire d'un complexe de Pt(II) carré plan monomère présentant des ligands avec un système π. Après agrégation des complexes, les orbitales d_{z^2} intéragissent fortement entre elles, résultant en une nouvelle transition (MMLCT), plus basse en énergie que celle du monomère (MP-LC, MLCT). Les orbitales frontières pour la partie principale des complexes utilisés dans cette thèse, L-Pt-Py, ont été calculées et représentées comme orbitales Kohn-Sham. gauche: HOMO du monomère; centre: HOMO du dimère; droite: LUMO du monomère (similaire pour le dimère)

Les effets observés du prolongement de la durée de vie de l'état excité ainsi que d'une forte augmentation du rendement quantique en fonction de l'auto-assemblage des

complexes peuvent être désignés sous le nom d'émission induite par agrégation (AIE, aggregation-induced emission). Il est important de noter que, même à des concentrations élevées, les propriétés photophysiques intéressantes telles que l'excitation et l'émission dans la région visible du spectre électromagnétique sont préservées. Des caractéristiques supplémentaires telles que de grands déplacements de Stokes, un rendement quantique élevé et une longue durée de vie à l'état excité, aident à une suppression facile de la fluorescence de fond possible provoquée par des matrices biologiques. De plus, un changement de la nature de l'émission de ^{3}LC basée sur ^{3}MMLCT se produit déjà à la formation de dimères et fournit ainsi une mesure spectroscopique pour de petits changements moléculaires et la perturbation des structures auto-assemblées.

But de la thèse

Le but de cette thèse est le développement de matériaux auto-assemblés à base de complexes de Pt (II), à géométrie plane carrée, neutres et phosphorescents, en exploitant une variété d'interactions supramoléculaires. Les changements dans les propriétés photophysiques peuvent être utiles à l'ouverture vers de nouvelles applications et permettre un aperçu profond de l'environnement des complexes, à savoir l'auto-assemblage, l'encapsulation, l'organisation multidimensionnelle et la détection par émission. En combinaison avec des protéines de capside de virus, la création de matériaux fonctionnels hybrides luminescents est envisagée.

Résultats et discussions

Un complexe éther couronne dinucléaire de Pt(II)

Un capteur ratiométrique pour le potassium est rapporté, basé sur des complexes N-métallocycliques phosphorescents Pt(II) présentant un éther couronne disubstitué *cis* comme unité de reconnaissance cationique (Figure 1). Les complexes métalliques sont luminescents de couleur bleue dans un état non agrégé mais deviennent émissifs dans la région de couleur orange lorsqu'ils sont dans une proximité physique étroite, comme c'est le cas lorsque le macrocycle est à l'état replié.

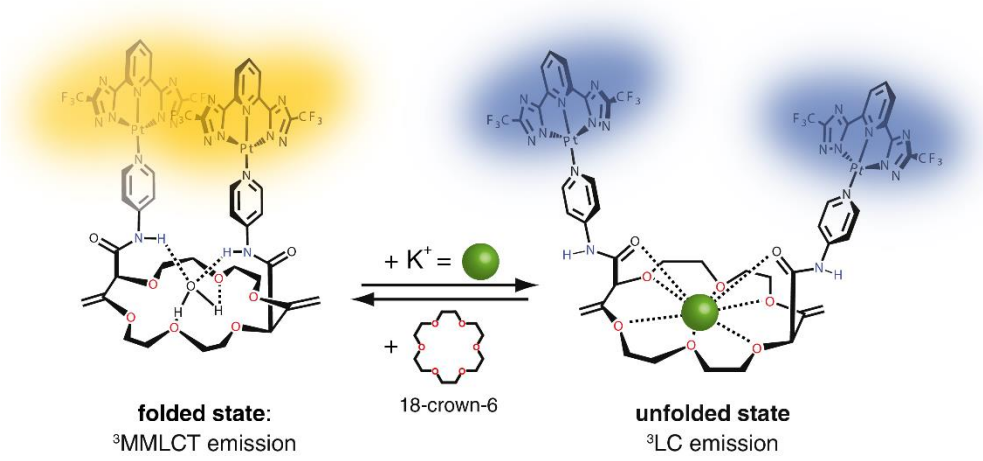

Figure 1: Changement réversible de la couleur d'émission du colorant platine-éther couronne après addition de sels de potassium et extraction de l'ion potassium par l'éther couronne « 18-crown-6 » non substitué. L'excitation peut-être réalisée dans la région aromatique.

Lors de la liaison du cation, un dépliement se produit, entraînant un changement prononcé des propriétés d'émission (par exemple la longueur d'onde d'émission), ce qui peut être utilisé pour des applications de détection ratiométrique.

Les éthers de couronne **Py_2-18C4** et **Py_2-18C6** portant des motifs 4-aminopyridine ont été préparés en deux étapes telles que résumées dans le Schéma 2. Tout d'abord, nous avons fait réagir le 2-diazo-3-oxobutanoate de méthyle avec THP et 1,4-dioxane en présence de Rh_2 $(Oct)_4$ pour donner des macrocycles de polyéther conjugués à 18 membres.[18, 19] Ces dérivés (Schéma 2, X = CH_2 ou O) ont ensuite été traités avec des mélanges de 4-aminopyridine et de KO^tBu pour induire des processus d'amidation-transposition en tandem et former les **Py_2-18C4** et **Py_2-18C6** *cis*-disubstitués sous forme de stéréoisomères racémiques (ratios stéréoisomériques, respectivement> 49: 1, 55% et 50% de rendements combinés) [20]

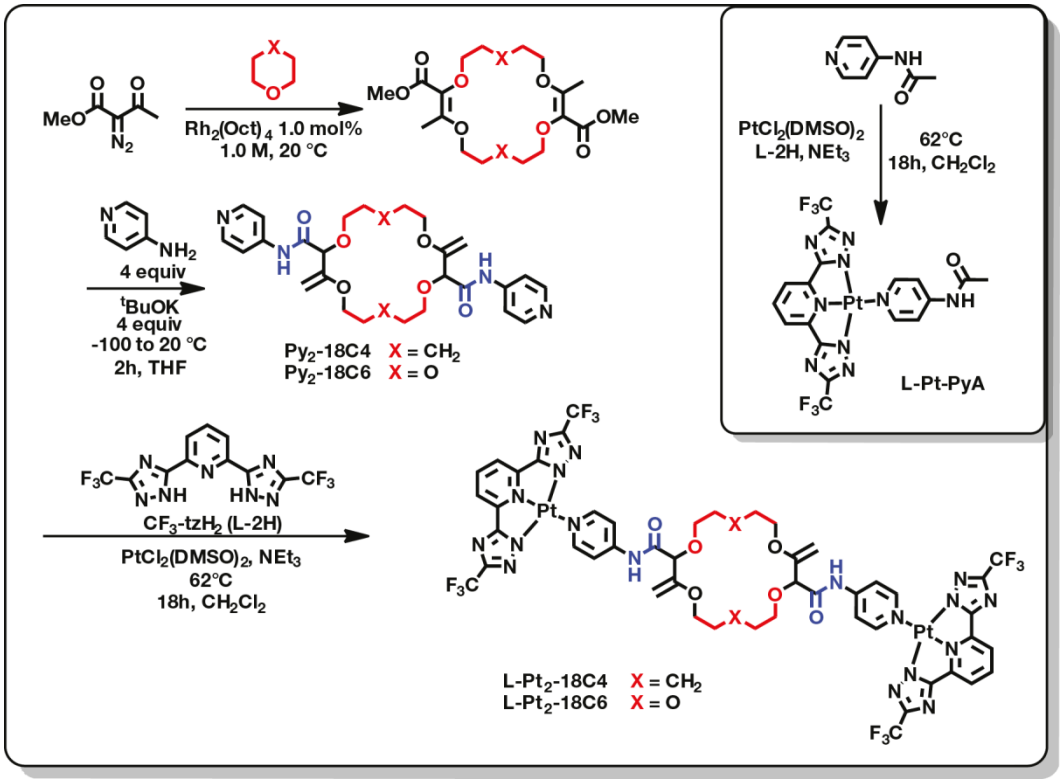

Schéma 2: Schéma de synthèse des molécules **L-Pt$_2$-18C6** et **L-Pt$_2$-18C4**, ainsi que la référence, **L-Pt-PyA**: $PtCl_2DMSO_2$, N-(pyridin-4-yl) acetamide, CF_3-tzH_2 (**L-2H**), $CHCl_3$, 70°C, 18h, 72%. **L-Pt$_2$-18C4**: $PtCl_2DMSO_2$, **L-2H**, **Py$_2$-18C4**, $CHCl_3$, 70°C, 18h, 37%. **L-Pt$_2$-18C6**: **L-2H**, **Py$_2$-18C6**, $CHCl_3$, 70°C, 18h, 39%.

Il est important de noter que les dérivés **Py$_2$-18C4** et **Py$_2$-18C6** présentent des conformations bien définies. En effet, les interactions allyliques présentent une déformation 1,3- se produisant entre les centres stéréogènes et les doubles liaisons exocycliques adjacentes. En conséquence, les groupements amides sont orientés sensiblement perpendiculairement au plan médian des macrocycles. Ce biais conformationnel induit une proximité spatiale entre les résidus aromatiques. Des interactions de liaison hydrogène se produisent également entre l'amide N-H et les atomes d'oxygène voisins. En conséquence, et en ce qui concerne la cavité, les liaisons N-H et C=O des amides sont respectivement tournées vers l'intérieur et vers l'extérieur.

En raison de leur géométrie carrée plane et de leur grande surface aromatique, les complexes de Pt avec des ligands N-métallocycliques tridantates (par exemple le 2,6-bis(3-(trifluorométhyl)-1H-1,2,4-triazol-5-yl) pyridine, CF_3-tzH_2, voir Schéma 2) forment facilement des adduits non covalents (dimères, agrégats, etc.) où les interactions métal···métal des centres Pt (II) augmentent fortement leurs propriétés d'émission.[21-27]

Dans cette étude, je focalise sur les caractéristiques luminescentes distinctement différentes des monomères et dimères de complexes de Pt(II) pour la conception d'un capteur ratiométrique pour le potassium, émettant dans la région du visible et montrant des changements plus conséquents dans les propriétés d'émission lors de la liaison cationique que les chromophores pyrène. Le processus de changement de couleur d'émission peut être inversé par l'ajout de l'éther couronne 18-C-6, et plusieurs cycles sont possibles. Les bandes d'absorption intense avec un début dans la région visible, le grand changement de Stokes de l'émission et la longue durée de vie d'excitation de la phosphorescence en solution sont des caractéristiques prometteuses pour la détection du cation. La réversibilité de la liaison a été confirmée par des expériences de titrage compétitives avec l'éther couronne 18-C-6 non substitué, comme représenté dans la Figure 2.

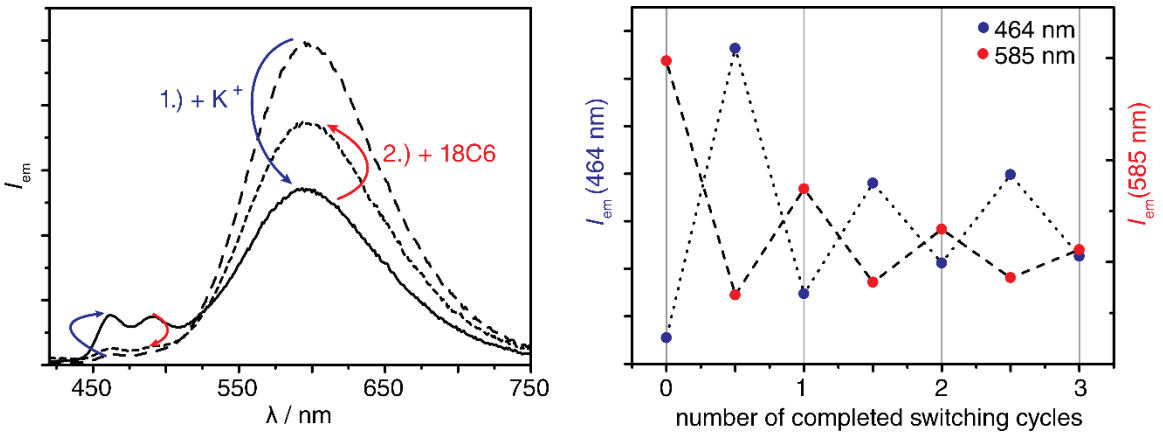

Figure 2: gauche: spectre d'émission de **Pt_2-18C6** seul (solvent: THF aéré, 0.1mM, ligne discontinue), après addition de trifluoromethanesulfonate de potassium (ligne continue), et après addition de l'éther couronne 18-C-6 (λ_{ex} = 343 nm). droite: cycles d'intensité d'émission après ajout de sel de potassium et de l'éther couronne 18-C-6.

Détection différentielle d'aza-hétérocycles

Une sonde phosphorescente réactive pour les médicaments et les toxines aza-hétérocycliques a été développée, offrant un test supramoléculaire de chemo-détection en solution aqueuse et dans les environnements biologiques en raison de leurs empreintes spectroscopiques. La formation des complexes de platine (II) avec des ligands hétérocycliques se déroule aisément dans des conditions ambiantes, ce qui permet un criblage facile de l'analyte. Cinquante-deux composés structurellement différents ont été

testés, dont 23 pyridines, imidazoles et triazoles, formant ainsi des agrégats complexes fortement émissifs (Figure 3).

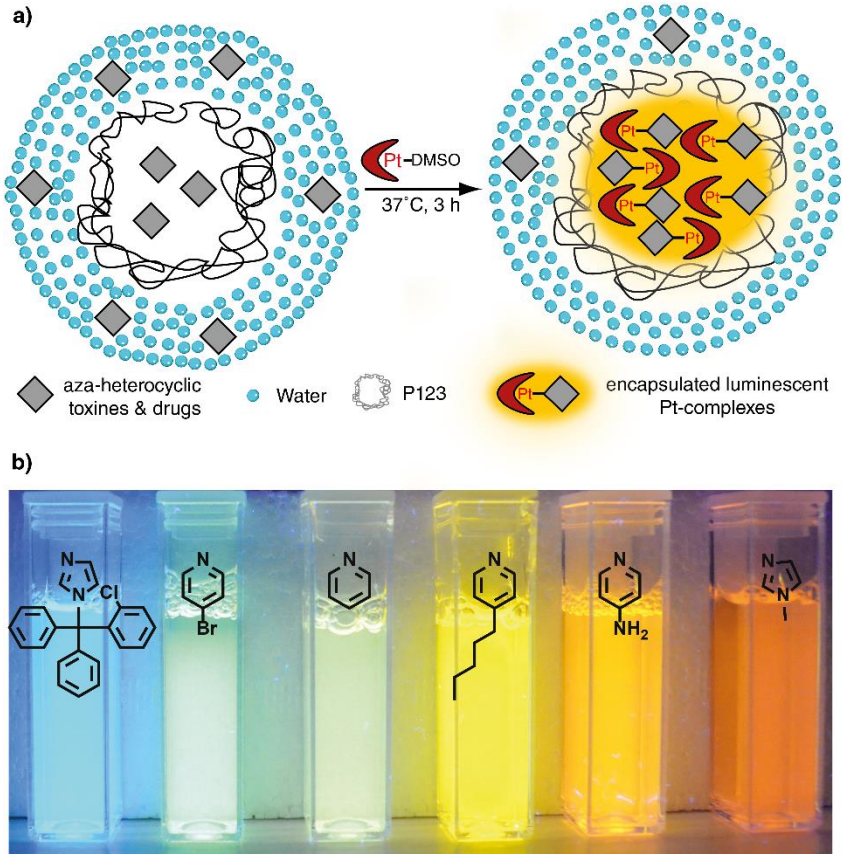

Figure 3: a) représentation schématique de la réaction entre les analytes aza-hétérocycliques et L-Pt-DMSO, dans de l'eau contenant le surfactant P123. Les complexes formés s'auto-assemblent et forment des espèces hautement émissives. b) Photographies de différents types de complexes luminescents étudiés dans ce chapitre sous excitation UV. De gauche à droite : **21, 9, 1, 6, 13, 17** (voir Schéma 3).

Le complexe précurseur L-Pt-DMSO développé peut réagir avec des fractions hétérocycliques sur des analytes, par exemple la pyridine (**1**), par échange du ligand DMSO labile conduisant à la formation d'une espèce émissive. Il est important de noter que la réaction peut se dérouler également dans l'eau ou dans un tampon aqueux à température ambiante et à pH neutre. L'addition de **1** à une solution de L-Pt-DMSO (schéma 3) dans de l'eau a donné en 1 h à 37 ° C un précipité rouge fortement émissif. A titre de comparaison, dans des protocoles de synthèse usuels, une source de Pt, **L-2H**, une base forte et un dérivé de pyridine réagissent dans un solvant organique polaire à 80 ° C pendant 12-18 h,[21, 28] rendant la procédure incompatible en biologie.

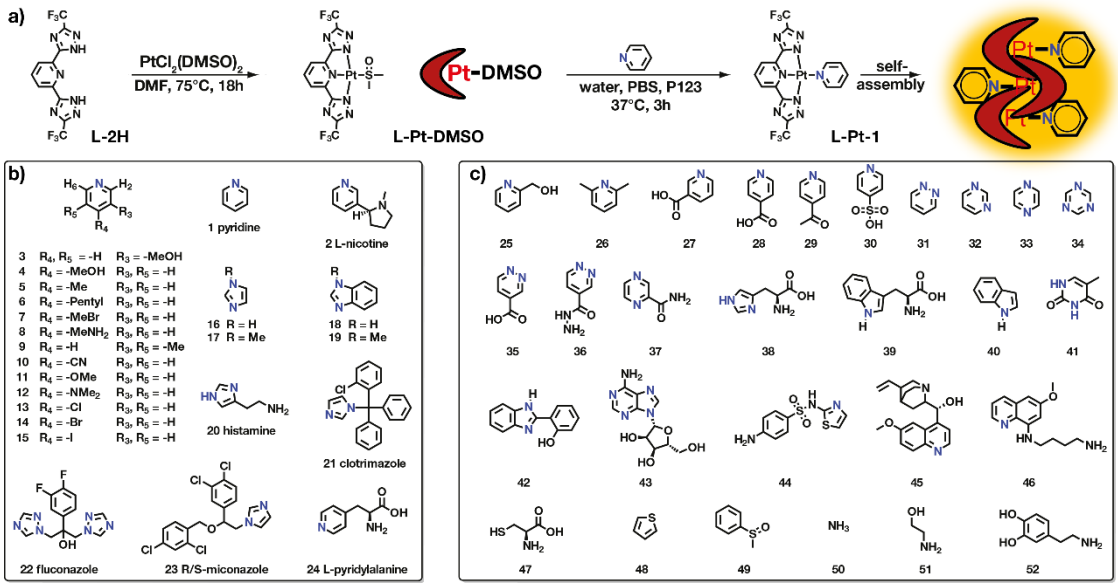

Schéma 3: a) Synthèse de la sonde réactive L-Pt-DMSO et un exemple de réaction avec la pyridine est décrit. Représentation schématique des agrégats émissifs formés à partir de L-Pt-**1**. b) Analytes aza-hétérocycliques formant des agrégats de complexes de Pt(II) hautement émissifs avec le précurseur de platine. c) Autres analytes étudiés et formant des complexes peu et non émissifs.

La précipitation des complexes hydrophobes est indésirable pour un protocole de détection basé sur une solution. Pour maintenir les agrégats en solution, nous avons utilisé le tensioactif Pluronic P123,[29] qui est connu pour former des micelles dans l'eau à une concentration plutôt faible (0,5% en masse, diamètre hydrodynamique ~ 15 nm). L'addition du précurseur L-Pt-DMSO à une solution de pyridine et de P123 dans du tampon PBS a entraîné une forte augmentation (facteur $3x10^3$) de l'intensité d'émission à 574 nm avec saturation du signal après 3 h à 37°C (Figure 1 & Tableau 1). Contrairement à la réaction dans l'eau, aucune précipitation des complexes n'a été observée. En comparaison avec d'autres tensioactifs (CTAB et SDS), P123 fournit le meilleur rapport signal / bruit et est biocompatible.[29-31] De plus, l'analyse peut également être effectuée dans l'urine, en montrant son applicabilité aux milieux biologiques.

Les bandes d'émission normalisées sont superposables à différents moments et l'intensité des émissions n'a pas notablement varié (≤ 4%) à la fin de la réaction. Pour L-Pt-**1**, l'absorption décalée vers le rouge (497 nm), la longueur d'onde d'émission maximale (571 nm), le PLQY élevé (45%) et la longue durée de vie à l'état excité (440 ns) sont toutes indicatives de l'agrégation du complexe de Pt par le biais d'interactions Pt•••Pt. Les résultats obtenus dans les cuvettes en quartz sont comparables à ceux obtenus

avec des cuvettes en plastique peu coûteuses (PMMA). Comme prévu, la détection par émission de l'analyte **1** après le marquage au Pt est plus sensible (linéarité jusqu'à 5 μM, détectabilité ≤ 1 μM) que la surveillance directe de l'absorbance, ceci indiquant le potentiel pour la détection de médicaments aza-hétérocycliques comme le clotrimazole (**21**, concentration plasmatique typique c_p = 40 μM - 440 mM),[32] le fluconazole (**22**, c_p = 35 - 100 μM)[33] et le miconazole (**23**, c_p = 3 - 94 μM)[34], ainsi que les toxines comme la nicotine (**2**, concentration d'urine typique du fumeur c_u = 6 - 31 μM).[35]

Il est important de noter que tous les analytes peuvent être distingués les uns des autres par leurs différences de couleur d'émission (grands changements du bleu au rouge) (Figure 3). De plus, les profils cinétiques de réaction et les caractéristiques d'émission résolues dans le temps peuvent fournir des informations précieuses pour la distinction des analytes. Les complexes de Pt(II) peuvent être appliqués comme marqueurs émissifs pour des médicaments et des biomolécules, en raison de leurs propriétés photophysiques avantageuses et de leur stabilité chimique dans des milieux biologiques tels que le sang. Une stratégie de détection différentielle conceptuellement liée par l'agrégation induite par les analytes a été développée par Swager *et al.* pour la détection des amines. Au mieux de notre connaissance, ce travail est la première méthode générale de détection par émission pour les composés hétérocycliques.

Afin de fournir une différenciation quantitative des complexes de Pt et de montrer le potentiel de la méthode de marquage pour l'application de détection différentielle, une analyse en composantes principales (PCA, principal component analysis)[37-39] a été réalisée. La PCA de routine multivariée non supervisée est le meilleur choix pour démontrer l'utilité des paramètres d'entrée, car seule une variance plus petite des mesures de répliques que pour des analytes différents donne lieu à l'apparition d'un regroupement de résultats.[37] Cinq paramètres photophysiques ont été déterminés pour chaque marqueur Pt et l'algorithme PCA a cartographié ces données d'entrée en un résultat distinct pour chacun des 23 analytes testés. Leur partition correspondante 2D et 3D est présentée à la Figure 4. Nous avons obtenu une clarification pertinente des résultats - indiqués par des ellipses environnantes - pour les mesures de répliques avec le même analyte, tandis que les résultats pour différents analytes ont rempli des zones clairement distinctes dans les graphiques 2D et 3D. Avant l'étiquetage par L-Pt-DMSO, pratiquement aucun analyte se distinguait l'un de l'autre par des moyens spectroscopiques (absorption, émission).

Les incertitudes de paramètre estimées de l'essai ont également été calculées, démontrant que même de grandes erreurs de mesure (15%) sont tolérables. Notamment, la différenciation des analytes aza-hétérocycliques est également réalisable même avec des mesures à haut débit basées sur un lecteur de plaques et en omettant des mesures résolues dans le temps. En outre, une analyse discriminante linéaire de type Fisherface (LDA) sur cet ensemble de données affiche un taux de classification élevé (94,44%) du système appliqué. De plus, dans un test dit « aveugle », un échantillon inconnu (échantillon X) d'une sélection des médicaments (**2**, **21**-**23**) a été choisi et correctement identifié comme **21** à travers l'analyse et l'ACP.

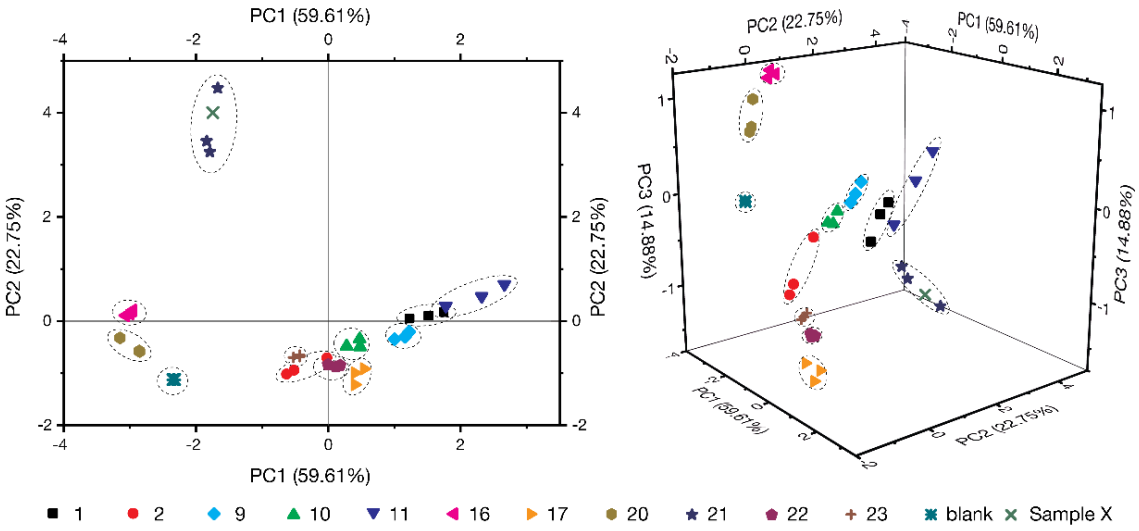

Figure 4: PCA des analytes sélectionés. gauche: résultats des deux principales composantes, PC1 = 59.61% et PC2 = 22.75%, somme = 82.36% ; droite : résultats des trois premières composantes principales, somme = 97.24%. L'essai réalisé sans analyte ajouté est nommé « blank ». Chaque ellipse indique un analyte étudié.

Architectures supramoléculaires polygonales

L'auto-assemblage moléculaire sur les surfaces est une approche polyvalente pour positionner des groupes fonctionnels avec une précision sous-nanométrique sur plusieurs centaines de μm^2 de surface et ainsi permettre le réglage fin de nombreuses propriétés physico-chimiques des nanostructures résultantes.[40-45] La conception de molécules comprenant des groupements actifs représente une voie prometteuse pour l'ingénierie de surfaces fonctionnelles et d'interfaces. Parmi les divers systèmes fonctionnels, les complexes Pt(II) ont attiré des intérêts considérables au cours de la dernière décennie en raison de leurs propriétés photophysiques et rédox attrayantes, y compris les fortes bandes d'absorption avec augmentation dans la région visible ainsi que l'émission à température

ambiante accompagnée d'un grand déplacement Stokes. [46] Les complexes neutres Pt(II) portant des ligands tridentates à base d'azolate et un ligand auxiliaire à base de pyridine possèdent une géométrie planaire carrée rigide. La substitution définie avec des motifs supramoléculaires permet ainsi des interactions intermoléculaires prévisibles et intéressantes. L'auto-assemblage résultant structuré par une approche ascendante est potentiellement intéressant pour des applications en micro- et nanoélectronique.[47]

Les systèmes supramoléculaires, où les ions Pt(II) sont directement coordonnés aux nucléobases, ont fait l'objet de nombreuses études.[48-51] Certains complexes de pyridine, de purine et de pyrimidine de platine présentent des propriétés prometteuses en tant que médicaments antitumoraux et dans divers milieux biomédicaux.[52-56]

La liaison hydrogène a été énormément utilisée comme interaction intermoléculaire directionnelle non covalente pour concevoir et contrôler la formation d'architectures supramoléculaires complexes. Sur des surfaces solides, des structures sophistiquées peuvent résulter de la formation de divers motifs liés à l'hydrogène, y compris des motifs linéaires et cycliques avec différents appariements tels que O–H···O, N–H···O and N–H···N.[57-61] Les nucléobases ont été précédemment rapportés pour former des structures de quatuor cyclique et hexamères en surface,[61-65] et des pentamères en solution.[66] A notre connaissance, la formation d'autres types de motifs cycliques n'a jamais été rapportée. Sur la base d'études antérieures sur l'isocytosine substituée,[65] l'effet des complexes de Pt(II) volumineux présentant une application potentielle dans l'optronique a été étudié de manière exhaustive.

Il est prouvé que l'isocytosine peut être utilisée pour diriger l'assemblage 2D des complexes Pt(II) par des interactions de type liaison hydrogène entre les bases nucléiques (Figure 5). Les résultats expérimentaux sont supportés par des calculs de DFT, permettant d'analyser à la fois la force de la liaison hydrogène et les interactions avec le substrat de graphite. De plus, afin de mieux comprendre les caractéristiques électroniques des architectures moléculaires, des images STM sont simulées.

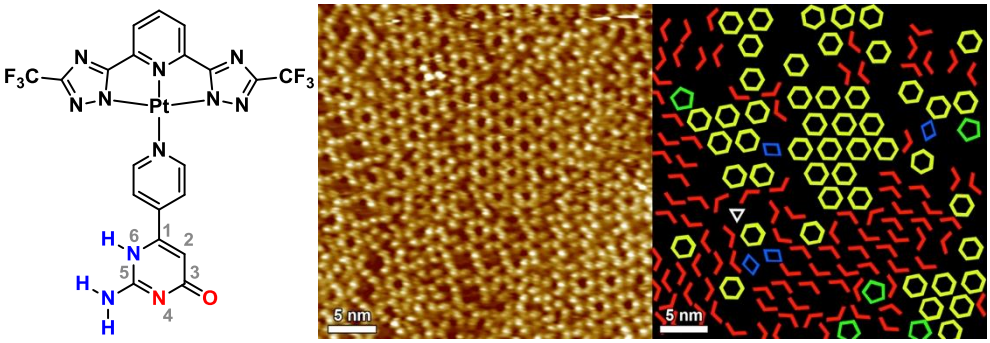

Figure 5: The complex is schematically depicted as well. a) image STM de **Pt-Py-iCyt** à l'interface de la solution de HOPG. Paramètres du balayage à effet tunnel: courant moyen (I_t) = 25 pA, tension à l'extémité (V_t) = 450 mV. b) Modèles de différents motifs d'auto-assemblages moléculaires.

Particulièrement, l'auto-assemblage du complexe **L-Pt-Py-iCyt** (Figure 5) en structures discrètes par liaisons hydrogène intermoléculaires entre différentes parties de l'isocytosine à l'interface solide-liquide est étudié. Il est montré que la formation de structures poly-cristallines composées de divers assemblages polygonaux comprenant des trimères, des tétramères, des pentamères et des hexamères est stabilisée par liaisons hydrogène distinctes.

Des études STM ont été réalisées sur la formation de différents motifs supramoléculaires cycliques discrets polygonaux formés par le complexe Pt(II) à base d'isocitosine **L-Pt-Py-iCyt** à l'interface solution / HOPG. Les résultats ont été appuyés par une analyse complète DFT incluant la simulation d'images STM. Les résultats du calcul concordent très bien avec les résultats acquis expérimentalement. Les résultats expérimentaux et théoriques ont fourni des preuves non équivoques que la formation de motifs hexamères et semi-hexamères de molécules **L-Pt-Py-iCyt** est thermodynamiquement favorisée (82% de toutes les molécules), comme en témoigne la force de l'association Énergie (Figure 6). Néanmoins, les pentamères, tétramères et trimères sont également observés à l'interface solide-liquide, bien que dans une moindre mesure (18% de toutes les molécules). L'approche décrite dans ce travail peut être exploitée pour contrôler la structure supramoléculaire des complexes de Pt(II) à la surface, et en général pour l'installation de plusieurs entités interagissant de manière intermoleculaire. Par conséquent, nous démontrons un moyen d'ajuster les propriétés photophysiques de tels matériaux organisés et des études actuelles visant à des structures multicouches permettant l'interaction Pt•••Pt sont en cours.

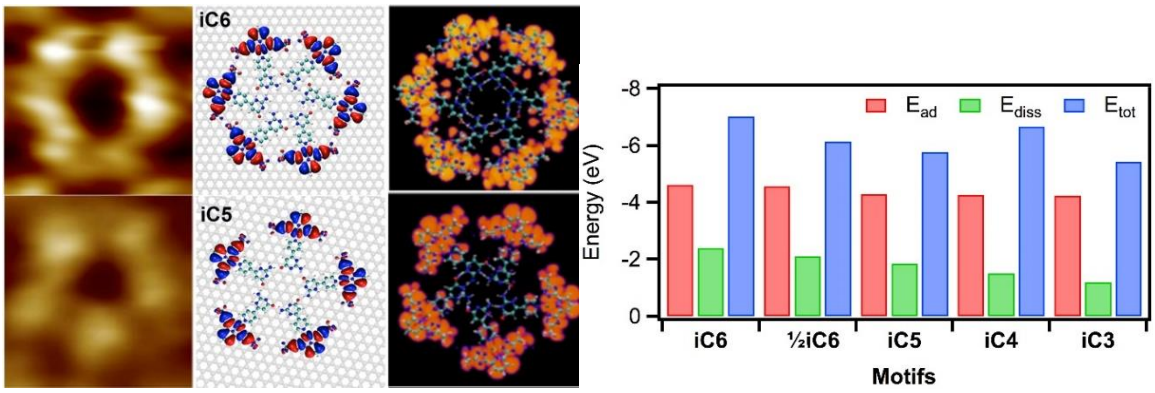

Figure 1: gauche: image STM des différents motifs **Pt-Py-iCyt**, structures simulées sur du graphène, Images STM simulées des différents motifs. Droite : énergie d'adsorption (E_{ad}, rouge), énergie de dissociation (E_{diss}, vert), et énergie totale (E_{tot} = E_{ad} + E_{diss}, bleu) calculées pour les différents motifs d'auto-assemblage moléculaire par le complexe **L-Pt-Py-iCyt**.

Particules luminescentes pseudo-virales

La formation de complexes de Pt(II) solubles dans l'eau nano conjugués et de protéines de capside CMMV a été examinée. Une série de complexes de Pt(II) amphiphiles a été synthétisée, caractérisée et photophysiquement sondée dans des solutions organiques et aqueuses (Schéma 4). Les complexes de Pt(II) sont constitués de la partie **L-Pt-Py** framework précédemment présentée déterminant principalement les propriétés photophysiques, qui définit le noyau hydrophobe et un benzène substitué par un groupement tétraéthylèneglycol attaché par une liaison amide à l'unité coordinante pyridyle, ce qui constitue la partie hydrophile du système. Les blocs de construction organiques possèdent la pyridine qui est substituée par un amide en position 4. La liaison amide lie soit la 3,5-bis(tétraéthylène glycolyl) phényle soit la 3,4,5-tris(tétraéthylène glycolyl) à la pyridine. Les oxygènes terminaux des chaînes éthylèneglycol sont soit présents sous forme de groupes hydroxyle, soit substitués par des groupes méthyle ou des groupes ester sulfite.

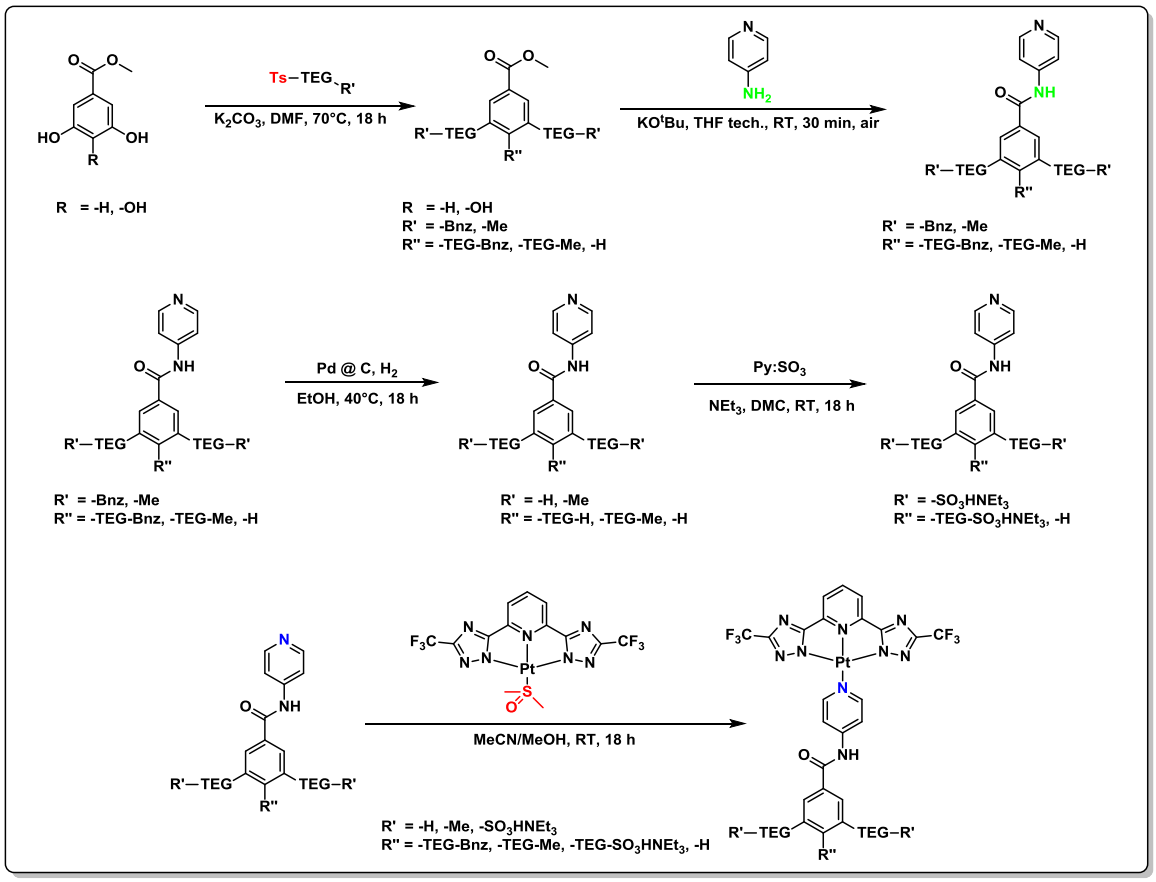

Schéma 4: Approche synthétique pour la préparation de complexes de Pt(II) amphiphiles.

Une solubilité appropriée dans l'eau et les solutions tampons (Tris, NaOAc) n'a été atteinte que par les composés **L-Pt-3xOMe**, **L-Pt-3xOH**, **L-Pt-2xSO4** et **L-Pt-3xSO4**. La concentration d'agrégation critique (CAC) a été étudiée avec une nouvelle méthode, développée pour les amphiphiles intrinsèquement luminescents basée sur leur durée de vie à l'état excité et comparée à des méthodes établies basées sur la diffusion dynamique de la lumière (DLS, « dynamic light scattering »). Les CAC se produisent à de faibles concentrations (environ 20 µM), avec des tailles allant de 10 à 20 nm pour les supermolécules, qui sont dans l'ordre de grandeur des capsides auto-assemblées (12 et 28 nm, T = 1 et T = 3, respectivement) du virus de niébé chlorotique taché (CCM, « cowpea chlorotic mottle »). Ces composés ont été soumis à un procédé d'encapsulation avec les protéines de capside virale dont la charge négative a montré un allumage de luminescence. La réversibilité de ce processus est une preuve supplémentaire d'une encapsulation réelle et pas seulement une couverture de surface.

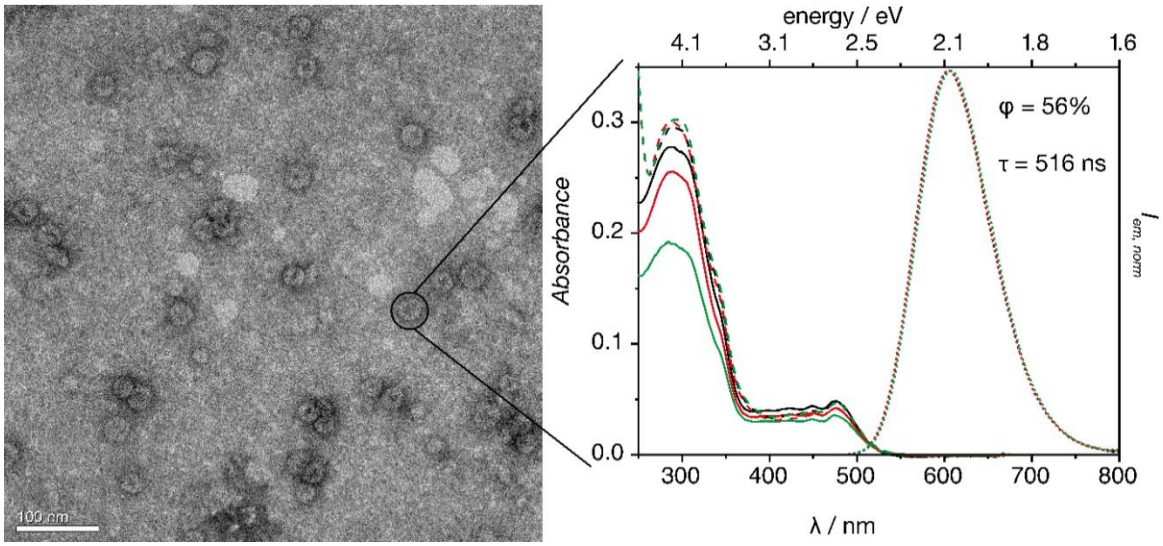

Figure 2: gauche: Image TEM d'un VLP avec un complexe amphiphile encapsulé, droite: spectres d'absorption (ligne continue), d'émission normalisée (pointillés) et excitation normalisée (ligne discontinue) de **VLP-3xOH**. La couleur indique la concentration d'encapsuation: 10^{-3} M (noir), $2\ 10^{-3}$ M (rouge), $4\ 10^{-3}$ M (vert). Les propriétés photophysiques ont été détectées dans des conditions aérées ambiantes.

Le processus d'encapsulation peut être facilement contrôlé par le choix approprié de la valeur du pH et de la force ionique. Elle a été évaluée par plusieurs méthodes telles que TEM, EDX, études photophysiques et chromatographie liquide rapide de protéine (FPLC). Toutes les particules isolées du virus (VLP) possèdent une luminescence prononcée (Figure 7 et 8) dans la région visible permettant une application potentielle en microscopie et biomédecine.

Une amélioration remarquable d'un facteur 13 fut observé pour les amphiphiles chargés négativement, fournissant un rendement quantique VLP de 59%. Une telle amélioration après encapsulation ainsi qu'un tel rendement quantique pour des VLPs n'a pas encore été publié.

De plus, un complexe Pt(II) a été synthétisé attaché à des chaînes alkyles sulfatées, ce qui a rendu la perturbation de la structure de la capside icosaédrique. C'est l'un des premiers exemples pour la formation de VLP cylindriques luminescentes par des complexes Pt(II) auto-assemblés.

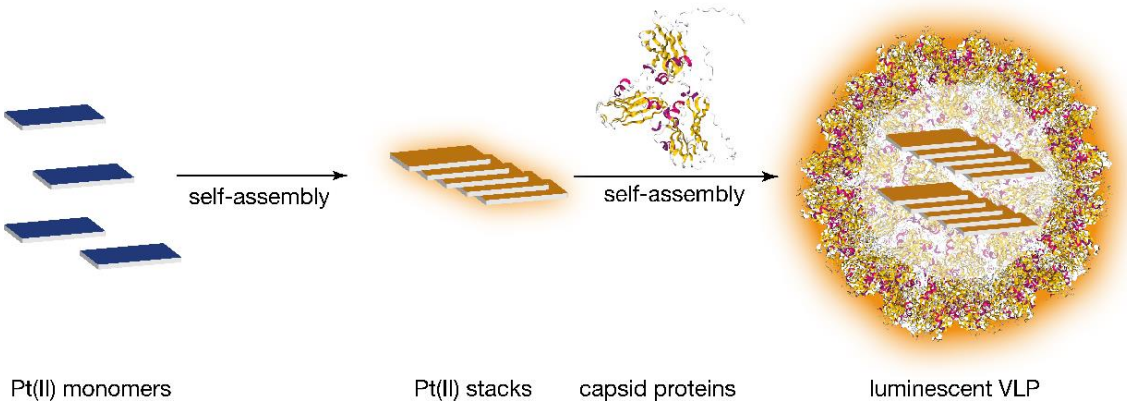

Figure 3: L'illustration de la formation des particules luminescentes pseudo-virales par encapsulation des agrégats de Pt(II) dans les protéine d'enveloppe, qui sont formés par auto-assemblage.

Conclusion

Les complexes **L-Pt$_2$-18C6** et **L-Pt$_2$-18C4** de type dinucléaire N-métallacyclique attachés à des squelettes de type éther-couronne 18C6 et 18C4, respectivement, ont été synthétisés avec succès et leurs propriétés photophysiques ont été sondées. L'architecture permet une détection ratiométrique luminescente des cations potassiques avec excitation possible dans la lumière visible. La constante de liaison déterminée est plus grande que les analogues d'aza-couronne parce que le système ici utilisé a utilisé des couronnes-éthers complètement oxygénées. Les propriétés d'émission des complexes de Pt sont beaucoup plus sensibles à la distance intra-moléculaire entre deux unités que celle des chromophores pyrène largement utilisés, ce qui provoque des signaux spectroscopiques plus importants. Le processus de changement de la nature de l'émission par un simple cation peut être inversé par l'addition de 18-C-6, et a été actif pendant plusieurs cycles.

Un nouveau précurseur de platine hautement réactif qui permet le marquage facile de composés aza-hétérocycliques (par exemple pyridines, imidazoles) dans des milieux aqueux par formation *in situ* d'agrégats complexes hautement émissifs de Pt(II) a été développé. Un dosage a été établi, qui permet l'identification d'analytes à l'aide des empreintes photophysiques de leurs complexes marqués. Des modèles variés tels que l'analyse des composantes principales (PCA) ont été utilisés pour analyser les données, montrant ainsi la formation de clusters distincts dans les diagrammes de résultats.

Nous avons effectué une étude STM et une analyse DFT sur la formation de différents motifs supramoléculaires cycliques discrets polygonaux formés par le complexe Pt(II) à base d'isocytosine à l'interface solution / HOPG par des interactions de type liaison hydrogène entre les groupes isocytosine de **L-Pt-Py-iCyt**. L'approche décrite dans ce travail peut être exploitée pour contrôler la structure supramoléculaire des complexes de Pt(II) à la surface, et par conséquent comme un moyen de modifier les propriétés photophysiques de ces matériaux.

Une série de complexes Pt(II) amphiphiles luminescents a été synthétisée et caractérisée avec succès, et une nouvelle méthode pour la détermination de la concentration d'agrégation critique a été établie. Des particules de type virus (VLP) ont été créées par l'encapsulation des complexes Pt(II) amphiphiles dans les protéines de la capside du virus CCM. Les particules sont luminescentes, excitables par la lumière visible et présentent une réactivité à l'émission lors de l'encapsulation et de la réouverture des capsides protéiques. Ces particules ont un grand potentiel en microscopie et en applications biomédicales, par exemple pour la thérapie photodynamique.

Références

1. G. M. Whitesides and B. Grzybowski, *Science*, 2002, **295**, 2418-2421.
2. J.-M. Lehn, *Angew. Chem. Int. Ed.*, 2013, **52**, 2836-2850.
3. J.-M. Lehn, *Angew. Chem. Int. Ed.*, 1988, **27**, 89-112.
4. F. Biedermann and H.-J. r. Schneider, *Chem. Rev.*, 2016, **116**, 5216-5300.
5. F. J. M. Hoeben, P. Jonkheijm, E. W. Meijer and A. P. H. J. Schenning, *Chem. Rev.*, 2005, **105**, 1491-1546.
6. L. J. Charbonnière, R. F. Ziessel, C. A. Sams and A. Harriman, *Inorg. Chem.*, 2003, **42**, 3466-3474.
7. S. A. McFarland and N. S. Finney, *Chem. Commun.*, 2003, 388-389.
8. M. E. Padilla-Tosta, J. M. Lloris, R. Martónez-Máñez, A. Benito, J. Soto, T. Pardo, M. A. Miranda and M. D. Marcos, *Eur. J. Inorg. Chem.*, 2000, **2000**, 741-748.
9. Miguel E. Padilla-Tosta, José M. Lloris, R. Martínez-Máñez, M. D. Marcos, Miguel A. Miranda, T. Pardo, F. Sancenón and J. Soto, *Eur. J. Inorg. Chem.*, 2001, **2001**, 1475-1482.
10. M. Schmittel, H.-W. Lin, E. Thiel, A. J. Meixner and H. Ammon, *Dalton Trans.*, 2006, 4020-4028.
11. R. Y. Lai, M. Chiba, N. Kitamura and A. J. Bard, *Anal. Chem.*, 2002, **74**, 551-553.
12. Subodh K. Dutta, D. Gan and Marc W. Perkovic, *Eur. J. Inorg. Chem.*, 2003, **2003**, 2812-2819.
13. J. V. Ros-Lis, R. Martinez-Manez, J. Soto, C. McDonagh and A. Guckian, *Eur. J. Inorg. Chem.*, 2006, 2647-2655.
14. J. Brandel, M. Sairenji, K. Ichikawa and T. Nabeshima, *Chem. Commun.*, 2010, **46**, 3958-3960.
15. M.-L. Ho, F.-M. Hwang, P.-N. Chen, Y.-H. Hu, Y.-M. Cheng, K.-S. Chen, G.-H. Lee, Y. Chi and P.-T. Chou, *Org. Biomol. Chem.*, 2006, **4**, 98-103.
16. M. Schmittel and H. Lin, *Inorg. Chem.*, 2007, **46**, 9139-9145.
17. V. Balzani and S. Campagna, *Topics in Current Chemistry - Photophysics of Coordination Compounds II*, 2007.
18. W. Zeghida, C. Besnard and J. Lacour, *Angew. Chem. Int. Ed.*, 2010, **49**, 7253-7256.
19. M. Vishe, R. Hrdina, L. Guénée, C. Besnard and J. Lacour, *Adv. Synth. Catal.*, 2013, **355**, 3161-3169.
20. M. Vishe, R. Hrdina, A. I. Poblador-Bahamonde, C. Besnard, L. Guénée, T. Bürgi and J. Lacour, *Chem. Sci.*, 2015, **6**, 4923-4928.
21. M. Mauro, A. Aliprandi, C. Cebrian, D. Wang, C. Kübel and L. De Cola, *Chem. Commun.*, 2014, **50**, 7269-7272.
22. L. De Cola, M. Mauro, N. Seda Kehr and C. A. Strassert (Westfälische Wilhelms-Universität Münster), WO 2012/117082 A1, 2014.
23. V. M. Miskowski and V. H. Houlding, *Inorg. Chem.*, 1989, **28**, 1529-1533.
24. M. Mydlak, M. Mauro, F. Polo, M. Felicetti, J. Leonhardt, G. Diener, L. De Cola and C. A. Strassert, *Chem. Mater.*, 2011, **23**, 3659-3667.
25. B. Ma, J. Li, P. I. Djurovich, M. Yousufuddin, R. Bau and M. E. Thompson, *J. Am. Chem. Soc.*, 2005, **127**, 28-29.
26. M. Mauro, A. Aliprandi, D. Septiadi, N. S. Kehr and L. De Cola, *Chem. Soc. Rev.*, 2014, **43**, 4144-4166.
27. V. W.-W. Yam, K. H.-Y. Chan, K. M.-C. Wong and B. W.-K. Chu, *Angew. Chem. Int. Ed.*, 2006, **45**, 6169-6173.
28. S. Sinn, F. Biedermann, M. Vishe, A. Aliprandi, C. Besnard, J. Lacour and L. De Cola, *ChemPhysChem*, 2016, **17**, 1829-1834.
29. A. V. Kabanov, E. V. Batrakova and V. Y. Alakhov, *J. Control. Release*, 2002, **82**, 189-212.
30. Z. Liu, D. Liu, L. Wang, J. Zhang and N. Zhang, *Int J Mol Sci*, 2011, **12**, 1684-1696.

31. Z. Wei, J. Hao, S. Yuan, Y. Li, W. Juan, X. Sha and X. Fang, *Int. J. Pharm.*, 2009, **376**, 176-185.
32. W. Ritter, *American Journal of Obstetrics and Gynecology*, 1985, **152**, 945-947.
33. F. G. Latimer, C. M. H. Colitz, N. B. Campbell and M. G. Papich, *American journal of veterinary research*, 2001, **62**, 1606-1611.
34. J. M. Cardot, C. Chaumont, C. Dubray, D. Costantini and J. M. Aiache, *British journal of clinical pharmacology*, 2004, **58**, 345-351.
35. T. P. Moyer, J. R. Charlson, R. J. Enger, L. C. Dale, J. O. Ebbert, D. R. Schroeder and R. D. Hurt, *Clin. Chem.*, 2002, **48**, 1460-1471.
36. A. Satrijo and T. M. Swager, *J. Am. Chem. Soc.*, 2007, **129**, 16020-16028.
37. S. Stewart, M. A. Ivy and E. V. Anslyn, *Chem. Soc. Rev.*, 2014, **43**, 70-84.
38. B. Rout, L. Unger, G. Armony, M. A. Iron and D. Margulies, *Angew. Chem. Int. Ed.*, 2012, **51**, 12477-12481.
39. P. Anzenbacher and M. A. Palacios, in *Chemosensors*, eds. B. Wang and E. V. Anslyn, John Wiley & Sons, Inc., Weinheim, 1st edn., 2011, pp. 345-368.
40. J. V. Barth, G. Costantini and K. Kern, *Nature*, 2005, **437**, 671-679.
41. M. Stöhr, M. Wahl, C. H. Galka, T. Riehm, T. A. Jung and L. H. Gade, *Angew. Chem. Int. Ed.*, 2005, **44**, 7394-7398.
42. J. A. A. W. Elemans, R. Van Hameren, R. J. M. Nolte and A. E. Rowan, *Adv. Mater.*, 2006, **18**, 1251-1266.
43. G. P. Spada, S. Lena, S. Masiero, S. Pieraccini, M. Surin and P. Samorì, *Adv. Mater.*, 2008, **20**, 2433-2438.
44. T. Kudernac, S. B. Lei, J. A. A. W. Elemans and S. De Feyter, *Chem. Soc. Rev.*, 2009, **38**, 402-421.
45. D. Bonifazi, S. Mohnani and A. Llanes-Pallas, *Chem. Eur. J.*, 2009, **15**, 7004-7025.
46. J. A. G. Williams, in *Top Curr Chem*, eds. V. Balzani and S. Campagna, Springer, Heidelberg, 1st edn., 2007, vol. 281, pp. 205-268.
47. W. Lu and C. M. Lieber, *Nat. Mater.*, 2007, **6**, 841-850.
48. B. T. Khan and S. M. Zakeeruddin, *Transition Met. Chem.*, 1991, **16**, 119-121.
49. H. Rauter, I. Mutikainen, M. Blomberg, C. J. L. Lock, P. AmoOchoa, E. Freisinger, L. Randaccio, E. Zangrando, E. Chiarparin and B. Lippert, *Angew. Chem. Int. Ed.*, 1997, **36**, 1296-1301.
50. D. Gupta, M. Huelsekopf, M. M. Cerda, R. Ludwig and B. Lippert, *Inorg. Chem.*, 2004, **43**, 3386-3393.
51. D. Gupta, M. Roitzsch and B. Lippert, *Chemistry A European Journal*, 2005, **11**, 6643-6652.
52. A. G. Quiroga, *J. Inorg. Biochem.*, 2012, **114**, 106-112.
53. X. Wang, X. Wang and Z. Guo, *Account. Chem. Res.*, 2015, **48**, 2622-2631.
54. Z. Xue, M. Lin, J. Zhu, J. Zhang, Y. Li and Z. Guo, *Chem. Commun.*, 2010, **46**, 1212-1214.
55. N. Margiotta, N. Denora, R. Ostuni, V. Laquintana, A. Anderson, S. W. Johnson, G. Trapani and G. Natile, *J. Med. Chem.*, 2010, **53**, 5144-5154.
56. I. Łakomska, *Inorg. Chim. Acta*, 2009, **362**, 669-681.
57. M. Lackinger, S. Griessl, W. M. Heckl, M. Hietschold and G. W. Flynn, *Langmuir*, 2005, **21**, 4984-4988.
58. A. Llanes-Pallas, C.-A. Palma, L. Piot, A. Belbakra, A. Listorti, M. Prato, P. Samorì, N. Armaroli and D. Bonifazi, *J. Am. Chem. Soc.*, 2009, **131**, 509-520.
59. J. M. MacLeod, O. Ivasenko, C. Fu, T. Taerum, F. Rosei and D. F. Perepichka, *J. Am. Chem. Soc.*, 2009, **131**, 16844-16850.
60. O. Ivasenko and D. F. Perepichka, *Chem. Soc. Rev.*, 2011, **40**, 191-206.
61. M. El Garah, R. C. Perone, A. S. Bonilla, S. Haar, M. Campitiello, R. Gutierrez, G. Cuniberti, S. Masiero, A. Ciesielski and P. Samorì, *Chem. Commun.*, 2015, **51**, 11677-11680.
62. R. Otero, M. Schock, L. M. Molina, E. Laegsgaard, I. Stensgaard, B. Hammer and F. Besenbacher, *Angew. Chem. Int. Ed.*, 2005, **44**, 2270-2275.

63. W. Xu, R. E. A. Kelly, H. Gersen, E. Laegsgaard, I. Stensgaard, L. N. Kantorovich and F. Besenbacher, *Small*, 2009, **5**, 1952-1956.
64. L. K. Wang, H. H. Kong, C. Zhang, Q. Sun, L. L. Cai, Q. G. Tan, F. Besenbacher and W. Xu, *ACS Nano*, 2014, **8**, 11799-11805.
65. A. Ciesielski, S. Colella, L. Zalewski, B. Bruchmann and P. Samorì, *CrystEngComm*, 2011, **13**, 5535.
66. M. Cai, A. L. Marlow, J. C. Fettinger, D. Fabris, T. J. Haverlock, B. A. Moyer and J. T. Davis, *Angew. Chem. Int. Ed.*, 2000, **39**, 1283.

Chapter I

General Introduction

Abstract

In this chapter, some general concepts forming the fundament for the understanding of the thesis are introduced and explained. Square planer Pt(II)-complexes are the unifying element of each chapter. Therefore, a fundamental discussion about the interaction of light and matter, basics about transition metal complexes with a particular attention to Pt(II)-complexes are presented herein. Furthermore, principals of supramolecular interactions and self-assembly are demonstrated as well as certain examples for binding motifs such as H-bonding in isocytosine and the self-organization of virus coat proteins. General aspects of chemical sensing, namely differential and single analyte sensing, are elucidated. A literature overview of each discussed field of interest renders a state-of-the-art prospect.

Light-matter interactions

Light can be understood as an electromagnetic wave consisting of synchronized oscillations of electronic and magnetic fields are propagating through space. The amplitude vectors for the magnetic and electronic parts are perpendicular to one another as well as to the direction of propagation (transverse wave). Electromagnetic waves are characterized either by their wavelength (UV-Vis spectroscopy) or their frequency (NMR spectroscopy), which are both expressions for the energy of the wave (see Eq. 1.1 and 1.3).

$$E = h\nu \qquad \text{Eq. 1.1}$$

Planck found a direct correlation (Eq. 1.1) between the energy (E) and the frequency (ν) of an electromagnetic wave with the constant of proportionality being the Planck constant h.[1] The frequency is linked to the wavelength *via* the de Broglie expression[2] (Eq. 1.2), in which c denotes the speed of light.

$$\lambda = \frac{c}{v} \qquad \text{Eq. 1.2}$$

Substitution of the frequency in Eq. 1.1 leads to Eq. 1.3 displaying the correlation between the wavelength and the energy of the electromagnetic wave.

$$E = \frac{hc}{\lambda} \qquad \text{Eq. 1.3}$$

A general deduction from these equations is: the longer the wavelength, the smaller the frequency, the lower the energy of the wave. Consideration of a small part of the electromagnetic spectrum being accessible to the human eye, namely the visible region (380 – 750 nm), allows a direct correlation between color and energy (Figure 1.1). The blue part indicates waves (short wavelength) of higher energy, whereas the red part is ascribed to waves (long wavelength) of lower energy within the visible region.

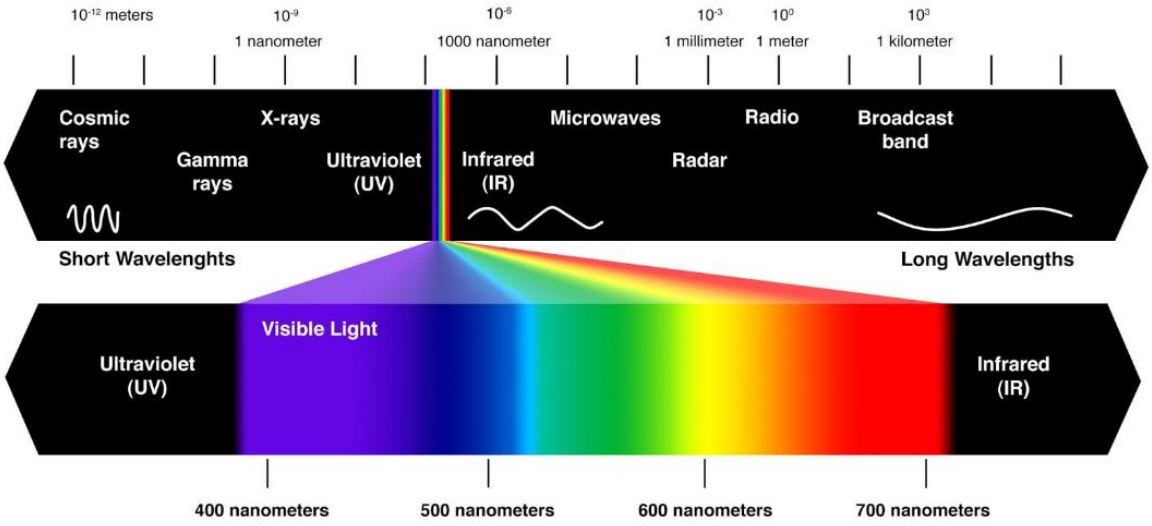

Figure 1.1: Electromagnetic spectrum of light with a closer insight into the visible region (380 - 750 nm).

Light as an oscillating field can interact with matter by means of an energetic perturbation of the ground state of the matter of concern (molecules, solid semiconductors). As a reasonable simplification, one can understand the interaction between light and matter as written in Eq. 1.4, where *A* denotes a molecule in the ground state, *hv* the energy of the incident light (photon) and *A** the molecule in its excited state.

$$A + hv \rightarrow A^* \qquad \text{Eq. 1.4}$$

Commonly, one molecule is excited by one photon (exceptions such as two-photon excitation do exist, but are not considered here) to its excited state.[3] A molecule possesses several degrees of freedom, namely translational, vibrational and rotational motions as

well as electronic degrees of freedom, which allows for an interaction with incident light. Light of different energy (different wavelength) interacts in distinct manners with matter. Therefore, microwave irradiation leads to an excitation of the rotational motion of molecule which renders higher friction and thus a heating effect (dipole excitation in the kitchen microwave). Vibrational motions are excited by Raman or Infrared spectroscopy, which are based on inelastic scattering or the absorption of light, respectively.[4, 5] Light can be also absorbed in the visible region by the excitation of electronic states. An electronic transition can be understood as the rearrangement of the electron density of the molecule by the incident light.

The electron-density distribution in a molecule is defined by the atomic orbitals interactions (LCAOMO principle: linear combinations of atom orbitals to molecule orbitals), which are in turn the bonds of the molecule such as σ and π. Therefore, an electronic excitation such as an electron promotion from a π to a π* orbital is accompanied by a change in the bond order. An overview of possible electronic excitations of the organic molecule formaldehyde by light is depicted in Scheme 1.1.

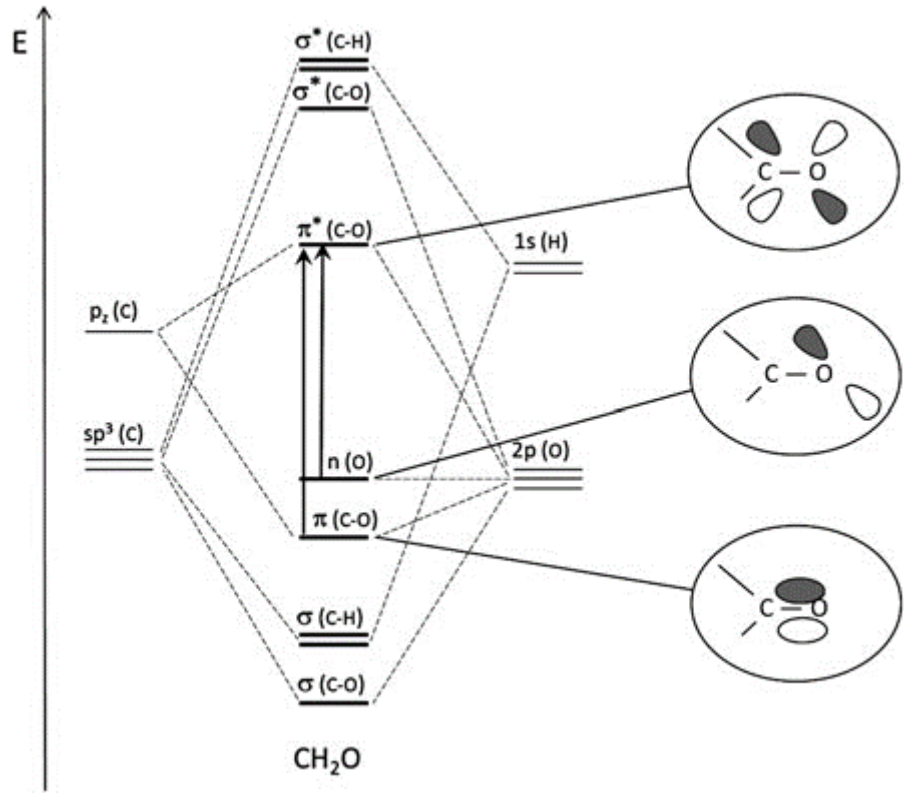

Scheme 1.1: Molecular orbital diagram of formaldehyde and possible interactions with light, namely the transitions n → π* and π → π*.[3] © 2012 Springer

A plot in which the strength of absorption (absorbance or optical density), namely the diminishing of the incident light intensity by the material, versus the wavelength is called absorption spectrum. Lambert and Beer found a direct correlation between the optical density (*A*), the concentration of a molecule (*c*), thickness of the illuminated layer (*d*) and the extinction coefficient (ε):

$$A = \lg\left(\frac{I_0}{I_1}\right) c \cdot d \cdot \varepsilon \qquad \text{Eq. 1.5}$$

In Eq. 1.5, I_0 denotes the intensity of the incident light without a sample in the light path and I_1 the intensity of the transmitted light.

The extinction coefficient is a materials constant defining the probability for an electronic transition (excitation). From a theoretical point of view the probability for a transition from an initial state *i* to and final state *f* is given by the transition dipole moment M_{if} [3, 6]:

$$M_{if} = \langle \Psi_i | \mu | \Psi_f \rangle \neq 0 \qquad \text{Eq. 1.6}$$

where, Ψ_i and Ψ_f denote the electronic wavefunctions in their initial state and final state, respectively and μ is the dipole moment operator. A transition is only possible, if the transition dipole moment does not vanish. Extensions of Eq. 1.6 enable a classification into allowed ($M_{if} \neq 0$) and forbidden ($M_{if} = 0$) transitions, the so-called selection rules. A correlation with the aforementioned experimentally obtained extinction coefficient thus allows for a classification of transitions by means of the magnitude of the ε values. For instance, the two major selection rules symmetry and spin selection rule result in very low ε values of about 1 and 10^2 M^{-1} cm^{-1}, respectively.[3, 7] Symmetry selection is determined by the geometry of the system and waveform of the incident light.[6] The spin has to be commonly preserved during an electronic transitions on account of the angular momentum conservation. Therefore, singlet-singlet as well as triplet-triplet transitions are allowed while singlet-triplet and triplet-singlet transitions are commonly forbidden (for exceptions, *e.g.*, through spin-orbit couplings, *vide infra*).

After the absorption of a photon the molecule results in an electronic excited state (Eq. 1.4) which is commonly transient state. The system relaxes to its thermodynamic ground state by several deactivation pathways. The excitation and relaxation for electronic transitions can be summarized in a Perrin-Jablonski term Scheme (Scheme 1.2).[8]

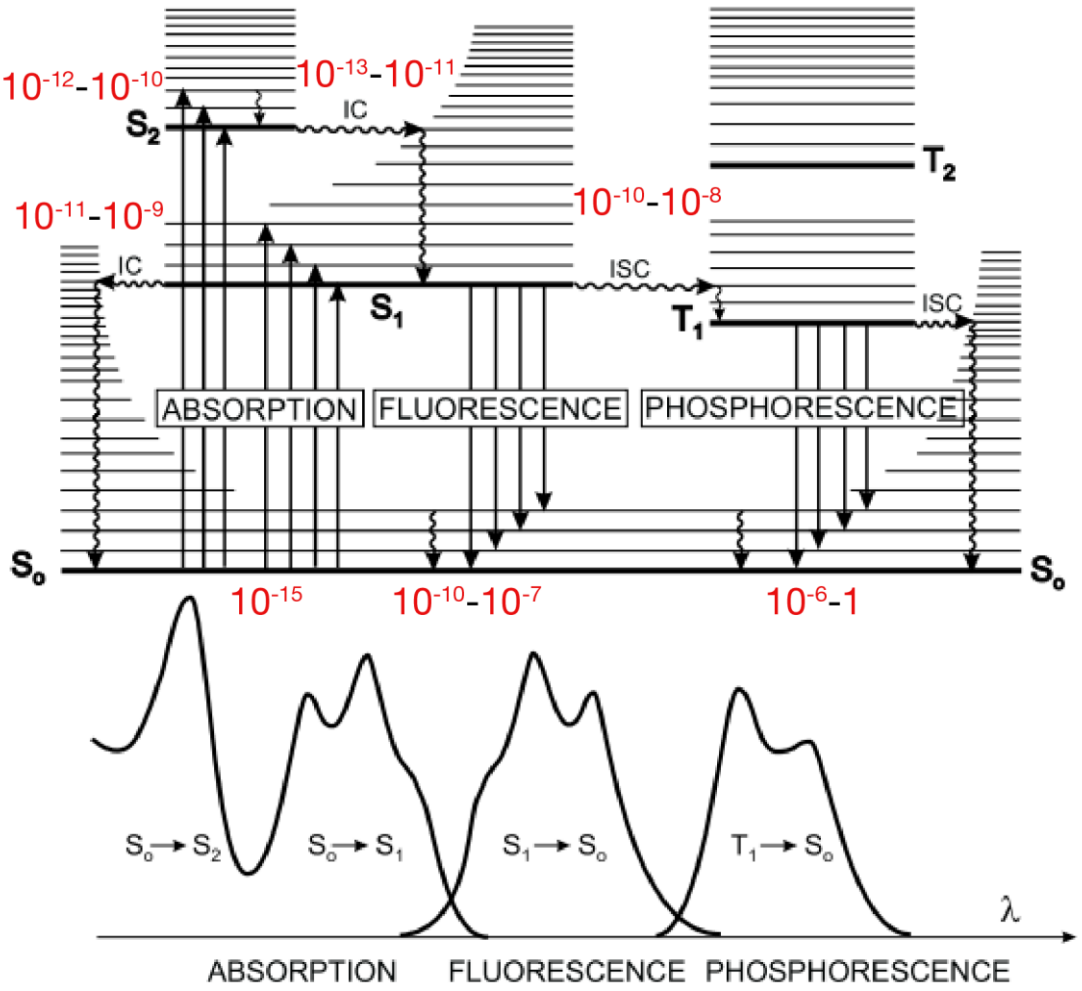

Scheme 1.2: Perrin-Jablonski term Scheme illustrating the absorption of light and resultant photophysical processes. Typical process times (in s) for each transition are depicted in red. Photochemical processes are omitted for simplicity.[7] © 2012 Wiley

In the Perrin-Jablonski diagram, S_0 denotes the singlet ground state, which represents the most common situation for closed-shell molecules (except oxygen for which the thermodynamic ground state is of triplet character). Molecules usually preserve in there electronic (S_0) and vibrational ground state (first horizontal line in S_0 in the diagram) ground state at room temperature. From this state, generally a very fast absorption of a photon (10^{-15} s) leads to the excitation into excited singlet states S_1, S_2 to S_N (spin selection rule, *vide supra*). Transitions are depicted as vertical arrows since it is assumed that atom coordinates do not change (geometry persistence) during an electronic transition (Born-Oppenheimer approximation).[9] In most cases the molecule relaxes quickly to its first excited electronic state (S_1) *via* internal conversion (IC, 10^{-13} - 10^{-11} s) and the lowest vibrational state (10^{-12} - 10^{-10} s) *via* vibrational relaxation (Kasha's rule[10],

for exceptions: azulenes[11] and metalporphyrins[12]). The system can now undergo several deactivation pathways in order to relax to its thermodynamic ground state. The process of the emission of a photon accompanied by a relaxation $S_1 \rightarrow S_0$ is called fluorescence (10^{-10} - 10^{-7} s). This phenomenon competes with non-radiative deactivations either to the singlet ground state ($S_1 \rightarrow S_0$) or to the lowest excited triplet state ($S_1 \rightarrow T_1$) *via* internal conversion (IC, 10^{-11}- 10^{-9} s) and intersystem crossing (ISC, 10^{-10} - 10^{-8} s), respectively. Noteworthy, the rate for the internal conversion process increases exponentially with a decreasing energy gap between the excited and the ground state (*energy gap law*).[13, 14] From the T_1 state, the excited molecule can relax to its singlet ground state ($T_1 \rightarrow S_0$) either radiationless *via* intersystem crossing (ISC, 10^{-10} - 10^{-8} s), or by the emission of a photon which is called phosphorescence (10^{-6} - 1 s).

The energy loss during the process of excitation of a luminophore and the subsequent emission (see Scheme 1.2) is called Stokes shift. The Stokes shift expresses the energy difference of the absorption (excitation) and the emission and is strongly dependent on the transition dipole moment (Lippert equation) and thus also on the polarity of the solvent. In order to determine the Stokes shift, the emission and absorption (excitation) spectra are depicted as functions of wavenumbers. The difference between the maximum of the first excitation (absorption) and the maximum of the emission renders then the Stokes shift.[7, 15, 16]

$$\nu_{SS} = \nu_{Em,max} - \nu_{Em,max} \qquad \text{Eq. 1.7}$$

In some cases such as imaging it is customary and more meaningful to display the obtained values in nm, since equal energetic differences can result in strongly varying spectral distinction depending on the region of the electromagnetic spectrum (ν_{SS} = 242.8 cm^{-1} : 303 – 300 nm = 3 nm, 764 – 750 nm = 14 nm).

Usually, the spin-changing intersystem crossing from the lowest excited singlet state to the triplet manifold follows the spin selection rule and is considered as forbidden (low probability) which explains why commonly no phosphorescence is observed for organic molecules in solution at room temperature. Nevertheless, the present coupling of spin with orbital motions (spin-orbit coupling, SOC) can lead to a redirecting of the spin-angular momentum of an electron and thus allow multiplicity changing transition. El-Sayed concluded on the basis of the SOC that the probability (experimentally the rate) for an intersystem crossing (ISC) accompanied by a change of the orbital type (*e.g.*

$^1\pi\pi^* \rightarrow {}^3n\pi^*$) is strongly increased in comparison to an ISC featuring an orbital type conservation (*e.g.* $^1\pi\pi^* \rightarrow {}^3\pi\pi^*$).[17] The SOC is dependent on the nuclear charge and is therefore pronounced under the influence of heavy atoms. So, the fluorescence can be efficiently quenched by for instance the collision with Iodine which enables an ISC (due to the enhanced SOC) to a non-emissive triplet manifold. On the other hand, the introduction of a heavy metal into the molecular framework can enable ISCs to emissive triplet-states and thus allow room temperature phosphorescence.

The rate constants for processes described above are experimentally accessible by the excited-state lifetime and the emission quantum yield. It is assumed that decay rate for emission depends only on the concentration of excited molecules, which leads to a first order kinetic:

$$\frac{\partial[A^*]}{\partial t} = -(\Gamma + k_{nr})\,[A^*] \qquad [A^*] = [A_0^*]\,e^{-(\Gamma + k_{nr})\,t} \qquad \text{Eq. 1.8}$$

where *t* denotes the time after excitation, *[A*]* and *[A_0*]* denotes the concentration of excited molecules at time *t* and 0, respectively, *Γ* the radiative decay rate and k_{nr} the non-radiative relaxation rate. The excited-state lifetime τ can be understood as the reciprocal of all decay rate:

$$\tau = \frac{1}{\Gamma + k_{nr}} \qquad \frac{[A^*]}{[A_0^*]} = \frac{I}{I_0} = e^{-\frac{t}{\tau}} \qquad \text{Eq. 1.9}$$

The substitution of the concentrations terms by the detectable emission intensity (photon counts) enables a photophysical interpretation of τ. Therefore, the excited-state lifetime τ can be seen either as the average time for a photon being emitted from the excited-state, or as the time at which the intensity decreased (*I*) to *1/e* (37%) of the initial onset intensity (I_0).

Consideration of the Perrin-Jablonski term diagram (Scheme 1.2) allows for a splitting of τ into parts for the fluorescence and phosphorescence emission:

$$\tau_F = \frac{1}{k_F + k_{ISC} + k_{IC}} \qquad \tau_P = \frac{1}{k_P + k'_{ISC}} \qquad \text{Eq. 1.10}$$

where, k_F and k_P denote the spin-conserving and spin-changing radiative decay rate, respectively, k_{ISC} refers to the intersystem crossing process rates and k_{IC} to the internal conversion decay rate.

The photoluminescence quantum yield φ is defined as the ratio between the number of emitted and absorbed photons.[15] An alternative definition is based on the ratio between

the radiative rate constant and the sum of all decay rate constants. This treatment in turn allows a sequestering of the terms into its fluorescence and phosphorescence describing parts:

$$\varphi = \frac{k_r}{\Gamma + k_{nr}} \quad \text{Eq. 1.11}$$

$$\varphi_F = \frac{k_F}{k_F + k_{ISC} + k_{IC}} \qquad \varphi_P = \frac{k_P}{k_P + k'_{ISC}} \varphi_{ISC} \quad \text{Eq. 1.12}$$

where φ_{ISC} refers to the quantum efficiency for the singlet-to-triplet intersystem crossing.[7] Substitution with the equations Eq. 1.9 and 1.10 lead to the following relationship between excited-state lifetime and quantum yield:

$$\varphi = k_r \, \tau \qquad \varphi_F = k_F \, \tau_F \quad \text{Eq. 1.13}$$

$$\varphi_{ISC} = \frac{k_{ISC}}{k_F + k_{ISC} + k_{IC}} = k_{ISC} \, \tau_F \quad \text{Eq. 1.14}$$

$$\varphi_P = \varphi_{ISC} \, k_P \, \tau_P \quad \text{Eq. 1.15}$$

Besides the calculation of the radiative decay rates, also the non-radiative decay rate are accessible by the quantum yield and excited-state lifetime measurements:

$$k_{nr} = \frac{\varphi - 1}{\tau} \quad \text{Eq. 1.16}$$

Transition metal complexes

The *d*-block metals of the periodic table of elements provide certain peculiarities compared to main group elements. Firstly, the fact, that degenerated *d* states are not fully occupied allows for these metals additional light-matter interactions, namely *d-d* transitions. Secondly, heavy atoms can promote the intersystem crossing towards emissive triplet-sates by enhancing the spin-orbit coupling. Coordination complexes featuring these *d*-block metals, also known as transition metals, not only enable additional electronic transitions (*d-d*) but can also render room temperature phosphorescence.[18] Thirdly, transition metals provide a variety of different coordination geometries, not only between the elements but also between different oxidation states and depending on the ligand-field strength (*vide infra*). Therefore, transition-metal complexes (TMCs) can serve as scaffolds for molecular and supramolecular architectures.[19]

Significant attention was devoted to the d^6, d^8 and d^{10} transition metals of the second and third row, namely Ru(II)[20-23], Os(II)[24], Re(I)[25], Ir(III)[26, 27], Pd(II)[28, 29], Pt(II)[30, 31], Ag(I)[32] and Au(I).[33-36] Nevertheless, complexes of Cu(I)[37-41] and Zn(II)[42-44] were also comprehensively studied on account of their appealing photophysical properties. In

general, the mentioned TMCs can enable light absorption covering the entire visible region, tunable emission at room temperature, long-excited lifetimes, high photoluminescence quantum yields and oxidation/reduction potentials approachable in a variety of electrochemical windows.

The particular photophysical and electrochemical properties of TMCs make them suitable for a broad range of application in several fields such as photocatalysis, [45-47] artificial photosynthesis,[48, 49] dye-sensitized solar cells,[23, 50-53] optoelectronics,[54, 55] electrochemieluminescence (ECL),[56, 57] non-linear optical materials,[58] metallogelators,[59] sensing [60-62] and bioimaging.[63, 64] A peculiar interest is present in the area of illumination devices, namely highly efficient organic light emitting diodes (OLEDs)[54] and light-emitting electrochemical cells (LEECs).[18]

Ligand-field theory

A first, qualitative and quantitative, insight into the photophysical and electrochemical properties of TMCs is given by ligand-field theory (LFT).[65] This theory is founded on the basis of the crystal-filed theory (CFT),[66] which interprets the ligands of a coordination compounds as point charges. Both theories use the term ligand field to describe the effect of the splitting of the originally degenerated *d*-orbitals.[67]

In CFT, the lone pairs of the coordinating ligands are interpreted as negative point charges which repel the *d*-orbitals of the central metal. The result of this repulsion is a splitting of the degenerated *d*-orbitals into sets of different energy, which in turn is determined by the electronic configuration. Each *d*-orbital is repelled to an individual extent due to its shape and orientation along the coordination axes (Figure 1.2).

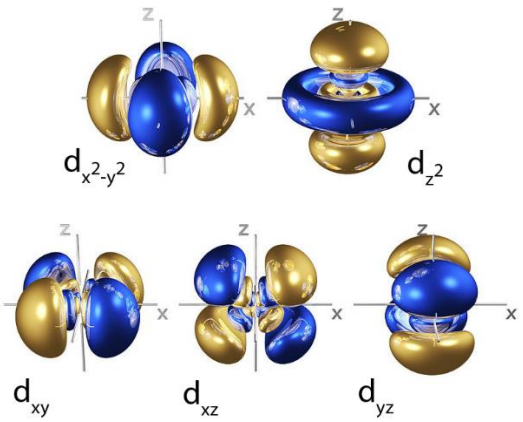

Figure 1.2: 3D representation of the *d*-orbitals of a transition metal.

The extent of the splitting is determined by ligand-field strength and is formulated as the ligand-field splitting parameter Δ_i, where i denotes the adopted geometry. The geometry which is finally adopted for the resulting complexes is based on the most stable thermodynamic configuration. TMCs featuring central metals with d^6 electron configuration such as Fe(II), Ru(II), Os (II) and Ir(III) commonly possess an octahedral geometry. The approaching ligand field strongly destabilizes the electrons of the *d*-orbitals oriented along the coordination axes, namely d_{z^2} and $d_{x^2-y^2}$. The electron in the orbitals oriented in between the coordination axes (d_{xy}, d_{xz}, d_{yz}) are repelled to a lesser extent resulting in a splitting into two sets of orbitals (t_{2g} and e_g*). The difference between the two resulting sets is described as the octahedral ligand-field splitting parameter Δ_O. This parameter directly describes the energy gap between the occupied (t_{2g}) and unoccupied (e_g*) orbitals, which lies often in the visible region explaining the color of many transition metal complexes (these transitions are comparably weak due to the Laporte selection rule[68]). Other commonly observed geometries in TMCs are linear, tetrahedral and square planar coordination. The later one is usually adopted by d^8 transition metals such as Rh(I), Ir(I), Au(III), Pd(II) and Pt(II) and is particularly interesting for this thesis.

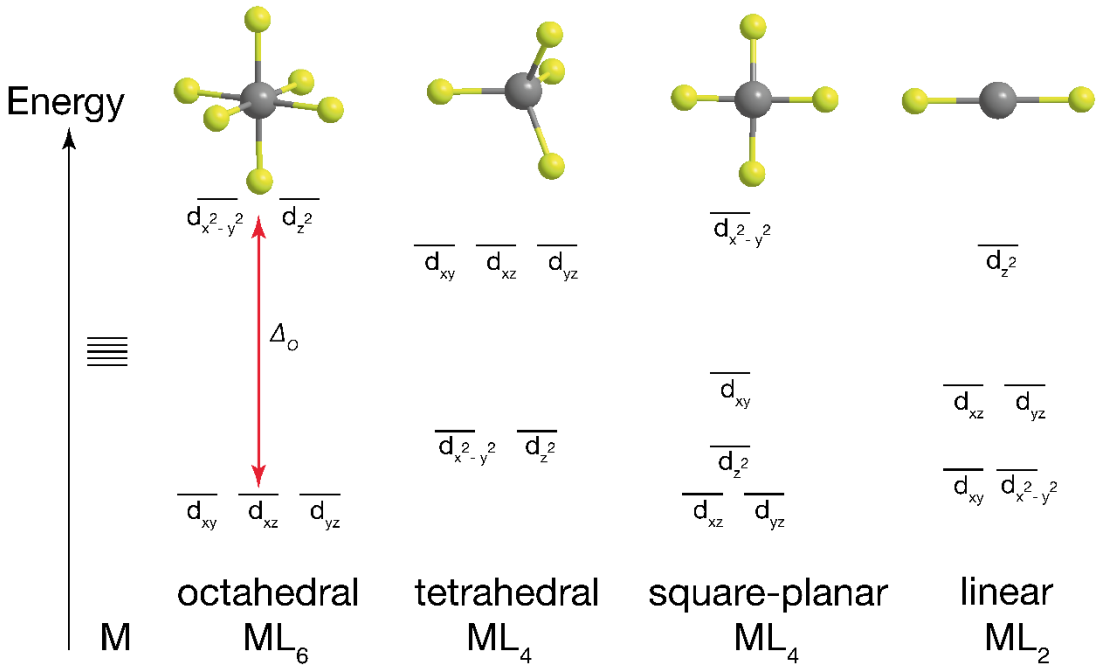

Scheme 1.3: Overview over the common coordination geometries for transition metal complexes (TMCs). The energetic diagrams are based on the crystal-field theory.

Pt(II)-complexes usually adopt a square-planar geometry in which the orbitals along the coordination axis (xy) are strongly repelled in contrast to those orbitals exhibiting only a small spatial distribution in the plane along the axis. The strongly simplified CFT does not account for certain observations such as unexpectedly strong binding. The more sophisticated extension of this model, the ligand-field theory (LFT), takes the molecular orbital (MO) theory and thus a mixing of metal and ligand orbitals into account. Similar to the LCAO-MO approach, a formation of symmetry-adapted linear combinations (SALCs) by the valence orbitals of central metal and the coordinating ligands is assumed.[67] Empirical overlap and energy consideration enables an estimation of the relative energy and positioning of the resulting molecular orbitals. These considerations are exemplified for an octahedral TMC for which the coordinated ligands feature a π-system in Scheme 1.4. The resulting SALCs are often named *d*π orbitals or π_M and π_L assigning the predominant contribution by the metal and ligand, respectively.

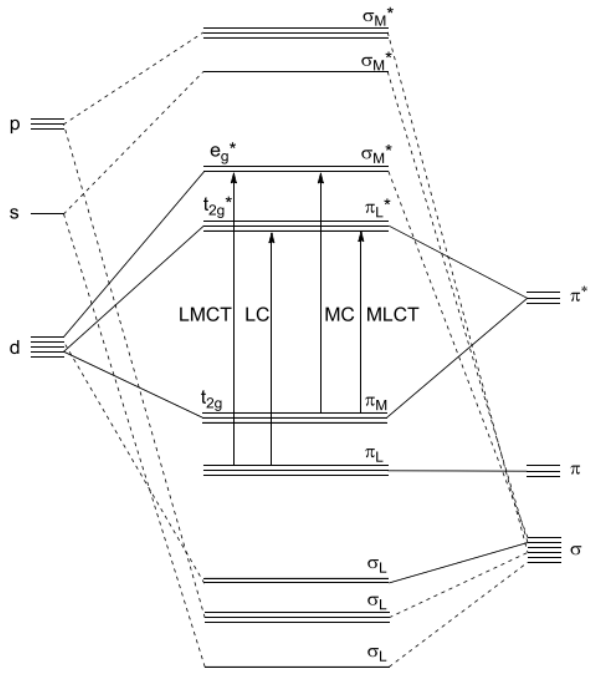

Scheme 1.4: Simplified MO diagram illustrating the mixing of metal *d* with ligand π orbitals to symmetry adapted linear combinations.[69] An octahedral geometry is assumed.

The excitation by light of a TMC complex featuring the formation of dπ orbitals can be classified as follows:

a) Ligand centered (LC) transitions involve mainly bonding π_L and anti-bonding π_L* orbitals of the ligand. The resulting excited state is ascribed as ligand-centered state and can give rise to an emission event. If the orbitals are

located on different ligands, then the excitation is accompanied by an inter-ligand or ligand-to-ligand charge transfer (LLCT).

b) Metal centered (MC) transitions involve mainly the metal *d*-orbitals (*d*-*d* transitions), which are forbidden by the Laporte selection rule in a strictly centrosymmetric complex.[68] The resulting metal centered excited state (MC) are mostly accompanied by a radiationless relaxation to the ground-state on account of the strongly perturbed geometry (antibonding e_g* is occupied)

c) Metal-to-ligand charge transfer (MLCT) transitions involve mainly the excitation from metal *d*-orbitals to ligand π* orbitals. Often these bands occur in the visible region featuring a relatively high oscillator strength.

d) Ligand-to-metal charge transfer (LMCT) transitions involve mainly ligand located π orbitals and anti-bonding metal *d*-orbitals. Both described charged-transfer states can be emissive, typically featuring a broad emission profile on account of the large dipole moment of the excited state. The coupling to the polar solvent molecules leads to a smearing out of the vibrational fine structure at ambient conditions, which is usually regenerated at lower temperature (77 K).[70, 71]

The relative energetic position of the mentioned states is very important for the resulting photophysical and electrochemical properties. For instance, a strong ligand field strength destabilizes the e_g* orbitals resulting in a strong energetic lifting of the MC states, which in turn enables luminescence at room temperature.[72] On the other hand, a destabilization of the t_{2g} orbitals leads to a shift of the oxidation potential to more negative values allowing for a more facile oxidation. Thus, the features of interest can be tuned by the variation of the ligand system (*e.g.* substitution, extension of π-system) and the central metal (*e.g.* size of the ion, electron configuration).

Photophysics of Pt(II)-complexes

In each chapter of this thesis, the special photophysical properties of square-planar Pt(II) are exploited in several ways. Therefore, a deeper insight into the photophysics of the single molecule and the emerging properties upon aggregation is presented. As mentioned above, Pt(II)-complexes adopt in most cases a square-planar geometry with a coordination number of four. This geometry enables a stacking (the complexes can be considered as flat molecular sheets). The z-directional supramolecular self-assembly is

most likely driven by dipole, quadrupole (π-π) interactions, hydrophobicity/solvatophobicity effects and dispersion interactions (London forces). The formation of ground-state dimers renders a dramatic change in the photophysical properties which is illustrated in Scheme 1.5.

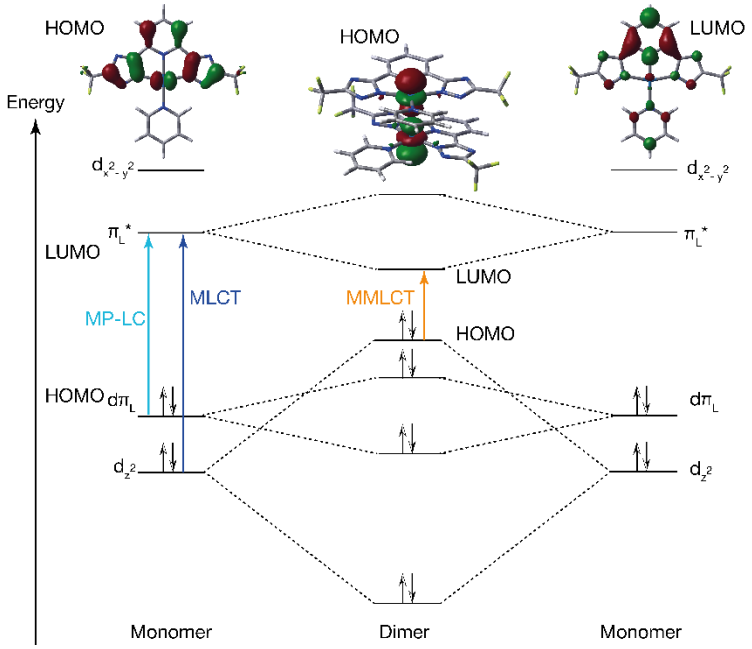

Scheme 1.5: Simplified MO diagram of a monomeric square-planar Pt(II)-complex featuring ligands with a π-system. Upon dimer formation/aggregation of Pt(II)-complexes, their d_{z^2} orbitals strongly interact with each other, resulting in novel transition (MMLCT) that are of lower energy than the ones of the monomeric species (MP-LC, MLCT). The frontier orbitals for the typical framework **L-Pt-Py** utilized in this thesis are calculated and depicted as Kohn-Sham orbitals (isovalue=0.04). Left: HOMO of the monomer, Center: HOMO of the dimer, Right: LUMO of the monomer (similar for dimer).

In a molecularly dissolved condition and thus in a monomeric state, the lowest energetic transitions are ascribed to as metal-perturbed ligand centered (MP-LC) and metal-to-ligand charge transfer (MLCT). The highest-occupied molecular orbital (HOMO) is predominantly of ligand π character with partial metal contribution (see Scheme 1.5 top) whereas the lowest-unoccupied molecular orbital (LUMO) is prevalently of ligand π* character. Although in most cases the lowest energetic transition is a spin allowed MLCT,[73] the lowest excited-state is of ligand centered character featuring a multiplicity of three (^{3}LC).[74] The facile transition from singlet-to-triplet excited state (ISC) is based on the strong spin-orbit coupling (SOC) of the heavy metal platinum. From this state, an emission with a structured profile arises featuring a short lifetime of a few nanoseconds and a very low quantum yield. Oftentimes, no room temperature emission

can be detected for the monomeric state, but 77K experiments enables the resolution of the emission and the measurement of then very long excited-state lifetimes (few μs) which is indicative of the phosphorescent character of the emission.[75, 76]

Upon aggregation, by for instance dimer formation, at higher concentrations or when covalently tied together by a molecular scaffold, the platinum centers interact with each other (close proximity of 3.5Å = van der Waals radius). The z-directional stacking event is directly correlated to an interaction of the d_{z^2} orbitals. The strong destabilization effect of these filled orbitals result in a novel HOMO in contrast to the monomeric state. The excitation of the aggregated form is therefore resulting in a HOMO-LUMO transition of lower energy in comparison the monomeric form. On account of the ground-state metal interactions this transition is called metal-metal-to-ligand charge transfer (MMLCT). The resultant lowest excited state is due to the strong SOC again of triplet character (^{3}MMLCT) and renders a stronger, now featureless emission with extraordinary long excited-state lifetime at room temperature. Importantly, the energy of the HOMO-LUMO gap depends on the Pt-Pt distance and can therefore be used as read out of the aggregation or the other way around: a difference in aggregation results in a different energy gap and thus emission wavelength.

Consideration of the CFT and the resultant MO diagram for a square planar Pt(II)-complex reveals the antibonding $d_{x^2-y^2}$ being strongly destabilized. A population of this orbital by excitation lead to an excited MC state (*d*-*d*). These states, as mentioned before, are considered to be non-emissive and efficiently decay to the ground state by release of heat. A strong ligand-field and, in particular, a strong σ-donation enables a stronger destabilization of the MC states omitting any thermal accessibility from the other states (Figure 1.3).

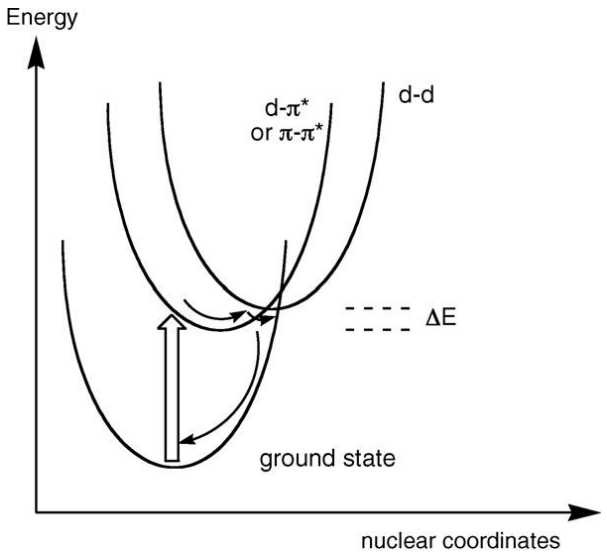

Figure 1.3: Harmonic potentials illustrating the ground and excited states of a Pt(II)-complex. The non-emissive *d-d* states are thermally accessible from other (emissive) states such as MLCT or LC.[77] © 2008 Elsevier

N-metallacycles

Chelating N-metalacyclic ligands provide certain advantages for the creation of photoactive metal complexes over their polypyridyl and N-heterocyclic carbene analogues. The strong σ- and π-donating abilities are commonly accompanied by a red shifted absorption enabling excitation over a broad spectrum in the visible region. Furthermore, metal-centered orbitals, which are often responsible for a fast radiationless decay to the ground-state, are destabilized and no longer thermally excitable resulting in room-temperature emission and long excited-state lifetimes.[36, 78, 79]

The formation of N-metallacycles is conceptually akin to a cyclometalation process, in which a C-M σ-bond formation (M = transition metal) is mediated by the coordination of an additional donor within a multidentate ligand. Firstly, the coordination of a donor towards the metal center leads to an activation of the C-H (N-H) bond on account of the electron density alteration on the metal center and steric constraints. The close proximity of cyclic intermediate is seen as the key feature for the reduction of the entropic and enthalphic costs.[80] Secondly, the deprotonation and M-C (M-N) σ–bond formation render the ring closure. In general, various kinds of C-R and N-R groups have been utilized in cyclometallated complexes and N-metallacycles, respectively, but mostly sp^2 hybridized in aromatic ring systems are applied providing additional π accepting/donor abilities.[79]

Throughout this thesis, a photophysically well understood coordination framework is used which enables an emission readout at room temperature not only for the aggregated but also for the disaggregated specimen.[81] The scaffold consists an N-metallacycling terdentate ligand (**L-2H**), a Pt(II) metal center and an ancillary ligand. **L-2H** is composed of a central pyridine substituted at position 2 and 6 with 1*H*-1,2,4 triazolyl groups. These flanking groups are substituted, remotely to the aza-proton, with electron-withdrawing trifluoromethyl groups. The deprotonation upon N-metallacyclation is often facilitated by addition of a base. The usage of pyridine as the ancillary ligand results in a thermodynamically stable and planar complex (π-system renders planarization). This complex, **L-Pt-Py**, exhibits a room temperature emission in organic solvents such as tetrahydrofuran (THF) or dichloromethane (DCM) featuring a structured emission profile (^{3}LC based) that peaks around 460 nm. Upon aggregation, the luminescence is strongly enhanced with a bathochromically shifted emission peak of now featureless emission profile (^{3}MMLCT based). For details about the photophysical properties the reader is referred to the remaining chapters of the thesis. The strong enhancement of the emission quantum yield can be understood as an aggregation-induced emission (AIE) which is contrary to most other luminophors.[82, 83] High concentrations are accompanied by high optical density for the excitation wavelength (primary inner filter effects) and the emission wavelength (secondary inner filter effects).[15] For luminophores (fluorophores) with a small stokes shift, these inner filter effects typically result in an aggregation-cause quenching (ACQ). The change of the nature of emission (^{3}LC to ^{3}MLCT based) and the accompanied AIE behavior of the large Stokes shift Pt(II)-complexes overcome this problem and therefore yield highly luminescent materials also at higher concentrations.

Chelating ligands, namely bi-, ter- and tetradenate, with a π-conjugated system are frequently utilized for the construction of luminescent Pt(II)-complexes.[84] In comparison to bidentate ligands, terdentate ligands generally afford isomeric free Pt(II)-complex featuring higher thermodynamic and kinetic stability. Tetradentate ligands provide an even more rigid supramolecular building block their terdentate analogues lacking the fourth coordination side for substitution with an ancillary ligand. In this thesis, the exchange of the ancillary ligand was utilized to tune the self-assembly properties, while the chromophoric system defined by the terdendate dianioic ligand is preserved.

The ancillary ligand is often based on pyridine derivatives. Noteworthy, substitution of the ancillary ligand enables the control of the self-assembly process, namely by

adjustment of solubility, bulkiness and the introduction of further supramolecular motifs. Therefore, the properties of a photophysically understood framework can be adjusted towards the demands of the application by the exchange of a single ligand.

Self-assembly

Supramolecular chemistry as the "chemistry beyond the molecule" (Jean-Marie Lehn[85, 86]) investigates complex, organized assemblies, which are formed by the association of single molecules *via* non-covalent interactions. Self-assembly can be understood as the autonomous organization of components (covalently linked molecules) into structures or pattern without an external intervention.[87] Processes featuring a self-assembly step are wide-spread in technology and nature (Figure 1.4). For instance, the formation of liquid crystalline materials is based on the self-assembly of the distinct components to supramolecular aggregates which in turn renders novel properties, not given by the individual components. [88] Self-assembly is based on intermolecular forces as seen in the natural example of folded, globular protein, in which several levels of molecular interplay (H-Bonds, dynamic S-S bonds, hydrophobicity effect) are necessary to realize the final active species.

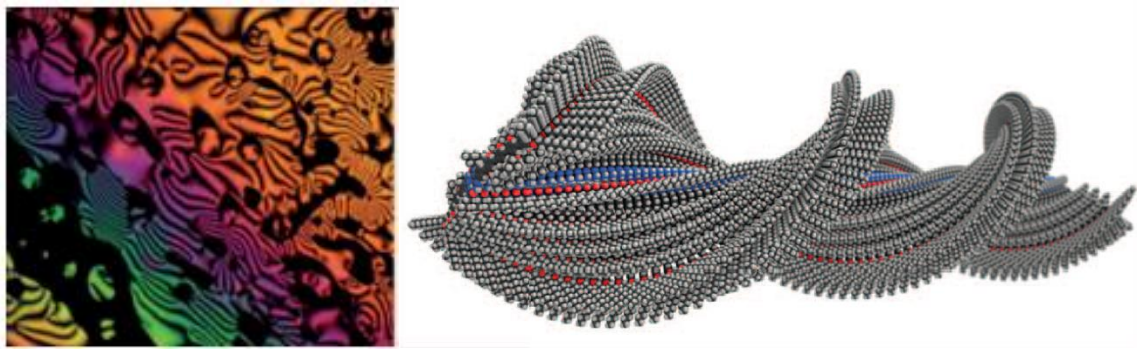

Figure 1.4: Examples for self-assembly utilized in science. Left: Nematic phase of liquid crystalline molecules.[88] © 2010 Wiley; Right: Ordered supramolecular polymer, that forms a twisted nanoribbon.[89] © 2012 Science

Supramolecular assemblies can be formed in various methods and can be summarized as follows[90]: *i)* Systems that are highly probable to retain for a long time due to the thermodynamic stability: equilibrium assemblies. *ii)* Systems that are transiently persistent, trapped in a local minimum of the energy landscape, which therefore need time or activation energy to convert towards other (more stable) states: kinetically trapped

assemblies. *iii)* Systems that only persist when a continuous energy supply (feed) is given. Stopping the energy supply leaves the system to fall into either a thermodynamic (global minimum) or kinetically trapped state (local minimum): far-from equilibrium assemblies. The constantly energetically driven transformation underwent by these assemblies can lead to unpredictable, emergent functions. In this thesis, only thermodynamic self-assemblies are considered.

For this purpose, several intermolecular interactions are exploited, which will be briefly discussed. An overview for typical molecular and supramolecular bonds is given in Table 1.1.

Table 1.1: Typical binding free energies for selected bonding interactions

interaction	-ΔG (kJ/mol)
covalent bond	100 - 400
coulomb	250
hydrogen bond	3 - 46
cation-π	1 - 3
anion-π	1 - 7
π-π	1 -50
hydrophobic	1 - 60
dispersive	7 - 46

Values are summarized from references [91] and [92].

While a covalent bond, in which an electron pair is shared by two atoms, exhibits a dissociation energy between 100 and 400 kJ/mol, making this type of bond stable and in most cases irreversible at ambient conditions. Noncovalent interactions between molecular entities are considerably weaker with strongly varying strength. A coordinative bond can, for instance, be very weak and unstable (metal precursor) enabling the facile substitution of thermodynamically more ligands that might form bonds of the strength of a covalent bond (transition metal complexes). Hydrogen bonds with approximately 8.5 to 24.5 kJ/mol are the dominant bonding motifs in the base pairing with DNA strands.[92] The directionality of this bond and the synergetic effects of well-chosen donor-acceptor pairs allows for the formation of stable organized matter, in solution and in solid

state.[93] The unidirectional hydrophobicity effect plays a major role not only in enzyme substrate binding but also in the formation of artificial supramolecular aggregates.[94] Among the weakest interactions are those based on the London dispersion forces, namely van der Waals and closed-shell metal-metal interactions.[95]

Self-assembly of Pt(II)-complexes

One commonly expects two closed-shell metal cations such as Pt(II) with d_{z^2} orbitals to repel each other. Nevertheless, when dispersive interaction[84] and relativistic effects are taken into account an attraction between heavy metal closed-shell ions was described (aurophily) and often denoted as metallophic interactions.[34, 96-98] In the last decades, metallophilic systems of d^{10},[99-102] d^8 [103-106] and combination of them in heterometallic systems[107-111] have been reported. The strength of an intermetallic bond is assessed to be in the same region as a weak hydrogen bond (29 - 46 kJ/mol)[99], which makes this directional bounding suitable for supramolecular assembling studies.

However, the simplified MO Scheme (Scheme 1.5) may not cover the overall energetic stabilization by the aggregation process, but highlights the occupancy of an anti-bonding metal centered orbital. Spectroscopic analysis in solution and solid state accompanied by theoretical calculations in the excited state suggest the correctness of this scheme. A shortening of the Pt-Pt bond was observed upon excitation, which is in agreement with the depopulation of an anti-bonding molecular orbital.[112-116] Especially, the consideration of dispersive contributions to the overall energy is a promising approach to the thermodynamic stabilization upon aggregation.[84, 117-120]

On account of the appealing photophysical changes upon self-assembly, a broad scope of Pt(II)-complexes were synthesized, characterized and investigated in various applications.[81, 121-134]

Che and co-workers demonstrated that a cationic Pt(II)-complex can pack in an ordered manner with alternating Pt-Pt distances of 3.38 and 3.34 Å (Figure 1.5, left). The self-assembled nanowires showed semiconducting properties as well as phosphorescence enabling the fabrication of organic light-emitting field-effect transistors (OLEFETs).[124] Emissive allenylidene Pt(II)-complexes were reported to assemble into nanorods and nanorings dependent on the water content.[123]

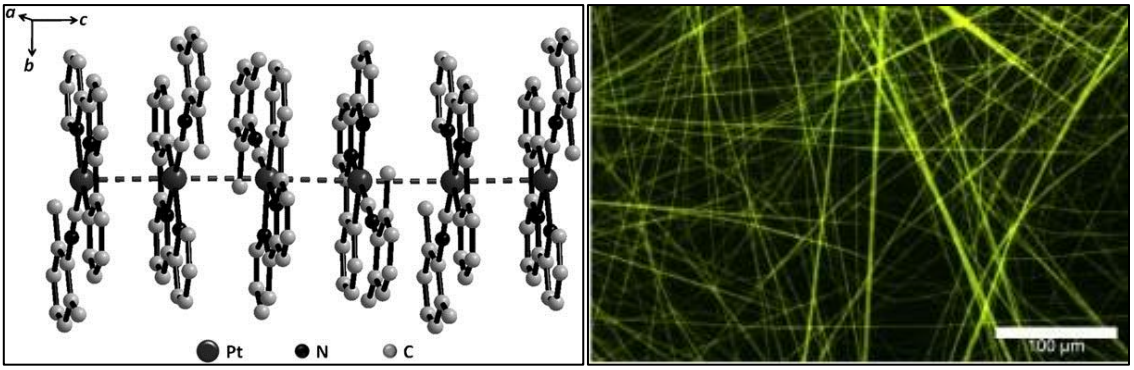

Figure 1.5: left: Crystal packing diagram of a cationic Pt(II)-complex with alternating Pt-Pt distance.[124] © 2008 Wiley; right: Luminescent fibers formed from a self-assembled neutral Pt(II)-complex.[81] © 2014 Royal Chemical Society

Luminescent neutral Pt(II)-complexes based on a terdentate dianionic bis(tetrazolate)-pyridine ligand were reported by De Cola and co-workers.[126, 135, 136] The complex is non-emissive in dilute solution, but self-assembles at higher concentrations to form gelating nanowires accompanied by a luminescence quantum yield of 90%. When a dianionic bis(triazolate)-pyridine ligand was employed decorated with bulky electron-withdrawing trifluoromethyl groups, the complexes emit at room temperature in organic solutions (φ = 2%) that peaks in the blue. Self-assembly leads to strongly emissive fibers with highly anisotropic photophysical properties and an enhanced quantum yield (φ = 58%) (Figure 1.5, right).

Yam *et. al.* investigated extensively supramolecular soft materials on the basis of alkynyl platinum(II)-complexes.[59] For instance, metallo-gels with a low critical gelation concentration of 4.4 mg mL^{-1} in DMSO were obtained.[130] The gelation process is followed by a drastic change in the emission color indicating that Pt•••Pt and π-π interactions are involved. Contrarily to organic supramolecular soft materials, in which H-bonding motifs and/or long alkyl chains drive the organization,[137] metallo-gels take advantage of hydrophobic, Pt•••Pt and π-π interactions.[130]

Besides one dimensional supramolecular structures, it was shown that neutral Pt(II)-complexes can also undergo self-assembly into quasi-2D nanosheets due to the orthogonal Pt•••Pt and C-H•••π(C≡C) interactions. The nanosheets display near-infrared phosphorescence.[138]

Mechanoluminescent (ML) materials are promising candidates for sensing and data storage applications. Self-assembled Pt(II) can render such materials in the solid-state,[128,

[139-143] since external stimuli such as pressure or shear forces alter the molecular packing arrangement of the triplet emitters. Examples for neutral mechanoluminescent Pt(II)-complexes featuring bi-, ter-, and tetradentate ligands are depicted in Figure 1.6.

A Pt(II)-complex coordinated by two identical bidentate anionic ligands was synthesized in the group of Pi-Tai Chou (Figure 1.6, left).[140] The complex is uniformly packed with a Pt-Pt distance of 8.6 Å and a π-π separation of 7.1 Å in its crystalline state accompanied by a blue emission peaking at 450 nm. The uniform arrangement enables each molecule to slide sideways as well as to move back and forth. Therefore, upon grinding the emission is bathochromically shifted to 550 nm. Fabricated white OLEDs (WOLEDs) with external quantum efficiencies of 15% demonstrated the applicability of tribologically controlled Pt(II)-phosphors.

Bruce *et. al.* utilized a Pt(II)-complex featuring a terdentate ligand decorated with long alkyl chains to obtain luminescent mesophases (Figure 1.6, center).[128] Produced spin coated thin films displayed a broad emission around 660 nm assigned as excimer emission. Annealing of the samples at 110°C rendered an emissive material displaying monomeric and excimeric emission properties. Rubbing of the annealed sample re-established the pure excimeric emission. The successful re-set to the mixed emission state by a heat-cool cycle displays the possibility of these materials for stimuli-responsive application.

Very recently, the group of Chi-Ming Che presented the first example of a Pt(II)-complex coordinated by a tetradentate ligand (Figure 1.6, right).[84] Monoclinic and triclinic crystal polymorphs were obtained with a Pt-Pt distance larger than 4.8 Å, thus, no Pt•••Pt interactions are present. This arrangement is reflected in a structured emission peaking at 541 nm. Grinding of the crystals resulted in an emission-profile change which appears now broad and featureless around 681 nm. Furthermore, an interconversion of the crystalline forms was investigated by PXRD measurements.

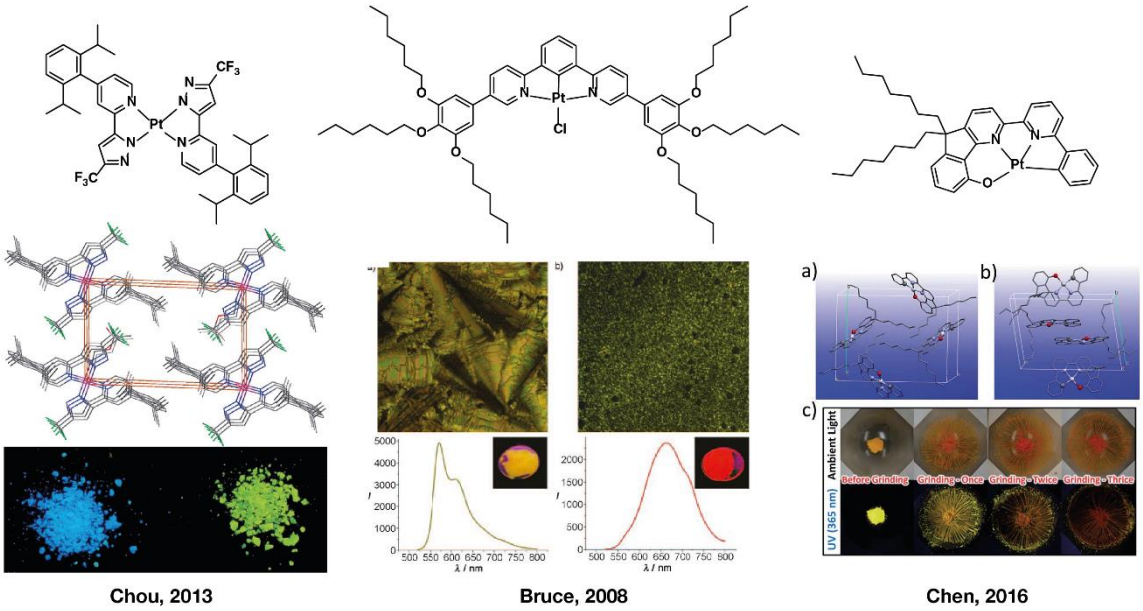

Figure 1.6: Examples of luminescent Pt(II) with chelating ligands for mechanoluminescent applications. left: Uniform packing of the blue emissive crystals (below) that allows for sideways sliding and back-and-forth movement of the complexes upon grinding (ground green emissive solid depicted below).[140] © 2013 Royal Chemical Society; center: Photomicrographs of the spin coated Pt(II)-complex taken between crossed polarizers together with the corresponding emission spectra. a) fast cooled from the liquid crystalline phase; b) fast cooled from isotropic pahse.[128] © 2008 Wiley; right: Crystal packing of the monoclinic (a) and triclinic (b) polymorph of the Pt(II)-complex. c) Photographs of the crystalline solid before and after grinding under ambient and UV irradiation.[84] © 2016 Royal Chemical Society

De Cola and co-workers recently investigated the mechanochromical responsiveness of a terdentate Pt(II)-complex similar to those reported in this thesis. A hydrostatic pressure experiment in a diamond anvil cell revealed the necessity of high pressure to induce spectral changes in the luminescence (24.2 kbar). A more facile induction of emission color changes was realized by an AFM tip, that served as writing pencil on a blue emissive fiber. Upon scratching with the tip, the emission color changes to yellow, while a written message can be erased by a photoconversion reaction induced by a 405 nm excitation.[143]

Cowpea Chlorotic Mottle Virus (CCMV)

The formation of hybrid nanomaterials composed of Pt(II)-complexes and virus coat proteins is one of the topics of this thesis. Therefore, an introduction to the field of virus like particles (VLPs) and interactions between proteins and Pt(II)-complexes is given.

In general, a complete virus particle (virion) consists of infectious RNA covered by a protecting protein shell (capsid). The positively charged coat proteins (CPs) self-assemble around the negatively charged nucleic acid. This dynamic arrangement enables the virus to enter host cells followed by the release of the RNA upon outer stimulus. The virus RNA reprograms genetic code of the host cell leading to an expression of virus proteins and multiplication of the viral RNA. To spread to other host cells, the CPs encapsulate the RNA to serve as a nanocarrier.

After the development of a facile method to control the disassembly and reassembly of capsid virus proteins, various materials were encapsulated. [144-149] The confined space of the protein cages was exploited in particular for mineralization[150, 151], synthesis and encapsulation of nanoparticles,[145, 152-160] drug delivery,[161-172] creation of fluorescent probes[173-177] and MRI contrast agents[178, 179, 180] and in catalysis.[181, 182, 183] In practice the rigid shell of a capsid provides high local density of encapsulated compounds while a dynamic exchange with the environment is given by capsid pores and the responsiveness to the pH-value, ionic strength and defined stimuli.[149, 161, 184-189 190]

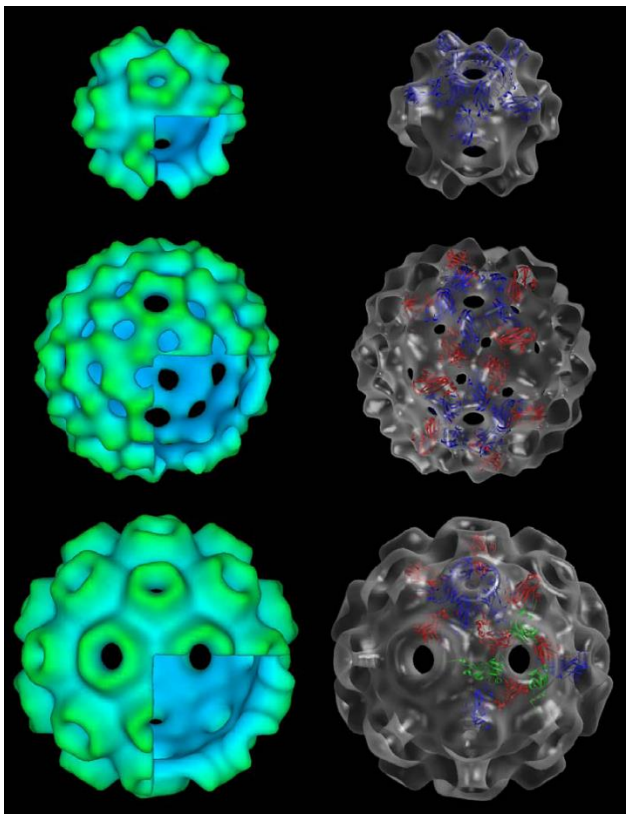

Figure 1.7: Cryo-EM reconstruction of the three possible structures (T = 1, "T = 2", T = 3) of CCMV (left) and corresponding electron-density models (right).[189] © 2006 Elsevier

Coat proteins

Cowpea chlorotic mottle virus (CCMV) belongs to a family (Bromoviddidae) of plant virus and is composed of 180 identical proteins. These proteins commonly self-assemble first to dimers and subsequently to pentamers (pentamers of dimers, POD), which serve as nuclei for the formation icosahedral protein cages (capsid). In the presence of an anionic cargo template such as RNA, 90 dimeric subunits (180 monomers) assemble into virus particle which is composed of 12 pentamer and 20 hexamers (T = 3)[191, 192] featuring an outer diameter of d_{out} = 29 nm (inner diameter of d_{in} = 21 nm), and 60 pores (1 - 2 nm pore size). [193]

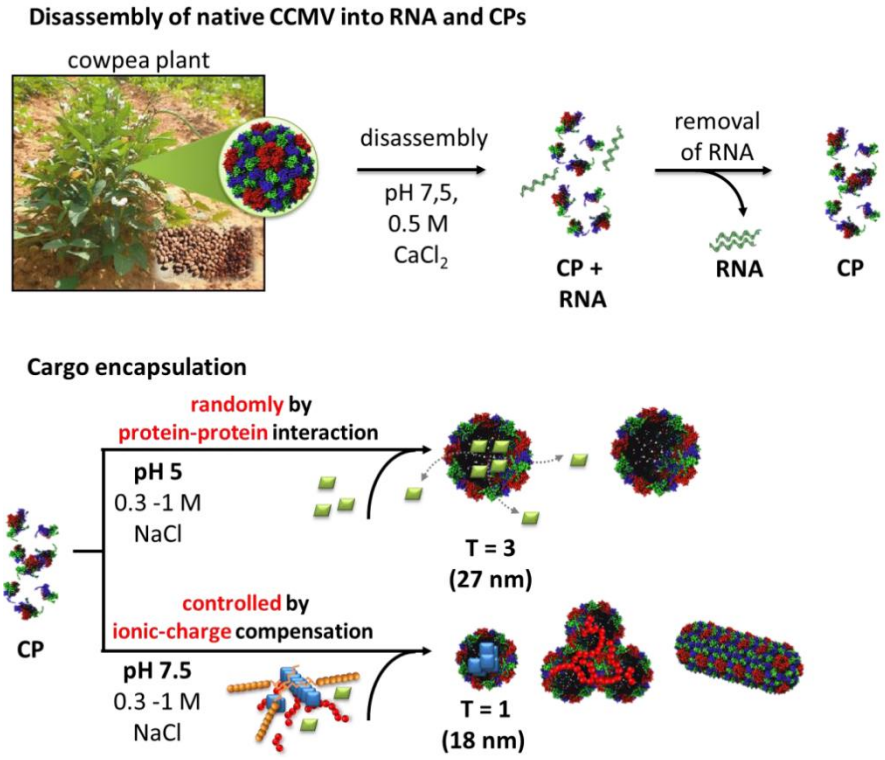

Figure 1.8: Top: Native cowpea chlorotic mottle virus (CCMV) extracted from cowpea plants and disassembled to remove the RNA. Bottom: The coat proteins (CPs) can be reassembled either driven by protein-protein interaction at pH = 5.0 or templated by an anionic cargo molecule at pH = 7.5 to form loaded virus like particles (VLPs).[196] © 2013 Melanie Brasch

The *in vitro* self-assembly of CCMV with and without a template can be controlled by the pH value and the ionic strength. Therefore, the removal of infectious RNA was realized and a reloading with other (templating) cargo molecules achieved. Two main strategies for the *in vitro* self-assembly exist: *i)* Virus like particles (VLPs) can be formed

in their T = 3 structure in slightly acidic conditions (pH = 5.0) and high ionic strength (I > 1 M). This method is based on the protein-protein interaction (POD nucleation) and the loaded cargo molecule does not need to possess a surface charge (no template effect). This method will lead to random encapsulation of present cargo molecules and thus a mixture of empty and filled VLPs is expected.[186, 189, 194] *ii)* In slightly basic conditions (pH = 7.5) and lowered ionic strength (I > 0.3) a templated assembly by electrostatic interactions with an anionic cargo forms VLPs. Due to the template effect and thus driven by ionic-charge compensation only filled VLPs are obtained.[153, 181, 186]

The flexibility and size of the cargo defines the structure of the resulting VLPs. VLPs of T = 1 (60 CPs, 12 pentamers, d_{out} = 18 nm, d_{in} = 10 nm), "T = 2" (120 CPs, 12 pentamers, 10 hexamers, d_{out} = 25 nm, d_{in} = 15 nm), which is a pseudo-icosahedral shape (dodecahedral) and T = 1 are achievable.[189] Furthermore, even a complete rearrangement from a rather spherical to rod-like structure could be obtained by the usage of DNA as template cargo.[188, 195]Additionally, the present pores in the VLPs enables substrate exchange by diffusion.[194]

Platinum(II)-complex-protein interactions

The groups of Chi-Ming Che and Tunik developed several Pt(II)-complexes for protein staining aiming on selective binding towards certain proteins (Figure 1.9).[197-203] Therefore, not only bioimaging with specific labeling of organelles are possible, but also fluorescence enzyme assays.

Complex **Che-1** is composed of the Pt(II) ion, chloride as ancillary ligand and a terdentate cyclometalating ligand substituted by poly ethylene glycol to ensure water solubility. The complex displays a broad featureless room-temperature emission peaking at 543 nm and 700 nm, which are ascribed to emanate from ^{3}MLCT and ^{3}MMCLT state, respectively, due to partial aggregation.[197] Addition of Bovine Serum Albumine (BSA) leads to a strong enhancement of the emission and the binding constant was determined from a Scatchard plot to be 2.7 10^4 M^{-1}. A 1:1 binding stoichiometry was utilized.[204] BSA possesses several hydrophobic cavities (pockets) in its folded state.[205] The addition of urea initially led to an enhancement of the emission intensity assigned to a helical twisting of the BSA accompanied by a tighter binding of the complex. A further increase of the urea concentration led to drastic decrease of the emission intensity, which is

ascribed to the denaturation, unfolding, of BSA. The authors conclude that the developed complex binds to the hydrophobic pockets of BSA, explaining the enhancement and the decrease of the emission intensity upon urea concentration variations. A similar approach was followed by the group of Nair.[206]

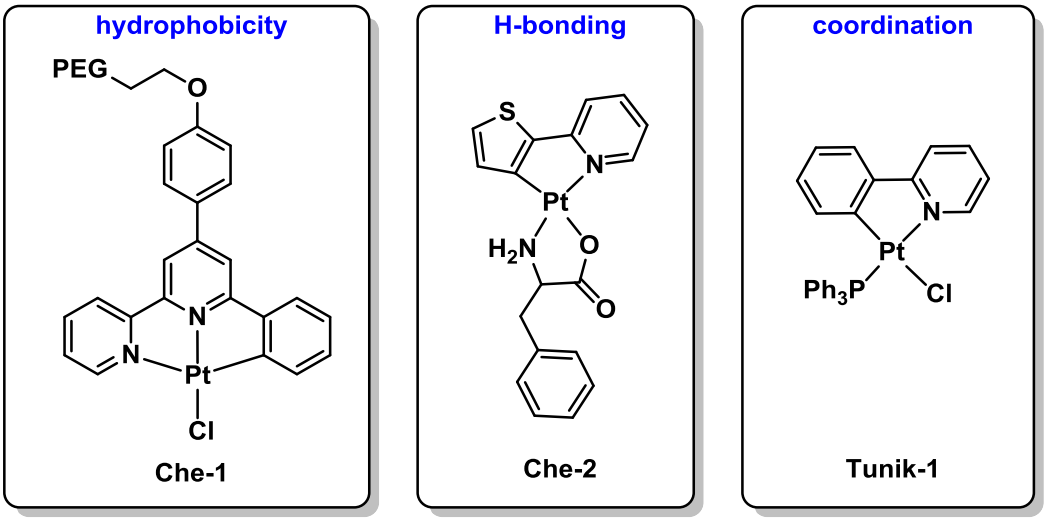

Figure 1.9: Complexes for protein labeling. The dominant complex-protein interaction is displayed in blue letter.[197, 202, 203]

Complex **Che-2** consists of the Pt(II) center, a bidentate cyclometalating ligand and a chelating amino acid. A weak structured emission peaking at 562 nm is observed in aqueous solution at ambient conditions. The addition of Human Serum Albumin (HAS) leads to a strong enhancement of the emission intensity and a binding constant of $1.0\ 10^6\ M^{-1}$ with a binding stoichiometry of 1:1 was detected. The authors show in cell experiments and *in vitro* studies that the complex binds selectively to HAS over other proteins. The H-bond interactions between the protein and the coordinated amino acid are presumably responsible for the high binding constant and the selectivity of the employed complexes.[198, 199]

Che and coworkers followed a non-covalent/non-coordinative approach based on weaker intermolecular interactions. Tunik and colleagues designed a complex with a vacant coordination side for protein labeling in order to increase the selectivity and stability. Complex **Tunik-1** contains the Pt(II) cation, a bidentate cyclometalating ligand, a monodentate triphenyl phosphine ligand and a labile bound chloride. The authors claim to have high selectivity for the coordination of imidazole and histidine, resulting in pronounced structured emission peaking at 477 nm. The complex was tested on the

protein ubiquitin, which possesses only a single histidine, to show the regioselectivity. A labeled HSA was further applied in a live cell lifetime imaging experiments (FLIM-PLIM). Another example for platinum(II) complex protein interaction addressing amyloid inhibition is also based on the coordination of histidines to the metal center.[207, 208, 209]

Therefore, for platinum(II) complex - protein interactions either a hydrophobic pocket need to be present at the protein or binding motifs such as a vacant coordination side or H-Bond donor/acceptors need to be present at the complex.

Supramolecular Sensing

Supramolecular analytical chemistry takes advantage of the rapid intermolecular interactions known from supramolecular chemistry.[62, 210] Therefore, a detection and discrimination of analytes that exhibit sluggish reaction rates for covalent bond formation becomes feasible.[211-213] Optical sensing methods such as absorption or fluorescence spectroscopy provide certain advantage over other analytical methods like mass spectrometry or NMR spectroscopy, namely a facile and quick sample preparation, low instrument costs and scalability to high-through put measurements.[6, 214, 215] In particular fluorescence assays provide often an advantageous signal-to-noise ratio over other methods due to a strong suppression of background signal (non-fluorescent media such as deionized water or organic solvents). A general topology for fluorescence sensing regards the binding mode formulating two key concepts. On one hand, a direct sensing approach in which the receptor is linked (covalently) to a signaling unit, the so-called indicator (fluorophore, phosphor), and analyte binding towards the receptor is accompanied by a signal transduction such as quenching, fluorescence enhancement or spectral shifts.[62] On the other hand, in an indicator-displacement assay (IDA) the receptor carries the indicator which is displaced upon binding of the analyte due to its higher binding constants. The release of the indicator is accompanied by the signal transduction.[216] A prominent example for an IDA are enzyme assays based on fluorescence anisotropy measurements.[6] Furthermore, two types of fluorescence based sensing paradigms exist, which are denoted as single analyte and differential sensing.

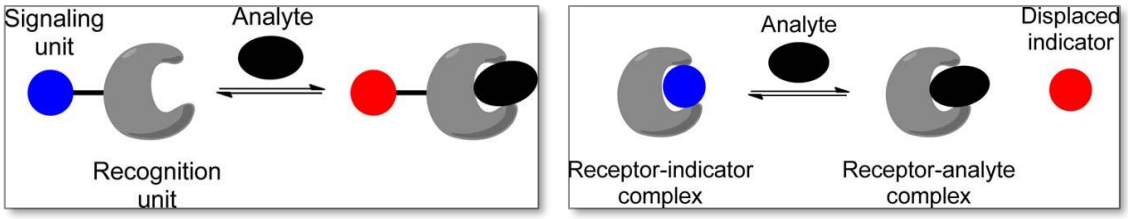

Figure 1.10: Illustrations of the receptor-spacer-reporter (direct sensing, left) and indicator displacement (IDA, right) approaches for fluorescence sensing.[62] © 2015 American Chemical Society

Single analyte sensing

The principle of single analyte sensing follows the idea derived from the selective interactions between enzymes and substrates defined by Emil Fischer as the "lock and key" principle.[62, 217] In the perspective of an analytical assay, a specific receptor (lock) needs to be developed for an analyte of interest (key). This design principle receptor - linker-reporter is envisaged for the direct sensing approach. This strategy was of great success and a broad scope of chemosensors were developed and commercialized.[218] In particular, a prototype platform in supramolecular chemistry, the crown-ether scaffold,[219, 220] enabled the detection of a broad scope of analytes, in particular cations.[221-223] The most common fluorescence technique applied in these system is the photoinduced electron transfer (PET), where an electron donation from the crown-ether scaffold (aza-crown) quenches the emission of the indicator in the initial state. Upon cation uptake, the coordination of the cation at the electron donating unit renders a fluorescence-on event. The feasible synthesis of indicator tethered crown-ethers featuring different sizes and heteroatoms enables the selective addressing of a broad scope of cations. Nevertheless, to gain specification towards a certain key (analyte) the lock (receptor) design becomes often sophisticated accompanied by increasing synthetic effort.[223, 224] Furthermore, a specification of the receptor cannot be probed to unknown substances that might be present in biological samples and disturb the signal transduction and thus the overall read-out.

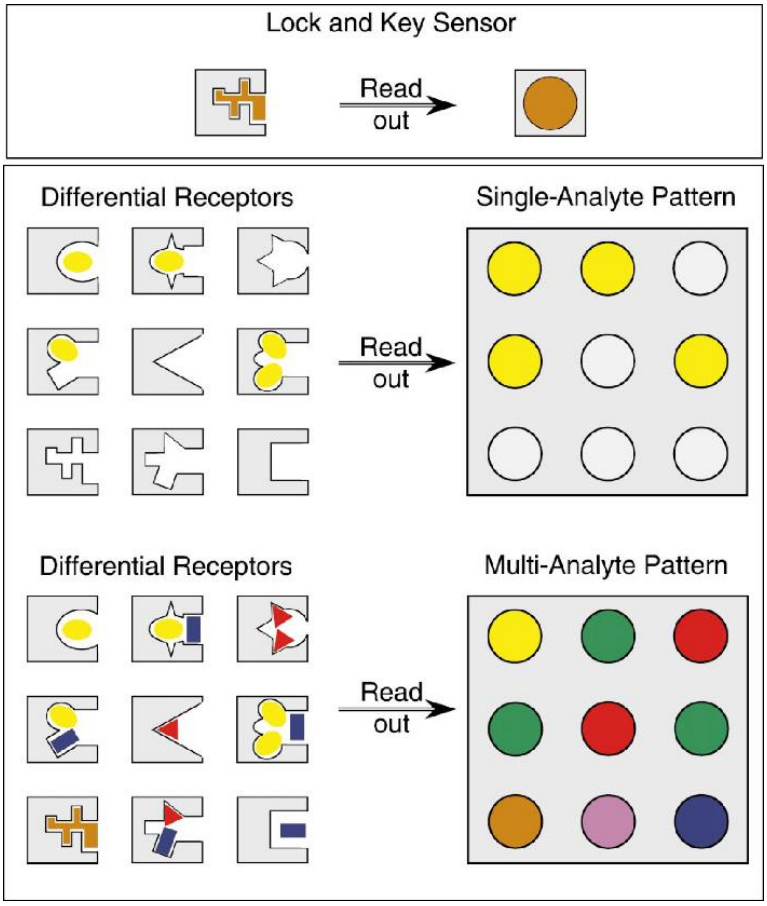

Figure 1.11: Illustration of the two sensing paradigms: single-analyte sensing (Lock and Key Sensor, top) and differential sensing (Differential Receptors, bottom).[225] © 2001 Wiley

Differential sensing

To overcome the challenges for single analyte sensing another strategy follows the paradigm of high cross reactivity over selectivity. The differential sensing method is inspired by nature, in particular by the nose and tongue. A nose, for instance, does not host receptors for each individual odor that exists in the environment which would simply exceed the limited space. Rather numerous receptors are present which interact with various analytes differentially and thus transduce different signals. The convoluted signals result in a pattern which clearly identifies the individual analytes (odors). To realize differential sensing multiple chemosensors are placed in array-like arrangement ("array sensing"). Cross-reactivity is one of the most important features for a differential-sensing assays, namely that receptors possess low selectively for a certain analyte. Therefore, the effort often decreases for the synthesis of the receptors and also unknown species can be detected. Nevertheless, the high cross-reactivity can lead to signal overexpression or blind states by undesired side reactions. Furthermore, the signal

analysis is no longer straight forward based on a univariate interpretation, *e.g.* signal on-off. The signal output from an array of chemosensors renders a multivariate dataset, which needs to be processed and analyzed by adequate methods in order to find a pattern ascribed to the analyte of interest.[226] These multivariate data analytical tools are more and more accessibly on account of more powerful computers. However, the data mining and processing for a reliable analyte recognition can be challenging. Differential sensing can be realized by both sensing strategies indicator-displacement assays[227-233] and direct sensing.[62, 210, 234, 235] As mentioned above, most differential sensing approaches are based on multiple receptor arrays, while single receptor approaches are scarcely described.[236, 237]

Scope of the thesis

The work presented herein is focused on the synthesis and photophysical characterization of phosphorescent square-planar Pt(II)-complexes on the dependence of their environment. In particular, the self-assembly, stimuli-responsive behavior, multidimensional organization and encapsulation in confined biomaterial for the formation of functional hybrid materials are considered. Their solvatochromistic and solid-state behavior are investigated with distinct focus on applications in aqueous media.

Thus, the development of a potassium chemosensor on the basis the aggregation behavior of the Pt(II)-complexes is presented in Chapter II. For this purpose, a crown-ether scaffold was tethered with two neutral Pt(II)-complexes.

In Chapter III, a showcase for analyte induced aggregation is demonstrated on the fundament of a reactive metal precursor. The multiple photophysical read-outs were processed by multivariate analysis tools rendering a differentiation of selected drugs and toxins.

The decoration of a predominantly stacking Pt(II) scaffold with H-bond donor and acceptor pseudo nucleobases is shown in Chapter IV. The competitive supramolecular binding motifs lead to 2D organized nanopattern at the liquid/solid interface and interrupt the z-directional organization.

Finally, highly luminescent virus-like particles (VLPs) were prepared by the encapsulation of water soluble Pt(II) amphiphiles into CCMV coat proteins. The hybrid materials show the highest emission quantum yield for VLPs reported so far and an enhancement of the emission quantum yield upon encapsulation.

References

1. M. Planck, *Vorlesungen über die Theorie der Warmestrahlung*, JA Barth, 1913.
2. L. de Broglie, *Foundations of Physics*, 1970, **1**, 5-15.
3. P. Ceroni, Springer Netherlands, 1st edn., 2012.
4. K. Nakamoto, in *Handbook of Vibrational Spectroscopy*, John Wiley & Sons, Ltd, Weinheim, 2006.
5. P. J. Larkin, *Infrared and Raman Spectroscopy: Principles and Spectral Interpretation*, Elsevier, Oxford, 2011.
6. P. J. Walla, *Modern Biophysical Chemistry*, Wiley, Weinheim, 2009.
7. B. Valeur and M. N. Berberan-Santos, *Molecular Fluorescence: Principles and Applications*, John Wiley & Sons, Inc., Weinheim, 2nd edn., 2012.
8. A. Jablonski, *Nature*, 1933, **131**, 21.
9. M. Born and R. Oppenheimer, *Annalen der Physik*, 1927, **389**, 457-484.
10. M. Kasha, *Discuss. Faraday Soc.*, 1950, **9**, 14-19.
11. N. Tetreault, R. S. Muthyala, R. S. H. Liu and R. P. Steer, *J. Phys. Chem. A*, 1999, **103**, 2524-2531.
12. T. Itoh, *Chem. Rev.*, 2012, **112**, 4541-4568.
13. R. Englman and J. Jortner, *Mol. Phys.*, 1970, **18**, 145-164.
14. J. V. Caspar and T. J. Meyer, *J. Phys. Chem.*, 1983, **87**, 952-957.
15. J. R. Lakowicz, *Principles of Fluorescence Spectroscopy*, Springer, 3rd edn., 2007.
16. A. D. McNaught, A. Wilkinson, P. International Union of and C. Applied, in *Compendium of Chemical Terminology: IUPAC Recommendations*, IUPAC Chemical Data Series, Blackwell Science, 1997.
17. M. A. El-Sayed, *Acc. Chem. Res.*, 1968, **1**, 8-16.
18. H. Yersin, *Highly efficient OLEDs with phosphorescent materials*, John Wiley & Sons, Weinheim, 2008.
19. M. Fujita, M. Tominaga, A. Hori and B. Therrien, *Acc Chem Res*, 2005, **38**, 369-378.
20. P. G. Bomben, T. J. Gordon, E. Schott and C. P. Berlinguette, *Angew. Chem. Int. Ed.*, 2011, **50**, 10682-10685.
21. J. P. Sauvage, J. P. Collin, J. C. Chambron, S. Guillerez, C. Coudret, V. Balzani, F. Barigelletti, L. De Cola and L. Flamigni, *Chem. Rev.*, 1994, **94**, 993-1019.
22. T. Bessho, E. Yoneda, J. H. Yum, M. Guglielmi, I. Tavernelli, H. Imai, U. Rothlisberger, M. K. Nazeeruddin and M. Grätzel, *J. Am. Chem. Soc.*, 2009, **131**, 5930-5934.
23. A. Hagfeldt, G. Boschloo, L. Sun, L. Kloo and H. Pettersson, *Chem. Rev.*, 2010, **110**, 6595-6663.
24. P.-T. Chou, Y. Chi, M.-W. Chung and C.-C. Lin, *Coord. Chem. Rev.*, 2011, **255**, 2653-2665.
25. Y. Shen and B. P. Sullivan, *J. Chem. Educ.*, 1997, **74**, 685.
26. Z. Q. Chen, Z. Q. Bian and C. H. Huang, *Adv Mater*, 2010, **22**, 1534-1539.
27. C. Li, M. Yu, Y. Sun, Y. Wu, C. Huang and F. Li, *J. Am. Chem. Soc.*, 2011, **133**, 11231-11239.
28. I. Eryazici, C. N. Moorefield and G. R. Newkome, *Chem. Rev.*, 2008, **108**, 1834-1895.
29. M. D. Santana, L. López-Banet, G. Sánchez, J. Pérez, E. Pérez, L. García, J. L. Serrano and A. Espinosa, *Dalton Trans.*, 2016.
30. D. R. McMillin and J. J. Moore, *Coord. Chem. Rev.*, 2002, **229**, 113-121.
31. K. Ohno, S. Yamaguchi, A. Nagasawa and T. Fujihara, *Dalton Trans.*, 2016.
32. S. P. Morcillo, D. Miguel, L. Alvarez de Cienfuegos, J. Justicia, S. Abbate, E. Castiglioni, C. Bour, M. Ribagorda, D. J. Cardenas, J. M. Paredes, L. Crovetto, D. Choquesillo-Lazarte, A. J. Mota, M. C. Carreno, G. Longhi and J. M. Cuerva, *Chem. Sci.*, 2016.
33. V. W.-W. Yam and E. C.-C. Cheng, *Chem. Soc. Rev.*, 2008, **37**, 1806-1813.
34. P. Pyykkö, *Chem. Rev.*, 1997, **97**, 597-636.
35. R. Visbal and M. C. Gimeno, *Chem. Soc. Rev.*, 2014.

36. V. Balzani and S. Campagna, *Photochemistry and Photophysics of Coordination Compounds I/II*, Topics in Current Chemistry, *280*, 2007.
37. A. Barbieri, G. Accorsi and N. Armaroli, *Chem. Commun.*, 2008, 2185-2193.
38. L. Bergmann, J. Friedrichs, M. Mydlak, T. Baumann, M. Nieger and S. Brase, *Chem. Commun.*, 2013, **49**, 6501-6503.
39. R. Czerwieniec and H. Yersin, *Inorg. Chem.*, 2015, **54**, 4322-4327.
40. Gneu, M. J. Leitl, L. H. Finger, N. Rau, H. Yersin and J. Sundermeyer, *Dalton Trans.*, 2015.
41. D. Volz, T. Baumann, M. Wallesch and S. Bräse, *SPIE Newsroom*, 2014.
42. G. Cheng, G. K.-M. So, W.-P. To, Y. Chen, C.-C. Kwok, C. Ma, X. Guan, X. Chang, W.-M. Kwok and C.-M. Che, *Chem. Sci.*, 2015.
43. T. Higashino and H. Imahori, *Dalton Trans.*, 2015.
44. A. Yella, H. W. Lee, H. N. Tsao, C. Yi, A. K. Chandiran, M. K. Nazeeruddin, E. W. Diau, C. Y. Yeh, S. M. Zakeeruddin and M. Grätzel, *Science*, 2011, **334**, 629-634.
45. P. Brueggeller, C. Strabler, S. Sinn, R. Pehn, J. Pann, J. Dutzler, W. Viertl, J. Prock, K. Ehrmann, A. Weninger, H. Kopacka and L. De Cola, *Faraday Discuss.*, 2016.
46. M. S. Lowry, J. I. Goldsmith, J. D. Slinker, R. Rohl, R. A. Pascal, G. G. Malliaras and S. Bernhard, *Chem. Mater.*, 2005, **17**, 5712-5719.
47. S. Rau, D. Walther and J. G. Vos, *Dalton Trans.*, 2007, 915-919.
48. D. Gust, T. A. Moore and A. L. Moore, *Acc. Chem. Res.*, 2009, **42**, 1890-1898.
49. R. E. Palacios, G. Kodis, S. L. Gould, L. d. l. Garza, A. Brune, D. Gust, T. A. Moore and A. L. Moore, *ChemPhysChem*, 2005, **6**, 2359-2370.
50. A. Hagfeldt and M. Graetzel, *Chem. Rev.*, 1995, **95**, 49-68.
51. P. J. Cameron, L. M. Peter, S. M. Zakeeruddin and M. Grätzel, *Coord. Chem. Rev.*, 2004, **248**, 1447-1453.
52. E. Galoppini, *Coord. Chem. Rev.*, 2004, **248**, 1283-1297.
53. B. Oregan and M. Grätzel, *Nature*, 1991, **353**, 737-740.
54. P. T. Chou and Y. Chi, *Chemistry–A European Journal*, 2007, **13**, 380-395.
55. M. Mauro, E. Q. Procopio, Y. Sun, C. H. Chien, D. Donghi, M. Panigati, P. Mercandelli, P. Mussini, G. D'Alfonso and L. De Cola, *Adv. Funct. Mater.*, 2009, **19**, 2607-2614.
56. M. Staffilani, E. Höss, U. Giesen, E. Schneider, F. Hartl, H.-P. Josel and L. De Cola, *Inorg. Chem.*, 2003, **42**, 7789-7798.
57. M. M. Richter, *Chem. Rev.*, 2004, **104**, 3003-3036.
58. S. Di Bella, *Chem. Soc. Rev.*, 2001, **30**, 355-366.
59. A. Y.-Y. Tam and V. W.-W. Yam, *Chem. Soc. Rev.*, 2013, **42**, 1540-1567.
60. J. Wang, H.-B. Liu, Z. Tong and C.-S. Ha, *Coord. Chem. Rev.*, 2015, **303**, 139-184.
61. Y. Guo, X. Feng, T. Han, S. Wang, Z. Lin, Y. Dong and B. Wang, *J. Am. Chem. Soc.*, 2014, **136**, 15485-15488.
62. L. You, D. Zha and E. V. Anslyn, *Chem. Rev.*, 2015, **115**, 7840-7892.
63. D. Septiadi, A. Aliprandi, M. Mauro and L. De Cola, *RSC Advances*, 2014, **4**, 25709-25718.
64. V. Fernández-Moreira, F. L. Thorp-Greenwood and M. P. Coogan, *Chem. Commun.*, 2010, **46**, 186-202.
65. C. J. Ballhausen, *Ligand field theory*, McGraw-Hill, New York, 1962.
66. J. H. Van Vleck, *Physical Review*, 1932, **41**, 208-215.
67. P. Atkins, *Shriver and Atkins' inorganic chemistry*, Oxford University Press, USA, 2010.
68. O. Laporte and W. F. Meggers, *J. Opt. Soc. Am.*, 1925, **11**, 459-460.
69. S. Sinn, Diploma, Friedrich-Schiller-Universität Jena, 2012.
70. H. Yersin, W. Humbs and J. Strasser, in *Electronic and Vibronic Spectra of Transition Metal Complexes II*, ed. H. Yersin, Springer Berlin Heidelberg, Berlin, Heidelberg, 1997, pp. 153-249.
71. G. A. Crosby, *Acc. Chem. Res.*, 1975, **8**, 231-238.
72. S. Sinn, B. Schulze, C. Friebe, D. G. Brown, M. Jager, E. Altuntas, J. Kubel, O. Guntner, C. P. Berlinguette, B. Dietzek and U. S. Schubert, *Inorg. Chem.*, 2014, **53**, 2083-2095.
73. C. Cornioley-Deuschel and A. Von Zelewsky, *Inorg. Chem.*, 1987, **26**, 3354-3358.

74. J. DePriest, G. Y. Zheng, N. Goswami, D. M. Eichhorn, C. Woods and D. P. Rillema, *Inorg. Chem.*, 2000, **39**, 1955-1963.
75. A. Galstyan, A. R. Naziruddin, C. Cebrián, A. Iordache, C. G. Daniliuc, L. De Cola and C. A. Strassert, *Eur. J. Inorg. Chem.*, 2015, **2015**, 5822-5831.
76. J. Sanning, P. R. Ewen, L. Stegemann, J. Schmidt, C. G. Daniliuc, T. Koch, N. L. Doltsinis, D. Wegner and C. A. Strassert, *Angew. Chem. Int. Ed.*, 2015, **54**, 786-791.
77. J. A. Gareth Williams, S. Develay, D. L. Rochester and L. Murphy, *Coord. Chem. Rev.*, 2008, **252**, 2596-2611.
78. S. Sinn, B. Schulze, C. Friebe, D. G. Brown, M. Jager, J. Kubel, B. Dietzek, C. P. Berlinguette and U. S. Schubert, *Inorg. Chem.*, 2014, **53**, 1637-1645.
79. B. Schulze, D. Escudero, C. Friebe, R. Siebert, H. Gorls, S. Sinn, M. Thomas, S. Mai, J. Popp, B. Dietzek, L. Gonzalez and U. S. Schubert, *Chem. Eur. J.*, 2012, **18**, 4010-4025.
80. M. Albrecht, *Chem. Rev.*, 2010, **110**, 576-623.
81. M. Mauro, A. Aliprandi, C. Cebrian, D. Wang, C. Kübel and L. De Cola, *Chem. Commun.*, 2014, **50**, 7269-7272.
82. B. Z. Tang and A. Qin, *Aggregation-induced emission: fundamentals*, John Wiley & Sons, Weinheim, 2013.
83. J. Mei, N. L. C. Leung, R. T. K. Kwok, J. W. Y. Lam and B. Z. Tang, *Chem. Rev.*, 2015, **115**, 11718-11940.
84. K. Li, G. S. Ming Tong, Q. Wan, G. Cheng, W.-Y. Tong, W.-H. Ang, W.-L. Kwong and C.-M. Che, *Chem. Sci.*, 2016, **7**, 1653-1673.
85. J.-M. Lehn, *Angew. Chem. Int. Ed.*, 1988, **27**, 89-112.
86. J. M. Lehn, *Science*, 2002, **295**, 2400-2403.
87. G. M. Whitesides and B. Grzybowski, *Science*, 2002, **295**, 2418-2421.
88. D. W. Bruce, P. Metrangolo, F. Meyer, T. Pilati, C. Präsang, G. Resnati, G. Terraneo, S. G. Wainwright and A. C. Whitwood, *Chemistry - A European Journal*, 2010, **16**, 9511-9524.
89. T. Aida, E. W. Meijer and S. I. Stupp, *Science*, 2012, **335**, 813-817.
90. E. Mattia and S. Otto, *Nat Nano*, 2015, **10**, 111-119.
91. F. J. M. Hoeben, P. Jonkheijm, E. W. Meijer and A. P. H. J. Schenning, *Chem. Rev.*, 2005, **105**, 1491-1546.
92. F. Biedermann and H.-J. r. Schneider, *Chem. Rev.*, 2016, **116**, 5216-5300.
93. H.-J. Schneider, *Angew. Chem. Int. Ed.*, 2009, **48**, 3924-3977.
94. F. Biedermann, W. M. Nau and H.-J. Schneider, *Angew. Chem. Int. Ed.*, 2014, **53**, 11158-11171.
95. R. Eisenschitz and F. London, *Zeitschrift für Physik*, 1930, **60**, 491-527.
96. P. Pyykkö, J. Li and N. Runeberg, *Chem. Phys. Lett.*, 1994, **218**, 133-138.
97. F. Scherbaum, A. Grohmann, B. Huber, C. Krüger and H. Schmidbaur, *Angew. Chem. Int. Ed.*, 1988, **27**, 1544-1546.
98. P. Pyykkö and M. Straka, *Phys. Chem. Chem. Phys.*, 2000, **2**, 2489-2493.
99. S. Sculfort and P. Braunstein, *Chem. Soc. Rev.*, 2011, **40**, 2741-2760.
100. H. Schmidbaur and A. Schier, *Chem. Soc. Rev.*, 2012, **41**, 370-412.
101. H. Schmidbaur, *Gold Bulletin*, 2000, **33**, 3-10.
102. H. Schmidbaur, *Chem. Soc. Rev.*, 1995, **24**, 391-400.
103. M. J. Katz, K. Sakai and D. B. Leznoff, *Chem. Soc. Rev.*, 2008, **37**, 1884-1895.
104. Y. Kajitani, K. Tsuge, Y. Sasaki and M. Kato, *Chemistry-A European Journal*, 2012, **18**, 11196-11200.
105. D. L. M. Suess and J. C. Peters, *Chem. Commun.*, 2010, **46**, 6554-6556.
106. T. Murahashi and H. Kurosawa, *Coord. Chem. Rev.*, 2002, **231**, 207-228.
107. M. Kim, T. J. Taylor and F. o. P. Gabbaï, *J. Am. Chem. Soc.*, 2008, **130**, 6332-6333.
108. E. J. Fernandez, A. Laguna and J. M. Lopez-de-Luzuriaga, *Dalton Trans.*, 2007, 1969-1981.
109. R. Jószai, I. Beszeda, A. C. Bényei, A. Fischer, M. Kovács, M. Maliarik, P. Nagy, A. Shchukarev and I. Tóth, *Inorg. Chem.*, 2005, **44**, 9643-9651.

110. Q.-J. Pan, X. Zhou, Y.-R. Guo, H.-G. Fu and H.-X. Zhang, *Inorg. Chem.*, 2009, **48**, 2844-2854.
111. B.-H. Xia, H.-X. Zhang, C.-M. Che, K.-H. Leung, D. L. Phillips, N. Zhu and Z.-Y. Zhou, *J. Am. Chem. Soc.*, 2003, **125**, 10362-10374.
112. B. Ma, J. Li, P. I. Djurovich, M. Yousufuddin, R. Bau and M. E. Thompson, *J. Am. Chem. Soc.*, 2005, **127**, 28-29.
113. D. Kim and J. L. Bredas, *J. Am. Chem. Soc.*, 2009, **131**, 11371-11380.
114. I. V. Novozhilova, A. V. Volkov and P. Coppens, *J. Am. Chem. Soc.*, 2003, **125**, 1079-1087.
115. Y. Ozawa, M. Terashima, M. Mitsumi, K. Toriumi, N. Yasuda, H. Uekusa and Y. Ohashi, *Chem. Lett.*, 2002, **32**, 62-63.
116. S. F. Rice and H. B. Gray, *J. Am. Chem. Soc.*, 1983, **105**, 4571-4575.
117. S. Grimme, *Wiley Interdisciplinary Reviews: Computational Molecular Science*, 2011, **1**, 211-228.
118. J. P. Wagner and P. R. Schreiner, *Angew. Chem. Int. Ed.*, 2015, **54**, 12274-12296.
119. L. Yang, C. Adam, G. S. Nichol and S. L. Cockroft, *Nat Chem*, 2013, **5**, 1006-1010.
120. D. J. Liptrot and P. P. Power, *Nature Reviews Chemistry*, 2017, **1**, 0004.
121. Y. Sun, K. Ye, H. Zhang, J. Zhang, L. Zhao, B. Li, G. Yang, B. Yang, Y. Wang, S. W. Lai and C. M. Che, *Angew. Chem.*, 2006, **118**, 5738-5741.
122. W. Lu, V. A. L. Roy and C.-M. Che, *Chem. Commun.*, 2006, 3972-3974.
123. X.-S. Xiao, W.-L. Kwong, X. Guan, C. Yang, W. Lu and C.-M. Che, *Chemistry-a European Journal*, 2013, **19**, 9457-9462.
124. M. Y. Yuen, V. A. L. Roy, W. Lu, S. C. F. Kui, G. S. M. Tong, M. H. So, S. S. Y. Chui, M. Muccini, J. Q. Ning, S. J. Xu and C.-M. Che, *Angew. Chem. Int. Ed.*, 2008, **47**, 9895-9899.
125. C.-M. Che, C.-F. Chow, M.-Y. Yuen, V. A. L. Roy, W. Lu, Y. Chen, S. S.-Y. Chui and N. Zhu, *Chem. Sci.*, 2011, **2**, 216-220.
126. C. A. Strassert, C. H. Chien, M. D. Galvez Lopez, D. Kourkoulos, D. Hertel, K. Meerholz and L. De Cola, *Angew. Chem. Int. Ed.*, 2011, **50**, 946-950.
127. M. Mydlak, M. Mauro, F. Polo, M. Felicetti, J. Leonhardt, G. Diener, L. De Cola and C. A. Strassert, *Chem. Mater.*, 2011, **23**, 3659-3667.
128. V. N. Kozhevnikov, B. Donnio and D. W. Bruce, *Angew. Chem. Int. Ed.*, 2008, **47**, 6286-6289.
129. F. Camerel, R. Ziessel, B. Donnio, C. Bourgogne, D. Guillon, M. Schmutz, C. Iacovita and J. P. Bucher, *Angew. Chem. Int. Ed.*, 2007, **46**, 2659-2662.
130. A. Y.-Y. Tam, K. M.-C. Wong, G. Wang and V. W.-W. Yam, *Chem. Commun.*, 2007, 2028-2030.
131. X.-S. Xiao, W. Lu and C.-M. Che, *Chem. Sci.*, 2014, **5**, 2482-2488.
132. W. Lu, Y. Chen, V. A. L. Roy, S. S. Y. Chui and C. M. Che, *Angew. Chem.*, 2009, **121**, 7757-7761.
133. N. K. Allampally, C. A. Strassert and L. De Cola, *Dalton Trans.*, 2012, **41**, 13132-13137.
134. J. Wang, Y. Chen, Y.-C. Law, M. Li, M.-X. Zhu, W. Lu, S. S.-Y. Chui, N. Zhu and C.-M. Che, *Chem. Asian J.*, 2011, **6**, 3011-3019.
135. N. K. Allampally, M. Bredol, C. A. Strassert and L. De Cola, *Chemistry (Weinheim an der Bergstrasse, Germany)*, 2014, **20**, 16863-16868.
136. C. Cebrian, M. Mauro, D. Kourkoulos, P. Mercandelli, D. Hertel, K. Meerholz, C. A. Strassert and L. De Cola, *Adv Mater*, 2013, **25**, 437-442.
137. A. R. Hirst, B. Escuder, J. F. Miravet and D. K. Smith, *Angew. Chem. Int. Ed.*, 2008, **47**, 8002-8018.
138. Y. Chen, K. Li, W. Lu, S. S. Y. Chui, C. W. Ma and C. M. Che, *Angew. Chem. Int. Ed.*, 2009, **48**, 9909-9913.
139. M. Krikorian, S. Liu and T. M. Swager, *J. Am. Chem. Soc.*, 2014, **136**, 2952-2955.
140. L.-M. Huang, G.-M. Tu, Y. Chi, W.-Y. Hung, Y.-C. Song, M.-R. Tseng, P.-T. Chou, G.-H. Lee, K.-T. Wong and S.-H. Cheng, *Journal of Materials Chemistry C*, 2013, **1**, 7582-7592.

141. J. Ni, X. Zhang, Y. H. Wu, L. Y. Zhang and Z. N. Chen, *Chemistry - A European Journal*, 2011, **17**, 1171-1183.
142. X. Zhang, Z. Chi, Y. Zhang, S. Liu and J. Xu, *Journal of Materials Chemistry C*, 2013, **1**, 3376-3390.
143. D. Genovese, A. Aliprandi, E. A. Prasetyanto, M. Mauro, M. Hirtz, H. Fuchs, Y. Fujita, H. Uji-I, S. Lebedkin, M. Kappes and L. D. Cola, *Adv. Funct. Mater.*, 2016.
144. K. W. Adolph and P. J. G. Butler, *J. Mol. Biol.*, 1974, **88**, 327-341.
145. T. Douglas, D. P. E. Dickson, S. Betteridge and J. Charnock, *Science*, 1995, **269**, 54.
146. T. Douglas and M. Young, *Nature*, 1998, **393**, 152-155.
147. A. Zlotnick, *J. Mol. Biol.*, 1994, **241**, 59-67.
148. L. O. Liepold, J. Revis, M. Allen, L. Oltrogge, M. Young and T. Douglas, *Physical biology*, 2005, **2**, S166.
149. L. Lavelle, M. Gingery, M. Phillips, W. M. Gelbart, C. M. Knobler, R. D. Cadena-Nava, J. R. Vega-Acosta, L. A. Pinedo-Torres and J. Ruiz-Garcia, *J. Phys. Chem. B*, 2009, **113**, 3813-3819.
150. T. Douglas, M. Allen and M. Young, *Biopolymers Online*, 2005.
151. A. A. Aljabali, F. Sainsbury, G. P. Lomonossoff and D. J. Evans, *Small*, 2010, **6**, 818-821.
152. C. Chen, M. C. Daniel, Z. T. Quinkert, M. De, B. Stein, V. D. Bowman, P. R. Chipman, V. M. Rotello, C. C. Kao and B. Dragnea, *Nano Lett*, 2006, **6**, 611-615.
153. F. D. Sikkema, M. Comellas-Aragones, R. G. Fokkink, B. J. M. Verduin, J. J. L. M. Cornelissen and R. J. M. Nolte, *Org. Biomol. Chem.*, 2007, **5**, 54-57.
154. C. E. Flynn, S.-W. Lee, B. R. Peelle and A. M. Belcher, *Acta Mater.*, 2003, **51**, 5867-5880.
155. H.-A. Hosein, D. R. Strongin, M. Allen and T. Douglas, *Langmuir*, 2004, **20**, 10283-10287.
156. A. de la Escosura, M. Verwegen, F. D. Sikkema, M. Comellas-Aragones, A. Kirilyuk, T. Rasing, R. J. M. Nolte and J. J. L. M. Cornelissen, *Chem. Commun.*, 2008, 1542-1544.
157. J. Sun, C. DuFort, M.-C. Daniel, A. Murali, C. Chen, K. Gopinath, B. Stein, M. De, V. M. Rotello and A. Holzenburg, *PNAS*, 2007, **104**, 1354-1359.
158. M. Allen, D. Willits, J. Mosolf, M. Young and T. Douglas, *Adv. Mater.*, 2002, **14**, 1562-1565.
159. S. L. Capehart, M. P. Coyle, J. E. Glasgow and M. B. Francis, *J. Am. Chem. Soc.*, 2013, **135**, 3011-3016.
160. A. Liu, M. Verwegen, M. V. de Ruiter, S. J. Maassen, C. H. H. Traulsen and J. J. L. M. Cornelissen, *J. Phys. Chem. B*, 2016, **120**, 6352-6357.
161. I. J. Minten, L. J. A. Hendriks, R. J. M. Nolte and J. J. L. M. Cornelissen, *J. Am. Chem. Soc.*, 2009, **131**, 17771-17773.
162. S. Deshayes and R. Gref, *Nanomedicine*, 2014, **9**, 1545-1564.
163. N. F. Steinmetz, *Nanomedicine: Nanotechnology, Biology and Medicine*, 2010, **6**, 634-641.
164. E. J. Lee, N. K. Lee and I.-S. Kim, *Advanced drug delivery reviews*, 2016, **106, Part A**, 157-171.
165. X.-T. Ji, L. Huang and H.-Q. Huang, *Journal of Proteomics*, 2012, **75**, 3145-3157.
166. R. Xing, X. Wang, C. Zhang, Y. Zhang, Q. Wang, Z. Yang and Z. Guo, *J. Inorg. Biochem.*, 2009, **103**, 1039-1044.
167. M. A. Kilic, E. Ozlu and S. Calis, *Journal of biomedical nanotechnology*, 2012, **8**, 508-514.
168. P. Pushko, P. Pumpens and E. Grens, *Intervirology*, 2013, **56**, 141-165.
169. Z. Yang, X. Wang, H. Diao, J. Zhang, H. Li, H. Sun and Z. Guo, *Chem. Commun.*, 2007, 3453-3455.
170. Y. Ma, R. J. Nolte and J. J. Cornelissen, *Advanced drug delivery reviews*, 2012, **64**, 811-825.
171. S. E. Aniagyei, C. Dufort, C. C. Kao and B. Dragnea, *J Mater Chem*, 2008, **18**, 3763-3774.

172. C. M. Soto and B. R. Ratna, *Curr. Opin. Biotechnol.*, 2010, **21**, 426-438.
173. L. Loo, R. H. Guenther, S. A. Lommel and S. Franzen, *Chem. Commun.*, 2008, 88.
174. I. J. Minten, R. J. M. Nolte and J. J. L. M. Cornelissen, *Macromolecular Bioscience*, 2010, **10**, 539-545.
175. R. D. Cadena-Nava, Y. Hu, R. F. Garmann, B. Ng, A. N. Zelikin, C. M. Knobler and W. M. Gelbart, *J. Phys. Chem. B*, 2011, **115**, 2386-2391.
176. J.-K. Rhee, M. Hovlid, J. D. Fiedler, S. D. Brown, F. Manzenrieder, H. Kitagishi, C. Nycholat, J. C. Paulson and M. G. Finn, *Biomacromolecules*, 2011, **12**, 3977-3981.
177. W. F. Rurup, F. Verbij, M. S. T. Koay, C. Blum, V. Subramaniam and J. J. L. M. Cornelissen, *Biomacromolecules*, 2014, **15**, 558-563.
178. E. A. Anderson, S. Isaacman, D. S. Peabody, E. Y. Wang, J. W. Canary and K. Kirshenbaum, *Nano Lett.*, 2006, **6**, 1160-1164.
179. L. Liepold, S. Anderson, D. Willits, L. Oltrogge, J. A. Frank, T. Douglas and M. Young, *Magnetic Resonance in Medicine*, 2007, **58**, 871-879.
180. M. Allen, J. W. M. Bulte, L. Liepold, G. Basu, H. A. Zywicke, J. A. Frank, M. Young and T. Douglas, *Magnetic Resonance in Medicine*, 2005, **54**, 807-812.
181. M. Comellas-Aragones, H. Engelkamp, V. I. Claessen, N. A. J. M. Sommerdijk, A. E. Rowan, P. C. M. Christianen, J. C. Maan, B. J. M. Verduin, J. J. L. M. Cornelissen and R. J. M. Nolte, *Nat Nano*, 2007, **2**, 635-639.
182. Z. Liu, J. Qiao, Z. Niu and Q. Wang, *Chem. Soc. Rev.*, 2012, **41**, 6178-6194.
183. Y. Wu, H. Yang and H.-J. Shin, *Korean J. Chem. Eng.*, 2013, **30**, 1359-1367.
184. R. M. Putri, J. J. L. M. Cornelissen and M. S. T. Koay, *ChemPhysChem*, 2015, **16**, 911-918.
185. J. G. Millán, M. Brasch, E. Anaya-Plaza, A. de la Escosura, A. H. Velders, D. N. Reinhoudt, T. Torres, M. S. T. Koay and J. J. L. M. Cornelissen, *J. Inorg. Biochem.*, 2014, **136**, 140-146.
186. L. Lavelle, J.-P. Michel and M. Gingery, *Journal of Virological Methods*, 2007, **146**, 311-316.
187. W. F. Ochoa, A. Chatterji, T. Lin and J. E. Johnson, *Chemistry & Biology*, 2006, **13**, 771-778.
188. S. Mukherjee, C. M. Pfeifer, J. M. Johnson, J. Liu and A. Zlotnick, *J. Am. Chem. Soc.*, 2006, **128**, 2538-2539.
189. J. Tang, J. M. Johnson, K. A. Dryden, M. J. Young, A. Zlotnick and J. E. Johnson, *Journal of structural biology*, 2006, **154**, 59-67.
190. S. Brumfield, D. Willits, L. Tang, J. E. Johnson, T. Douglas and M. Young, *The Journal of general virology*, 2004, **85**, 1049-1053.
191. D. L. D. Caspar and A. Klug, *Cold Spring Harb Symp Quant Biol.*, 1962, **27**, 1-24.
192. M. Goldberg, *Tohoku Mathematical Journal, First Series*, 1937, **43**, 104-108.
193. J. A. Speir, S. Munshi, G. Wang, T. S. Baker and J. E. Johnson, *Structure*, 1995, **3**, 63-78.
194. M. Brasch, A. de la Escosura, Y. Ma, C. Uetrecht, A. J. Heck, T. Torres and J. J. Cornelissen, *J. Am. Chem. Soc.*, 2011, **133**, 6878-6881.
195. A. d. l. Escosura, P. G. A. Janssen, A. P. H. J. Schenning, R. J. M. Nolte and J. J. L. M. Cornelissen, *Angew. Chem. Int. Ed.*, 2010, **49**, 5335-5338.
196. M. Brasch, PhD, University of Twente, 2013.
197. C.-M. Che, J.-L. Zhang and L.-R. Lin, *Chem. Commun.*, 2002, 2556-2557.
198. K. K.-W. Lo, in *Photofunctional Transition Metal Complexes*, ed. V. W. W. Yam, Springer Berlin Heidelberg, Berlin, Heidelberg, 2007, pp. 205-245.
199. P. Kit-Man Siu, D.-L. Ma and C.-M. Che, *Chem. Commun.*, 2005, 1025-1027.
200. S.-W. Lai and C.-M. Che, in *Transition Metal and Rare Earth Compounds: Excited States, Transitions, Interactions III*, ed. H. Yersin, Springer Berlin Heidelberg, Berlin, Heidelberg, 2004, pp. 27-63.
201. C.-M. Che and F.-M. Siu, *Curr. Opin. Chem. Biol.*, 2010, **14**, 255-261.
202. P. Wu, E. L. M. Wong, D. L. Ma, G. S. M. Tong, K. M. Ng and C. M. Che, *Chemistry - A European Journal*, 2009, **15**, 3652-3656.

203. A. I. Solomatina, P. S. Chelushkin, D. V. Krupenya, I. S. Podkorytov, T. O. Artamonova, V. V. Sizov, A. S. Melnikov, V. V. Gurzhiy, E. I. Koshel and V. I. Shcheslavskiy, S.P. Tunik, *Bioconjugate Chem.*, 2016.
204. L. Peng, R. Wei, K. Li, Z. Zhou, P. Song and A. Tong, *Analyst*, 2013, **138**, 2068-2072.
205. B. X. Huang, H.-Y. Kim and C. Dass, *J. Am. Soc. Mass. Spectrom.*, 2004, **15**, 1237-1247.
206. V. G. Vaidyanathan and B. U. Nair, *Eur. J. Inorg. Chem.*, 2005, **2005**, 3756-3759.
207. I. Sasaki, C. Bijani, S. Ladeira, V. Bourdon, P. Faller and C. Hureau, *Dalton Trans.*, 2012, **41**, 6404-6407.
208. C. Hureau and P. Faller, *Dalton Trans.*, 2014, **43**, 4233-4237.
209. D. Valensin, C. Gabbiani and L. Messori, *Coord. Chem. Rev.*, 2012, **256**, 2357-2366.
210. B. Wang and E. V. Anslyn, *Chemosensors: Principles, Strategies, and Applications*, Wiley, Weinheim, 2011.
211. J. Wu, B. Kwon, W. Liu, E. V. Anslyn, P. Wang and J. S. Kim, *Chem. Rev.*, 2015, **115**, 7893-7943.
212. M. Schäferling, *Angew. Chem. Int. Ed.*, 2012, **51**, 3532-3554.
213. R. Martínez-Máñez and F. Sancenón, *Chem. Rev.*, 2003, **103**, 4419-4476.
214. O. S. Wolfbeis, *Angew. Chem. Int. Ed.*, 2013, **52**, 9864-9865.
215. X. Li, X. Gao, W. Shi and H. Ma, *Chem. Rev.*, 2014, **114**, 590-659.
216. B. T. Nguyen and E. V. Anslyn, *Coord. Chem. Rev.*, 2006, **250**, 3118-3127.
217. E. Fischer, *Berichte der deutschen chemischen Gesellschaft*, 1894, **27**, 2985-2993.
218. R. A. Bissell, A. Prasanna de Silva, H. Q. Nimal Gunaratne, P. L. Mark Lynch, G. E. M. Maguire, C. P. McCoy and K. R. A. Samankumara Sandanayake, in *Photoinduced Electron Transfer V*, ed. J. Mattay, Springer Berlin Heidelberg, Berlin, Heidelberg, 1993, pp. 223-264.
219. C. J. Pedersen, *J. Am. Chem. Soc.*, 1967, **89**, 7017-7036.
220. C. J. Pedersen, *J. Am. Chem. Soc.*, 1967, **89**, 2495-2496.
221. A. P. de Silva and S. A. de Silva, *J. Chem. Soc., Chem. Commun.*, 1986, 1709-1710.
222. A. P. de Silva, H. Q. N. Gunaratne, T. Gunnlaugsson, A. J. M. Huxley, C. P. McCoy, J. T. Rademacher and T. E. Rice, *Chem. Rev.*, 1997, **97**, 1515-1566.
223. G. W. Gokel, W. M. Leevy and M. E. Weber, *Chem. Rev.*, 2004, **104**, 2723-2750.
224. J. F. Callan, A. P. de Silva and D. C. Magri, *Tetrahedron*, 2005, **61**, 8551-8588.
225. J. J. Lavigne and E. V. Anslyn, *Angew. Chem. Int. Ed.*, 2001, **40**, 3118-3130.
226. S. Stewart, M. A. Ivy and E. V. Anslyn, *Chem. Soc. Rev.*, 2014, **43**, 70-84.
227. S. Rochat, J. Gao, X. Qian, F. Zaubitzer and K. Severin, *Chem. Eur. J.*, 2010, **16**, 104-113.
228. T. Minami, N. A. Esipenko, B. Zhang, M. E. Kozelkova, L. Isaacs, R. Nishiyabu, Y. Kubo and P. Anzenbacher, *J. Am. Chem. Soc.*, 2012, **134**, 20021-20024.
229. T. Minami, N. A. Esipenko, B. Zhang, L. Isaacs and P. Anzenbacher, *Chem. Commun.*, 2014, **50**, 61-63.
230. T. Minami, N. A. Esipenko, A. Akdeniz, B. Zhang, L. Isaacs and P. Anzenbacher Jr, *J. Am. Chem. Soc.*, 2013, **135**, 15238-15243.
231. R. Nishiyabu and P. Anzenbacher, *J. Am. Chem. Soc.*, 2005, **127**, 8270-8271.
232. C. J. Musto and K. S. Suslick, *Curr. Opin. Chem. Biol.*, 2010, **14**, 758-766.
233. O. R. Miranda, B. Creran and V. M. Rotello, *Curr. Opin. Chem. Biol.*, 2010, **14**, 728-736.
234. S. Rochat and K. Severin, *J Comb Chem*, 2010, **12**, 595-599.
235. M. G. Caglayan, S. Sheykhi, L. Mosca and P. Anzenbacher, *Chem. Commun.*, 2016, **52**, 8279-8282.
236. P. N. Basa and A. G. Sykes, *J. Org. Chem.*, 2012, **77**, 8428-8434.
237. S. Rochat and T. M. Swager, *Angew. Chem. Int. Ed.*, 2014, **53**, 9792-9796.

Chapter II

A Ratiometric Luminescent Switch Based on Platinum Complexes Tethered to a Crown-Ether Scaffold

---

Abstract

In this chapter, a ratiometric chemosensor for potassium is reported, based on phosphorescent dinuclear N-metallacyclic Pt(II)-complexes featuring a cis-crown ether as the cation-recognition unit (Figure 2.1). The metal complexes are blue luminescent in a non-aggregated state but become strongly orange emissive when in a close physical proximity, as is the case when the macrocycle is in the folded state. Upon binding of the cation, unfolding occurs, resulting in a pronounced change in the emission properties (*e.g.* emission wavelength), which can be used for ratiometric sensing applications. The reversibility of the binding was confirmed by competitive titration experiments with unsubstituted 18-crown-6; the system shows supramolecular switching behavior.

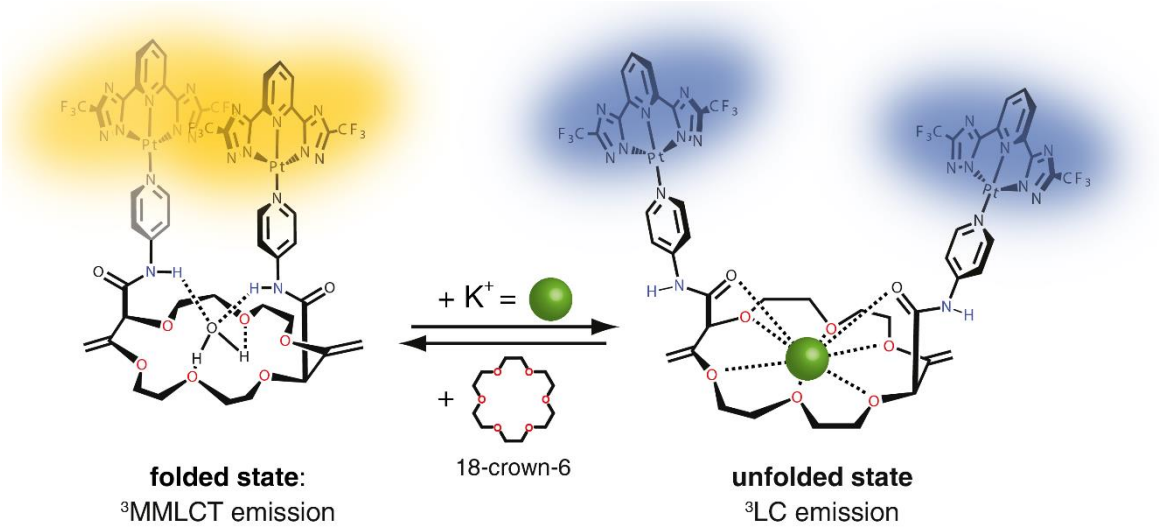

Figure 2.1: Reversible emission-color switch of Pt-dye pendant crown ether upon addition of potassium salts and subsequent back-switch by extraction with unsubstituted 18-crown-6.

Introduction

Sensing metal cations by crown ethers

Sensing of first and second row metal cations has received wide interest because of the important role played by these ions in biological systems.[1-6] Crown ethers, in particular, are extensively used as cation-recognition scaffolds in supramolecular assemblies and sensor applications.[7-10] For the latter, mostly aza-crowns serve as the cation-binding units and photoinduced electron transfer (PET) of tethered organic fluorophores is used as reader of the cation binding event. Indeed, upon coordination of the ion an increase in the emission intensity is monitored which corresponds to the inhabitation of the PET.[5, 6] Others, such as BODIPY-linked azacrown ethers enable ratiometric cation detection.[11] However, the substitution of oxo- by aza-moieties in crown ethers has the effect of significantly reducing the affinity for cations,[12] *e.g.*, the binding constant for K^+ in acetonitrile is $5 \cdot 10^5\ M^{-1}$ with 18-crown-6[10] and only $2 \cdot 10^3\ M^{-1}$ with BODIPY-linked azacrowns.[11] Alternatively, a dye-disaggregation strategy can be used to allow for signal transduction with "native" crown ethers.[13-20] For example, two pyrene moieties linked through long flexible arms to an 18-crown-6 ether reside in close spatial proximity in the cation-free state, which is indicated by an excimer emission band (480 – 490 nm).[13, 14] In the cation-bound state, a larger fraction of the pyrene-monomer emission (370 – 430 nm) is observed because of a conformation change of the crown ether. This approach has the drawback that suitable dyes are rare that show a distinct monomer and excimer emission, and that can be excited in the visible wavelength range. Furthermore, with the known chromophores, large conformational changes may be needed to obtain suitable spectroscopic effects, *e.g.*, pyrene molecules even at more than 10 Å spatial distance still show a marked excimer emission band.[21]

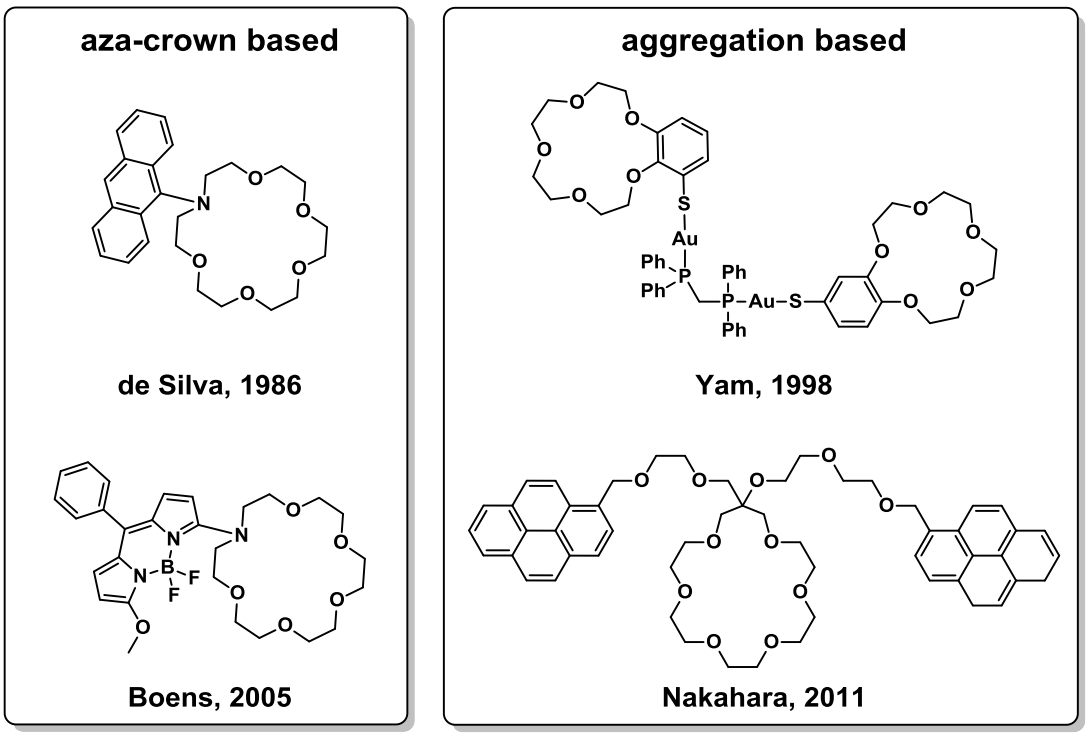

Figure 2.2: Literature examples for crown-ether based cation sensors. Aza-crown based systems[11, 22] suffer from lower binding constants than the entirely oxygenated crown-ethers[12] based on aggregation and disaggregation.[23, 24]

Transition metal complexes as phosphorescent reporters

Taking advantage of the beneficial photophysical properties of many transition-metal complexes, several cation-chemosensors based on Ru(II),[25-31] Os(II),[32] Re(I),[33] Ir(III),[34-36] Au(I)[23, 37-39] complexes were developed. In the last few decades, luminescent Pt(II)-complexes have received growing attention on account of their appealing photophysical (*e.g.* absorbance and luminescence in the visible region, large Stokes shifts, high emission quantum yields) and redox properties.[24, 40-47] In particular, neutral Pt(II)-complexes bearing terdentate azolate-based ligands possess extraordinary high phosphorescence quantum yields and long excited-state lifetimes.[46, 48] Reported cation sensors utilizing platinum-complex scaffolds were based on spectroscopic changes that were induced by alteration of the electron-density or orbital energies upon cation binding.[43, 44] For instance, an aza-crown moiety in proximity to a Pt-complex caused emission quenching of the ^{3}MLCT state through photoelectron transfer (PET); as for their fluorescent organic analogues, the luminescence is then restored upon cation binding.[43] An alternative strategy takes advantage of strongly electron donating ligands (acetylide, aza-crowns) that render these Pt-complexes to be non-emissive because of the low lying

^{3}LLCT state. Upon cation binding a lowering of the donating strength of the ligand occurs, raising the energy of the ^{3}LLCT above the ^{3}MLCT state, such that phosphorescence can be observed.[41].

Neutral Pt(II)-complexes with pronounced supramolecular features

Due to their square-planar geometry and large aromatic surface area, Pt(II)-complexes with terdentate cyclometalating ligands (*e.g.*, 2,6-bis(3-(trifluoromethyl)-1*H*-1,2,4-triazol-5-yl) pyridine, **CF$_3$-tzH$_2$** see Figure 2.3) readily form non-covalent adducts (dimers, aggregates, etc.) where emerging metal•••metal interactions of the Pt(II) centers strongly augment their emission properties.[24, 45, 49-53] On account of its superior photophysical properties, when coordinated to Pt(II) together with a further ancillary ligand, this terdentate ligand will be frequently used throughout the entire thesis and abbreviated as **L-2H** and **L** for the free ligand and in a coordination complex, respectively. This chapter focuses on the distinctly different luminescent features of monomeric and dimerized Pt-complexes for the design of a ratiometric sensor for potassium, that and emits in the visible region and which shows stronger changes in the emission properties upon cation binding than pyrene chromophores. As depicted in Figure 2.1, the system is reversible since an extraction of the potassium is rendered by an unsubstituted crown ether.

Results and discussion

Crown ethers **Py$_2$-18C4** and **Py$_2$-18C6** carrying 4-aminopyridine units were prepared in two steps as summarized in Table 2.1. First, methyl 2-diazo-3-oxobutanoate was reacted with tetrahydropyran (THP) and 1,4-dioxane in presence of $Rh_2(Oct)_4$ to yield 18-membered conjugated polyether macrocycles.[54, 55] These derivatives (Table 2.1, X = CH_2 or O) were then treated with mixtures of 4-aminopyridine and potassium *tert*-butoxide (KO^tBu) to induce tandem amidation-transposition processes and form the *cis*-disubstituted **Py$_2$-18C4** and **Py$_2$-18C6** macrocycles as single racemic stereoisomers (*d.r.* > 49:1, 55% and 50% combined yields respectively).[56]

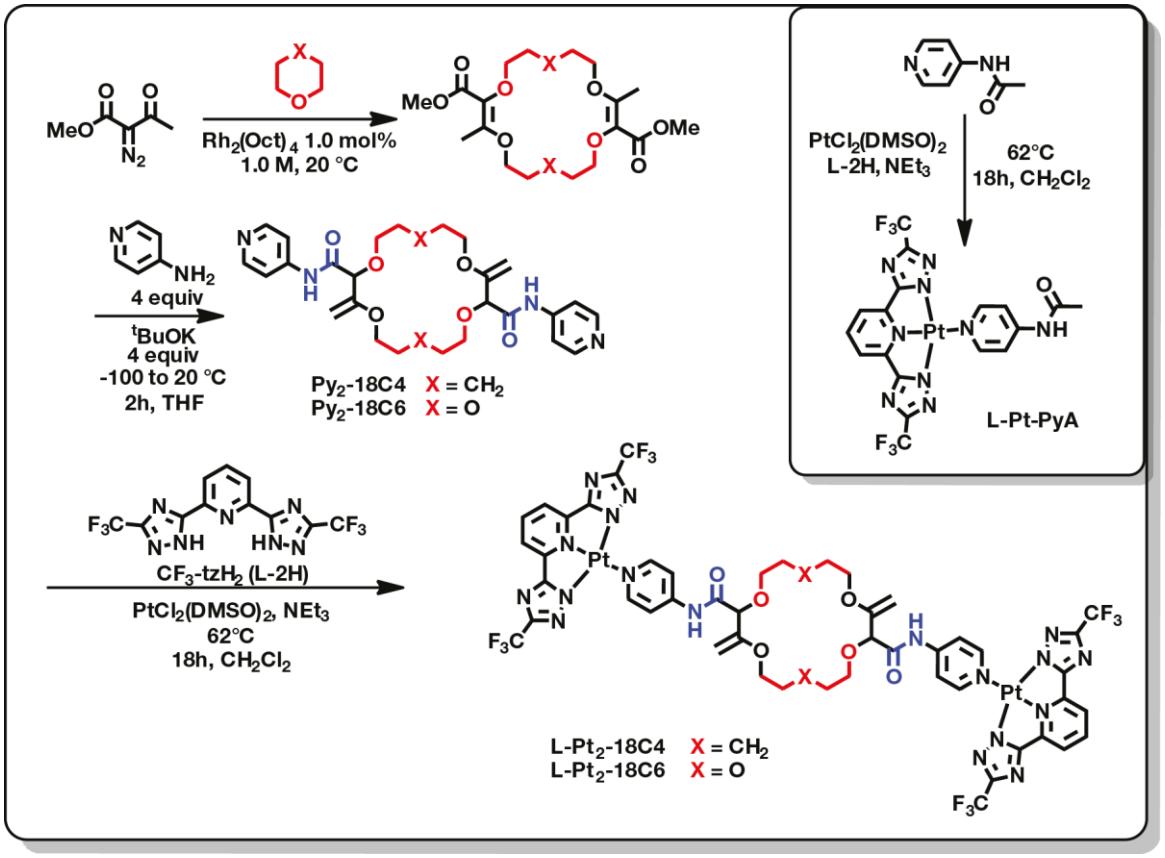

Scheme 2.1: Synthetic Scheme for of the molecules investigated **Pt_2-18C6**, **Pt_2-18C4** and the reference compound **L-Pt-PyA**. **L-Pt-PyA**: $PtCl_2DMSO_2$, N-(pyridin-4-yl) acetamide, CF_3-tzH_2 (**L-2H**), $CHCl_3$, 70°C, 18h, 72%. **L-Pt_2-18C4**: $PtCl_2DMSO_2$, **L-2H**, **Py_2-18C4**, $CHCl_3$, 70°C, 18h, 37%. **L-Pt_2-18C6**: **L-2H**, **Py_2-18C6**, $CHCl_3$, 70°C, 18h, 39%.

Defined conformation of the crown ether scaffolds

Importantly, both **Py_2-18C4** and **Py_2-18C6** derivatives adopt well-defined conformations. In fact, allylic 1,3-strain interactions occur between the stereogenic centers and adjacent exocyclic double bonds. In order to minimize the strain, the amide groups are oriented essentially perpendicular to the mean plane of the macrocycles. This conformational bias induces a spatial proximity between the aromatic residues.[56, 57] Hydrogen bonding interactions also occur between the amide N-H and neighboring oxygen atoms. Consequently, and in respect to the cavity, the N-H and C=O bonds of the amides are turned respectively inwards and outwards (see Figure 2.3).

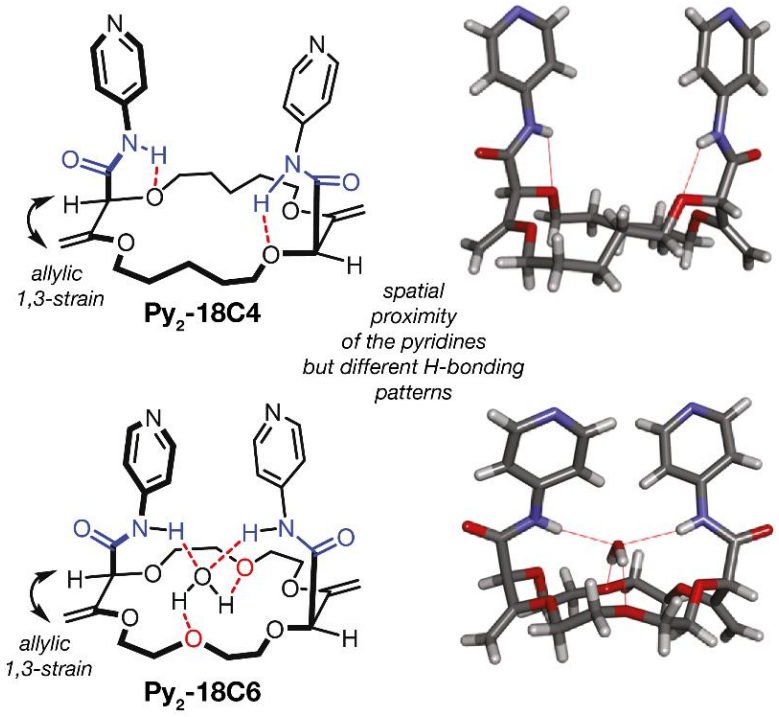

Figure 2.3: Schematic representation of the solid state "diaxial" conformations (left) and the corresponding X-ray structures (right) of **Py$_2$-18C4** and **Py$_2$-18C6**.

However, there are some differences which are essential for the following properties of the complexes. In the case of compound **Py$_2$-18C4**, the N-H···O interactions take place with the proximal oxygen atoms attached to the stereogenic centers while, with **Py$_2$-18C6**, they occur with a guest water molecule. The described H-bond conditions were also found for other 18C6 and 18C4 derivatives irrespective to the nature of the aromatic ring.[54-56] Noteworthy, for **Py$_2$-18C4** intermolecular N-H···O interactions between neighboring molecules were also observed in the solid state which can result in packing. Nevertheless, these bonds are most likely not preserved in a diluted THF solution. This condition modifies the orientation of the amide functional groups and the relative position of the aromatic residues.[58] This can be observed in the X-ray diffraction analyses depicted in Figure 2.4. As a consequence, in the solid state, the distances between the sp^2-nitrogen atoms of the pyridine units are 7.50 and 6.84 Å within **Py$_2$-18C4** and **Py$_2$-18C6** respectively. Hence, a larger separation of the nitrogen atoms in the **Py$_2$-18C4** derivative can be observed. Detailed parameters of the X–ray structures are given in the Appendix.

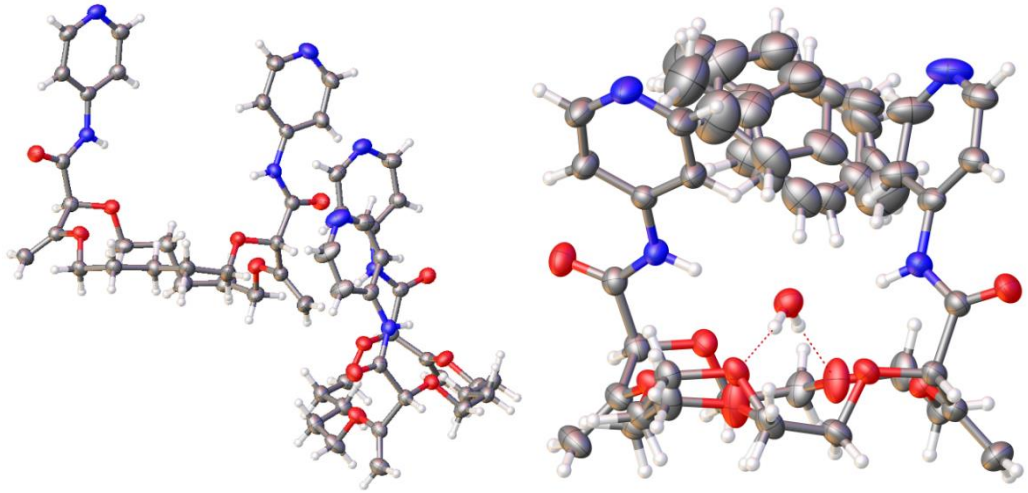

Figure 2.4: Solid-state structures determined by X-ray diffraction analysis of **Py_2-18C4** (left) and **Py_2-18C6** (right) featuring an ellipsoid probability of 50%. Solvent molecules are omitted for clarity.

Pt(II)-complex installation onto the scaffold

With the pyridine substituted crown ether derivatives **Py_2-18C6** and **Py_2-18C4** in hand, two N-metalacycled Pt(II)-complexes were attached on the scaffold of **Py_2-18C6** through a complexation reaction with $PtCl_2(DMSO)_2$ and **L-2H** in $CHCl_3$ for 18 h at 62°C (see Experimental section for more details). In the resulting **L-Pt_2-18C6**, the coordinated Pt(II)-complexes can come into close proximity in the cation-free state, as confirmed by crystal structures of the macrocyclic ligands (see Figure 2.4) and similar structures.[59] The analogous 18-crown-4-based complex **Pt_2-18C4** serves as a control-substance, since its different H-bonding condition suggests as well a different aggregation of the Pt-complex chromophores (see Figure 2.3). A reference complex without a crown ether motif, **L-Pt-PyA**, with a 4-pyridyl acetamide ligand, was also prepared (see Scheme 2.1).

Photophysical analysis in solution and solid state

Photophysical properties of the complexes were investigated in solution and in solid state (Figure 2.5 and Table 2.1). The solution titration experiments were carried out in tetrahydrofuran (THF) because of the good solubility of the investigated Pt(II)-complexes in this solvent. The results are summarized in Table 2.1. All compounds display characteristic absorption bands in the UV region (270 − 350 nm), related to ligand centered transitions, while at lower energy (350 − 430 nm) metal-to-ligand charge transfer transitions (MLCT) are observed (Figure 2.5). The reference complex **L-Pt-PyA**

displays a structured emission spectrum (464 − 567 nm) attributable to arise from a ligand centered state[12] (^{3}LC). The relatively short excited-state lifetimes of a few nanoseconds in solution are typical for molecularly dissolved Pt(II)-complexes with **L-2H** as the N-metalacycling ligand (see Table 2.1).[24, 45, 46, 48, 50, 60] Absence of *inter*molecular aggregate formation at the utilized concentration range (0.1 - 0.01 mM) was confirmed by the observed Lambert-Beer behavior, *i.e.*, the absorbance was linear proportional to the concentration. For **L-Pt$_2$-18C4** resembles qualitatively well the absorption spectrum of **L-Pt-A** indicating a non-aggregated ground state complex. The absorption spectrum of **L-Pt$_2$-18C4** shows higher extinction coefficients than determined for **L-Pt-A** which are attributed to the enlarged chromophoric system (two chromophoric moieties at one crown). In the emission spectrum of **L-Pt$_2$-18C4** a second intense unstructured emission band peaking at 575 nm, which is arising from a metal-metal ligand charge transfer state (^{3}MMLCT).[45, 46, 50] This emission is indicative of Pt•••Pt interactions (*vide infra*).

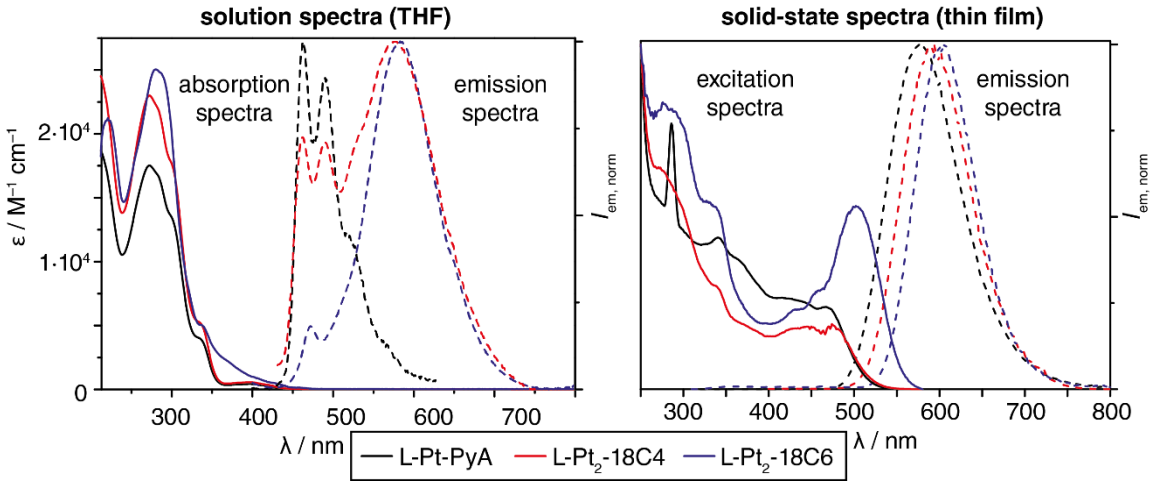

Figure 2.5: left: UV/Vis absorption (solid) and normalized emission (dashed, λ_{ex} = 300 nm) spectra in aerated THF (10 µM) at ambient conditions. right: Normalized excitation (solid) and emission(dashed) spectra (λ_{ex} = 300 nm) in the solid state. Color code: **L-Pt-PyA** (black), **L-Pt$_2$-18C4** (red) and **L-Pt$_2$-18C6** (blue).

In contrast to the aforementioned complexes, **L-Pt$_2$-18C6** exhibits strongly pronounced bands in the absorption from 350 to 450 nm attributed to allowed MMLCT transitions (see Chapter I Scheme I) suggesting the formation of ground-state aggregates. The emission spectrum (λ_{max} = 595 nm, ^{3}MMLCT emission) shows as well features that are indicative of Pt•••Pt interactions.[51] The experimental data shows that for **L-Pt$_2$-18C4** and **L-Pt$_2$-18C6** the Pt(II) chromophores interact *intra*molecularly. Notably, the more red-shifted ^{3}MMLCT emission of **L-Pt$_2$-18C6** is in agreement with the shorter distance of the sp^2-nitrogen atoms found in the crystal structures of the pyridine analogues (*vide supra*).

Comparison of the spectroscopic features of the folded state adopted in solution by the platinum substituted crown ethers, and those of the aggregated Pt(II)-complexes in the solid state (neat film) provides further evidence for the proposed molecular conformations. **L-Pt-PyA** shows, in the solid state, a red shifted absorption onset in the excitation spectrum (Figure 2.11) and ^{3}MMLCT based emission. Thus, if the Pt(II) centers of **L-Pt-PyA** also came into close proximity in solution, similar spectroscopic features to its solid-state spectra would have been observed.

Table 2.1: Summary of the photophysical properties of the complexes.

	solution				solid state		
	λ / nm [a] (ε / $M^{-1}cm^{-1}$)	λ_{em} [a,b] / nm	φ [a,c]	τ / ns [a,d,e]	λ_{em} [b,f] / nm	φ [c,f]	τ / ns [f]
L-Pt-PyA	273 (17525), 299 sh (13565), 335 (3991), 397 (434)	463, 490, 527, 567	<1%	2.1	577	65%	226 (22%) 436 (78%) [g]
L-Pt$_2$-18C4	270 (23363), 303 sh (17690), 337 (5054), 397 (570)	463, 490, 575	<1%	3.3 (31%) 1.2 (69%)	594	69%	609 (45%) 439 (55%) [h]
L-Pt$_2$-18C6	280 (25054), 337 (5054), 368 (2273), 405 (891)	585 (464, 489) [j]	<1%	464 nm: 3.6 585 nm: 121.9 (40%) 21.3 (45%) 3.8 (15%)	607	40%	278 [i]

[a] measured in aerated THF (10 µM); [b] λ_{ex} = 300 nm; [c] average of scanning λ_{ex} = 280 - 400 nm (10 nm interval), [d] λ_{ex} = 375 nm; [e] λ_{em} = 461 nm if not mentioned differently; [f] neat film; [g] λ_{em} = 577 nm, [h] λ_{em} = 594 nm; [i] λ_{em} = 607 nm; [j] transitions in brackets appearing upon cation addition

Noteworthy, the bathochromic shift within the solid state spectra from **L-Pt-PyA** (λ_{max} = 577 nm) to **L-Pt$_2$-18C4** (λ_{max} = 591 nm) to **L-Pt$_2$-18C6** (λ_{max} = 607 nm) indicates a closer proximity of the Pt centers when linked by a crown ether, since the HOMO-LUMO gap is strongly dependent on the Pt-Pt distance.[50, 51] The absorbance and emission spectra of **L-Pt$_2$-18C4** and **L-Pt$_2$-18C6** show similar features in solution. However, in solid state the absorption onset is 4781 cm^{-1} and 5084 cm^{-1} bathochromically-shifted and 556 cm^{-1} and 620 cm^{-1} red-shifted emission bands are detected, respectively. The fact that the emission energy is almost unchanged going from solution to solid state and it is

lower than for the other complexes (in the solid state) suggest that for **L-Pt$_2$-18C4** and **L-Pt$_2$-18C6** the electronic interaction between the Pt units is *intra*molecular in solution and most likely, as for **L-Pt-PyA**, an *inter*molecular aggregation occurs in the solid state. The presence of such a strong electronic coupling, when the crown ether is not coordinated to a cation, is the basis for the sensing behavior.

Sensing of potassium

The sensing and switching capabilities of **L-Pt$_2$-18C4** and **L-Pt$_2$-18C6** were studied using potassium ions as coordinating units. Based on previous studies with pyrene-labelled crown ethers,[59] it was expected that binding of potassium to **L-Pt$_2$-18C6** would lead to a conformational change by a perturbation of the favorable H-bond interaction (see Figure 2.6 for NMR experiments) of the crown-ether moiety resulting in a breakdown of the intramolecular electronic interaction between the Pt(II) centers.

In the ^{1}H-NMR spectrum of **L-Pt$_2$-18C6**, the protons of the amide groups (see Figure 2.3) are assigned to the singlet peak at a chemical shift of 10.37 ppm. This peak is low-field shifted (10.21 ppm) upon potassium uptake. The other peaks assigned to the aromatic part of the Pt complexes (9.26, 8.04, 7.59, 7.48 ppm) as well as the peaks assigned to the protons of the methanetriyl (CH) and ethenyl (CH_2) groups (4.55, 4.49, 4.41 ppm) are all high-field shifted, which is indicative of a disaggregation of the system.

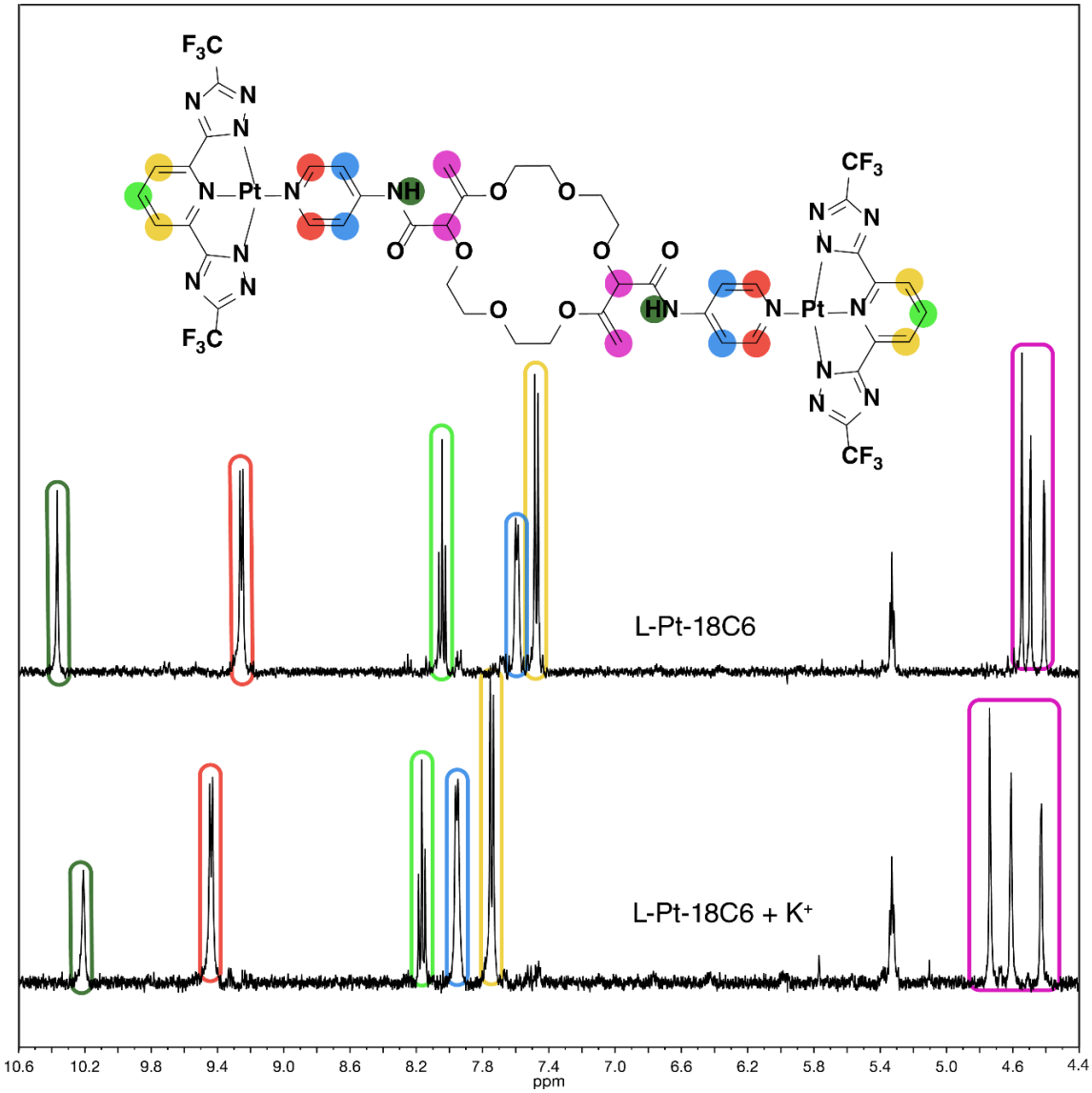

Figure 2.6: ^{1}H-NMR (400 MHz, THF-d_8) of **L-Pt$_2$-18C6** at a concentration of 0.1 mM without potassium salt (top, red) and with an excess of potassium trifluoromethanesulfonate (23 mM, bottom, green).

The fluorescence detection during the titration of **L-Pt$_2$-18C6** in THF with potassium trifluoromethanesulfonate yielded a strong decrease in the ^{3}MMLCT emission (585 nm) intensity, resulting in its almost complete quenching (Figure 2.7). At the same time, the ligand-centered (464 nm) emission of the monomeric Pt(II)-complexes increased, enabling ratiometric sensing applications that are often practically preferred over switch-on or switch-off assays. A similar behavior was found in the more polar solvent methanol lacking the raise of the ^{3}LC based emission (Figure 2.7).

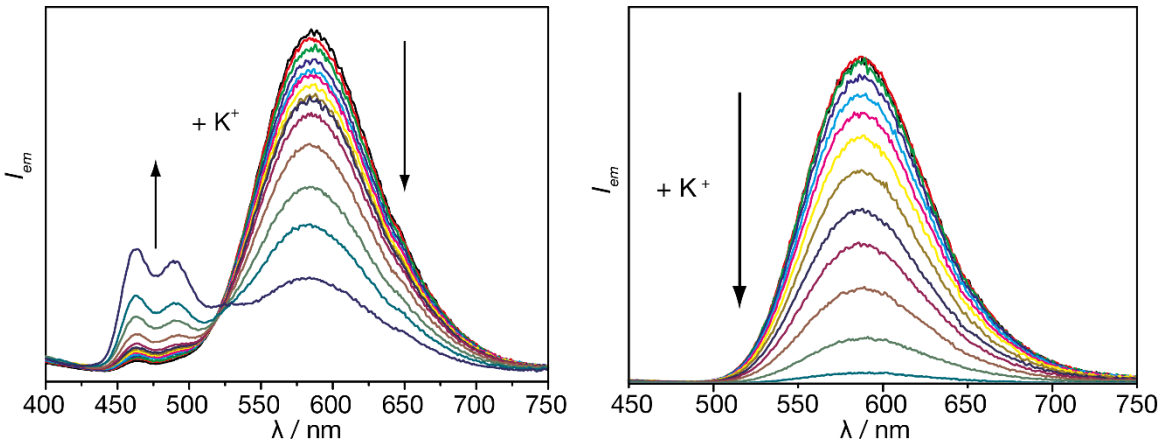

Figure 2.7: left, top: Emission spectra for the titration of **L-Pt$_2$-18C6** (0.01 mM) with potassium trifluoromethanesulfonate (10 mM) in THF at ambient conditions (λ_{ex} = 343 nm). right, bottom: emission spectra for the titration of **L-Pt$_2$-18C6** (0.01 mM) with potassium trifluoromethanesulfonate (10 mM) in methanol at ambient conditions (λ_{ex} = 343 nm).

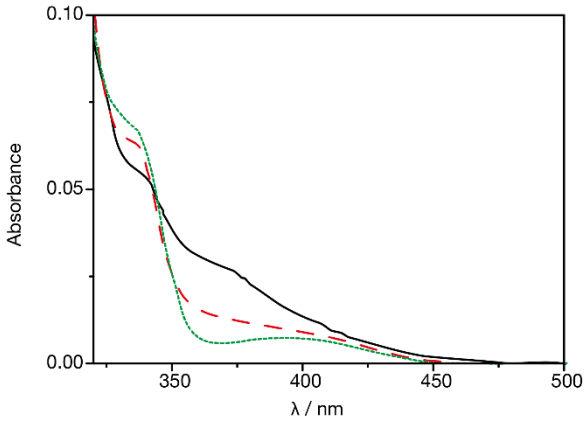

Figure 2.8: Zoom in to the absorption band between 350 – 450 nm of **L-Pt$_2$-18C6** (0.1 mM) at $[CF_3SO_3K]_0$ = 0 M (black solid line), at $[CF_3SO_3K]_{limit}$ = 10 mM (red dashed line) and the reference compound **L-Pt-PyA** (green dotted line).

Determination of the binding constants

An isoemissive point was observed at 525 nm and the method of continuous variations[61] (Figure 2.9) revealed a 1:1 binding stoichiometry. Absorbance spectra also confirm the breaking-up of the Pt•••Pt contacts upon addition of K^+, and the appearance of one isosbestic point at 343 nm is in line with the proposed 1:1 host:guest binding model (Figure 2.8).

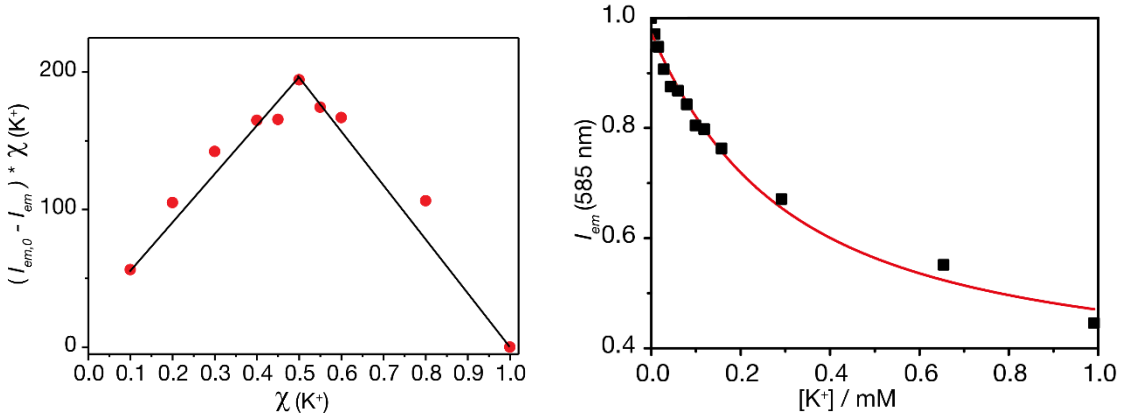

Figure 2.9: left: Job's plot of **L-Pt$_2$-18C6** featuring KCF_3SO_3 in aerated THF with a constant overall concentration of 0.01 mM at ambient conditions. The black lines are inserted for visual guidance. right: least-square fit of the normalized emission intensity at 585 nm to a 1:1 host-guest binding model.

Fitting of the normalized emission titration data with a 1:1 binding model yielded a binding constant (lg K_a = 3.6), which is similar to that of other 18-crown-6 derivatives in polar aprotic solvents, [9, 10, 62] but markedly higher than for ratiometric aza-crown sensors.[11] The equation for the determination of the binding constant of **L-Pt$_2$-18C6** was used as follows[63, 64]:

$$I = I_0 + \frac{(I_{lim} - I_0)}{2\,[Pt]}\left\{[Pt] + [M^+] + \frac{1}{K_S} - \left(\left([Pt] + [M^+] + \frac{1}{K_S}\right)^2 - 4\,[Pt][M^+]\right)^{\frac{1}{2}}\right\} \quad \text{Eq. 2. 1}$$

Conversely, the H-bond arrangement of complex **L-Pt$_2$-18C4** is assumed to remain unaffected in the presence of salt (*vide supra*). Control experiments carried out with **L-Pt$_2$-18C4** and **L-Pt-PyA** confirmed that their emission spectra were not affected by the presence of the salt (Figure 2.10).

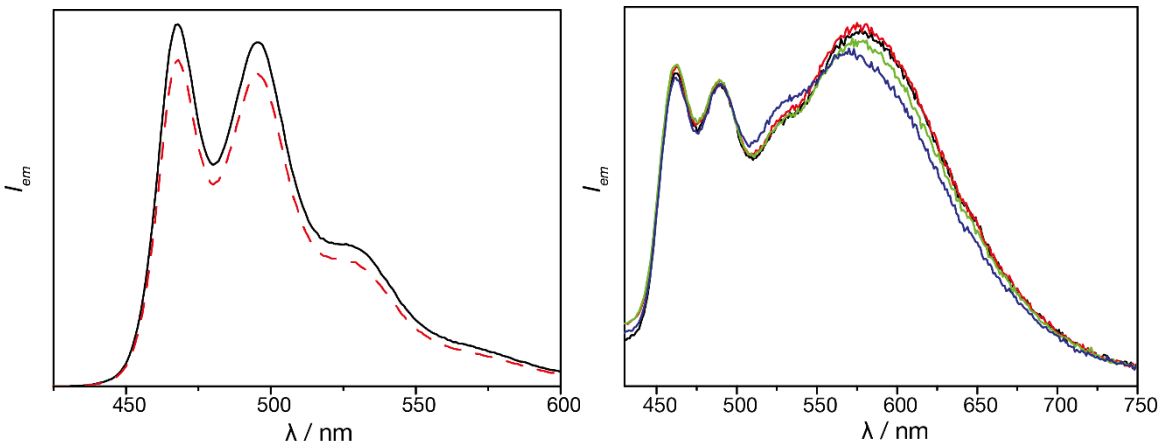

Figure 2.10: left: Emission spectrum of **L-Pt-PyA** (1 mM) in aerated THF before (black solid line) and after the addition of CF_3SO_3K (10 mM, red dashed line). right: Emission spectra of **L-Pt$_2$-18C4** (0.01 mM) in aerated THF (black solid line) and with additional CF_3SO_3K salt (0.04 mM, red, 0.23 mM, green, 0.60 mM blue).

The use of Pt(II)-complexes as signaling units instead of previously reported pyrene chromophores provide significant practical advantages.[59] First of all, excitation is now possible in the visible wavelength range (see Figure 2.9 and Figure 2.12; for pyrene λ_{ex}=346 nm) and the large Stokes shift of Pt(II)-complexes (monomer: 59 nm for [Pt], 38 nm for pyrene; dimer: 180 nm for [Pt], 143 nm for pyrene)[59] facilitates the experimental set-up. Also, the long excited-state lifetime of phosphorescent dyes can be used for background suppression through time-gated measurements. Secondly, the Pt(II)-complexes show much larger free to bound signal differences (factor ~ 21) than pyrene chromophores (factor ~ 5) in their ratiometric emission intensities. Unlike pyrene-excimer formation, Pt•••Pt interactions only occur when orbital-overlap is reached and thus cannot display perturbing signals at distances larger than 3-3.5 Å (*vide supra*).[51] Thus, a more accurate detection of small concentration changes could be possible when the more intramolecular-distance responsive Pt(II) chromophores are used instead of pyrene. On account of the facile distinguishability (*vide supra*) of the emission properties of the unfolded species and the folded one, the displayed system allows for direct insight into the actual molecular arrangement by emission spectroscopy.

Reversible switching of the luminescence

The reversibility of the nature of the luminescence enables the understanding of the working mechanism and the realization of a reversible supramolecular switch with a

ratiometric emission read-out. Such emission-colorimetric switches are rare.[65, 66] In the developed system **L-Pt$_2$-18C6** in THF, the long-lived and featureless emission around 585 nm is converted into a short-lived, structured emission at 464 nm upon a molecular deformation by a potassium salt (switch off @ 585 nm & switch on @ 464 nm: process I) when excited at its isosbestic point. Subsequent addition of 18-crown-6 (lg K_a > 4, determined by NMR titration, Figure 2.13), that competitively binds potassium ions reverses this process (switch on @ 585 nm & switch off @ 464 nm: process II), see Figure 2.11. The process can be cycled at least three times, before the effect of the increasing salt-load affects the functionality of the switch.

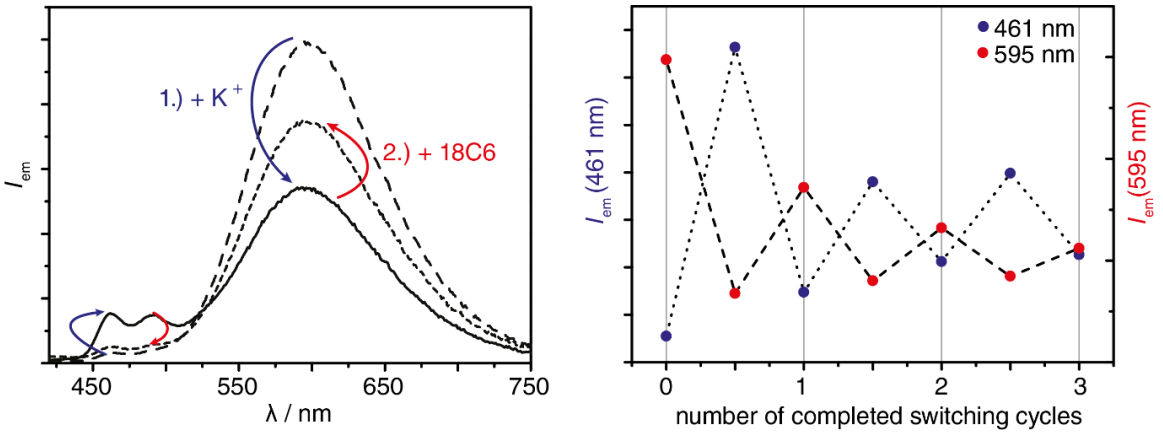

Figure 2.11: left. Emission spectra of **L-Pt$_2$-18C6** in aerated THF (0.01 mM) without any additive (dashed), after addition of potassium trifluoromethanesulfonate (solid) and after further addition of 18-crown-6 (λ_{ex} = 343 nm). right: Cycling of emission intensities for subsequent additions of potassium trifluoromethanesulfonate and 18-crown-6 in each switching cycle.

A similar behavior was observed when the excitation wavelength was shifted to the visible light. (Figure 2.12) The emissive properties of the compounds in solid-state suggest that the switching capabilities might be improved if the **L-Pt$_2$-18C6** switch is surface-immobilized, and thus washable. This proof-of-concept demonstrates the often-assumed reversibility of sensing systems based on crown ethers.[9, 44, 59] Furthermore, this system allows for direct insights into molecular arrangement and might help clarify more complex systems such as muscle-like rotaxanes or the bonding situation of self-assembling Pt-complexes.[51, 67, 68]

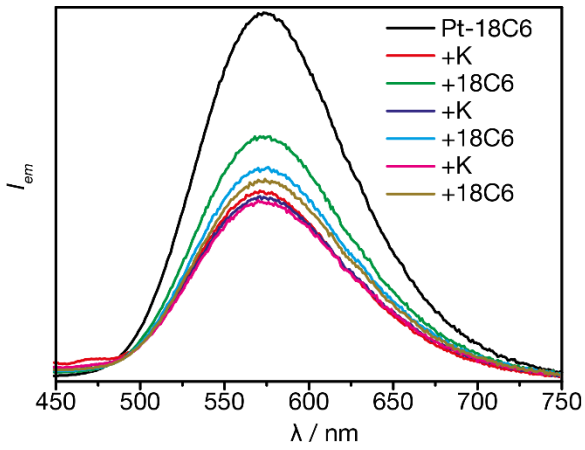

Figure 2.12: Emission spectra of **L-Pt$_2$-18C6** in aerated THF (0.01 mM) without any additive (black), after addition of potassium trifluoromethanesulfonate (red) and after further addition of 18-crown-6 (green). Further additions are also depicted. (λ_{ex} = 400 nm).

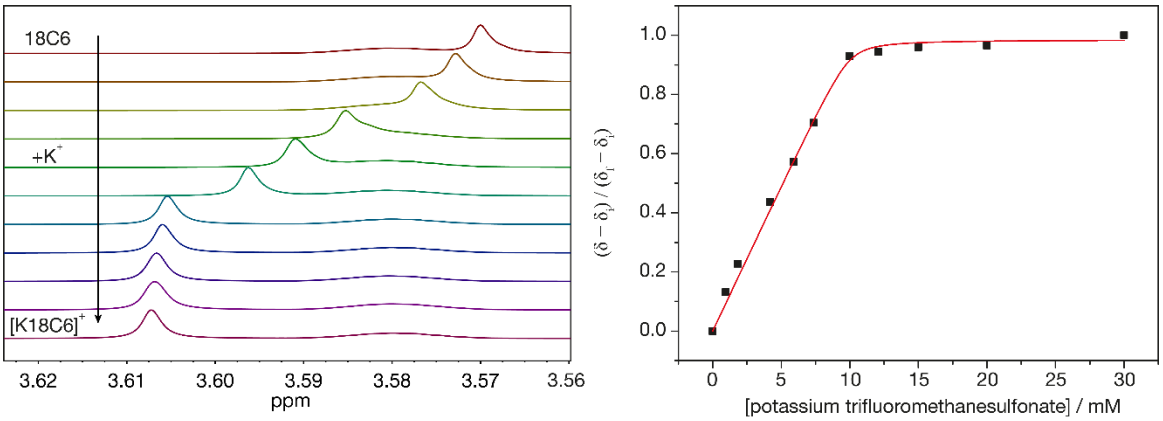

Figure 2.13: left: ^{1}H-NMR (400 MHz, d_8-THF) Titration at 25 °C of potassium trifluoromethanesulfonate (100 mM) to 18C6 (10mM). right: Least-square fit of the change of the chemical shift of 18C6 upon potassium titration.

The equation for the determination of the binding constant of unsubstituted 18C6 was used as follows[64]:

$$\frac{\delta - \delta_i}{\delta_f - \delta_i} = \frac{P}{2[H]} \left\{ [H] + [G] + \frac{1}{Ka} - \left(\left([H] + [G] + \frac{1}{Ka} \right)^2 - 4[H][G] \right)^{\frac{1}{2}} \right\} \quad \text{Eq. 2. 2}$$

Initially the reversibility of the system based on **L-Pt$_2$-18C6** was probed with [2,2,2]-cryptand (abbreviated as [2,2,2]), which possesses a higher binding constant towards potassium than 18C6. An unexpected behavior was observed by the addition of [2,2,2] to a solution of **L-Pt$_2$-18C6** with potassium salt, exhibiting first an increase of the ^{3}MMLCT

emission band, but at higher concentrations of [2,2,2] a decrease of that band. Thus, the cryptand was probed on its potential quenching behavior towards **L-Pt$_2$-18C6**, revealing that only the ^{3}MMLCT seems to be quenched. The aza lone-pair electrons of [2,2,2] can possibly serve as electron donating units in a quenching oxidative intermolecular photoinduced electron transfer (PET).[5, 69] This finding led to the exclusion of [2,2,2] to trigger the back-reaction in the switching cycle.

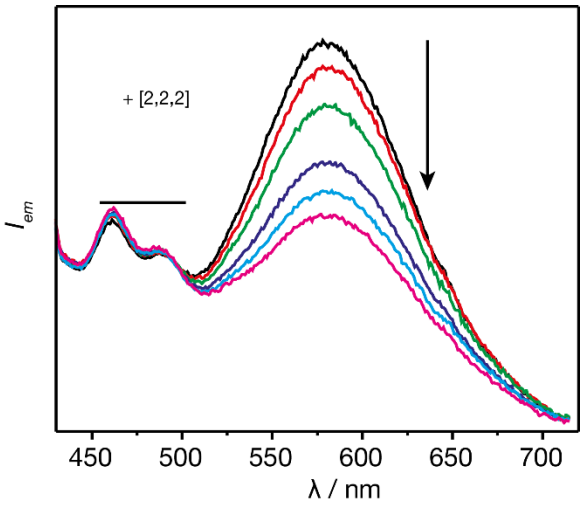

Figure 2.14: Emission spectra for the titration of **L-Pt$_2$-18C6** (0.01 mM) with [2,2,2] (10 mM) in THF at ambient conditions (λ_{ex} = 343 nm).

Conclusion

In summary, the N-metalacyclic dinuclear Pt(II)-complexes **L-Pt$_2$-18C6** and **L-Pt$_2$-18C4**, were successfully synthesized and their photophysical properties were probed. These crown ether derivatives display ^{3}MMLCT based emission in solution arising from intramolecular Pt•••Pt interactions. Only **L-Pt$_2$-18C6** exhibits a luminescence that is sensitive to potassium cations, which enables this architecture to serve for a luminescent ratiometric sensing of potassium cations with possible excitation in the visible light. The determined binding constant is larger than aza-crown analogues because native, fully oxyganted crown-ethers were used as binding motifs. The emission properties of the Pt-complexes are much more sensitive to the intra-molecular distance between two units, than that of widely used pyrene chromophores, causing larger spectroscopic signals. Upon cation uptake, not only a switch-off of the ^{3}MMLCT emission is observed, but also a rise of a blue-shifted ^{3}LC emission occurs, enabling the change of the nature of luminescence by simple cations. This process can be reversed by

the addition of 18-crown-6, and cycled for several times. The intense absorption bands with an onset in the visible region, the large Stokes shift of the emission and the long excited-state lifetime of the phosphorescence in solution are promising features for cation sensing. Based on this model system, further adjustments of the compounds to increase the selectivity for cations and water solubility will be part of future investigations.

Experimental part

The synthesis of the organic building blocks **Py_2-18C4** and **Py_2-18C6** was performed by Mahesh Vishe in the group of Jérôme Lacour at the University of Geneva, who is gratefully acknowledged. The X-ray analysis was performed by Céline Besnard from the University of Geneva, who is gratefully acknowledged.

Synthesis of CF_3-tzH_2 (L-2H)

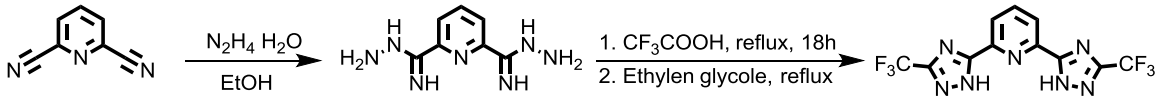

Following the literature in parts[45], pyridine-2,6-dicarbonitrile (5 g, 39 mmol, 1 eq.) was dissolved in EtOH (140 mL). To this, Hydrazine monohydrate (65%, 30 mL, 400 mmol, 10 eq.) was added, which led to an immediate precipitation. The reaction mixture was stirred for 24h at room temperature and subsequently the solvents were evaporated *in vacuo* to obtain a white solid, which in turn was dissolved in trifluoroacetic acid (50 mL). This mixture was heated to 80°C for 18 h and afterwards concentrated *in vacuo*. Ethylene glycol (50 mL) was added and the mixture heated to 140 °C for 2h. After cooling down to room temperature, the product was precipitated in an excess of water and filtered. The subsequent recrystallization from acetone yielded pure crystals (5.18 g, 14.8 mmol, 38%).

^{1}H NMR (400 MHz, CD_2Cl_2) δ 13.69 (s, 2H), 8.31 (d, J = 7.8 Hz, 2H), 8.14 (t, J = 7.5 Hz, 1H). ^{19}F {1H} NMR (377 MHz, CD_2Cl_2) δ -65.64 (s). HR-ESI-MS (negative scan, *m/z*): $[M-H]^-$ calcd. 677.0566; found 677.0559.

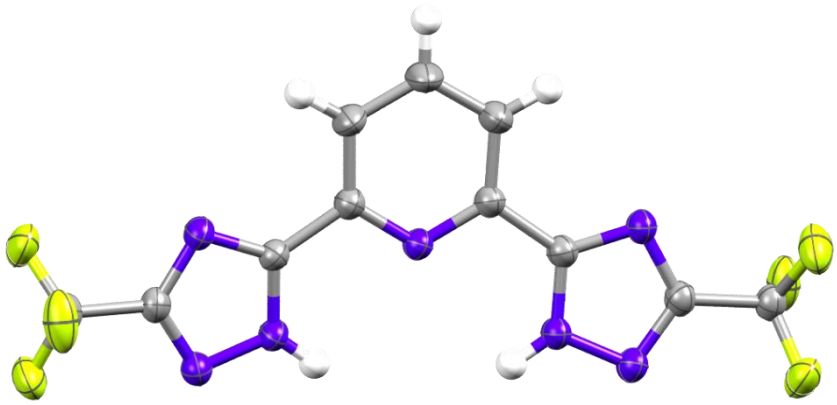

Figure 2.15: Solid-state structures determined by X-ray diffraction analysis of **L-2H** featuring an ellipsoid probability of 50%. Solvent molecules are omitted for clarity.

Synthesis of $PtCl_2(DMSO)_2$

Following the literature procedure[70], K_2PtCl_4 (9.98 g, 24 mmol) was dissolved in distilled H_2O (80 mL) and DMSO (35 mL) and stirred at room temperature for 2 h. The yellow solid was filtered, thoroughly washed with H_2O, EtOH and eventually with diethyl ether and dried on air to yield $PtCl_2(DMSO)_2$ as a yellow solid (9.59 g, 0.023 mol, 96%).

Synthesis of L-Pt-PyA

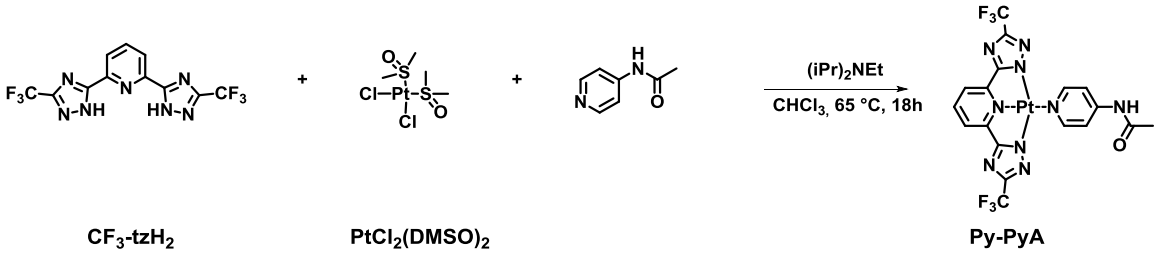

$PtCl_2(DMSO)_2$ (65 mg, 0.19 mmol, 0.9 eq.), **L-2H** (51 mg, 0.15 mmol, 0.86 eq.) and N-pyridin-4-yl acetamide (23 mg, 0.17 mmol, 1 eq.) were suspended in $CHCl_3$ (4 mL). Subsequently, iPr_2NEt (40 µL, 0.23 mmol, 1.35 eq.) was added portion wise and the reaction mixture heated to 65°C for 18 h in round bottom flask equipped a reflux condenser. Subsequently, the volatiles were evaporated *in vacuo* and the crude product recrystallized from acetone. In order to increase the yield, the filtrate was concentrated *in vacuo* and eventually dried and subsequently the remaining solid recrystallized from MeOH and subsequently filtered to obtain a pale green solid (77.2 mg, 0.113 mmol,

78%). ^{1}H NMR (400 MHz, THF) δ 10.13 (s, 1H), 9.49 (d, ^{3}J = 7.2 Hz, 2H), 8.22 (d, ^{3}J = 7.9 Hz, 1H), 7.88 (d, ^{3}J = 8.0 Hz, 2H), 7.85 (d, ^{3}J = 7.5 Hz, 2H), 2.18 (s, 3H). ^{19}F {^{1}H} NMR (377 MHz, THF) δ -66.95 (s). HR-ESI-MS (negative scan, *m/z*): $[M-H]^-$ calcd. 677.0566; found 677.0559.

Synthesis of L-Pt$_2$-18C4

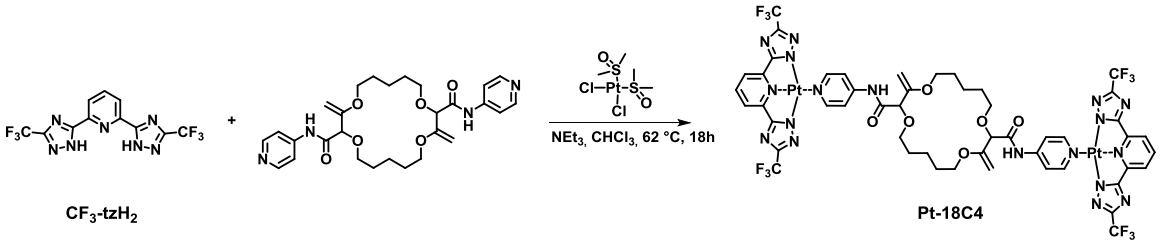

PtCl$_2$(DMSO)$_2$ (23.3 mg, 0.06 mmol, 1 eq.) and **L-2H** (20 mg, 0.06 mmol, 1 eq.) were suspended in $CHCl_3$ (2 mL). Subsequently, NEt_3 (18.3 µL, 0.13 mmol, 2.2 eq.) was added portion wise and the reaction mixture heated to 62°C. Afterwards, **Py$_2$-18C4** (11 mg, 0.02 mmol, 0.3 eq.) was added and the reaction mixture was held at 62°C for 18 h. The reaction mixture was allowed to cool to room temperature. All volatiles were evaporated *in vacuo* and the crude product subjected to column chromatography (SiO_2, EtAc). Subsequently, the dried product was subjected to a second column chromatography (SiO_2, THF/CH_2Cl_2, 3:2) to obtain 11.3 mg (0.007 mmol, 35%) of a pure yellow solid.

^{1}H NMR (400 MHz, THF) δ 9.30 – 9.21 (m, 6H), 8.04 (d, *J* = 7.9 Hz, 2H), 7.67 (d, *J* = 7.3 Hz, 4H), 7.51 (d, *J* = 7.9 Hz, 4H), 4.43 (s, 4H), 4.40 (s, 2H). ^{19}F {^{1}H} NMR (377 MHz, THF) δ -66.87 (s). HR-ESI-MS (positive scan, *m/z*): $[M+Na]^+$ calcd. 1609.2703; found 1609.2760.

Synthesis of L-Pt$_2$-18C6

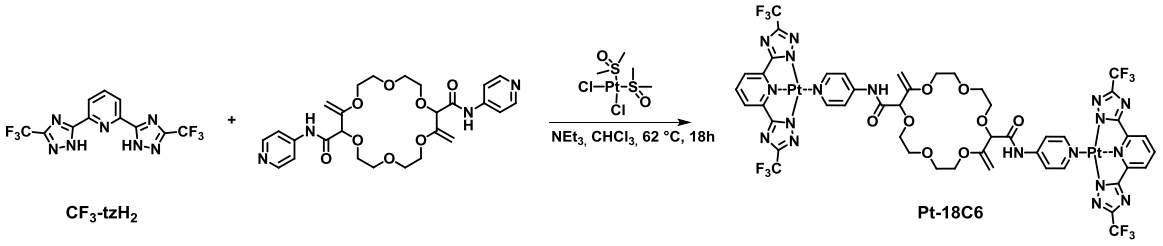

PtCl$_2$(DMSO)$_2$ (23.3 mg, 0.06 mmol, 1 eq.) and **L-2H** (20 mg, 0.06 mmol, 1 eq.) were suspended in $CHCl_3$ (2 mL). Subsequently, NEt_3 (18.3 µL, 0.13 mmol, 2.2 eq.) was added portion wise and the reaction mixture heated to 62°C. Afterwards, **Py$_2$-18C6** (11 mg, 0.02 mmol, 0.3 eq.) was added and the reaction mixture stirred at 62°C for 18 h. The reaction mixture was allowed to cool to room temperature and all volatiles were evaporated *in vacuo*. The crude product was subjected to column chromatography (SiO_2, EtAc). Subsequently, the dried product was dissolved in hot THF and dropped into Diethyl ether for further purification. A second column chromatography (SiO_2, THF/CH_2Cl_2, 3:2) was conducted to obtain 9.7 mg (0.006 mmol, 30%) of a pure orange solid.

^{1}H NMR (400 MHz, THF) δ = 10.37 (s, 2H), 9.26 (d, *J*=6.8, 3H), 8.04 (t, *J*=7.9, 2H), 7.59 (d, *J*=6.3, 4H), 7.48 (d, *J*=7.9, 3H), 4.55 (s, 2H), 4.49 (d, *J*=2.3, 2H), 4.41 (d, *J*=2.3, 2H). ^{19}F {^{1}H} NMR (377 MHz, THF) δ -66.79 (s). HR-ESI-MS (positive scan, *m/z*): $[M+Na]^+$ calcd. 1635.2107; found 1635.2200.

References

1. J. Yin, Y. Hu and J. Yoon, *Chem. Soc. Rev.*, 2015, **44**, 4619-4644.
2. M. C. Yeung and V. W. Yam, *Chem. Soc. Rev.*, 2015, **44**, 4192-4202.
3. Q. Zhao, F. Li and C. Huang, *Chem. Soc. Rev.*, 2010, **39**, 3007-3030.
4. J. F. Callan, A. P. de Silva and D. C. Magri, *Tetrahedron*, 2005, **61**, 8551-8588.
5. A. P. de Silva, H. Q. N. Gunaratne, T. Gunnlaugsson, A. J. M. Huxley, C. P. McCoy, J. T. Rademacher and T. E. Rice, *Chem. Rev.*, 1997, **97**, 1515-1566.
6. B. Valeur and I. Leray, *Coord. Chem. Rev.*, 2000, **205**, 3-40.
7. C. J. Pedersen (DU Pont), US3361778DA, 1968.
8. C. J. Pedersen, *J. Am. Chem. Soc.*, 1967, **89**, 7017-7036.
9. J. W. Steed and J. L. Atwood, *Supramolecular Chemistry*, Wiley VCH, Weinheim, 2009.
10. G. W. Gokel, W. M. Leevy and M. E. Weber, *Chem. Rev.*, 2004, **104**, 2723-2750.
11. M. Baruah, W. Qin, R. A. L. Vallée, D. Beljonne, T. Rohand, W. Dehaen and N. Boens, *Org. Lett.*, 2005, **7**, 4377-4380.
12. E. S. Meadows, S. L. De Wall, P. W. Salama, E. Abel and G. W. Gokel, *Supramol. Chem.*, 1999, **10**, 163-171.
13. Y. Nakahara, T. Kida, Y. Nakatsuji and M. Akashi, *J. Org. Chem.*, 2004, **69**, 4403-4411.
14. Y. Nakahara, Y. Matsumi, W. Zhang, T. Kida, Y. Nakatsuji and I. Ikeda, *Org. Lett.*, 2002, **4**, 2641-2644.
15. Y. Nakatsuji, M. Nakamura, T. Oka and M. Muraoka, *Chem. Lett.*, 2011, **40**, 1226-1228.
16. Y. Suzuki, T. Morozumi, H. Nakamura, M. Shimomura, T. Hayashita and R. A. Bartsh, *J. Phys. Chem. B*, 1998, **102**, 7910-7917.
17. F. A. Khan, K. Parasuraman and K. K. Sadhu, *Chem. Commun.*, 2009, 2399-2401.
18. M. G. Choi, H. J. Kim and S. K. Chang, *Bull. Korean Chem. Soc.*, 2008, **29**, 567-570.
19. Z. Wang, S. H. Chang and T. J. Kang, *Spectrochim. Acta Mol. Biomol. Spectrosc.*, 2008, **70**, 313-317.
20. D. Udhayakumari, S. Velmathi, P. Venkatesan and S. P. Wu, *Anal. Methods*, 2015, **7**, 1161-1166.
21. G. K. Bains, S. H. Kim, E. J. Sorin and V. Narayanaswami, *Biochemistry*, 2012, **51**, 6207-6219.
22. A. P. de Silva and S. A. de Silva, *J. Chem. Soc., Chem. Commun.*, 1986, 1709-1710.
23. V. Wing-Wah Yam, C.-K. Li and C.-L. Chan, *Angew. Chem. Int. Ed.*, 1998, **37**, 2857-2859.
24. M. Mydlak, M. Mauro, F. Polo, M. Felicetti, J. Leonhardt, G. Diener, L. De Cola and C. A. Strassert, *Chem. Mater.*, 2011, **23**, 3659-3667.
25. L. J. Charbonnière, R. F. Ziessel, C. A. Sams and A. Harriman, *Inorg. Chem.*, 2003, **42**, 3466-3474.
26. S. A. McFarland and N. S. Finney, *Chem. Commun.*, 2003, 388-389.
27. M. E. Padilla-Tosta, J. M. Lloris, R. Martónez-Máñez, A. Benito, J. Soto, T. Pardo, M. A. Miranda and M. D. Marcos, *Eur. J. Inorg. Chem.*, 2000, **2000**, 741-748.
28. Miguel E. Padilla-Tosta, José M. Lloris, R. Martínez-Máñez, M. D. Marcos, Miguel A. Miranda, T. Pardo, F. Sancenón and J. Soto, *Eur. J. Inorg. Chem.*, 2001, **2001**, 1475-1482.
29. M. Schmittel, H.-W. Lin, E. Thiel, A. J. Meixner and H. Ammon, *Dalton Trans.*, 2006, 4020-4028.
30. R. Y. Lai, M. Chiba, N. Kitamura and A. J. Bard, *Anal. Chem.*, 2002, **74**, 551-553.
31. Subodh K. Dutta, D. Gan and Marc W. Perkovic, *Eur. J. Inorg. Chem.*, 2003, **2003**, 2812-2819.
32. J. V. Ros-Lis, R. Martinez-Manez, J. Soto, C. McDonagh and A. Guckian, *Eur. J. Inorg. Chem.*, 2006, 2647-2655.
33. Y. Shen and B. P. Sullivan, *J. Chem. Educ.*, 1997, **74**, 685.

34. J. Brandel, M. Sairenji, K. Ichikawa and T. Nabeshima, *Chem. Commun.*, 2010, **46**, 3958-3960.
35. M.-L. Ho, F.-M. Hwang, P.-N. Chen, Y.-H. Hu, Y.-M. Cheng, K.-S. Chen, G.-H. Lee, Y. Chi and P.-T. Chou, *Org. Biomol. Chem.*, 2006, **4**, 98-103.
36. M. Schmittel and H. Lin, *Inorg. Chem.*, 2007, **46**, 9139-9145.
37. C.-K. Li, X.-X. Lu, K. M.-C. Wong, C.-L. Chan, N. Zhu and V. W.-W. Yam, *Inorg. Chem.*, 2004, **43**, 7421-7430.
38. X. He, E. C.-C. Cheng, N. Zhu and V. W.-W. Yam, *Chem. Commun.*, 2009, 4016-4018.
39. F. K.-W. Hau, X. He, W. H. Lam and V. W.-W. Yam, *Chem. Commun.*, 2011, **47**, 8778-8780.
40. P. H. Lanoe, H. Le Bozec, J. A. Williams, J. L. Fillaut and V. Guerchais, *Dalton Trans.*, 2010, **39**, 707-710.
41. Q.-Z. Yang, L.-Z. Wu, H. Zhang, B. Chen, Z.-X. Wu, L.-P. Zhang and C.-H. Tung, *Inorg. Chem.*, 2004, **43**, 5195-5197.
42. Phyllis K. M. Siu, S.-W. Lai, W. Lu, N. Zhu and C.-M. Che, *Eur. J. Inorg. Chem.*, 2003, **2003**, 2749-2752.
43. W.-S. Tang, X.-X. Lu, K. M.-C. Wong and V. W.-W. Yam, *J. Mater. Chem.*, 2005, **15**, 2714-2720.
44. H.-S. Lo, S.-K. Yip, K. M.-C. Wong, N. Zhu and V. W.-W. Yam, *Organometallics*, 2006, **25**, 3537-3540.
45. M. Mauro, A. Aliprandi, C. Cebrian, D. Wang, C. Kübel and L. De Cola, *Chem. Commun.*, 2014, **50**, 7269-7272.
46. C. A. Strassert, C. H. Chien, M. D. Galvez Lopez, D. Kourkoulos, D. Hertel, K. Meerholz and L. De Cola, *Angew. Chem. Int. Ed.*, 2011, **50**, 946-950.
47. J. A. G. Williams, *Top Curr Chem*, 2007, **281**, 205-268.
48. N. K. Allampally, C. A. Strassert and L. De Cola, *Dalton Trans.*, 2012, **41**, 13132-13137.
49. L. De Cola, M. Mauro, N. Seda Kehr and C. A. Strassert (Westfälische Wilhelms-Universität Münster), WO 2012/117082 A1, 2014.
50. V. M. Miskowski and V. H. Houlding, *Inorg. Chem.*, 1989, **28**, 1529-1533.
51. B. Ma, J. Li, P. I. Djurovich, M. Yousufuddin, R. Bau and M. E. Thompson, *J. Am. Chem. Soc.*, 2005, **127**, 28-29.
52. M. Mauro, A. Aliprandi, D. Septiadi, N. S. Kehr and L. De Cola, *Chem. Soc. Rev.*, 2014, **43**, 4144-4166.
53. V. W.-W. Yam, K. H.-Y. Chan, K. M.-C. Wong and B. W.-K. Chu, *Angew. Chem. Int. Ed.*, 2006, **45**, 6169-6173.
54. W. Zeghida, C. Besnard and J. Lacour, *Angew. Chem. Int. Ed.*, 2010, **49**, 7253-7256.
55. M. Vishe, R. Hrdina, L. Guénée, C. Besnard and J. Lacour, *Adv. Synth. Catal.*, 2013, **355**, 3161-3169.
56. M. Vishe, R. Hrdina, A. I. Poblador-Bahamonde, C. Besnard, L. Guénée, T. Bürgi and J. Lacour, *Chem. Sci.*, 2015, **6**, 4923-4928.
57. R. W. Hoffmann, *Chem. Rev.*, 1989, **89**, 1841-1860.
58. B. C. Lynn, M. Tsesarskaja, O. F. Schall, J. C. Hernandez, S. Watanabe, T. Takahashi, A. Kaifer and G. W. Gokel, *Supramol. Chem.*, 1993, **1**, 253-260.
59. Z. Jarolimova, M. Vishe, J. Lacour and E. Bakker, *Chem. Sci.*, 2016, **7**, 525-533.
60. P.-K. Chow, G. Cheng, G. S. M. Tong, W.-P. To, W.-L. Kwong, K.-H. Low, C.-C. Kwok, C. Ma and C.-M. Che, *Angew. Chem.*, 2015, **127**, 2112-2117.
61. P. Job, *Annali di Chimica Applicata*, 1928, **9**, 113-203.
62. R. M. Izatt, J. S. Bradshaw, S. A. Nielsen, J. D. Lamb, J. J. Christensen and D. Sen, *Chem. Rev.*, 1985, **85**, 271-339.
63. V. W.-W. Yam, R. P.-L. Tang, K. M.-C. Wong, X.-X. Lu, K.-K. Cheung and N. Zhu, *Chem. Eur. J.*, 2002, **8**, 4066-4076.
64. P. Thordarson, *Chem. Soc. Rev.*, 2011, **40**, 1305-1323.
65. A. K. Chan, W. H. Lam, Y. Tanaka, K. M. Wong and V. W. Yam, *PNAS*, 2015, **112**, 690-695.
66. M. Han, H. Y. Zhang, L. X. Yang, Q. Jiang and Y. Liu, *Org. Lett.*, 2008, **10**, 5557-5560.

67. P. Pyykkö, *Chem. Rev.*, 1997, **97**, 597-636.
68. A. Aliprandi, M. Mauro and L. De Cola, *Nat Chem*, 2016, **8**, 10-15.
69. R. A. Bissell, A. Prasanna de Silva, H. Q. Nimal Gunaratne, P. L. Mark Lynch, G. E. M. Maguire, C. P. McCoy and K. R. A. Samankumara Sandanayake, in *Photoinduced Electron Transfer V*, ed. J. Mattay, Springer Berlin Heidelberg, Berlin, Heidelberg, 1993, pp. 223-264.
70. J. H. Price, A. N. Williamson, R. F. Schramm and B. B. Wayland, *Inorg. Chem.*, 1972, **11**, 1280-1284.

Chapter III

Differential Sensing of Aza-heterocyclic Drugs and Toxins in Water by Specific Emission Colors of Platinum Complexes

Abstract

A reactive phosphorescent probe for aza-heterocyclic drugs and toxins was developed, affording a supramolecular emission-switch-on chemosensor in water. Complex formation of the heterocycles with a platinum(II) precursor proceeds readily at ambient conditions, allowing for facile analyte screening. 52 structurally diverse compounds were tested, out of which 23 pyridines, imidazole, and triazoles formed strongly emissive complex aggregates. Importantly, they all can be clearly distinguished from each other through a principal component analysis, but often already by simple visual inspection, *e.g.*, by their emission-color differences (large shifts from blue to red, see Figure 3.1). Also, kinetic reaction profiles and time-resolved emission features can provide valuable information for analyte distinction. The Pt(II)-complexes can be applied as emissive labels for drugs and biomolecules, owing to their advantageous photophysical properties and chemical stability in biological media such as blood.

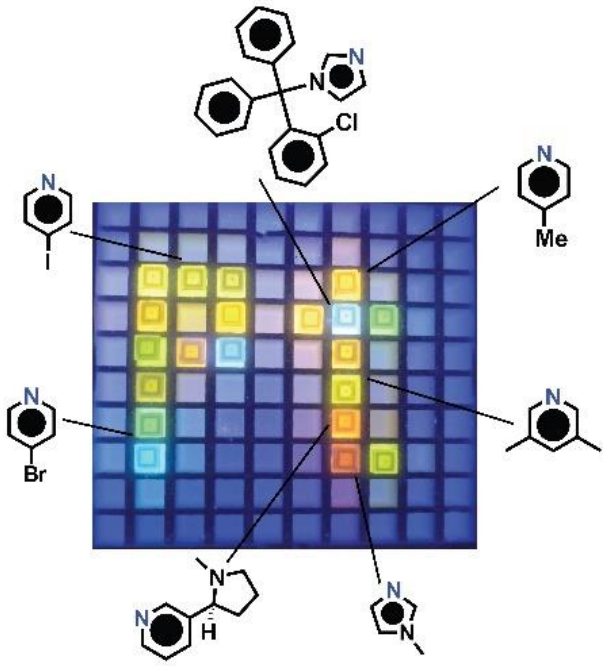

Figure 3.1: Shiny new light from Pt(II)-complexes for the detection of various analytes.

Introduction

Emission-based sensing is a widely used method because of its high sensitivity, its applicability to *in vitro* and *in vivo* systems, its low cost of instrumentation and ease of sample preparation.[1-5] Most naturally occurring analytes are not emissive so synthetic reporter dyes are widely used labels, in particular through a covalent functionalization of the analytes.[6-10] Preferably, the dye-labelled analyte exhibit a distinct emission profile from the (ideally non-emissive) label-precursor and matrix components.[11] Moreover, the functionalization should be feasible in aqueous media to enable the detection/labelling of analytes in biological samples.[12]

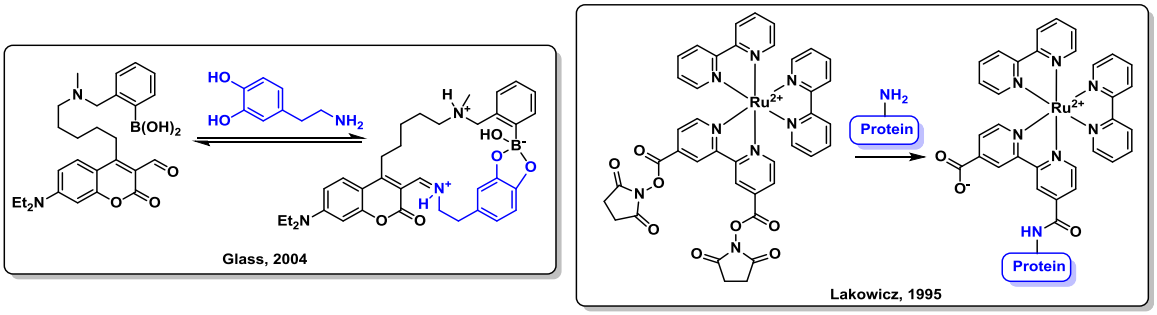

Figure 3.2: Representative examples for photochemical sensors. left: organic label to demonstrate typical binding motifs: boron-diol reaction and imine formation from aldehydes.[13] right: metalorganic label based on $[Ru(bpy)_3]^{2+}$ featuring a covalent amide bond formation towards proteins.[14] The analytes are depicted in blue.

Metal complexes as luminescent labels

Phosphorescent metal-complexes are widely employed as emissive labels due to their excellent photophysical properties, *e.g.*, excitation/emission in the visible region, high brightness, good photostability, and long excited-state lifetime.[6, 9, 15] Thus, they are well suited for sensing applications in inherently chromophoric and fluorescent media, *e.g.* in biological matrices that contain proteins, vitamins or cofactors. Labels based on kinetically "inert" Ru- and Ir-complexes have been commercialized,[14, 16] however, their conjugation to analytes is limited to organic reactions in the periphery of the preformed complex. Fluorescent organic probes are therefore still predominantly used to detect reactive amine-, thiol-, or carboxyl-containing analytes through *in situ* formation of fluorescent species. Heterocycles such as pyridines and imidazoles are omnipresent in synthetic drugs (*e.g.*, clotrimazole) and toxins (*e.g.*, nicotine) displaying plasma and urine

concentrations, respectively, in the μM range (*vide infra*). They are therefore an attractive target for molecular sensors.[17-19]

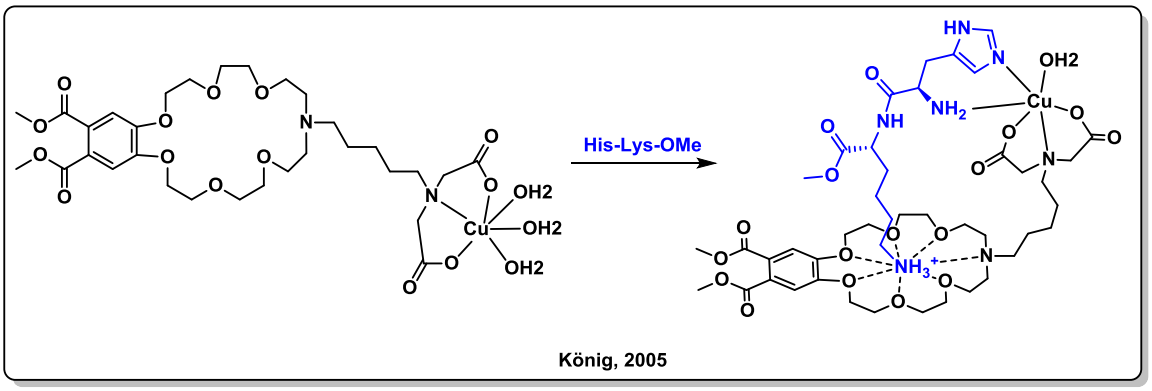

Figure 3.3: Example for a supramolecular approach for analyte detection utilizing multiple intermolecular interactions, namely cation-binding in an crown ether and metal coordination.[20] The analyte is depicted in blue.

Recently, indicator-displacement as well as coordinative labelling assays for histidine and histamine were reported, taking advantage of its specific binding towards certain metal cations such as Cu^{+},Zn^{2+} or Ni^{2+}.[20-28] However, spectrometric sensing of non-chelating imidazole- or pyridine-type drugs remains a challenge.[29]

A luminescent-based assay for the *in situ* labelling, detection and differentiation of pyridines, imidazoles and related species in aqueous solution and biological environments owing to their spectroscopic fingerprints was developed (see Figure 3.4). A conceptually related differential sensing strategy through analyte-induced aggregation was developed by Swager et al. for the detection of amines.[30] To the best of my knowledge, this work is the first general emission-based detection method for heterocyclic compounds.

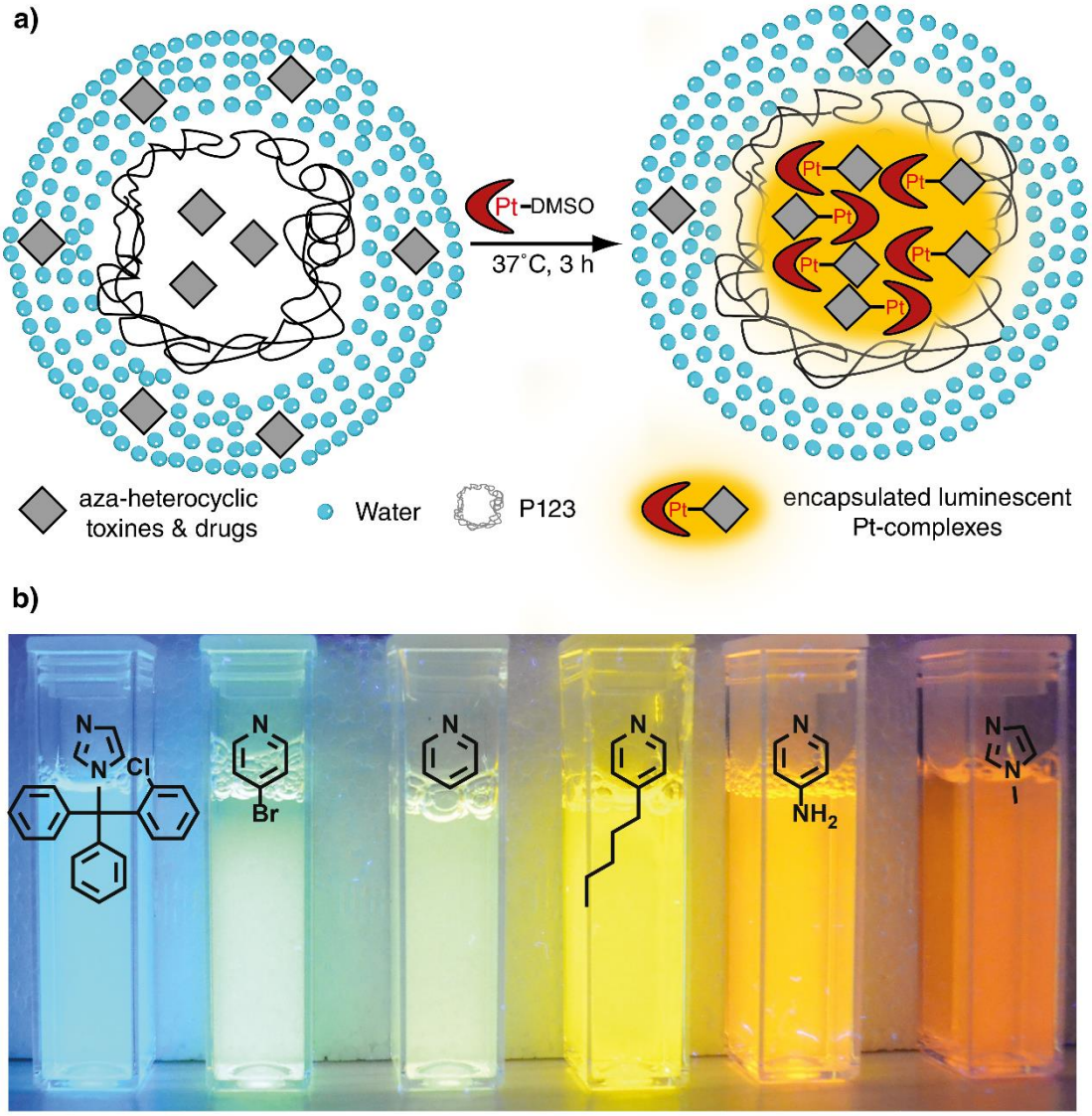

Figure 3.4: a) Schematic representation of the reaction of aza-heterocyclic analytes with a L-Pt-DMSO, in water containing P123 surfactant (Figure 3.10). The formed complexes self-assemble into highly luminescent species. b) Photographs of the different luminescence (UV excitation) of the Pt(II)-complexes, in the reaction medium, generated by the coordination of the different analytes. From left to right: **21**, **9**, **1**, **6**, **13**, **17** (see Scheme 1.4 in Chapter I).

Results and discussion

Heterocycles are known ligands for transition metals (*vide supra*) but often their complexes are non- or only weakly emissive in aerated solutions and their formation requires harsh conditions (*vide infra*).[15, 31] Square-planar Pt(II)-complexes display a high tendency to self-assemble;[32-37] and those based on the terdentate N-metallacycling ligand **L-2H** (see Scheme 3.1 & the other chapters) bearing a pyridine derivative as ancillary ligand are highly emissive in their aggregated state as well as exhibit aggregation dependent photophysical properties.[38, 39]

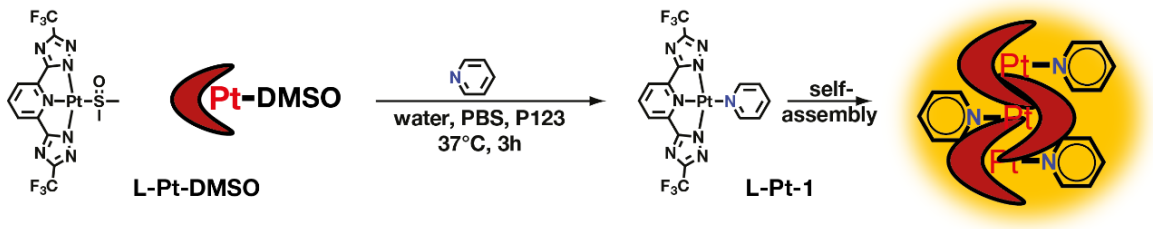

Scheme 3.1: Schematic representation of the general concept of the developed strategy for sensing aza-heterocycles. As an example, the assay accompanied by the formed emissive aggregates of the resulting L-Pt-**1** is depicted.

In order to exemplify the luminescent features of these kind of Pt(II)-complexes, L-Pt-**1** was synthesized and characterized. For this, L-Pt-DMSO was reacted together with pyridine (**1**) in PBS (pH=7.4) for 3 h. After centrifugation and washing a pure product could be obtained (see Experimental part for details and NMR/MS analysis). The different natures of the luminescence of L-Pt-**1** were investigated by solvatochromic experiments. In the nonpolar solvent THF, where the complex is molecularly dissolved, the absorption onset occurs around 450 nm featuring a broad band in the visible range (400 nm, $\varepsilon = 875\ M^{-1}cm^{-1}$) attributed to a metal-to-ligand charge transfer. The stronger bands in the ultra violet region, namely at 328 ($\varepsilon = 3537\ M^{-1}cm^{-1}$), 312 (sh, $\varepsilon = 12875\ M^{-1}cm^{-1}$), 300 ($\varepsilon = 18837\ M^{-1}cm^{-1}$), 264 (sh, $\varepsilon = 24637\ M^{-1}cm^{-1}$) and 254 nm ($\varepsilon = 27500\ M^{-1}cm^{-1}$), are all ascribed to π-π^* transitions. A structured emission profile structured peaking at 461, 487 and 520 nm was detected (λ_{ex} = 375 nm) (Figure 3.5), which is ascribed to a ligand-centered (^{3}LC) based emission.[40] The short excited-state lifetimes of a few ns (see other Chapters for comparable structures) and a low quantum yield below 1% together with the aforementioned absorption and emission spectra are typical features of disaggregated (no Pt•••Pt interactions) Pt(II)-complexes.[37, 40-42] Oftentimes Pt(II)-complexes are even less emissive at room temperature and aerated solvents, when present in a molecularly dissolved state, but the installation of **L-2H** allows for a detection of the blue emission at ambient conditions.[43-45]

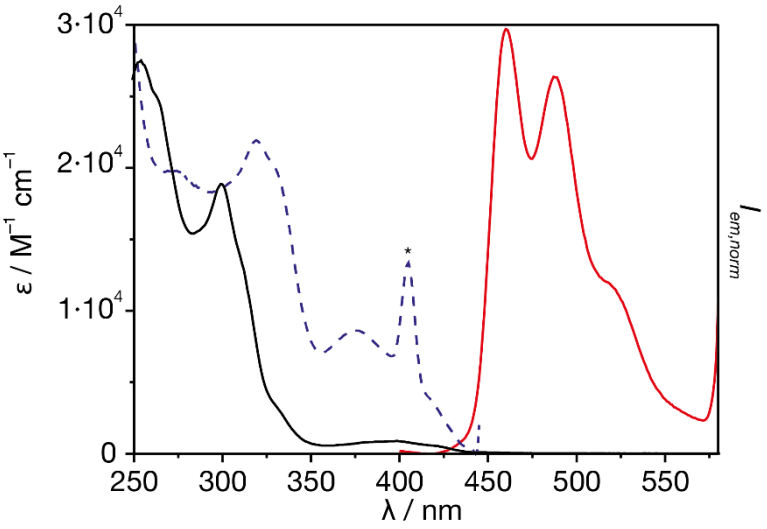

Figure 3.5: Absorbance spectrum (solid, black), normalized excitation spectrum (dashed, blue, λ_{em} = 461 nm) and emission spectrum (solid, red, λ_{exc} = 375 nm) of L-Pt-**1** in THF (80 µM) at ambient conditions. The asterisk marks an instrumental artefact due to the emission wavelength.

Upon aggregation, for instance by self-assembly of the hydrophobic monomeric unit L-Pt-**1**, either in solid state or in an aqueous medium, close shell Pt-Pt interactions lead to new metal-metal-to-ligand charge transfer (MMLCT) transitions in the visible region. Furthermore, the lowest excited state becomes the strongly polar ^{3}MMLCT, which is reflected in a broadened bathochromically shifted emission (λ_{max} = 574 nm Figure 3.6) accompanied by prolongated excited-state lifetimes of 548 ns and enhanced quantum yield (φ = 20%) were measured. A red/orange precipitate is formed after flash injection from a THF solution into a PBS solution. The homogeneity of the dispersion can be traced by visual inspection and emission spectroscopy. This solid is fine dispersed shortly after the injection leading to a normally shaped emission profile (Gaussian[46], Figure 3.6 left). After one night "ripening", the precipitate is clearly sedimented in the aqueous solution while exhibiting an abnormal emission band shape. This observation can be explained by two points: *i)* The emission energy depends on the Pt-Pt distance, thus formed polymorphs (uncontrolled, fast solid formation) emit at different wavelengths resulting in the determined multi band emission profile (Figure 3.6 right). *ii)* The inhomogeneity of the system becomes rather high, so that homogenic-media-probing spectroscopy techniques, as a fluorimeter is, are not appropriate (Figure 3.7).

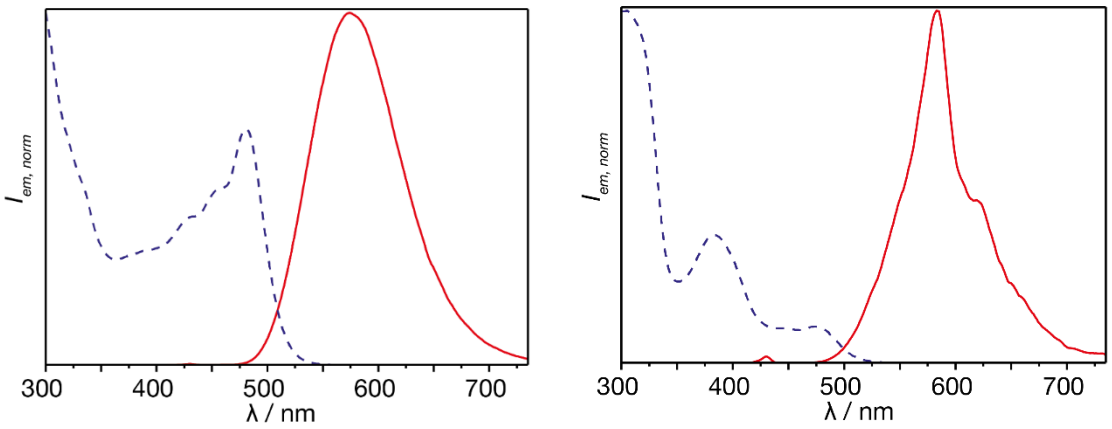

Figure 3.6: Normalized emission (red, solid, λ_{ex} = 375 nm) and excitation (blue, dashed, $\lambda_{em} = \lambda_{em,max}$) spectra of the complex L-Pt-**1** flash injected from a 0.4 mM THF solution (250 µL) into 3000 µL of PBS (pH = 7.4). left: directly after the flash injection; right: after one day leaving the cuvette untouched.

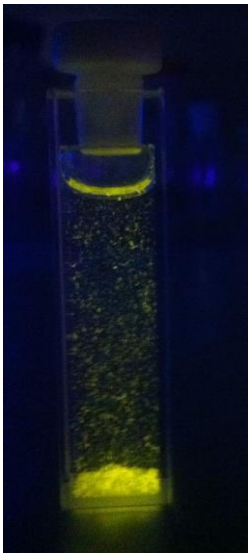

Figure 3.7: Visual snapshots of quartz cuvettes under UV irradiation of L-Pt-**1** flash injected from a THF solution in PBS after 1 day "ripening".

The important photophysical parameters can be summarized as follows: In the monomeric form a blue, relatively weak and structured ^{3}LC based emission is observed while in the aggregated state Pt•••Pt interactions lead to a red-shifted, strongly enhanced and featureless ^{3}MMLCT based luminescence.[37, 40, 42, 47] The complexes are photostable, can be excited in the visible region, and – due to the packing – retain their high photoluminescence quantum yield (PLQY) in the presence of oxygen.[48]

L-Pt-DMSO as reactive luminescent probe for aza-heterocycles

A Pt-DMSO precursor complex was developed, which can react with heterocyclic moieties on analytes, *e.g.*, pyridine (**1**), through exchange of the labile DMSO-ligand resulting in the formation of an emissive species. Importantly, the reaction can proceed also in water or in aqueous buffer at ambient temperature and neutral pH. The addition of **1** to a solution of L-Pt-DMSO in water yielded in 1 h at 37°C a red precipitate that is highly emissive, see Figure 3.8. Structural characterization by NMR & MS reveal the identity between the pre-synthesized (*vide supra*) flash injected compound and this red precipitate, namely L-Pt-**1**. Nonetheless, the emission spectrum reveals several peaks, most likely owing to the same reasons as described above for the ripened flash-injected one, which does not resemble the spectrum of L-Pt-**1** freshly flash-injected.

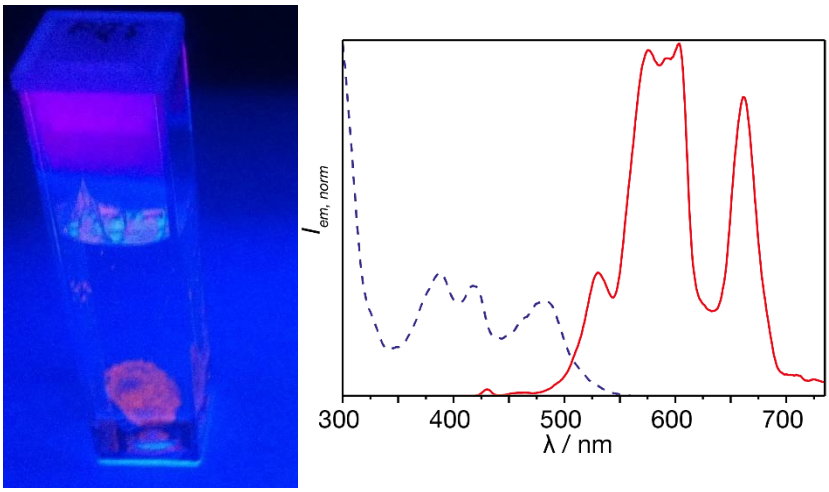

Figure 3.8: left: Visual snapshots of PMMA cuvettes under UV irradiation of L-Pt-DMSO reacted with **1** (33.3 μM) in PBS. right: Normalized emission (red, solid, λ_{ex} = 375 nm) and excitation (blue, dashed, $\lambda_{em} = \lambda_{em,max}$) spectra of the formed complex in PBS.

For comparison, in common synthetic protocols, a Pt-source, **L-2H**, a strong base and a pyridine derivative are reacted in a polar organic solvent at 80°C for 12-18 h,[38, 40] making the procedure incompatible with biological samples (see Experimental part in Chapter II). The new strategy for final complex formation can be understood as a pre-activation of the Pt(II) species by a preceding N-metallacyclation allowing for a smaller activation energy. Therefore, reactions at mild conditions, which are necessarily needed for a fluorescence assay, can be accomplished.

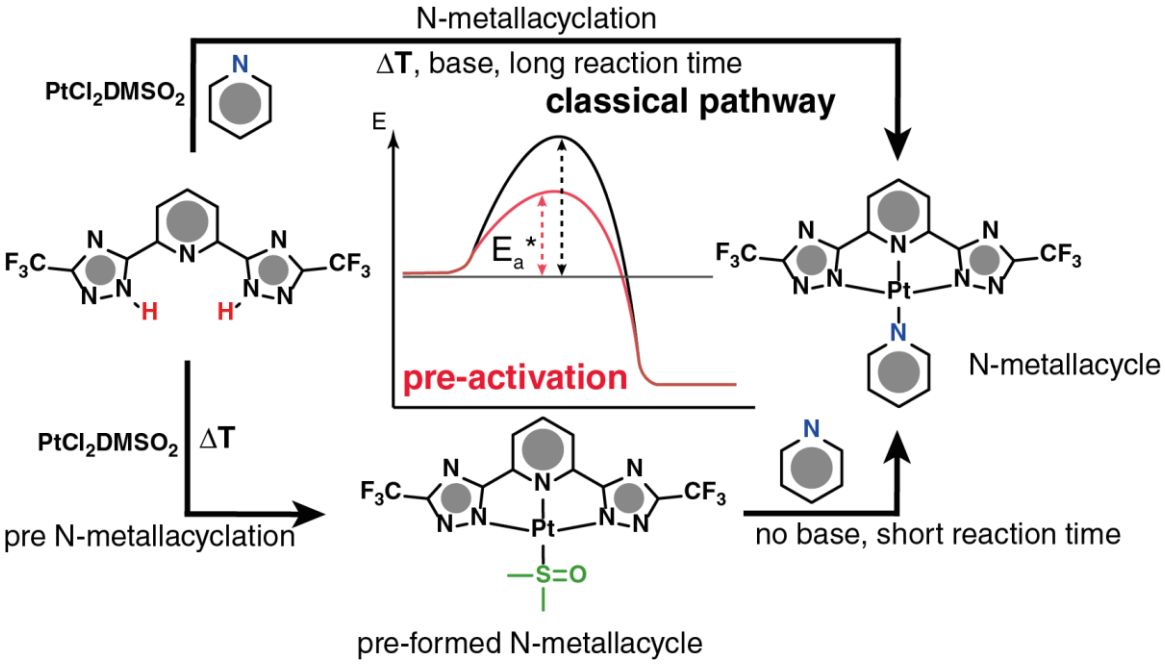

Figure 3.9: Classical literature pathway in comparison to the new pre-activation pathway for the formation of aza-coordinated N-metallacycles.

Enhanced robustness by the use of surfactants

Precipitation of the hydrophobic complexes is undesirable for a solution-based sensing protocol due to large-batch and reaction-time dependent shifts of the emission band (see Figure 3.8). In order to maintain the aggregates in solution, standard commercially available surfactants were probed. The positively charged cetyltrimethylammonium bromide (CTAB), negatively charged sodium dodecyl sulfate (SDS) and the neutral micelle forming triblock copolymer Pluronic P-123 (M_n ~ 5800 g/mol, P123) were tested (Figure 3.10).

The physical parameters are summarized in Table 3.1. The critical micelle concentration of the neutral P123 (CMC = 0.01 %wt; 0.017 mM)[49] is remarkably low in comparison to the charged surfactants SDS (3.42 mM)[50] and CTAB (0.074 mM)[51] This low CMC allows for less detergent within the assay mixture. The hydrodynamic diameter (D_{hyd}), determined by dynamic light scattering (DLS), shows an increasing spherical micelle size from CTAB (D_{hyd} ~ 3 nm) to SDS (~4 nm) to P123 (~17 nm) at the measured concentration (see Table 3.1). A relatively large hydrodynamic diameter is preferable for the purpose of stabilizing Pt(II)-aggregates, which are known to form extended fibril systems. [40]

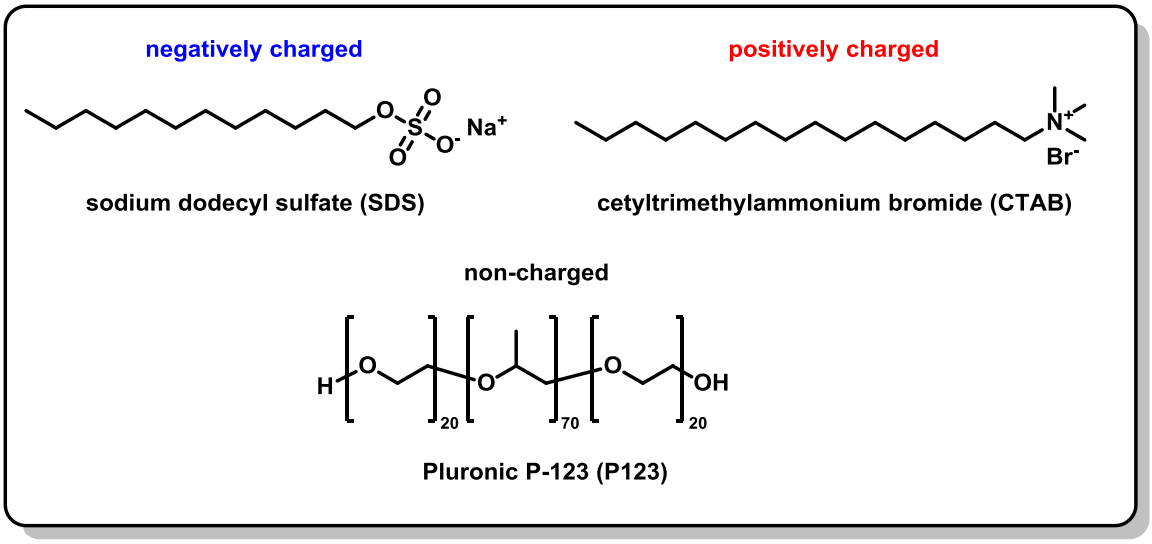

Figure 3.10: Schematic representation of the discussed surfactants.

Table 3.1: Summary of the physical properties of the surfactants.

Surfactant	CMC [a]	D_{hyd} / nm [b]	S/N L-Pt-DMSO [c]	S/N L-Pt-**1** [c]	S/N [d]
SDS	3.42 mM	2.8 ± 1.3 (0.86 mM)	4.77	112.11	23.5
CTAB	0.074 mM	3.7 ± 2.2 (43 mM)	11.31	108.26	9.6
P123	0.01 %wt	17.5 ± 3.6 (0.5 %wt)	0.76	133.24	175.3

[a] critical micelle concentration determined in water, take from literature values (see text) [b] hydrodynamic radius measured in water by dynamic light scattering (DLS, Delsauer) [c] signal-to-noise ratio, determined by dividing the phosphorescence band intensity at $\lambda_{em,max}$ by the intensity of the water Raman peak at 430 nm λ_{ex} = 375 nm. [d] ratio of S/N L-Pt-**1** and S/N L-Pt-DMSO.

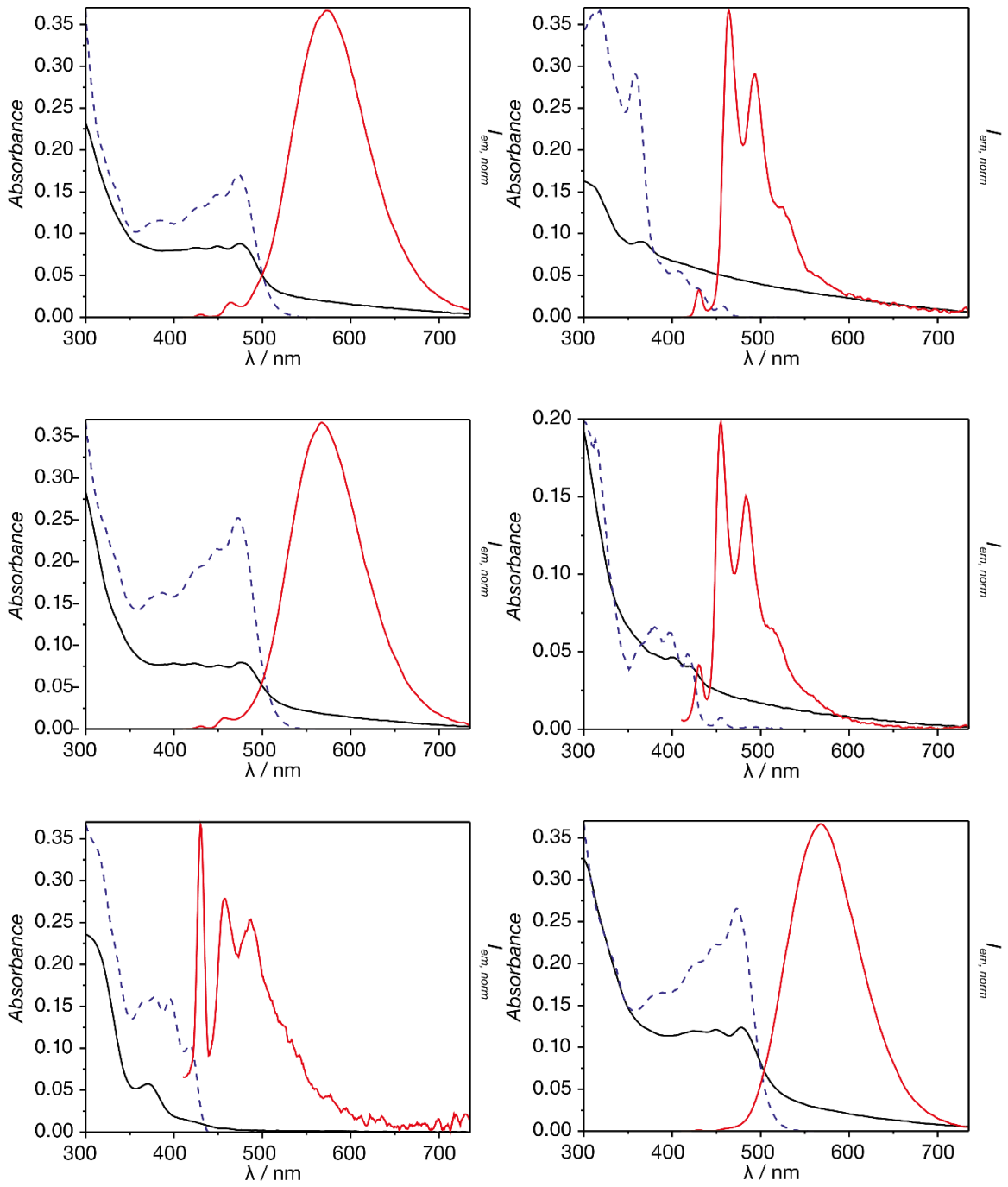

Figure 3.11: Absorption (black, solid), normalized emission (red, solid, λ_{ex} = 375 nm) and excitation (blue, dashed, $\lambda_{em} = \lambda_{em,max}$) spectra of the complex L-Pt-**1** (left) and L-Pt-DMSO (right, no analyte added) after a performed assay in PBS (pH = 7.4) with 0.9 mM CTAB (top), with 43 mM SDS (middle) and 0.5 %wt P123 (bottom).

Furthermore, the surfactants were probed on their performance for the aimed assay. Therefore, the precursor L-Pt-DMSO (10 µL, 10 mM in DMSO) was added to a solution of pyridine (100 µM) either in pure saline PBS buffer or buffered solutions with each surfactant (at the same concentration as used for DLS measurements) in disposable

PMMA cuvettes. After 3 h reaction time at a shaking speed of 100 rpm and 37°C the samples were analyzed with a fluorescence spectrometer with λ_{ex} = 375 nm and $\lambda_{em} = \lambda_{em,max}$ for excitation spectra.

Unlike the reaction in water, no precipitation of the complex was observed (Figure 3.12) and the emission profiles resembles the freshly flash-injected L-Pt-**1** (*vide supra*). As reference the assay was also performed only with L-Pt-DMSO avoiding pyridine. The signal-to-noise ratios were calculated by using the water Raman band as reference at fixed bandwidths (see Table 3.1 for details). In contrast to P123, CTAB and SDS strongly stabilize the reactive precursor leading to a pronounced structured emission after 3 h reaction time. In the case of P123, most likely a non-emissive aquo complex is formed, when no aza-heterocycle is present. The aquo complex is more inert than the DMSO complex rendering a sluggishly reactive Pt(II)-complex- This explanation is supported by the finding, that a prepared stock solution of L-Pt-DMSO in water became non-emissive after several days stored. Furthermore, this aqueous stock solution underwent no reaction with pyridine within the given conditions of the assay.

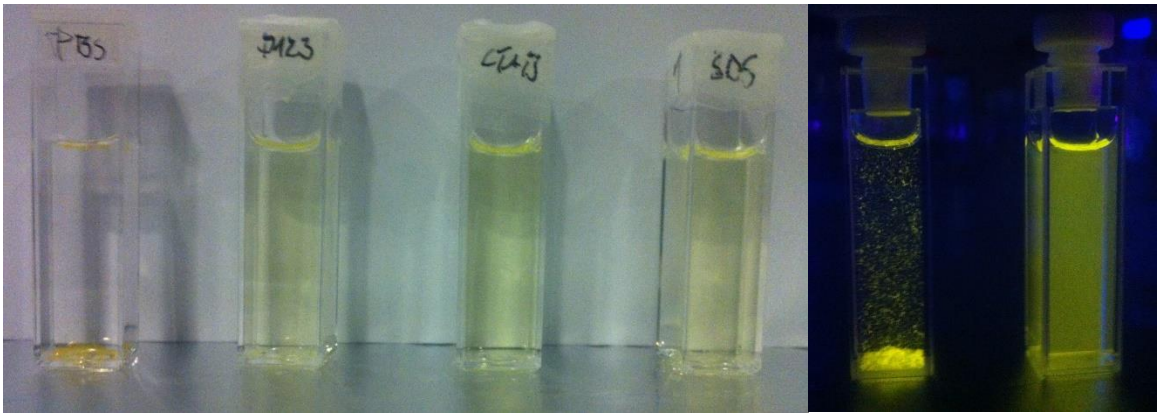

Figure 3.12: Visual snapshots of PMMA cuvettes containing different surfactants; from left to right: pure PBS, P123, CTAB, SDS. Assay performed in different media with equally concentrated **1** and L-Pt-DMSO. Visual snapshots of quartz cuvettes under UV irradiation of L-Pt-**1** flash injected from a THF solution. left: in PBS, right: in PBS with 0.5 %wt P123.

In comparison to the other surfactants (CTAB & SDS), P123 provided the best signal-to-noise ratio and is biocompatible.[49, 52, 53] Furthermore, it forms micelles at rather low concentration[49] while providing the largest hydrodynamic radius of the spherical micelles. Thus, the assay was performed featuring P123 in saline buffer PBS at a concentration of 0.5 %wt.

Addition of the precursor L-Pt-DMSO to a solution of pyridine and P123 in saline PBS buffer resulted in a strong increase (factor of $1.5x10^3$) of the emission intensity at 574 nm with signal saturation after 3 h at 37°C (low steepness see Figure 3.13). In order to assess the temperature dependency of the assay, kinetic studies of L-Pt-DMSO (33.3 μM) with pyridine (**1**, 100 μM) in PBS (pH = 7.4) with 0.5 wt% of P123 were carried out at different temperatures and probed by emission spectroscopy. The assay is in principle also performable at 25°C but suffers from more sluggish kinetics in comparison to the 12°C warmer conditions. The normalized emission bands were superimposable at different points in time, and the emission intensity did not notably vary (≤4% over 3 h) after the reaction reached completion (Figure 3.13).

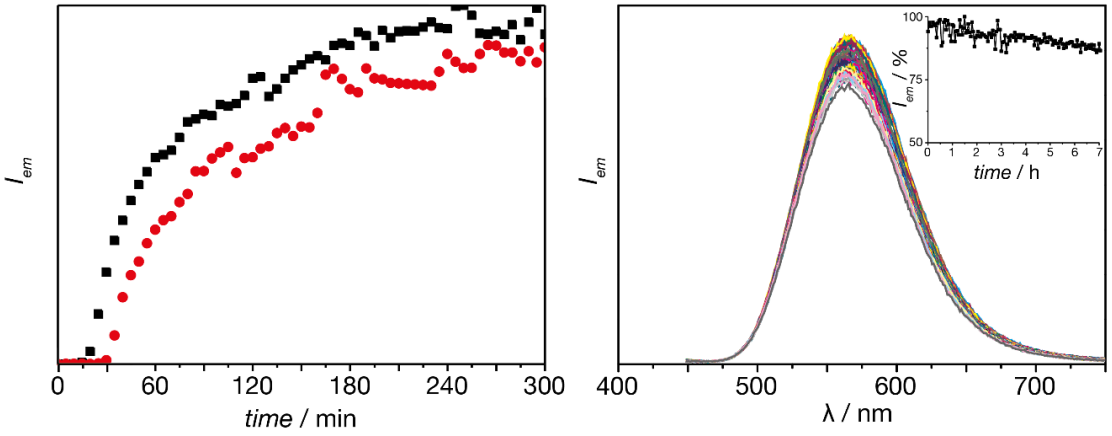

Figure 3.13: left: Emission based kinetic study of L-Pt-**1** at 37°C (black squares) and 25°C (red dots) with constant stirring. right: Long term stability test of L-Pt-**1**, which was formed in the assay conditions. Inset: development of the emission intensity (%) at $\lambda_{em,max}$ over 7 hours (λ_{ex}=375 nm).

For L-Pt-**1** the red-shifted absorption onset (497 nm), emission wavelength maximum (571 nm) (Figure 3.14), high PLQY (45%) and long excited-state lifetime (440 ns) are all indicative of the Pt-complex aggregation (Table 3.3) accompanied by Pt•••Pt interactions. The photophysical spectra resemble those of the flash-injected in PBS (fresh) and PBS with 0.5% P123 suggesting that the analyzed compounds are of the same chemical structure.

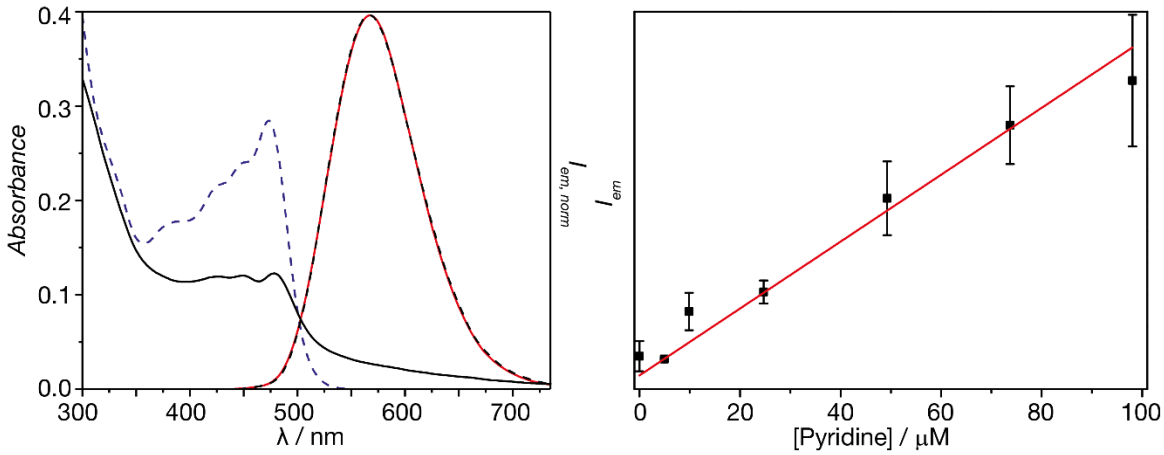

Figure 3.14: left: Absorption (black, solid), normalized emission (red, solid, λ_{ex} = 375 nm; black, dashed, λ_{ex} = 410 nm) and excitation (blue, dashed, $\lambda_{em} = \lambda_{em,max}$) spectra of the complex L-Pt-**1** after a performed assay in saline buffer PBS (pH = 7.4) with 0.5% P123. τ = 440 ns, φ = 45 %. right: Concentration linearity test utilizing a micro-well plate reader featuring filter-based emission spectroscopy. λ_{ex} = 355 nm; λ_{em} = 535 nm.

The results obtained in quartz cuvettes, were comparable to those obtained with inexpensive plastic (PMMA) cuvettes and in micro-well plates (Figure 3.14). As expected, emission-based detection of analyte **1** after Pt-labelling is more sensitive (linearity down to 5 µM, detectability $\leq$ 1µM) than direct absorbance monitoring displaying the potential for the detection of aza-heterocyclic based drugs like clotrimazole (**21**, typical plasma concentration c_p = 40 µM – 440 mM)[54], fluconazole (**22**, c_p = 35 – 100 µM)[55] and miconazole (**23**, c_p = 3 – 94 µM)[56] and toxins such as nicotine (**2**, typical smoker's urine concentration c_u = 6 – 31 µM)[57].

The assay can also be performed in urine, displaying its applicability to biologically relevant media (Figure S8). For this experiment, a highly-concentrated stock solution of P123 in PBS (pH = 7.4, 10%wt, 30 µL) was added to the pyridine solution (30 µM) in Surine Negative Urine Control (2960 µL). Subsequently, the phosphorescence probe L-Pt-DMSO (10 µL, 10 mM in DMSO) was added and the assay performed for 3 h at 37°C. The assay was also performed in blood serum (Bovine Albumin Serum) yielding no luminescent L-Pt-**1** complex, most likely due to the high number of possible coordinative compounds within the serum. Nevertheless, tracing of an already labeled analyte, and thus using the precursor as tag, is possible in blood (*vide infra*).

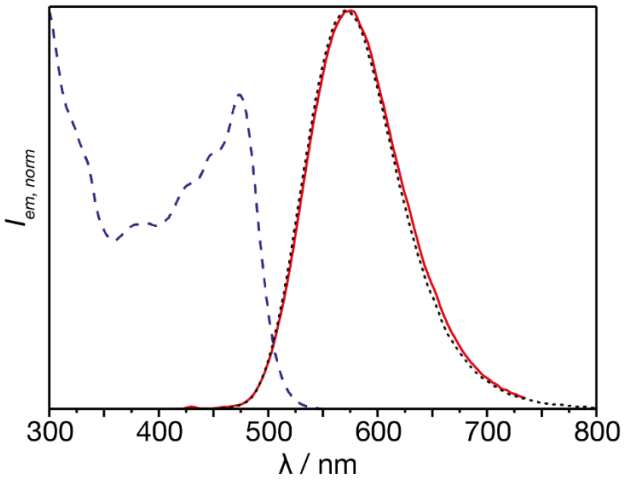

Figure 3.15: Normalized emission (red, solid, λ_{ex} = 375 nm; black, dotted, λ_{ex} = 410 nm) and excitation (blue, dashed, $\lambda_{em} = \lambda_{em,max}$) spectra of the complex L-Pt-**1** after a performed assay in Surine Negative Urine Control. τ = 317 ns, φ = 20.6 %.

Analyte discrimination by their unique emission spectra

The generality of the described protocol for aza-heterocyclic components was probed with a library of 52 representative compounds, including toxins such as nicotine (**2**) and commonly used antifungal drugs (Scheme 3.2 & Scheme 3.3).

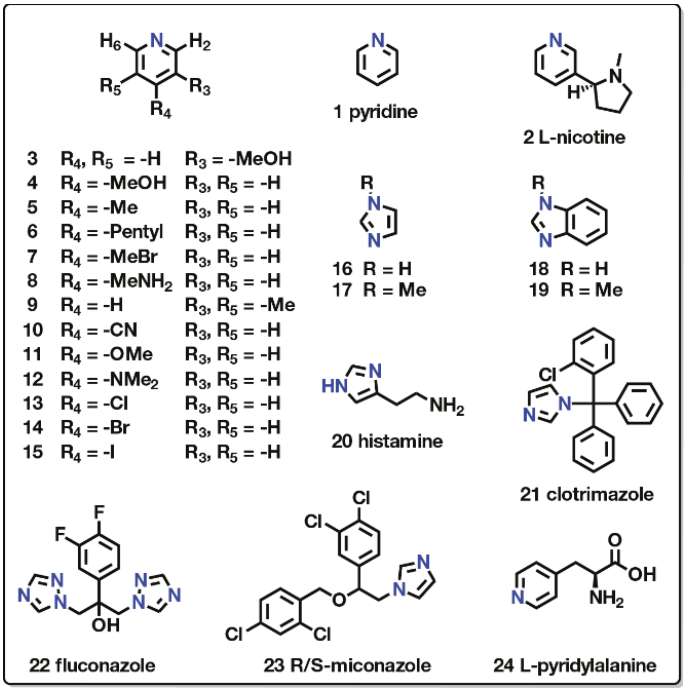

Scheme 3.2: Aza-heterocyclic analytes that form strongly emissive Pt(II)-complex aggregates with the Pt-precursor SiNo > 3.

The fluorescence analysis revealed a strong enhancement of emission intensity for 24 analytes, while the other 28 analytes exhibited only weak emission intensities. The measure for 'weak' and 'strong' emission-intensity enhancement is the calculated signal-to-noise ratio given by

$$SiNo = \sqrt{\frac{Signal-Noise}{Noise}} \qquad \text{Eq. 3.1}$$

where "Signal" denotes the integrated intensity over the entire emission spectrum (410 – 735 nm, λ_{exc} = 375 nm) of the analyte reacted with the Pt-DMSO, and "Noise" denotes the integrated intensity over the entire emission spectrum (410 – 735 nm, λ_{exc} = 375 nm) of L-Pt-DMSO in the absence of analyte (blank) subjected to the same assay conditions (37°C, 3 h). If the signal-to-noise ratio (*SiNo*) was greater than 3, the analyte was assigned as significantly emissive. Histamine served as a show case example, demonstrating that also a lower *SiNo* still enables processability for the analyte detection and discrimination (see multivariate data analysis). The *SiNo* values for all tested analytes are listed in Table 3.2. The weakly emissive compounds are depicted in Scheme 3.3.

Amongst the strongly emissive analyte, 13 were chosen as representative analytes and their photophysical data summarized in Table 3.3. Photographs of selected vials are depicted in Figure 3.4. The spectroscopic features of several analytes after reacted with the precursor L-Pt-DMSO are discussed in the following section.

Table 3.2: Signal-to-noise ratio (*SiNo*) for all analyzed compounds.

Analyte [a]	*SiNo*	Analyte [a]	*SiNo*
1	20.41	**28**	0.54
2	8.95	**29**	0.03
3	15.61	**30**	0.02
4	15.38	**31**	1.20
5	19.83	**32**	1.88
6	13.39	**33**	1.72
7	20.33	**34**	0.59
8	13.37	**35 ***	0.22
9	20.56	**36**	0.73
10	15.59	**37**	0.62
11	24.22	**38**	1.37
12	3.98	**39**	0.09
13	19.95	**40**	0.02
14	20.07	**41**	0.03
15	20.60	**42**	AFBA [b]
16	5.55	**43 ***	0.92
17	9.11	**44 ***	0.01
18	2.92	**45**	0.02
19	29.80	**46**	AFBA [b]
20	4.30	**47**	0.02
21	7.90	**48 ***	0.47
22	9.20	**49 ***	0.68
23	7.40	**50 ***	0.66
24	0.13	**51 ***	0.81
25	0.01	**52**	0.02
26	0.01	**blank**	1.00
27	0.78	**unknown** [c]	7.57

[a] See Scheme 3.2 for chemical structures. [b] AFBA – autofluorescence by analyte. [c] Unknown sample in blind study (*vide infra*). *SiNo* was calculated with constant bandpasses of 2 nm for excitation and emission. The asterisk indicates the samples, for which the calculation has been carried out for bandpasses of 5 nm.

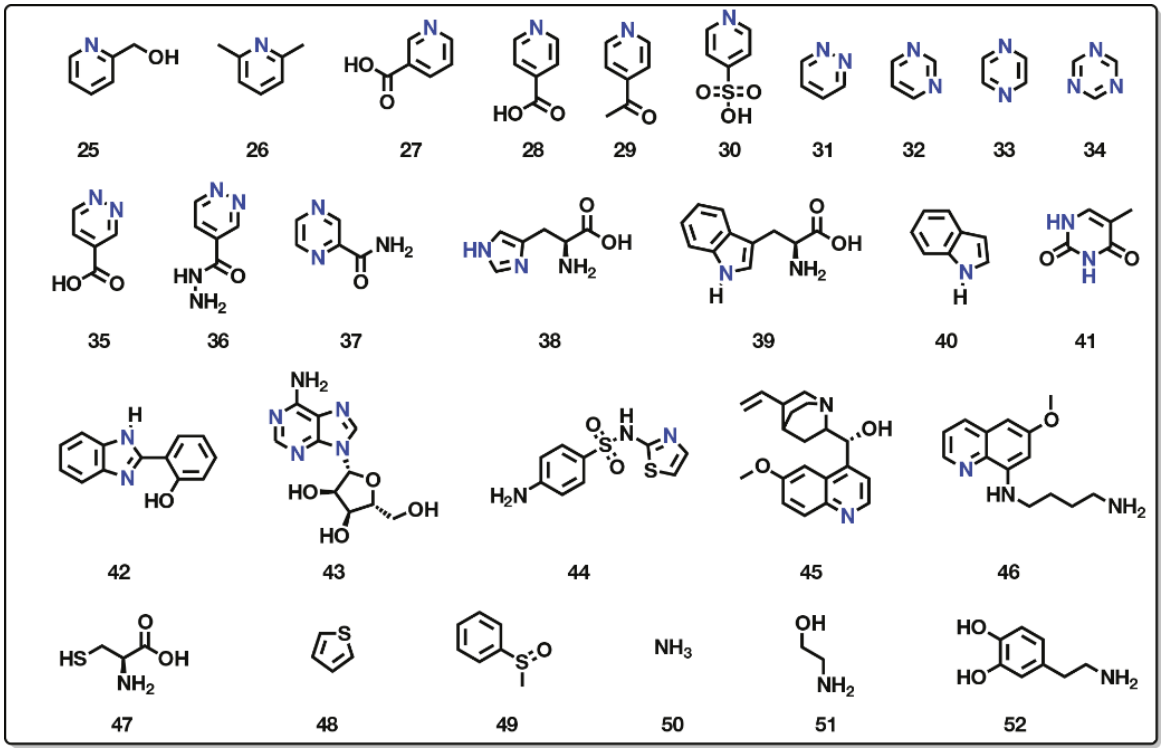

Scheme 3.3: Analytes that form only weakly or non-emissive complexes (*SiNo* < 3).

The spectroscopic distinction of structurally similar analytes is a major challenge for direct sensing methods with both reactive organic probes and indicator-displacement assays.[7, 58-60] This limitation is overcome in the developed system, where several analytes could be already distinguished from each other by their emission color observed by the naked eye. Furthermore, when the emission spectra are recorded, then most Pt-complexes of aza-heterocyclic analytes could be readily distinguished from each other by visual inspection of the spectra features. For instance, complexes of **1** and **2** differ by 835 cm^{-1} (24 nm) in their emission wavelength maxima and a factor of nine in their PLQYs (Table 3.3). The structure of the absorption and excitation spectra (Figure 3.16) strongly differ from each other displaying a bathochromically shifted onset for **1** (375 cm^{-1}, 8 nm). The excited-state lifetime, detected for **1** is 4.8 times higher than for **2**.

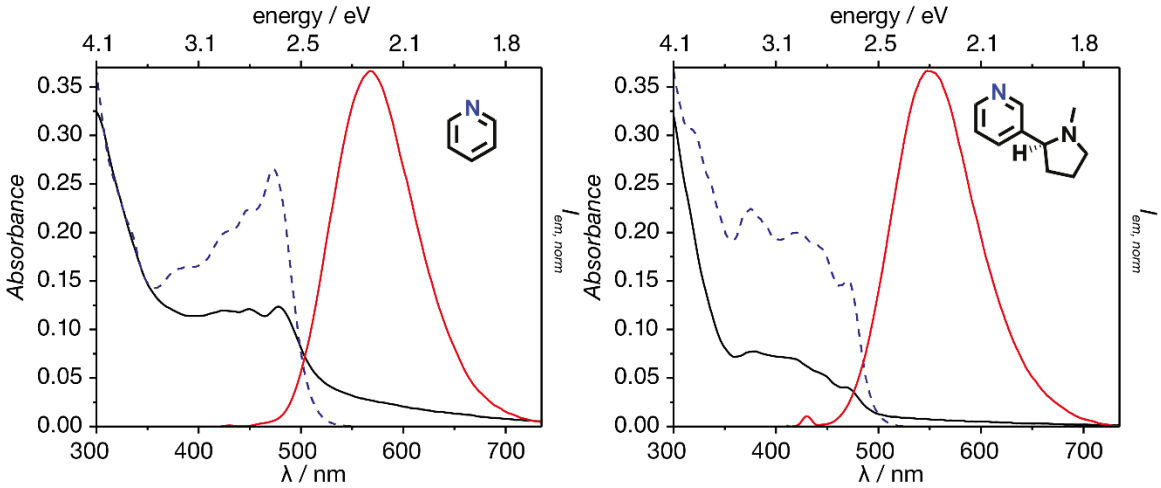

Figure 3.16: Absorption (black, solid), normalized emission (red, solid, λ_{ex} = 375 nm) and excitation (blue, dashed, $\lambda_{em} = \lambda_{em,max}$) spectra of the **1** (pyridine, left) and **2** (L-nicotine, right) after the assay at ambient conditions.

Typically, substituted pyridines detected in the assay gave rise to distinguishable emission spectra, featuring electron-rich pyridines (OMe, **11** & Me(*m*,*m*'), **9**) displaying red-shifted emission maxima compared to their electron-poor analogues (-CN, **10**) (Figure 3.17). The structure of the emission spectrum remains the same, but the energy is lowered from **10** (546 nm) to **9** (555 nm) to **11** (578 nm), which is most likely due to a destabilization of the metal-centered HOMO by the stronger electron donation of the ancillary ligand. Furthermore, a pronounced electron-withdrawing character of the analyte can change the nature of the lowest excited charge-transfer state (*vide infra*). Additionally, the measured excited-state lifetimes and quantum yields significantly differ from each other with 199, 175 and 542 ns as well as 27, 17 and 54% for **9**,**10** and **11**, respectively. These findings demonstrate that electron density changes at the same substitution position lead to different photophysical read-outs.

Table 3.3: Summary of the photophysical properties of the complexes.

Analyte [a]	λ_{abs} [b] / nm	$\lambda_{em,max}$ [c] / nm	$\delta_{\tilde{\upsilon}}$ [d] / cm^{-1}	τ [e] / ns	φ [f] / %
1	478	571	3407	440	45
2	470	545	2928	91	5
3	483	571	3190	532	20
4	476	570	3464	270	21
9	473	555	3123	199	27
10	471	546	2916	175	17
11	479	578	3576	542	54
16	413	467,494,526,579	2800	140	2
17	494	601	3604	278	8
18	425	469, 497, 526, 571	2208	31	0.6
19	467	559	3525	643	50
20	364	468, 490	6105	16	1
21	403	464,494,527,570	3262	2740	13
22	465	587	4470	296	7
23	451	570	4195	338	4

[a] Assays (triple replica), were carried out with 100 μM analyte and 33.3 μM L-Pt-DMSO at 37°C in PBS buffer (pH = 7.4) with 0.5 %wt P123 for 3 h reaction time (see Table 3.4 & estimated errors) [b] maximum of energetically lowest absorption band. [c] emission wavelength at peak maximum; λ_{ex} = 375 nm. [d] Stokes shift.[61] [e] amplitude average of multiexponential decay calculated by most likelihood estimation (MLE). [f] absolute PLQY from integrating sphere

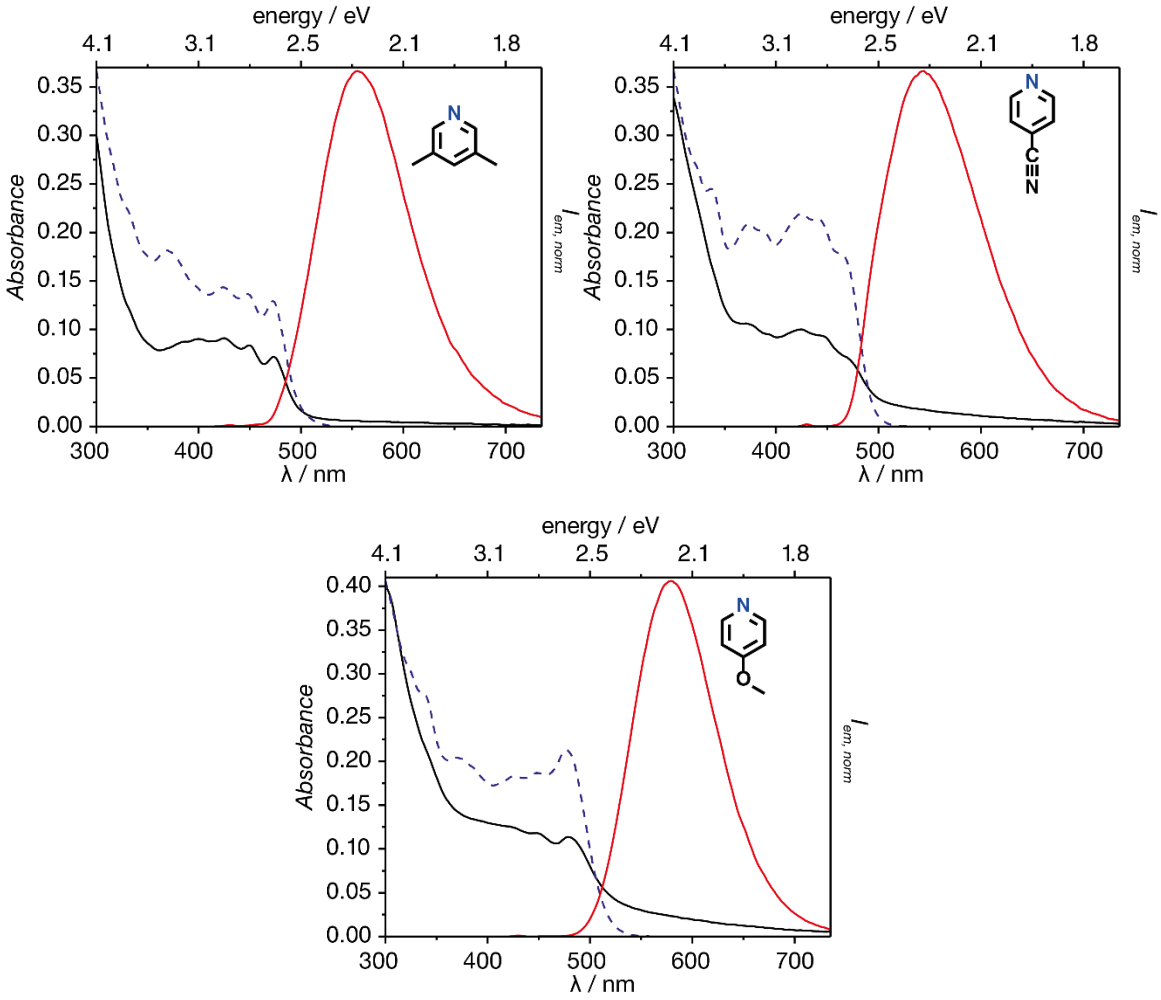

Figure 3.17: Absorption (black, solid), normalized emission (red, solid, λ_{ex} = 375 nm) and excitation (blue, dashed, $\lambda_{em} = \lambda_{em,max}$) spectra of the analytes **9** (3,5-lutidine, top left), **10** (4-cyano pyridine, top right) and **11** (4-methoxy pyridine, bottom) after the assay at ambient conditions.

Furthermore, the assay enables the detection of most pyridine derivatives with multiple substitutions at the *m*- and *p*-substitution; *e.g.*, **2**, **11** and *m*/*p*-pyridinemethanol (**3**, **4** Scheme 3.2, Figure 3.18). The minor changes from **3** to **4** are also reflected by only small spectral differences featuring equal emission maxima and only slightly shifted absorption maxima of the lowest energetic absorption band (Table 3.3). Also, the quantum yields display no significant differences with 20 and 21% for **3** and **4**, respectively. A stronger distinction is in that specific comparison only feasible by the excited-state lifetimes, which diverge by a factor of almost 2. Nevertheless, also small differences can lead to a clear distinction, when bearing orthogonal information (*vide infra*).

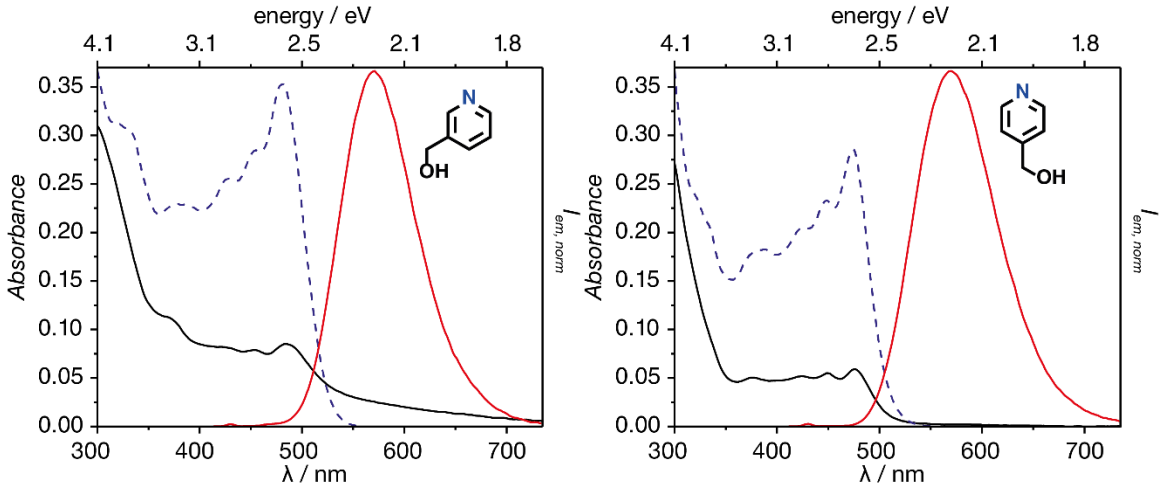

Figure 3.18: Absorption (black, solid), normalized emission (red, solid, λ_{ex} = 375 nm) and excitation (blue, dashed, $\lambda_{em} = \lambda_{em,max}$) spectra of the **3** (pyridine-3-yl methanol, left) and **4** (pyridine-4-yl methanol, right) after the assay at ambient conditions.

Noteworthy, some *o*-substituted pyridines also react with L-Pt-DMSO, but the reaction is slower and the products are only weakly emissive. Thereby, *o*-pyridine methanol (**25**) is directly distinguishable from its regioisomers **3** and **4** in the assay. In order to assess the reactivity of L-Pt-DMSO towards differently substituted pyridines, the geometries of the complexes regioisomers L-Pt-**3**, L-Pt-**4** and L-Pt-**25** were optimized at their ground states. For this purpose, density functional theory calculations were carried out utilizing the paramter-free hybrid functional Perdew-Burke-Ernzerhof PBE0.[62-64] The standard valence basis set 6-31G(d,p) for C,H,N and F was employed.[65] The Stuttgart-Dresden effective core potential[66, 67] along with its corresponding basis set was employed for Pt. The found stationary points possess no imaganiry frequencies (checked by frequency analysis) and therefore assumed to be true minima. All calculations were performed and visulaized with the Gaussian09 programm package.[68] The resultant energies of the complexes were compared by means of the following approach and equations guessing an isodesmic reaction:

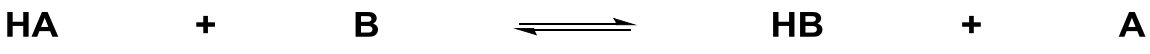

$$\Delta E = \big(E(HB) + E(A)\big) - \big(E(HA) + E(B)\big)$$

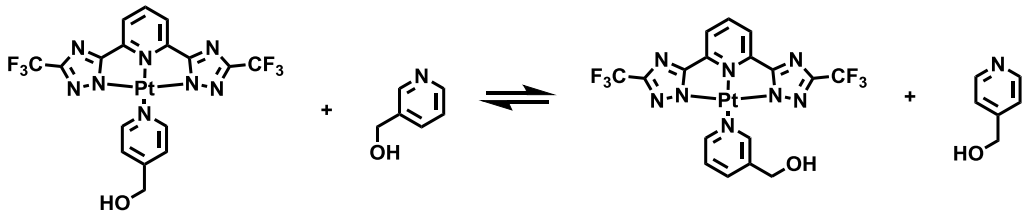

$$\Delta E_{4\rightarrow3} = \left(E([Pt_3]) + E(Py^4)\right) - \left(E([Pt_4]) + E(Py^3)\right) = -2.614\,\frac{kJ}{mol} = -1.05\,RT$$

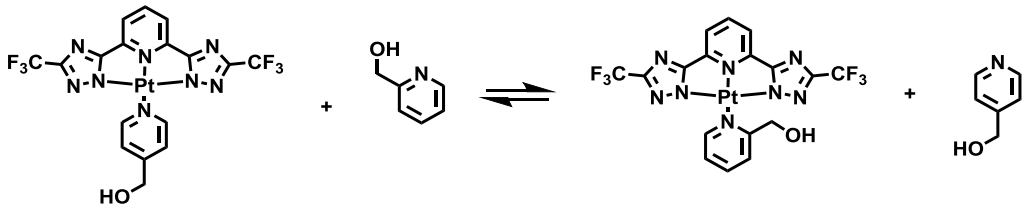

$$\Delta E_{4\rightarrow2} = \left(E([Pt_2]) + E(Py^4)\right) - \left(E([Pt_4]) + E(Py^2)\right) = 19.597\,\frac{kJ}{mol} = 7.905\,RT$$

The DFT calculations reveal that the coordination of an ortho-substituted pyridine towards the Pt center is strongly unfavored in comparison to its meta and para regioisomers. The calculated exchange energies are considerably low for a substitution reaction from para to meta (4→3; $\Delta E_{4\rightarrow3} =$ 1.05 RT, with T = 25°C) and rather high for para to ortho ($\Delta E_{4\rightarrow2} =$ 7.91 RT). Consideration of the molecular geometries of the Pt-complexes display a tilted-out condition for the *o*-Py-MeOH (**25**), while the other isomers show flattened complexes, which is favored for a z-directional aggregation.

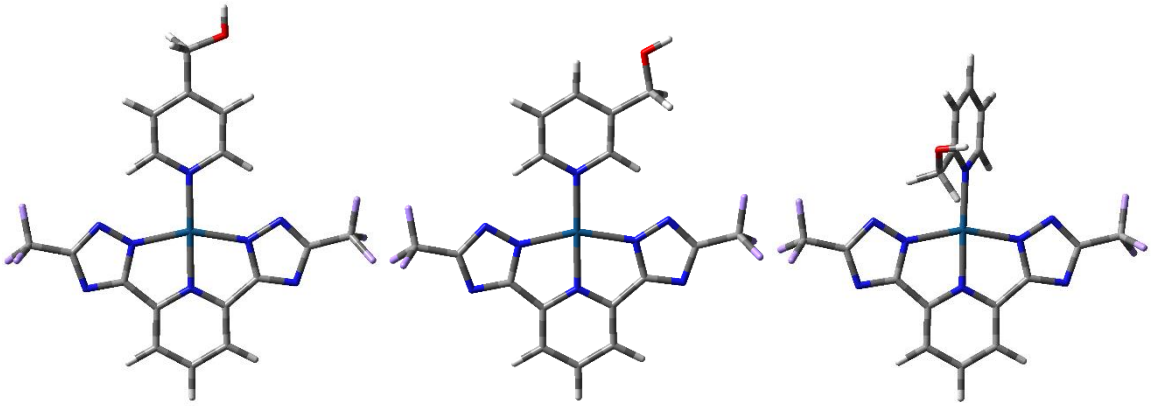

Figure 3.19: Ground-state (S_0) geometries of the complexes L-Pt-**3** (left), L-Pt-**4** (center) and L-Pt-**25** (right)**.**

In order to gain further insights into the coordination of differently substituted pyridines in the conditions of the assay, two assays were performed in pure PBS (33 µM

L-Pt-DMSO, 100 µM analyte). One assay with **25** and the other with its regioisomer **4**. After the assay the suspensions were centrifuged, the supernatants removed and subsequently washed with PBS and again centrifuged. After that the precipitates were washed with deionized water and centrifuged including the subsequent removal of the supernatant. The latter procedure was repeated one further time and the solids were subjected to lyophilization. The resultant solids were analyzed in ESI-ToF MS and NMR spectroscopy revealing that both complexes are formed (L-Pt-**4**, *m/z*: $[M-H]^-$ calcd. 650.0446; found 650.0318. L-Pt-**25**, *m/z*: $[M-H]^-$ calcd. 650.0446; found 650.0354). In the NMR spectra shown in Figure 3.20 a peak assignment has been done for both complexes. In contrast to L-Pt-**4**, the spectrum of L-Pt-**25** still displayed unconverted precursor (triplet at 8.34 ppm, doublet at 8.00 ppm). The sluggish kinetics due to the sterical hindrance of **25** as well as the constraints within the resulting complex (*vide supra*) explain why a full conversion of L-Pt-DMSO when reacted with **4**, and an incomplete conversion when reacted with **25** was observed. Consideration of the torsion angles of the resulting complexes further shows that a z-directional stacking is favored (planar arrangement) by the meta ($\measuredangle C_3N_3PtN_{trz} = 0.3°$) and para ($\measuredangle C_4N_4PtN_{trz} = 0.4°$) regioisomers but not by the ortho ($\measuredangle C_{25}N_{25}PtN_{trz} = 57°$) substituted one.

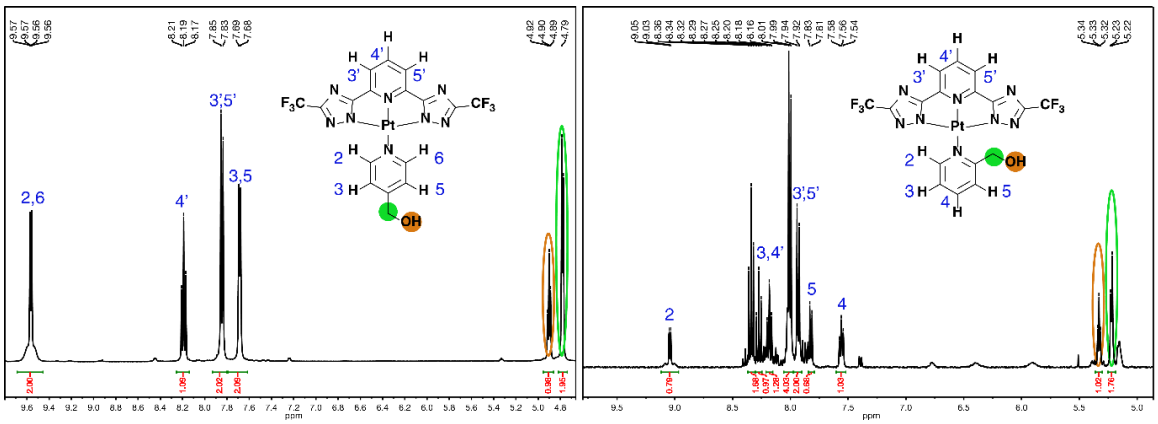

Figure 3.20: ^1H NMR (400 MHz, THF-d_8) spectrum of L-Pt-**4** and L-Pt-**25** after the synthesis described (see text).

The impact of sterical hindrance displays a greater effect, when the regioisomers 3,5 (**9**) and 2,6 dimethyl pyridine (**26**) are examined. Similar to the findings for the methanol pyridine derivatives, the doubly meta substituted **9** exhibits a strong emission intensity after the performed assay with L-Pt-DMSO, but the doubly ortho substituted **26** did not yield an emissive product (Figure 3.17).

Thus, the separated reactions were performed as described above for **4** and **25**. The formed complex L-Pt-**9** was characterized by mass spectrometry (L-Pt-**9**, *m/z*: $[M+Na]^+$ calcd. 672.0629; found 672.0668) and NMR spectroscopy (Figure 3.22) featuring a straight forward peak assignment. Although the energetic penalty ($\Delta E_{3,5\rightarrow2,6} = 7.82$ RT), that must be paid for the isodesmic exchange reaction, is in the same range as for **25** (*vide supra*), the resulting complex of L-Pt-**26** could not be detected in ESI-ToF MS or NMR. Therefore, most likely no formation of the complex takes place at the ambient assay conditions.

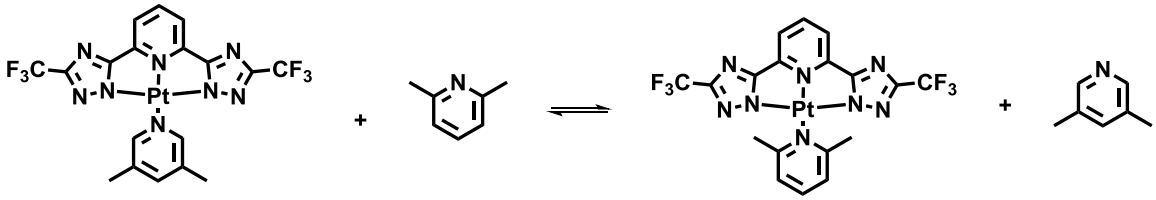

Figure 3.21: Isodesmic exchange reaction for L-Pt-**9** towards L-Pt-**26**.

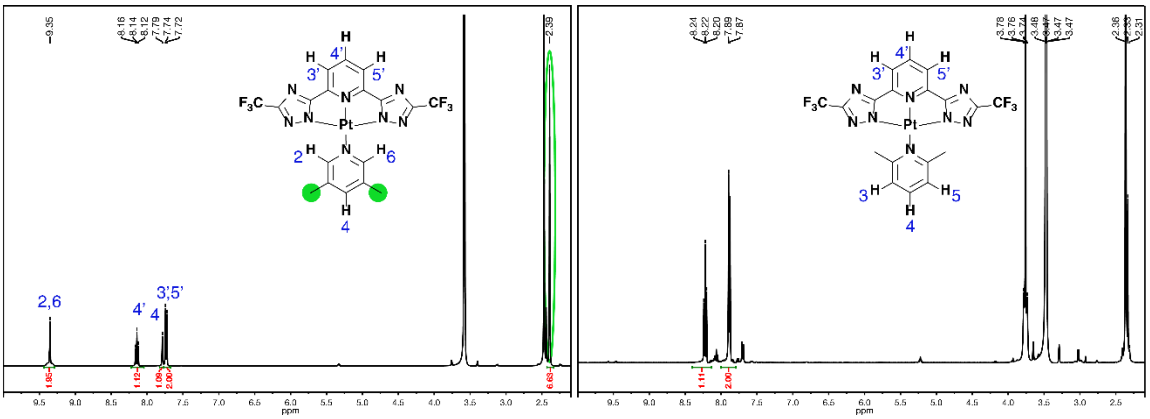

Figure 3.22: ^{1}H NMR (400 MHz, THF-d_8) spectrum of L-Pt-**9** and L-Pt-**26** after the described synthesis (see text).

The calculated structure of L-Pt-**9** allows for a z-directional stacking, and thus in turn Pt•••Pt interactions, on account of the planar arrangement ($\measuredangle C_9N_9PtN_{trz} = 0.5°$) of the ancillary ligand featuring methyl groups that point opposite to the metal center (Figure 3.23). The sterical hindrance of the both flanking methyl groups pointing towards the metal center in **26** lead for the ground state optimized complex to a strongly tilted arrangement of the ancillary ligand with a torsion angle of ($\measuredangle C_{26}N_{26}PtN_{trz} = 69°$).

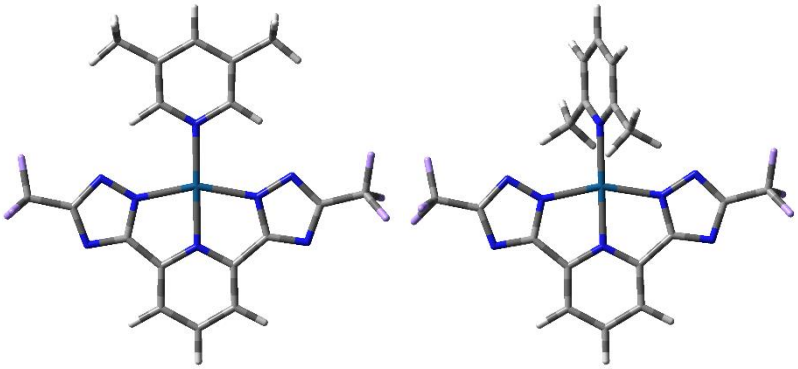

Figure 3.23: Ground-state (S_0) geometries of the complexes L-Pt-**9** (left) and L-Pt-**26** (right).

Halogenated pyridines (**13**-**14**) display unique emission features, *i.e.*, a shoulder at short wavelengths. Interestingly, when an iodine (**15**) substitution is present, this shoulder is not observed (Figure 3.24). The absorption spectra of **13** and **14** show pronounced bands around 400 – 480 nm and excitation spectra (resembling the absorption spectrum well) that peak at 378 and 417 nm as well as 378 and 420 nm, respectively. These bands can be assigned as π-π* transitions. This observation strongly differs from the excitation and absorption spectra of **15**, which rather resembles the shape and intensity of the parent complex of **1**. Here, weaker MLCT and π-π* transitions are observed with a pronounced excitation transition at 473 nm. The excited-state lifetimes measured for **13** and **14** are 228 and 260 ns, respectively, which are significantly shorter than for **15** (453 ns) and **1** (440 ns). Similar photophysical features as determined for **13** and **14** are observed for the complex of the strongly electron withdrawing (π-accepting) 4-cyano pyridine **10** (vide supra) featuring an excited-state lifetime of 200 ns. The electron-withdrawing abilities of halides are based on a negative (electron-withdrawing) inductive effect. The inductive effect is affecting the σ-system and the π-system.[69] Furthermore, the reduction potential of the ligand is shifted to more positive values enabling a more facile reduction of the ancillary ligand with increasing electron-withdrawing inductive effect.[70, 71] The electronegativity (χ) after Pauling[72] can serve as a measure for the extent of the electron-withdrawing inductive effect. This reveals a series with declining χ from chlorine (χ = 3.16) to bromine (χ = 2.96) to iodine (χ = 2.66).

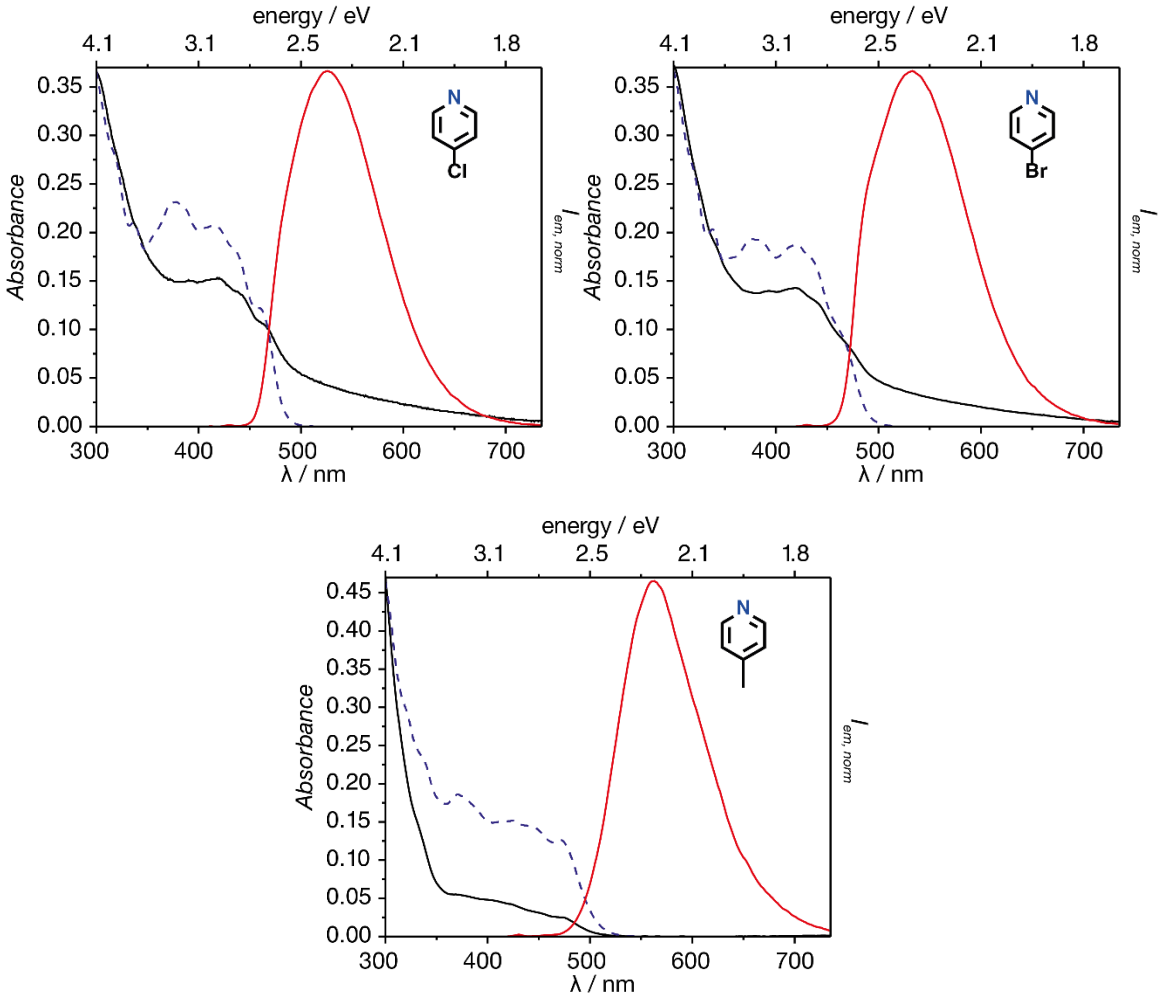

Figure 3.24: Absorption (black, solid), normalized emission (red, solid, λ_{ex} = 375 nm) and excitation (blue, dashed, $\lambda_{em} = \lambda_{em,max}$) spectra of the **13** (4-chloro pyridine, top left), **14** (4-bromo pyridine, top right) and **15** (4-iodo pyridine, bottom) after the assay at ambient conditions.

Therefore, most likely a pronounced electron-withdrawing ability of the ancillary ligand (analyte) is reflected in a hypsochromic shouldering of the featureless emission profile and a shortening of the excited-state lifetime. The stabilization of the π-system of the ancillary ligand leads enables the acceptance of electrons during an excitation process. This explanation is based on the consideration of the frontier orbitals of L-Pt-**1** and L-Pt-**10** which are depicted in Figure 3.25. The HOMOs are very similar and show strong contributions from the π-system of L and a d-orbital of the Pt center. Contrarily, the LUMO of L-Pt-**1** is predominantly located on the N-metalacycling ligand **L** with small contributions of metal d-orbitals and π-orbitals of pyridine. The LUMO of L-Pt-**10** is prevalently located on the π-system of the ancillary ligand with minor contributions of the π-system of L and almost no Pt d-orbital contribution is present. It is assumed that the

lowest energetic excitation is the HOMO-LUMO transition[73, 74], which is also revealed from TD-DFTcalculations of L-Pt-**1** featuring the lowest singlet excitation in THF at 385 nm with an oscillator strength of f = 0.0096 being entirely a HOMO-LUMO transition. Thus, most likely the lowest excited state is resembled by the electron distribution for HOMO and LUMO, which in turn means for L-Pt-**1** a metal-ligand(L)-to-ligand(L) charge transfer state and for L-Pt-**10** a metal-ligand(L)-to-ligand (**10**) charge transfer state on account of the π-stabilization of the pyridyl moiety by the electron-withdrawing cyano group. In terms of the rule of Kasha,[75] the emission usually occurs from the lowest excited vibronic state. Therefore, the nature of the emissive state in L-Pt-**1** and L-Pt-**10** are varying explaining the differences in the photophysical properties.

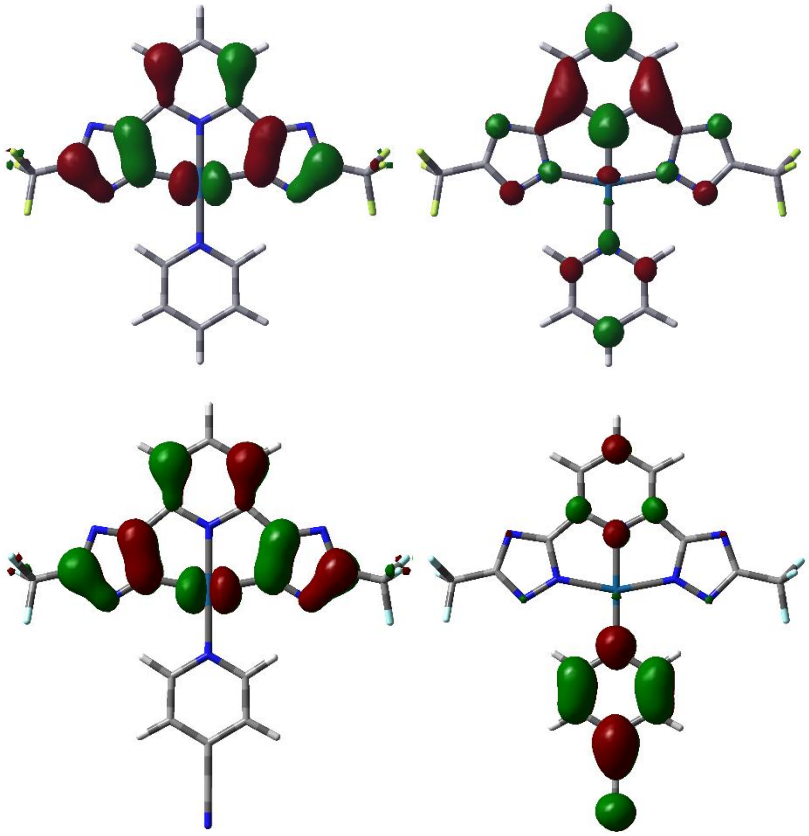

Figure 3.25: Kohn-Sham plots of the frontier orbitals of L-Pt-**1** (top) and L-Pt-**10** (bottom). left: Highest occupied molecular orbitals (HOMOs) right: Lowest unoccupied molecular orbitals (LUMOs). Hybrid functional Perdew-Burke-Ernzerhof with split basis sets 6-31G(d,p) for C,H,N and F and SSD (including pseudo core potential) for Pt.

Additionally, poly-aza-heterocycles (**31**-**34**) are also linked to a weak emission intensity of the corresponding Pt-complexes (Table 3.2). The series of varying positioning of the aza moiety demonstrates another type sterical hindrance. Hereby, the adjacent

nitrogen atoms in pyridazine (**31**, *SiNo* = 1.2) prevent a double coordination featuring a planar geometry of the resulting complex and thus only a singly coordinated species or tilted doubly coordinated can be formed. In any of the possible ways for coordination, the activation energy will be rather high. A similar observation is present for pyrimidine (**32**, *SiNo* = 1.88), where one carbon atom spaces the two nitrogen atoms within the aromatic ring system. The emission spectra of **31** and **32** are structured and peaking at 456 and 465 nm, respectively. This finding indicates for no conversion in the case of **31** (resembles the emission profile of L-Pt-DMSO, see Figure 3.11) and a coordinated species that prevents z-directional stacking, and thus Pt•••Pt interactions.

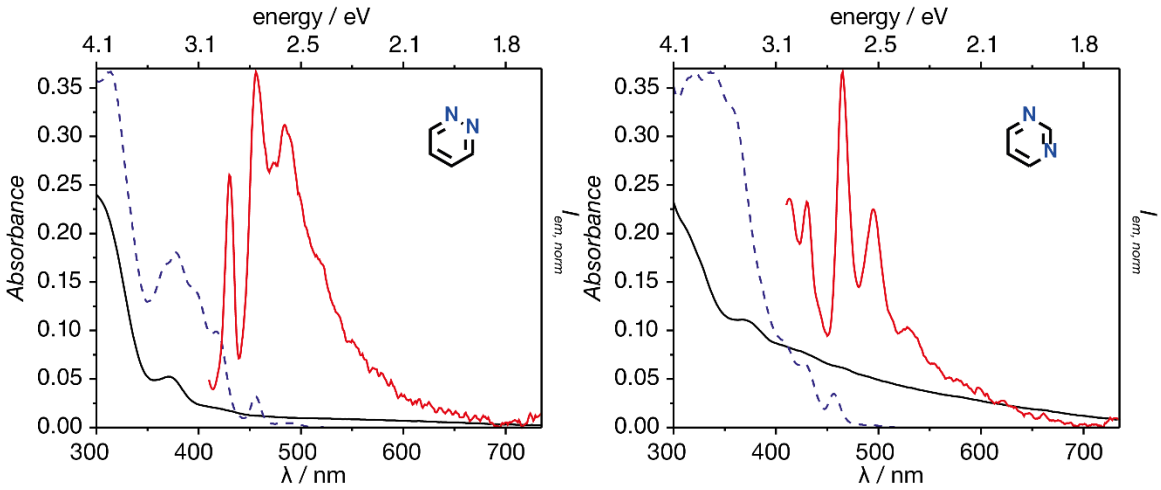

Figure 3.26: Absorption (black, solid), normalized emission (red, solid, λ_{ex} = 375 nm) and excitation (blue, dashed, $\lambda_{em} = \lambda_{em,max}$) spectra of the **31** (pyridazine, left) and **32** (pyrimidine, right) after the assay at ambient conditions.

Supposedly, the double coordination is eased for a 1,4 aza positioning (pyrazine, **33**) than for a 1,2 (pyridazine, **31**) and 1,3 (pyrimidine, **32**). Indeed, for pyrazine a featureless emission centered around 529 nm was observed and a bathochromically shifted excitation onset, indicating of Pt•••Pt interactions (Figure 3.27). Nevertheless, also for **33** (*SiNo* = 1.72), as for the other multi-aza components such as cis-triazine (**34**, *SiNo* = 0.59) only weakly emissive compounds are detected. Formation of the final complexes of **31** and **32** is possible, which was demonstrated in a collaboration[76] but higher temperatures and thus activation energies are necessary to overcome the sterical hindrance. For those doubly-coordinated complexes, low quantum yields were observed, most likely due to a tilted structure in which both Pt centers face each other on a distance preventing interactions.

In general, the poly aza-heterocycles are less electron-rich than the single aza-heterocycles with the parent pyridine. The lowered basicity renders a lower affinity for metal coordination. Therefore, a double coordination is most likely not only sterical hindered (**31**, **32** & **34**) but also electronically and needs higher activation energy (higher reaction temperature). The reduced electron-density of the poly aza-heterocycles might have similar effects as described for analytes bearing electron-withdrawing group (*vide supra*). The resulting lowest charge-transfer (CT) states might be dark states competing with the emissive states and thus leading to a low quantum yield. Furthermore, the free nitrogen of a singly coordinating poly aza-heterocycle can form H-bonds towards the surrounding solvent molecules enabling a quenching by low lying CT states.[77]

Although the lone-pair energy of an sp^2 hybridized nitrogen is lower than the one of an sp^3-nitrogen, it cannot be excluded that the aggregated emissive state is quenched by the uncoordinated aza-moieties (In Chapter II it is shown that [2,2,2] cryptand renders the quenching of the ^{3}MMLCT based emission)

However, the signals were still detectable conditions for strongly emissive compounds at the fluorescence spectrometer. Therefore, the assay can be further tailored to multi-aza compounds.

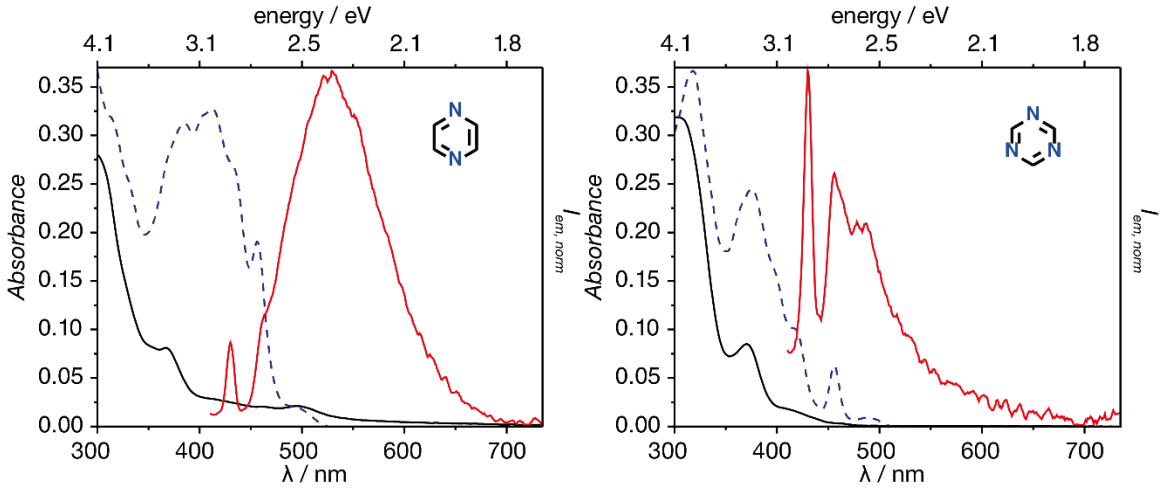

Figure 3.27: Absorption (black, solid), normalized emission (red, solid, λ_{ex} = 375 nm) and excitation (blue, dashed, $\lambda_{em} = \lambda_{em,max}$) spectra of the **33** (left) and **34** (right) after the assay at ambient conditions.

Certain substituents on the pyridine moiety show a very low PLQY, *e.g.* carbonyl- (*e.g.*, -COO^- (**27**, **28**, **35**) & $CONHNH_2$ (**36**)) and sulfonyl- (-SO_3^-) (**30**) (Table S1). Here,

the typical structural characteristic is either a lone pair (**36**) or even a full negative charge (**30**), which presumably quenches the phosphorescence by PET.

The Pt-complex of imidazole (**16**) shows a structured emission profile peaking at 465 nm, (Figure 3.28), which fundamentally differs from those of pyridine derivative complexes. The structured emission of **16**, which is accompanied by a relatively short excited-state lifetime of 140 ns and a low quantum yield (φ = 2%), can be ascribed to a different nature of the emitting state, namely a triplet ligand centered state (^{3}LC).[40, 78] A minor molecular change, namely the substitution to a methyl group at the protonated nitrogen atom (**17**), causes a major change in the photophysical properties. The observed featureless emission appears at strongly lowered energies (ΔE = 0.57 eV) featuring a prolonged excited-state lifetime (τ = 278 ns) and an enhanced quantum yield of 8%. Therefore, the emission can be described as ^{3}MMLCT based evolving from Pt•••Pt interactions. Out of all analyzed compounds the Pt(II)-complex of **17** displays the most bathochromically shifted absorption profile with λ_{abs} = 494 nm and an excitation onset of 519 nm.

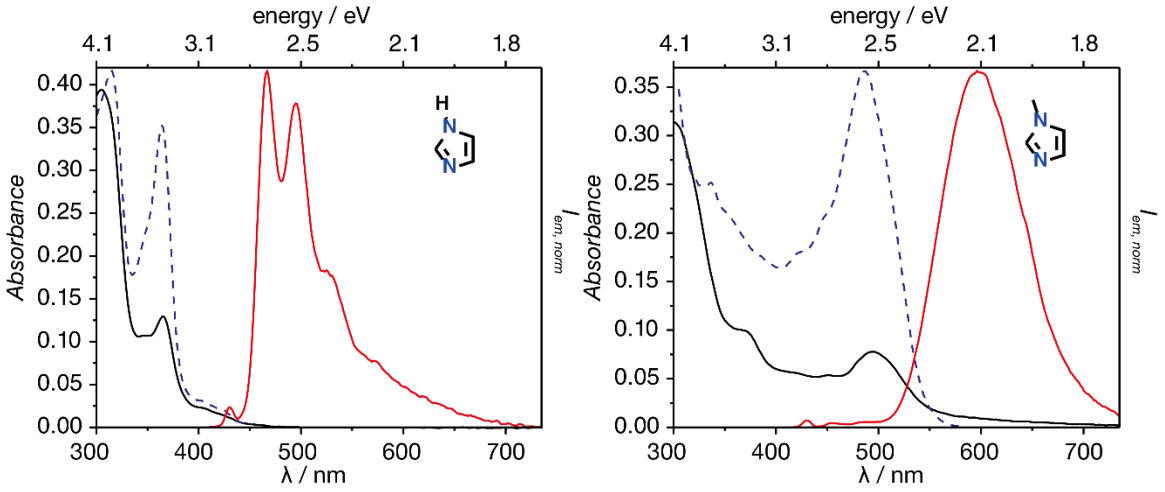

Figure 3.28: Absorption (black, solid), normalized emission (red, solid, λ_{ex} = 375 nm) and excitation (blue, dashed, $\lambda_{em} = \lambda_{em,max}$) spectra of the **16** (imidazole, left) and **17** (N-methyl imidazole, right) after the assay at ambient conditions.

The photophysical analysis of the reacted analytes benzimidazole (**18**) and methyl benzimidazole (**19**) are fundamentally akin to the observations for the parent imidazole ligands **16** and **17**. For **18** a structured emission (^{3}LC based) peaking at 469 nm, hypsochromically shifted absorption (λ_{abs} = 425 nm) and excitation spectra (in comparison to L-Pt-**1**), a very weak emission intensity (φ = 0.6%) and short excited-state

lifetime (τ = 31 ns) is observed. Similar to the parent imidazole derivatives, substitution of the ancillary ligand from benzimidazole (**18**) to N-methyl benzimidazole (**19**) is accompanied by change in the nature of the emission (^{3}MMLCT based). The absorption spectrum is bathochromically shifted with λ_{abs} = 467 nm and an excitation onset of 473 nm. The featureless emission is peaking at lower energies (ΔE = 0.42 eV), the excited-state lifetime strongly prolongated to 643 ns with a quantum yield of 50%.

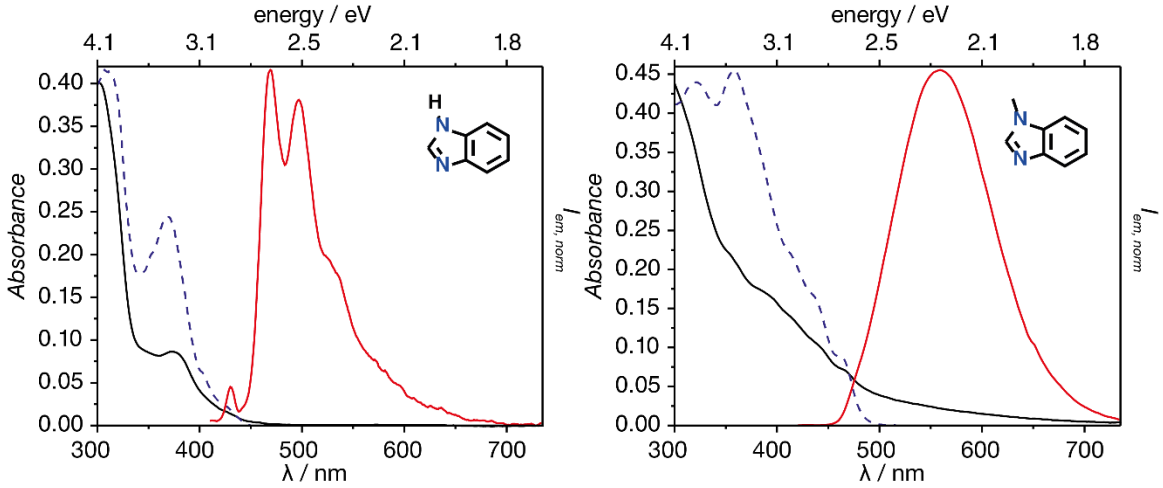

Figure 3.29: Absorption (black, solid), normalized emission (red, solid, λ_{ex} = 375 nm) and excitation (blue, dashed, $\lambda_{em} = \lambda_{em,max}$) spectra of the **18** (benzimidazole, left) and **19** (N-methyl benzimidazole, right) after the assay at ambient conditions.

Why Pt•••Pt interactions are prevented for imidazole and benzimidazole, but are present in the case of N-methyl imidazole ligands is currently unknown. The protonated uncoordinated aza-moiety might serve as a hydrogen donor enabling a 2D networks (see Chapter IV) *via* hydrogen bonding towards surrounding acceptors (H_2O, DMSO, PEG chains). These competitive supramolecular interactions might hinder a z-directional stacking but enabling an aggregation, which explains the high quantum yield and long excited state lifetimes. Additionally, H-bond interactions with surrounding solvent molecules can in principal have strong influences on the photophysical features, namely changing the lowest excited-state state and therefore changing the nature of emission.[79] A tilted arrangement for imidazole based ligands in the final complexes is not expected, according to DFT calculations which display a planar arrangement for L-Pt-**16** and L-Pt-**17**.

Also, the antifungal drugs (**21** – **23**) can be readily distinguished from each other by both their emission and excitation spectra (Figure 3.30). In contrast to the observation for

the substituted imidazole derivatives **17** and **19**, for **21** a structured emission (^{3}LC based) profile peaking at 464 nm with an extraordinary long excited-state lifetime (τ = 2740 ns) is observed. Together with the hypsochromically shifted absorption and excitation spectra (λ_{abs} = 405 nm), one concludes that no Pt•••Pt interactions take place. Most likely, a strong aggregation of the bulky ligand **21** merging from quadrupole (π-π) and dipole interactions lead to such kind of aggregation avoiding an interaction of the Pt(II) centers. This arrangement further renders a strong rigidochromic effect, *e.i.* a freezing of the excited-state preventing deactivation from thermally equilibrated excited states (geometry change). This explanation is supported by the long excited-state lifetime and relatively high quantum yield (φ = 13%), which is in the same order of magnitude as comparable structures in PMMA films.[45]

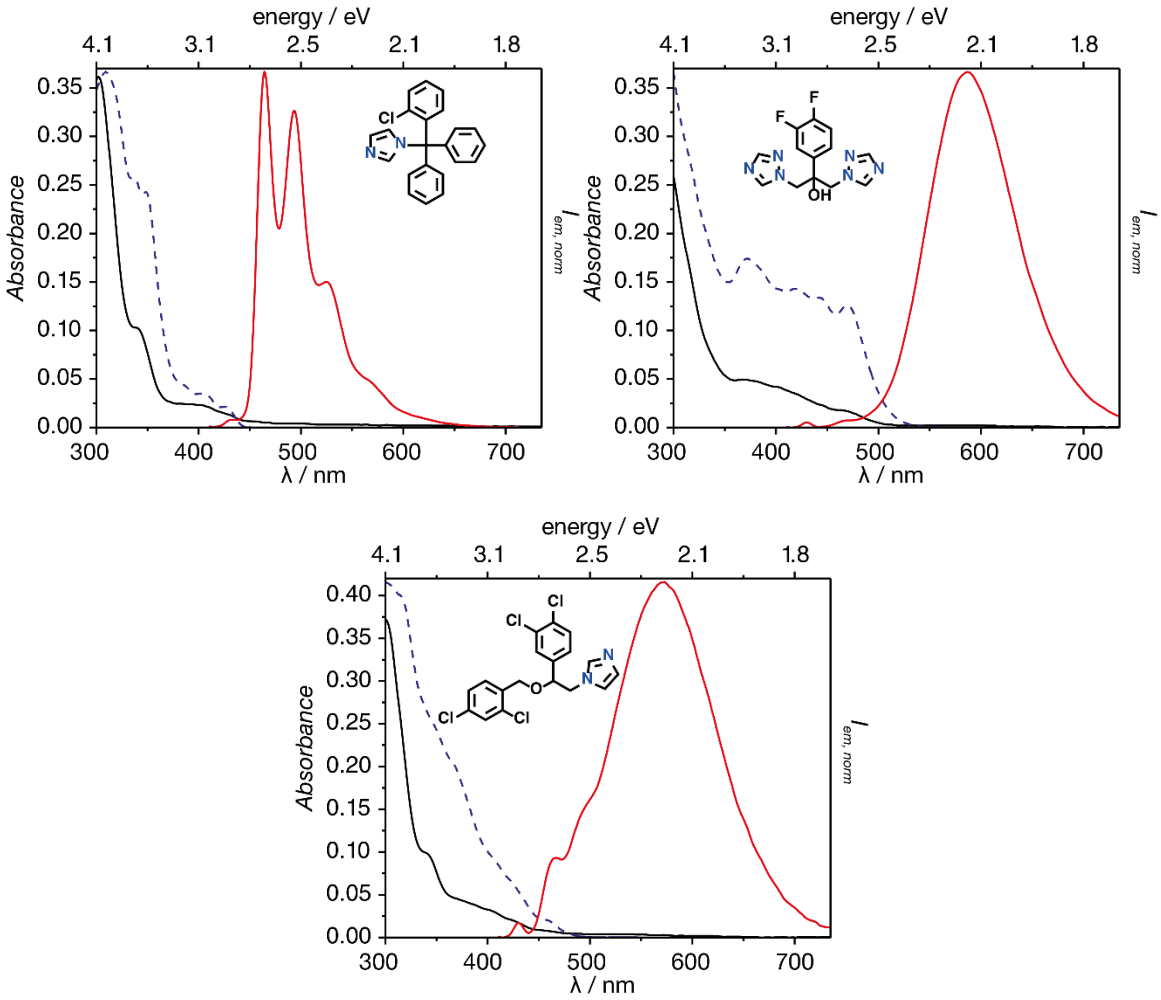

Figure 3.30: Absorption (black, solid), normalized emission (red, solid, λ_{ex} = 375 nm) and excitation (blue, dashed, $\lambda_{em} = \lambda_{em,max}$) spectra of the **21** (top, left), **22** (top, right) and **23** (bottom) after the assay at ambient conditions.

Consideration of the photophysical data arising from a reaction with miconazole (**23**), which is also a derivative of N-methyl imidazole a different picture than for **21** is drawn. Now, the emission profile is peaking at 570 nm with a small peak at 461 nm indicating of partially aggregated and disaggregated Pt(II) species. The excited-state lifetime of 338 ns suggests an ^{3}MMCLT based emission, which is as well supported by the broad emission profile. Nevertheless, the absorption and the excitation spectra rather resemble the profiles of a monomeric species with λ_{max} = 451 nm. That the excitation spectrum, measured at 570 nm (aggregation) is similar to the absorption spectra of the monomer suggests the formation of excited state dimers (excimer).[80] It is not uncommon to observe excimer emission from Pt(II)-complexes accompanied by a decrease of the Pt-Pt distance, due to the depopulation of the anti-bonding HOMO.[42, 47, 81-83] Concluding the results of **17**, **21** and **23**, the substitution pattern on the aza-bound carbon probably plays a major role. From **17** to **23** to **21**, the bulkiness of the substituents increases accompanied by a hypsochromic shift of the emission and a change in its profile.

The Pt(II)-complex of the 1,2,4 triazole based anti-fungal drug fluconazole (**22**) exhibits an absorption spectrum featuring λ_{max} = 465 nm and an excitation onset of 488 nm. Together with the featureless emission profile peaking at 587 nm and an excited-state lifetime of 296 ns the emission is ascribed to by ^{3}MMLCT based, which arises from Pt•••Pt interactions.

The significant spectral difference between **11** and **13** was exploited to analyze the stability of the formed platinum complexes against substitution reactions. For the experiments, an excess (20 times) of the competing ligand was added to an already completed assay sample and the emission spectra was determined over a duration of 140 min. The experiments revealed that no exchange reaction takes place, in either direction, even after 4 h duration time.

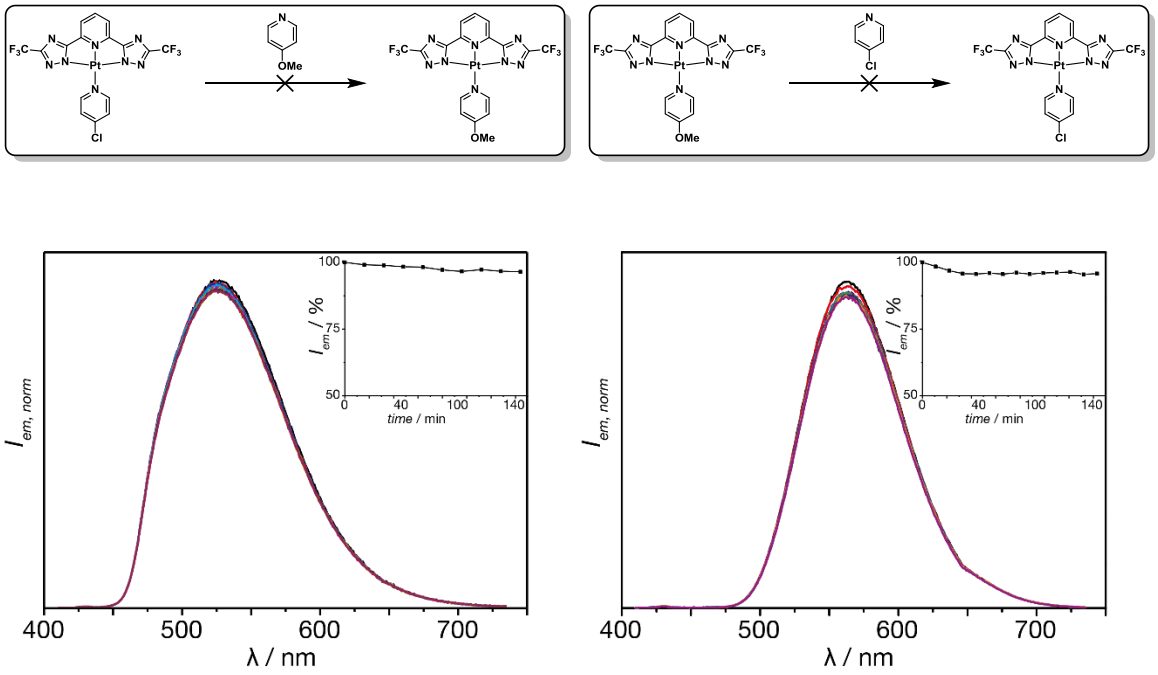

Figure 3.31: Emission spectra collected during competitive reactions (duration: 4 h); left: L-Pt-**13** with addition of **11**; right: L-Pt-**11** with addition of **13**. Insets: development of the emission intensity (%) at $\lambda_{em,max}$ over 140 min. The appropriate reactions are depicted above the graphs.

Analyte differentiation and deconvolution by TRES

Analyte detection by means of time-resolved emission spectroscopy, *e.g.*, through measurement of the excited state lifetime, can be superior to steady-state emission detection if the samples of interest are highly scattering or show sizeable inner filter effects.[84, 85] Moreover, the time domain can offer some additional useful information to assist analyte differentiation. For instance, the Pt-complexes of analyte **2** and **10** coincidentally show very similar values for their emission maxima (545 and 546 nm for **2** and **10**, respectively) and absorption onsets (470 and 471 nm), see Table 3.3. However, their excited-state lifetime (91 and 175 ns, respectively) differ by a factor of almost 2, which can be routinely determined[73] such that analyte **2** and **10** can be readily distinguished with high confidence. It is important to note that the self-aggregation of the Pt-analyte complexes renders the phosphorescence *insensitive* to dynamic quenching by dissolved oxygen, such that the excited state lifetimes are similar under aerated and deaerated conditions.[48]

The comparably long and analyte-dependent excited-state lifetimes of the Pt(II)-analyte complexes can also be exploited for spectral deconvolution of mixtures of the labelled

analytes by means of time-resolved emission spectroscopy (TRES).[1, 86] For example, an 1:1 mixture of the drugs **21** and **22** that was subjected to the assay, gave clearly different TRES spectra (Figure 3.32). Here the time gates are set to be 2 - 60 ns for the relatively short excited-state lifetime of L-Pt-**22** (τ = 296 ns) and 4 - 8 ms for the strongly delayed emission event of L-Pt-**21** (τ = 2740 ns). The resultant TRES spectra clearly resemble the emission spectra of the compounds subjected to separate assays (Figure 3.30).

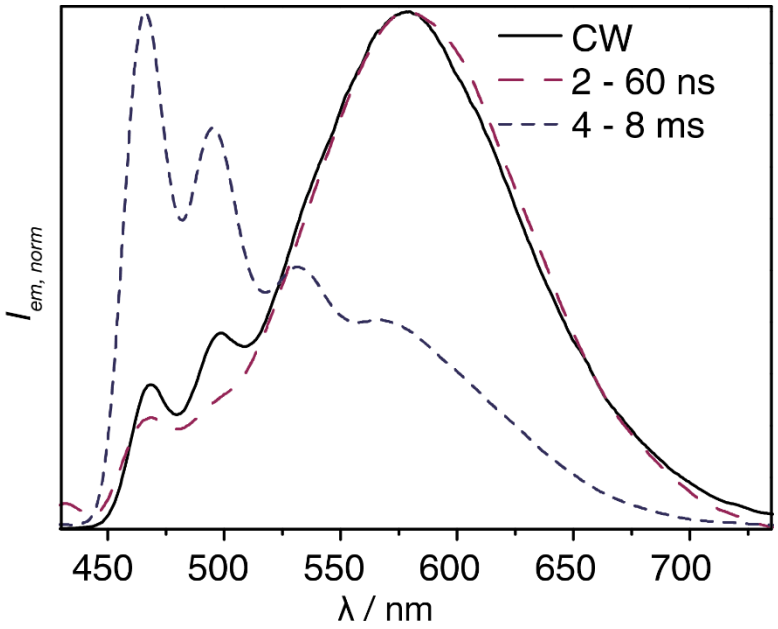

Figure 3.32: Emission spectrum featuring an excitation with a continuous wave (CW) of the assay-reaction mixture with equimolar **21** and **22**, and analyte-mixture deconvolution through TRES.

Mathematical models for analyte differentiation

In order to provide a more quantitative differentiation of the Pt-complexes and to show the potential of the tagging method for differential sensing application, a principal component analysis (PCA)[87-89] was performed. The unsupervised multivariate routine PCA is the best choice to demonstrate the utility of input parameters, because only a smaller variance of the replica measurements than for different analytes results in the appearance of a score clustering.[87] Five photophysical parameters were determined (for all values please see table in Appendix) for each Pt-labelled analyte and the PCA algorithm mapped this input data into a distinct score for each of the 23 tested analytes: the emission wavelength maximum in cm^{-1} (λ_{max}), the excitation onset in cm^{-1} ($\lambda_{exc,onset}$), the reference weighted integral of the emission spectrum (*Int*), the amplitude weighted

excited-state lifetime (τ) and the signal-to-noise ratio (*S/N*) (see Appendix for data table). Since the input variables differ strongly in their numerical magnitude, the eigenvalue problem for the PCA was solved for the correlation matrix, instead of the covariance matrix. Not all samples revealed clearly defined excitation bands, therefore the excitation onset was determined as the inflection point of the longest-wavelength band in the excitation spectrum. The inflection point was determined through fitting of a Gaussian peak.[46] In order to facilitate the instrumental effort as well as allowing reproducibility in other laboratories without an integrating sphere setup, reference weighted integral of the emission spectrum instead of the quantum yield was utilized in the PCA.[90] The amplitude weighted excited-state lifetime was detected by time-correlated single photon counting measurements with the FT300 setup from PicoQuant, utilizing the most likelihood estimation method.

In order to give a general picture about the applied mathematical model, the discussion is initially limited to representative analytes – their corresponding score 2D and 3D scores plots are shown in Figure 3.33.

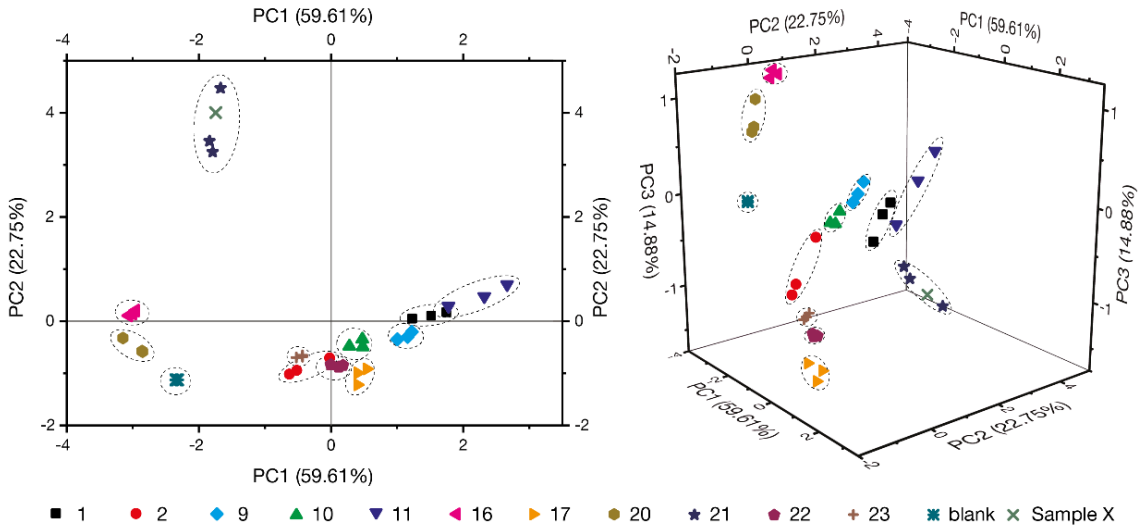

Figure 3.33: Principal component analysis (PCA) of selected analytes. left: Scores plot of the first two principal components, PC1 = 59.61% and PC2 = 22.75%, together 82.36 %; right: Scores plot of the first three principal components, together 97.24 %. The assay performed without added analyte is denoted as "blank". The arbitrary ellipses indicate the clustering of each analyte (Figure 3.35 for 95% confidence ellipses, see Video S1 for 3D animation).

A clear clustering of the scores – indicated by the surrounding ellipses – was obtained for replica measurements with the same analyte, while the scores for different analytes populated clearly distinguishable areas in the 2D and 3D plot in most cases. Few analytes

stayed indistinguishable from each other when only two principle components were considered, but all analytes became clearly discriminable when three principle components were taken into account (see Figure 3.33). Prior to the labeling by L-Pt-DMSO, almost none of the analytes were distinguishable from each other by spectroscopic means (absorption, emission).

Consideration of the entire PCA (Figure 3.34) revealed two main clusters besides clearly separated components (the Pt precursor named blank, **17**, **19**, **21**) (Figure 3.34 & Video S2). Therefore, two sub-analyses were performed, resulting in separated scores even for structurally closely related pyridines such as **13**−**15** (R = -Cl, -Br, -I), 3−6 (R = alkyl) and the drugs **2**, **20**−**23**.

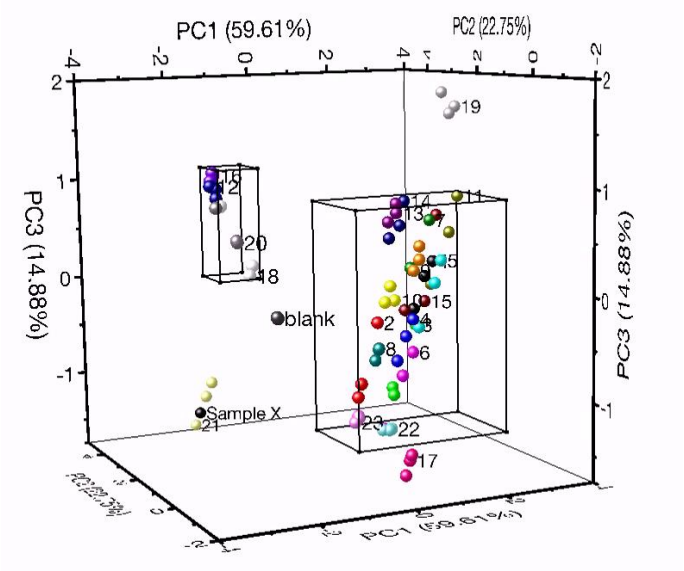

Figure 3.34: Principal component analysis (PCA) of the 23 analytes yielding strongly emissive Pt(II) derivative (*SiNo* > 3) after subjected to the assay (Video S2 for animation). The big cuboid frames subset-1 (Figure 3.37, left & Video S3) and the small cuboid subset-2 (Figure 3.37, right & Video S4). PC1 = 59.61% and PC2 = 22.75% & PC3 = 14.88%, together 97.24 %.

A reasonable representation of three dimensionality data as inherently two dimensional images is difficult, therefore the reader is referred to the attached video files for a detailed review. Although the scores are well separated and cluster for each analyte, the input parameters possess certain errors, namely the standard deviation given by sampling and the instruments as well as assay uncertainties (Table 3.4).

Table 3.4: Errors for all analyzed compounds.

Index	Analyte	λ_{max} / cm^{-1}	$\lambda_{exc,onset}$ / cm^{-1}	Int	τ / ns	*SiNo*
1	pyridine	71	22	64	14	3
2	L-nicotine	155	37	65	5	5
3	3-pyridinemethanol	62	75	96	31	4
4	4-pyridinemethanol	18	14	47	13	3
5	4-picoline	18	31	85	14	4
6	4-pentylpyridine	48	28	77	82	5
7	4-bromomethylpyridine	19	62	78	7	3
8	4-aminomethylpyridine	19	2	15	33	1
9	3,5-lutidine	68	7	25	7	2
10	4-cyanopyridine	174	7	23	17	1
11	4-methoxypyridine	30	27	125	20	4
12	dimethylaminopyridine	55	193	3	2	1
13	4-chloropyridine	95	9	25	9	1
14	4-bromopyridine	89	47	56	17	2
15	4-iodopyridine	354	38	138	43	2
16	imidazole	27	2	7	18	1
17	N-methylimidazole	70	36	13	83	1
18	benzimidazole	53	1455	5	10	2
19	N-methylbenzimidazole	116	73	26	27	1
20	histamine	428	268	1	9	1
21	clotrimazole	0	11	12	55	1
22	fluconazole	138	7	9	9	1
23	miconazole	36	14	4	3	1
blank	L-Pt-DMSO	0	29	0	1	0

The estimated parameter uncertainties of the assay were also computed, demonstrating that even large measuring errors (15%) are tolerable. The certainty of the given data can be assessed by 95% confidence ellipses, which present very well the clear separation in the 2D space.

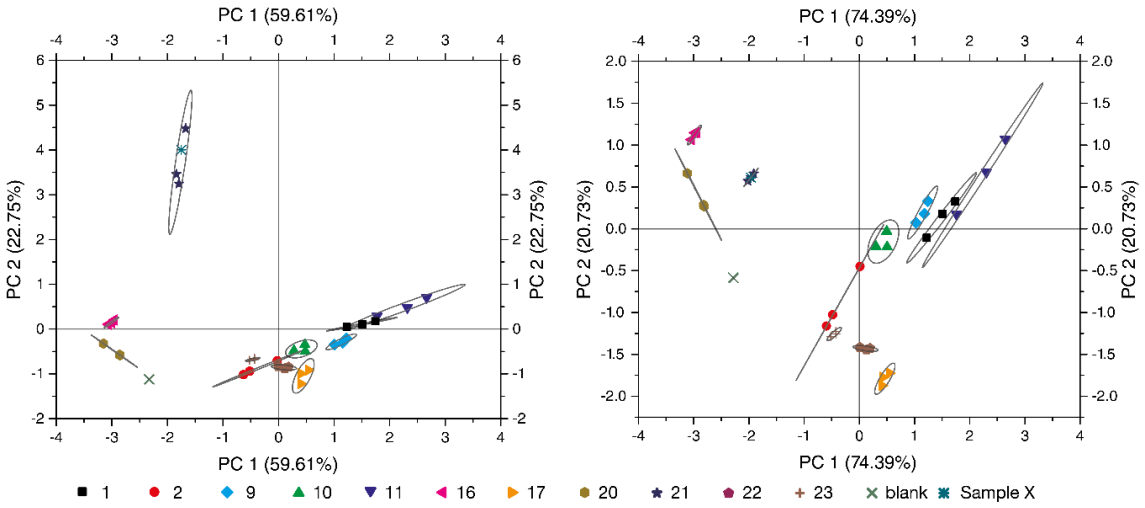

Figure 3.35: 2D Scores plots including 95% confidence ellipses resulted from the principal component analysis of the photophysical data of representative compounds. left: The excited-state lifetime (τ) was included as input factor for the PCA (see also Video S1), PC1 = 59.61% and PC2 = 22.75%, together 82.36 %; right: The excited-state lifetime (τ) was excluded from the input matrix for the PCA (see also Video S5), PC1 = 74.39% and PC2 = 20.73%, together 95.12%.

The error estimation for 3D data can be conducted by using the same principle as for 2D data, namely the calculation of 95% confidence ellipsoids. For both cases, ellipses and ellipsoids, the calculation is fundamentally akin to a PCA. If a square matrix (n *X* n) possesses any eigenvector, it possesses *n* eigenvectors. The eigenvector *v* of a dataset matrix *A* can be used to describe the matrix A via the eigenvalue λ:

$$Av = \lambda v \qquad \text{Eq. 3.2}$$

Therefore, a linear combination with the eigenvectors and eigenvalues allows for a projection of the data onto space of lower dimension (*e.g.*, 4D → 3D). This projection can then be used as a description of the data of higher dimension and its distribution. The later one is used to visualize the spreading of the scores within the 2D (ellipses) or 3D (ellipsoids) space by solving the eigenvalue problem on the covariance matrix of each score cluster, namely the colored groups in the score plots. For visualization, the ellipses were calculated as follows:

$$X = X_0 + a * \cos\alpha * \cos\theta - b * \sin\alpha * \sin\theta \quad \text{Eq. 3.3}$$

$$Y = Y_0 + a * \sin\alpha * \cos\theta - b * \cos\alpha * \sin\theta \quad \text{Eq. 3.4}$$

With $0 < \theta < 2\pi$; X_0 and Y_0 denoting the center of the ellipse, and α being the angle between the major axis of the ellipse and the X-axis; a and b are factors defining the spreading of the ellipse. The values can be obtained using the following equations:

$$X_0 = \frac{\sum_0^n X_i}{n} \qquad Y_0 = \frac{\sum_0^n Y_i}{n} \quad \text{Eq. 3.5}$$

$$a = 2.4477\sqrt{\lambda_{max}} \qquad b = 2.4477\sqrt{\lambda_{min}} \quad \text{Eq. 3.6}$$

$$\alpha = \text{atan2}(v_{max}, v_{min}) \quad \text{Eq. 3.7}$$

Where X_i and Y_i denote the individual score coordinates, λ_{max} and λ_{min} being the eigenvalues to the corresponding largest and smallest eigenvector v_{max} and v_{min}, respectively. For the ellipsoids, the build function of Matlab was utilized and a matrix based visualization realized in Origin. The ellipsoids (see Figure 3.36) were exemplary calculated for the selection depicted in Figure 3.33.

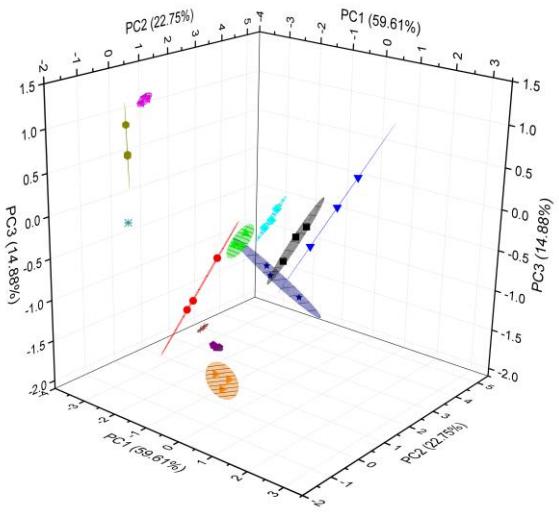

Figure 3.36: 2D Scores plots including 95% confidence ellipsoids resulted from the principal component analysis of the photophysical data of representative compounds, PC1 = 59.61% and PC2 = 22.75% & PC3 = 14.88%, together 97.24 %.

Due to the small sample size of three scores, the ellipsoids surely spread only within 2D planes oriented in a 3D space. Therefore, error-clouds were calculated, which

represent computed data points within the error intervals of the given scores data. The clouds were calculated for the subsets of the entire PCA taking all 23 strongly emissive analytes into account. Only a few cross sections exist demonstrating on one hand the good separation of the clusters and thus a distinguishability of the analytes and further the orthogonality of the chosen input factors.

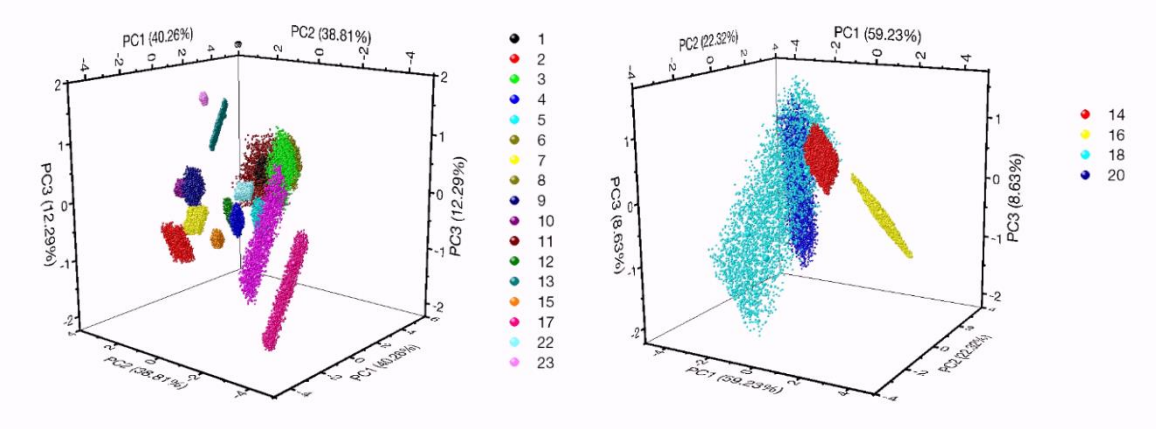

Figure 3.37: Simulated data spreading by error-clouds of the scores resultant from principal component analysis (PCA) of the subsets arising from the PCA of 23 analytes described in Figure 3.34. left: Subset-1 with PC1 = 40.26% and PC2 = 38.81% & PC3 = 12.29%, together 91.36%. right: Subset-2 with PC1 = 59.23% and PC2 = 22.32% & PC3 = 8.63%, together 90.18%.

On the other hand, wide spreading as observed for **18**, **20** and **15** is most likely due to the big standard deviation arising from the small sample size. Therefore, a transfer of the system towards an instrumentation such as a micro-well plate reader enabling a higher through put and thus a bigger sample size is desirable. Consequently, the system was tested on the omission of the excited-state lifetime as factor being the most sophisticated to be determined. The principle applicability of a plate reader was shown in Figure 3.14 and PCAs were conducted either with τ as an input factor and without (Figure 3.35 & Video S1 & S5). These analyses demonstrate that the differentiation of aza-heterocyclic analytes is also feasible even with high-throughput plate-reader-based measurements and omission of time-resolved measurements.

Additionally, a Fisherface-type linear discriminant analysis (LDA) on the selected dataset of Figure 3.33 displays a high classification rate (94.44%) of the applied system (see Figure 3.38). The classification errors are rather low in consideration of the small sample size and are higher for the eigenvector system covering less data. Commonly, LDAs are a well-established tool for classification utilizing large sample sizes. At a small

sample size (number of variables being lower than factors) the singularity of the within-scatter matrix leads to a failure for the calculation. Thus, again a bigger sample size is preferable for classification algorithms such as LDA and support vector machines. Nevertheless, the unsupervised PCA outperforms the supervised LDA methods in terms of direct assessment of the chosen factors, since a clustering is directly dependent on the variance differences between and within the score groups.[87]

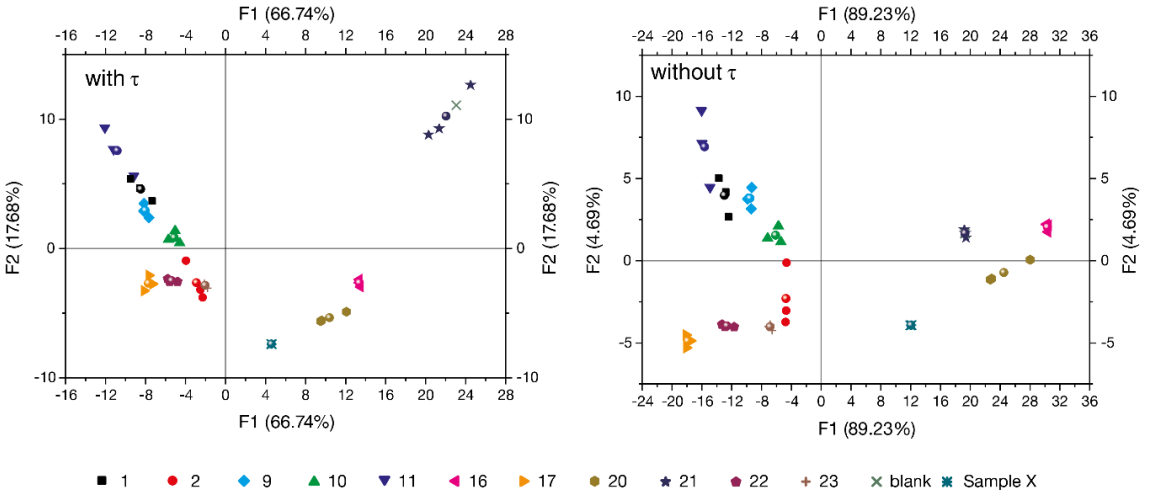

Figure 3.38: Fisherface-type[91, 92] linear discriminant analysis of the compounds discussed in the main text either with (left, 11.11% classification error) or without (right, 5.56 % classification error) the excited-state lifetime taken as input.

Furthermore, in a blind study, an unknown sample (Sample X) from a selection of the drugs (**2**, **21**-**23**) was chosen and correctly identified as **21** through the assay and PCA (Figure 3.33). For this experiment, triple replica of the unknown compound were subjected to the assay as described above and the average values were taken as inputs for the PCA.

Beyond the aforementioned "end-point" detection approach, the time domain can also be used for analyte identification. Exploratory kinetic studies yielded remarkably different reaction profiles even for the structurally similar analytes **1** and **9** (Figure 3.39). The chosen representative analytes display all different kinetic profiles, and thus distinguishable reaction rates. Furthermore, all kinetic profiles have a certain delay time in the beginning in common and an abrupt increase rendering a sigmodal function. This finding is in agreement with the currently investigated cooperative supramolecular growth mechanism of these types of Pt(II)-complexes in aqueous medium.[39, 93] First seeds are

formed reacting at a critical concentration as initiators for the supramolecular polymerization.

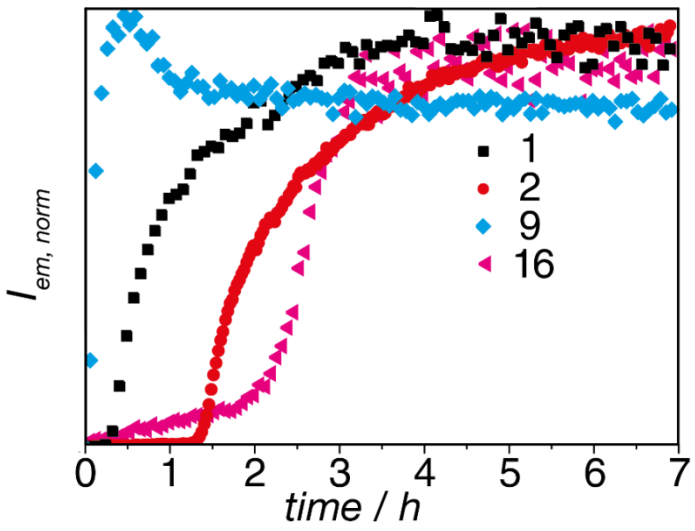

Figure 3.39: Kinetic study for reaction of L-Pt-DMSO with **1** (pyridine), **2** (L-nicotine), **9** (3,5-lutidine) and **16** (imidazole) under the assay conditions.

L-Pt-DMSO as reactive luminescent tag for aza-heterocycles

Emissive labels for the medically relevant imidazole- and triazole-type drugs are rare; the presented Pt-labels may close this gap. Importantly, Pt-complexes of the biologically omnipresent amino acid histidine (**38**) and its derived neurotransmitter histamine (**20**) are only weakly emitting compared to that of the labelled imidazole/triazole-type drugs (**21 - 23**) and additionally show significantly different excitation and emission spectra (Table 3.3 & Figure 3.30). Besides, engineered proteins in which phenyl alanine is replaced by its non-canonical analogue pyridyl alanine (**24**) could be selectively labelled by L-Pt-DMSO for molecular tracking applications.[94]

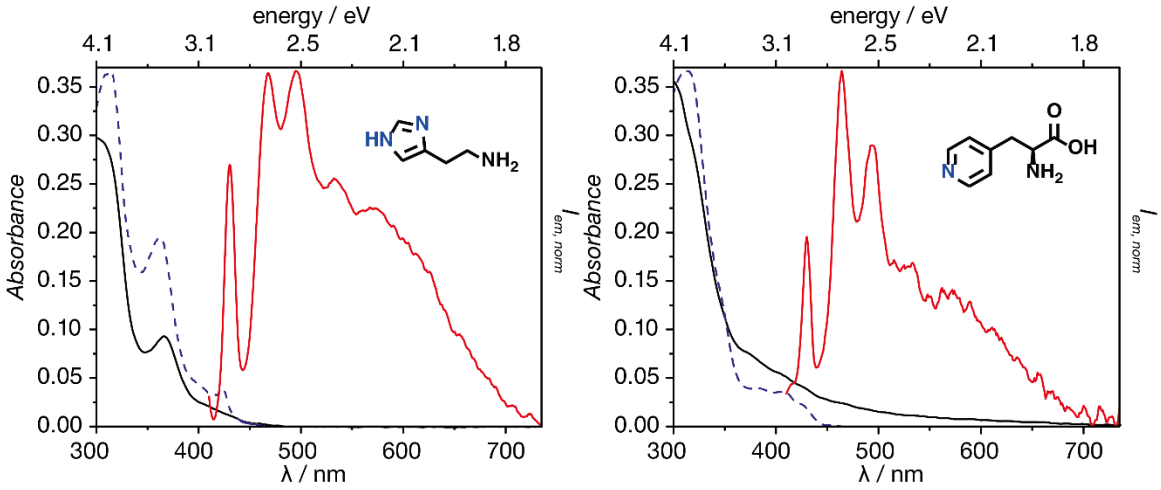

Figure 3.40: Absorption (black, solid), normalized emission (red, solid, λ_{ex} = 375 nm) and excitation (blue, dashed, $\lambda_{em} = \lambda_{em,max}$) spectra of the **20** (left) and **24** (right) after the assay at ambient conditions.

Notably, the Pt-complex labelled products are photostable[48] and kinetically inert, as was confirmed for L-Pt-**11** and L-Pt-**13** in the presence of competitive ligands (*vide supra*). Finally, the Pt(II)-phosphors possess large Stokes shifts (Table 3.3), which is also favorable for imaging applications.[9]

Time-resolved emission spectroscopy as applied for the deconvolution of the emission spectra of two analytes reacted in the assay (*vide supra*) is also valuable for the monitoring of Pt(II)-analyte complexes in autofluorescent matrices, such as blood serum (Figure 3.41).

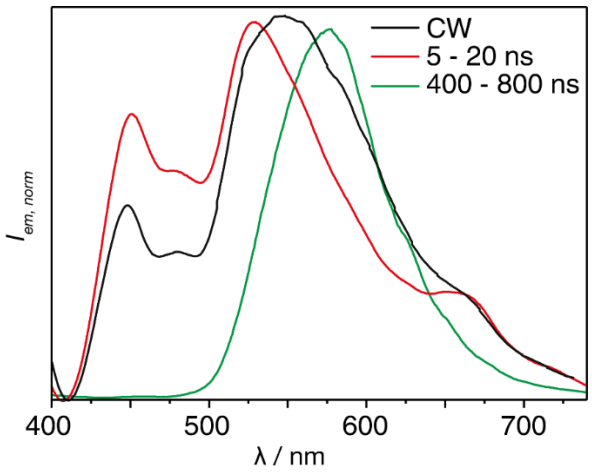

Figure 3.41: Time-resolved emission spectra (TRES) of the preformed L-Pt-**1** complex in Bovine Serum Albumin at 25°C. λ_{ex}=375 nm, f_{pulse}=150 kHz. First time gate was set to 5 - 20 ns (red line), second time gate to 400 - 800 ns (green line) leading to the deconvolution of the overlapping emission spectra at continuous excitation (CW).

Bovine Serum was tested as substrate for the assay and as blood analogue to probe a trackability of the labeled analytes. The protein Bovine serum albumin (BSA) is known to provide several reactive sides enabling this protein on one hand for applications in differential sensing.[7] On the other hand, these reactive sides are most likely responsible for the deactivation of L-Pt-DMSO preventing a successful assay in blood. The strong background signal of autofluorescent amino acids, predominantly tryptophan, is a common problem in bioimaging. The utilized Bovine Serum possesses such a strong fluorescent background signal. Typically, fluorescent excited states exhibit a short lifetime around 1-10 ns, whereas the phosphorescent Pt-labeled aza-heterocycles show excited-state lifetimes of hundreds of nanoseconds (see Table 3.3). With gated emission detection, the convoluted spectra of L-Pt-**1** (pre-reacted in a separate assay and then injected into the blood sample) and the background signal (black curve, Figure 3.41) can be deconvoluted into each separate emission profile (red – blood, green – L-Pt-**1**, Figure 3.41). Studies that exploit the herein presented phosphorescent Pt(II)-tags for spatiotemporal-resolved imaging are currently underway.

Conclusion

In conclusion, in this chapter a novel, highly reactive platinum precursor is presented that enables facile labelling of aza-heterocyclic compounds (*e.g.*, pyridines, imidazoles)

in aqueous media through the formation of highly emissive Pt(II)-complex aggregates. The labeled analytes are also detectable when a strongly autofluorescent background signal is present enabling tracking in biological relevant media such as blood. The resultant mostly hydrophobic Pt(II)-complexes are stabilized by the micelle forming block copolymer P123 allowing for reproducible photophysical analysis over a long time span. An assay was established that renders analyte identification by means of the photophysical fingerprints of their labelled complexes. The developed method exhibits stability towards competing substitution reactions and is performable in urine. Moreover, the concentration calibration is linear down to 5 μM enabling the facile detection of toxins and drugs. Differentiation can be achieved either by visual inspection of the obtained datasets or by multivariate analyses such as PCA and LDA.

The remarkable differential sensitivity towards even structurally similar analytes can be summarized as follows: *i*) A first selectivity criterion is established by the exclusive responsiveness of the Pt-DMSO probe towards sterically unhindered, deprotonated heterocyclic ligands that can coordinate on the Pt(II)-metal center by substitution for the labile DMSO ligand. *ii*) The emission-based assay is selective for those Pt(II)-analyte complexes that self-aggregate in aqueous media, because only those show a marked, mostly red-shifted emission. The tendency for self-assembly depends on the steric properties of the analytes and the interplay with the surfactant. *iii*) Different Pt-analyte complexes that aggregate show readily distinguishable spectroscopic features (*e.g.* emission color) because the photophysics of the assemblies is highly dependent on the Pt-Pt distance between adjacent complexes and the stereoelectronics of the coordinated analyte.

This study provides a showcase for the superior analyte discrimination capabilities of a combined reactive-probe and supramolecular assay. The simplicity of the method relies on the unique spectroscopic properties that each analyte induces.

This work was developed in collaboration with Frank Biedermann from the Karlsruhe Institute of Technology (KIT), who is kindly acknowledged.

Experimental part

Synthesis of L-Pt-DMSO

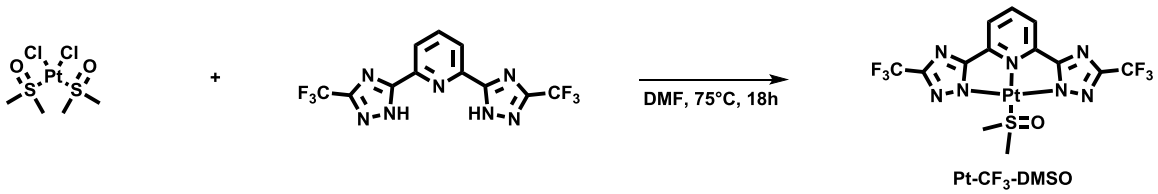

$PtCl_2(DMSO)_2$ (419 mg, 0.99 mmol) and **L-2H** (213 mg, 0.99 mmol) were dissolved in DMF and heated to 75 °C in a round bottom equipped with a reflux condenser overnight. The reaction mixture was allowed to cool to room temperature and the volatiles removed *in vacuo*. The crude product was subsequently distributed in DCM, sonicated and afterwards centrifuged. The supernatant was taken off the solid and this procedure was repeated once with DCM and another time with MeOH to obtain a pure red solid (390 mg, 0.629 mmol, 64 %). ^{1}H NMR (400 MHz, MeOD, ppm) δ 8.26 (s, 1H), 7.89 (d, *J* = 7.9 Hz, 2H), 2.71 (s, 6H). ^{19}F {^{1}H} NMR (377 MHz, MeOD, ppm) δ -65.66 (s). HR-ESI-MS (positive scan, *m/z*): $[M+Na]^+$ calcd. 643.0071; found 643.0034.

Synthesis of L-Pt-1

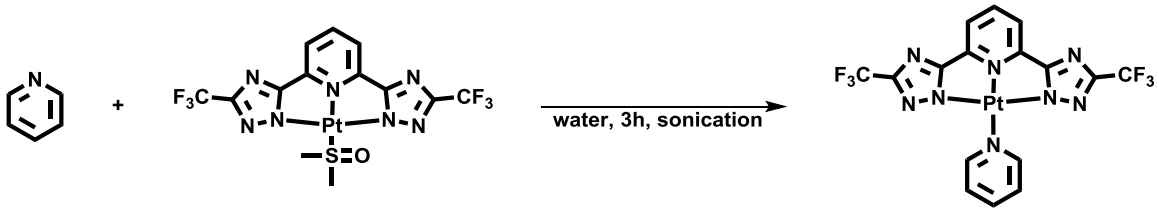

100 μL of a L-Pt-DMSO solution in DMSO (10mM) was dropped into 300 μL of a solution of pyridine (**1**) in PBS (pH=7.4, 10 mM) and sonicated for 3 h. Subsequently, the crude product was centrifuged and the supernatant removed. This procedure was three times repeated with Water, one time with ethanol and once with $CHCl_3$ yielding the green solid. ^{1}H NMR (400 MHz, THF-d_8, ppm) δ = 9.72 (d, *J*=5.8, 2H), 8.24 (q, *J*=8.2, 2H), 7.89 (d, *J*=7.8, 2H), 7.76 (t, *J*=6.7, 2H). ^{13}C {^{1}H} NMR (101 MHz, THF-d_8, ppm) δ = 154.7, 150.0, 145.0, 141.3, 127.7, 119.5. ^{19}F {^{1}H} NMR (377 MHz, THF, ppm) δ = -65.61 (s). HR-ESI-ToF-MS (positive scan, *m/z*): $[M+H]^+$ calcd. 622.0491; found 622.0481.

References

1. M. Schäferling, *Angew. Chem. Int. Ed.*, 2012, **51**, 3532-3554.
2. A. P. de Silva, H. Q. N. Gunaratne, T. Gunnlaugsson, A. J. M. Huxley, C. P. McCoy, J. T. Rademacher and T. E. Rice, *Chem. Rev.*, 1997, **97**, 1515-1566.
3. J. F. Callan, A. P. de Silva and D. C. Magri, *Tetrahedron*, 2005, **61**, 8551-8588.
4. R. Parkesh, E. B. Veale and T. Gunnlaugsson, in *Chemosensors*, eds. B. Wang and E. V. Anslyn, John Wiley & Sons, Inc., 1st edn., 2011, pp. 229-252.
5. K. L. Bicker, S. L. Wiskur and J. J. Lavigne, in *Chemosensors*, eds. B. Wang and E. V. Anslyn, John Wiley & Sons, Inc., 1st edn., 2011, pp. 275-295.
6. V. W.-W. Yam and K. K.-W. Lo, *Coord. Chem. Rev.*, 1999, **184**, 157-240.
7. L. You, D. Zha and E. V. Anslyn, *Chem. Rev.*, 2015, **115**, 7840-7892.
8. Y. Guo, X. Feng, T. Han, S. Wang, Z. Lin, Y. Dong and B. Wang, *J. Am. Chem. Soc.*, 2014, **136**, 15485-15488.
9. J. Wang, H.-B. Liu, Z. Tong and C.-S. Ha, *Coord. Chem. Rev.*, 2015, **303**, 139-184.
10. S. Rochat and T. M. Swager, *Angew. Chem. Int. Ed.*, 2014, **53**, 9792-9796.
11. N. P. Oien, L. T. Nguyen, F. E. Jernigan, M. A. Priestman and D. S. Lawrence, *Angew. Chem. Int. Ed.*, 2014, **53**, 3975-3978.
12. L. Basabe-Desmonts, D. N. Reinhoudt and M. Crego-Calama, *Chem. Soc. Rev.*, 2007, **36**, 993-1017.
13. K. E. Secor and T. E. Glass, *Org. Lett.*, 2004, **6**, 3727-3730.
14. E. Terpetschnig, H. Szmacinski, H. Malak and J. R. Lakowicz, *Biophys. J.*, 1995, **68**, 342-350.
15. V. Balzani and S. Campagna, *Photochemistry and Photophysics of Coordination Compounds I/II*, Topics in Current Chemistry, *280*, 2007.
16. R. Cysewski, L. De Cola, J. M. Fernandez Hernandez, H.-P. Josel, E. Longhi and G. H. M. Vondenhoff (Roche Diagnostics Operations, Inc.), US 2015/0148536 A1, 2015.
17. F. Weber and G. Sedelmeier, *Nachr. Chem.*, 2014, **62**, 997-997.
18. C. Elosua, C. Bariain, I. R. Matias, A. Rodriguez, E. Colacio, A. Salinas-Castillo, A. Segura-Carretero and A. Fernandez-Gutiérrez, *Sensors*, 2008, **8**, 847-859.
19. G. R. Deviprasad and F. D'Souza, *Chem. Commun.*, 2000, 1915-1916.
20. M. Kruppa, C. Mandl, S. Miltschitzky and B. König, *J. Am. Chem. Soc.*, 2005, **127**, 3362-3365.
21. J.-T. Hou, K. Li, K.-K. Yu, M.-Y. Wu and X.-Q. Yu, *Org. Biomol. Chem.*, 2013, **11**, 717-720.
22. U. R. G, H. Agarwalla, N. Taye, S. Ghorai, S. Chattopadhyay and A. Das, *Chem. Commun.*, 2014, **50**, 9899-9902.
23. Z. Huang, J. Du, J. Zhang, X.-Q. Yu and L. Pu, *Chem. Commun.*, 2012, **48**, 3412-3414.
24. T. Chen, L. Yin, C. Huang, Y. Qin, W. Zhu, Y. Xu and X. Qian, *Biosens. Bioelectron.*, 2015, **66**, 259-265.
25. M. Kruppa and B. König, *Chem. Rev.*, 2006, **106**, 3520-3560.
26. L. Fabbrizzi, G. Francese, M. Licchelli, A. Perotti and A. Taglietti, *Chem. Commun.*, 1997, 581-582.
27. Y. Zhang, R. Yang, F. Liu and K. Li, *Anal Chem*, 2004, **76**, 7336-7345.
28. B. Gruber, S. Balk, S. Stadlbauer and B. König, *Angew. Chem. Int. Ed.*, 2012, **51**, 10060-10063.
29. B. Wang and E. V. Anslyn, *Chemosensors: Principles, Strategies, and Applications*, Wiley, 2011.
30. A. Satrijo and T. M. Swager, *J. Am. Chem. Soc.*, 2007, **129**, 16020-16028.
31. M. Albrecht, *Chem. Rev.*, 2010, **110**, 576-623.
32. J. A. G. Williams, in *Top Curr Chem*, eds. V. Balzani and S. Campagna, Springer, Heidelberg, 1st edn., 2007, vol. 281, pp. 205-268.

33. K. Venkatesan, P. H. J. Kouwer, S. Yagi, P. Muller and T. M. Swager, *J. Mater. Chem.*, 2008, **18**, 400-407.
34. Y. Zhang, J. Clavadetscher, M. Bachmann, O. Blacque and K. Venkatesan, *Inorg. Chem.*, 2014, **53**, 756-771.
35. M. Mauro, A. Aliprandi, D. Septiadi, N. S. Kehr and L. De Cola, *Chem. Soc. Rev.*, 2014, **43**, 4144-4166.
36. C. A. Strassert, C. H. Chien, M. D. Galvez Lopez, D. Kourkoulos, D. Hertel, K. Meerholz and L. De Cola, *Angew. Chem. Int. Ed.*, 2011, **50**, 946-950.
37. V. M. Miskowski and V. H. Houlding, *Inorg. Chem.*, 1989, **28**, 1529-1533.
38. S. Sinn, F. Biedermann, M. Vishe, A. Aliprandi, C. Besnard, J. Lacour and L. De Cola, *ChemPhysChem*, 2016, **17**, 1829-1834.
39. A. Aliprandi, M. Mauro and L. De Cola, *Nat Chem*, 2016, **8**, 10-15.
40. M. Mauro, A. Aliprandi, C. Cebrian, D. Wang, C. Kübel and L. De Cola, *Chem. Commun.*, 2014, **50**, 7269-7272.
41. P.-K. Chow, G. Cheng, G. S. M. Tong, W.-P. To, W.-L. Kwong, K.-H. Low, C.-C. Kwok, C. Ma and C.-M. Che, *Angew. Chem.*, 2015, **127**, 2112-2117.
42. B. Ma, J. Li, P. I. Djurovich, M. Yousufuddin, R. Bau and M. E. Thompson, *J. Am. Chem. Soc.*, 2005, **127**, 28-29.
43. V. W.-W. Yam, K. M.-C. Wong and N. Zhu, *J. Am. Chem. Soc.*, 2002, **124**, 6506-6507.
44. N. K. Allampally, C. A. Strassert and L. De Cola, *Dalton Trans.*, 2012, **41**, 13132-13137.
45. A. Galstyan, A. R. Naziruddin, C. Cebrián, A. Iordache, C. G. Daniliuc, L. De Cola and C. A. Strassert, *Eur. J. Inorg. Chem.*, 2015, **2015**, 5822-5831.
46. H. H. Perkampus, *UV-VIS Spectroscopy and Its Applications*, Springer Science & Business Media, Heidelberg, 1st edn., 2013.
47. D. Kim and J. L. Bredas, *J. Am. Chem. Soc.*, 2009, **131**, 11371-11380.
48. D. Septiadi, A. Aliprandi, M. Mauro and L. De Cola, *RSC Advances*, 2014, **4**, 25709-25718.
49. A. V. Kabanov, E. V. Batrakova and V. Y. Alakhov, *J. Control. Release*, 2002, **82**, 189-212.
50. E. Fuguet, C. Ràfols, M. Rosés and E. Bosch, *Anal. Chim. Acta*, 2005, **548**, 95-100.
51. A. Techen, C. Hille, C. Dosche and M. U. Kumke, *J. Colloid Interface Sci.*, 2012, **377**, 251-261.
52. Z. Liu, D. Liu, L. Wang, J. Zhang and N. Zhang, *Int J Mol Sci*, 2011, **12**, 1684-1696.
53. Z. Wei, J. Hao, S. Yuan, Y. Li, W. Juan, X. Sha and X. Fang, *Int. J. Pharm.*, 2009, **376**, 176-185.
54. W. Ritter, *American Journal of Obstetrics and Gynecology*, 1985, **152**, 945-947.
55. F. G. Latimer, C. M. H. Colitz, N. B. Campbell and M. G. Papich, *American journal of veterinary research*, 2001, **62**, 1606-1611.
56. J. M. Cardot, C. Chaumont, C. Dubray, D. Costantini and J. M. Aiache, *British journal of clinical pharmacology*, 2004, **58**, 345-351.
57. T. P. Moyer, J. R. Charlson, R. J. Enger, L. C. Dale, J. O. Ebbert, D. R. Schroeder and R. D. Hurt, *Clin. Chem.*, 2002, **48**, 1460-1471.
58. M. S. T. Gonçalves, *Chem. Rev.*, 2009, **109**, 190-212.
59. P. Held, *Nature Methods*, 2006.
60. Y. Cheng, X. Yang and B. Wang, in *Chemosensors*, eds. B. Wang and E. V. Anslyn, John Wiley & Sons, Inc., 1st edn., 2011, pp. 25-40.
61. B. Valeur and M. N. Berberan-Santos, *Molecular Fluorescence: Principles and Applications*, John Wiley & Sons, Inc., 2nd edn., 2012.
62. C. Adamo and V. Barone, *J. Chem. Phys.*, 1999, **110**, 6158-6170.
63. J. P. Perdew, K. Burke and M. Ernzerhof, *Phys. Rev. Lett.*, 1997, **78**, 1396-1396.
64. J. P. Perdew, K. Burke and M. Ernzerhof, *Phys. Rev. Lett.*, 1996, **77**, 3865-3868.
65. M. M. Francl, W. J. Pietro, W. J. Hehre, J. S. Binkley, M. S. Gordon, D. J. DeFrees and J. A. Pople, *J. Chem. Phys.*, 1982, **77**, 3654-3665.
66. M. Dolg, U. Wedig, H. Stoll and H. Preuss, *J. Chem. Phys.*, 1987, **86**, 866-872.

67. D. Andrae, U. Häußermann, M. Dolg, H. Stoll and H. Preuß, *Theoret. Chim. Acta*, 1990, **77**, 123-141.
68. M. J. Frisch, G. W. Trucks, H. B. Schlegel, G. E. Scuseria, M. A. Robb, J. R. Cheeseman, G. Scalmani, V. Barone, B. Mennucci, G. A. Petersson, H. Nakatsuji, M. Caricato, X. Li, H. P. Hratchian, A. F. Izmaylov, J. Bloino, G. Zheng, J. L. Sonnenberg, M. Hada, M. Ehara, K. Toyota, R. Fukuda, J. Hasegawa, M. Ishida, T. Nakajima, Y. Honda, O. Kitao, H. Nakai, T. Vreven, J. A. Montgomery Jr., J. E. Peralta, F. Ogliaro, M. J. Bearpark, J. Heyd, E. N. Brothers, K. N. Kudin, V. N. Staroverov, R. Kobayashi, J. Normand, K. Raghavachari, A. P. Rendell, J. C. Burant, S. S. Iyengar, J. Tomasi, M. Cossi, N. Rega, N. J. Millam, M. Klene, J. E. Knox, J. B. Cross, V. Bakken, C. Adamo, J. Jaramillo, R. Gomperts, R. E. Stratmann, O. Yazyev, A. J. Austin, R. Cammi, C. Pomelli, J. W. Ochterski, R. L. Martin, K. Morokuma, V. G. Zakrzewski, G. A. Voth, P. Salvador, J. J. Dannenberg, S. Dapprich, A. D. Daniels, Ö. Farkas, J. B. Foresman, J. V. Ortiz, J. Cioslowski and D. J. Fox, *Journal*, 2009.
69. L. M. Stock, *J. Chem. Educ*, 1972, **49**, 400.
70. M. P. Scannell, G. Prakash and D. E. Falvey, *J. Phys. Chem. A*, 1997, **101**, 4332-4337.
71. J. M. Saveant, *Acc. Chem. Res.*, 1993, **26**, 455-461.
72. P. Muller, *Pure Appl. Chem.*, 1994, **66**, 111.
73. P. J. Walla, *Modern Biophysical Chemistry*, Wiley, 2009.
74. P. Ceroni, Springer Netherlands, 1st edn., 2012.
75. M. Kasha, *Discuss. Faraday Soc.*, 1950, **9**, 14-19.
76. A. Ruiz-Carretero, S. Sinn and L. De Cola, *Unpublished results*.
77. J. Herbich, M. Kijak, A. Zielinska, R. P. Thummel and J. Waluk, *J. Phys. Chem. A*, 2002, **106**, 2158-2163.
78. M. Mydlak, M. Mauro, F. Polo, M. Felicetti, J. Leonhardt, G. Diener, L. De Cola and C. A. Strassert, *Chem. Mater.*, 2011, **23**, 3659-3667.
79. G.-J. Zhao, B. H. Northrop, K.-L. Han and P. J. Stang, *J. Phys. Chem. A*, 2010, **114**, 9007-9013.
80. F. M. Winnik, *Chem. Rev.*, 1993, **93**, 587-614.
81. I. V. Novozhilova, A. V. Volkov and P. Coppens, *J. Am. Chem. Soc.*, 2003, **125**, 1079-1087.
82. Y. Ozawa, M. Terashima, M. Mitsumi, K. Toriumi, N. Yasuda, H. Uekusa and Y. Ohashi, *Chem. Lett.*, 2002, **32**, 62-63.
83. S. F. Rice and H. B. Gray, *J. Am. Chem. Soc.*, 1983, **105**, 4571-4575.
84. J. R. Lakowicz, *Principles of Fluorescence Spectroscopy*, Springer, 3rd edn., 2007.
85. C. L. Hutchinson, J. R. Lakowicz and E. M. Sevick-Muraca, *Biophys. J.*, 1995, **68**, 1574-1582.
86. C. Marquez, H. Fang and W. M. Nau, *IEEE Trans. Nanobiosci.*, 2004, **3**, 39-45.
87. S. Stewart, M. A. Ivy and E. V. Anslyn, *Chem. Soc. Rev.*, 2014, **43**, 70-84.
88. B. Rout, L. Unger, G. Armony, M. A. Iron and D. Margulies, *Angew. Chem. Int. Ed.*, 2012, **51**, 12477-12481.
89. P. Anzenbacher and M. A. Palacios, in *Chemosensors*, eds. B. Wang and E. V. Anslyn, John Wiley & Sons, Inc., 1st edn., 2011, pp. 345-368.
90. A. T. R. Williams, S. A. Winfield and J. N. Miller, *Analyst*, 1983, **108**, 1067-1071.
91. P. N. Belhumeur, J. P. Hespanha and D. J. Kriegman, *IEEE Trans. Pattern Anal. Mach. Intell.*, 1997, **19**, 711-720.
92. A. Sharma and K. K. Paliwal, *International Journal of Machine Learning and Cybernetics*, 2015, **6**, 443-454.
93. M. E. Robinson, D. J. Lunn, A. Nazemi, G. R. Whittell, L. De Cola and I. Manners, *Chem. Commun.*, 2015, **51**, 15921-15924.
94. S. Ziegler, V. Pries, C. Hedberg and H. Waldmann, *Angew. Chem. Int. Ed.*, 2013, **52**, 2744-2792.

Chapter IV

Discrete Polygonal Supramolecular Architectures of Isocytosine-Based Pt(II)-complexes at the Solution/Graphite Interface

Abstract

Polygonal supramolecular architectures of a Pt(II)-complex including trimers, tetramers, pentamers and hexamers were self-assembled on flat surfaces *via* hydrogen bonding between isocytosine moieties; their structure at the solid/liquid interface was unraveled by *in situ* scanning tunneling microscopy imaging. Density functional theory calculations provided in-depth insight into thermodynamics of their formation by exploring the different energy contributions attributed to the molecular self-assembly and adsorption processes.

Introduction

Molecular self-assembly at surfaces is a versatile approach to position functional groups with sub-nanometer precision over several hundreds of μm^2 areas and thereby it allows the fine-tuning of numerous physico-chemical properties of the resulting nanostructures.[1-6] The design of molecules comprising active groups represents a promising route for engineering functional surfaces and interfaces. Among various functional systems, luminescent Pt(II)-complexes have attracted a great interest during the last decade due to their appealing photophysical and redox properties, including strong absorption bands featuring onsets in the visible region as well as room temperature emission accompanied by a large Stokes shift.[7] Neutral Pt(II)-complexes bearing tridentate azolate-based ligands possess extraordinary high phosphorescence quantum yields and a long excited state lifetimes.[8, 9] Furthermore, due to their square-planar geometry such complexes display high propensity to undergo aggregation by means of the solvatophobic effects, π–π and dispersive interactions. These properties can lead to supramolecular assemblies holding attractive features, because closed-shell metal–metal interactions of the Pt(II) centers strongly augment the emission properties.[10-13]

Supramolecular systems, where Pt(II) ions have been directly coordinated to nucleobases are the subject of numerous studies.[14-17] Certain platinum complexes of pyridine, purine and pyrimidine derivatives (Figure 4.1) were found to present promising properties as antitumor drugs and in a variety of biomedical applications.[18-22]

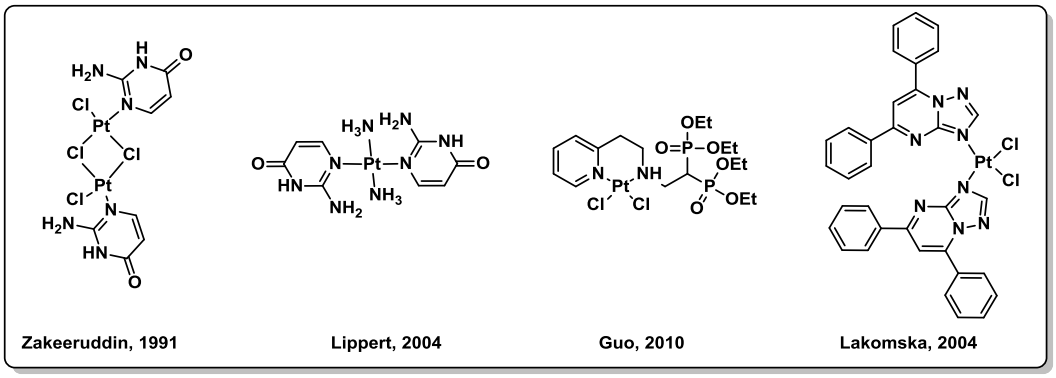

Figure 4.1: Examples for Pt(II)-complexes coordinated with nucleobases[14, 16] and for biomedical applications bearing pyridine[20] and pyrimidine[22, 23] derivatives.

Scanning tunnelling microscopy (STM) is an extremely powerful tool to investigate supramolecular materials featuring atomic resolution. In particular, it is the method of choice for imaging structures and dynamics in molecular self-assembly on surfaces.[24-28] Furthermore a direct insight into the frontier allows for the investigation of structure-property relations and thus the tuning of photophysical properties.[29]

Hydrogen bonding has been extensively used as a directional, non-covalent intermolecular interaction for designing and controlling the formation of complex supramolecular architectures. On solid surfaces, sophisticated structures can result from the formation of various hydrogen bonded patterns, including linear and cyclic motifs with different pairing such as O–H···O, N–H···O and N–H···N.[30-34] Nucleobases have been previously reported to form cyclic quartet and hexameric structures on the surface[34-38] and pentamers in the solution.[39] To the best of my knowledge, the formation of other types of cyclic motifs has not been discussed. On the basis of previous investigations on substituted isocytosine,[38] the effect of bulky Pt(II)-complexes featuring potential application in optotronics was comprehensively studied.

In this chapter, it is demonstrated that in particular isocytosine can be used to steer the 2D assembly of Pt(II)-complexes through hydrogen bonding interactions between nucleobases. The experimental findings are supported by density functional theory (DFT) calculations, enabling the analysis of both the strength of hydrogen bonding and the

interactions with the graphite substrate. Additionally, STM images are simulated in order to get an in-depth understanding of the electronic features of the molecular architectures.

Specifically, the self-assembly of the Pt(II)-complex **L-Pt-Py-iCyt** (Scheme 4.1) into discrete supramolecular architectures held together *via* intermolecular hydrogen bonds between isocytosine moieties at the solid/liquid interface is investigated. It is particularly shown that the formation of polycrystalline structures composed of various polygonal assemblies including trimers, tetramers, pentamers and hexamers is stabilized by distinct hydrogen bond pairing.

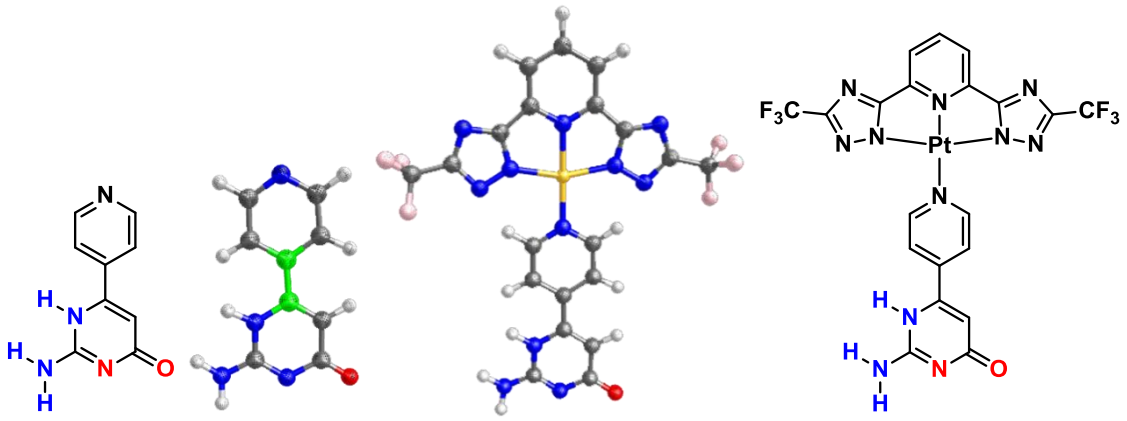

Figure 4.2: Schematic and corresponding 3D representations of the investigated molecules. left: Ligand **Py-iCyt** with highlighted rotatable C-C bond (green) right: Complex **L-Pt-Py-iCyt**. 3D color code: C-grey, H-white, N-blue, O-red, F-rose, Pt-yellow.

Results and discussion

Design and synthesis of the H-bond scaffolds

As known from literature and shown in the previous chapters, the Pt(II)-complexes bearing the N-metalacycling ligand L-2H and a pyridine derivative exhibit a square planar geometry, if bulky substituents at the ancillary ligand are absent. Due to this geometry, these complexes display a high tendency to assemble in z-directional fashion, also known as "stacking".[40] The photophysical consequences of this stacking are comprehensively discussed in the previous chapter. This aggregate formation is most likely driven by π-π, dipole, dispersive interactions (Pt•••Pt) and the hydrophobicity/solvatophobiticy effect.

In order to organize the system in a 2-dimensional fashion *via* hydrogen interactions, isocytosine (**iCyt**) was chosen as a platform bearing H-bond acceptor and donor moieties (*vide supra* for schematic representations of the interactions & Figure 4.4). On account of the arising competition between the supramolecular interactions, z-directional (stacking)

vs. xy-organization (H-bonds), the degree of rotational freedom within the molecule was increased by linking **iCyt** *via* a rotatable C-C bond (Figure 4.2) to the coordinative pyridine at the para position of the sp^2 hybridized nitrogen (**Py-iCyt**). With this arrangement, the strong tendency for stacking is lowered allowing for a more facile organization in a 2-dimensional monolayer on graphene.

In order to obtain the ligand **Py-iCyt**, ethyl 3-oxo-3-(pyridin-4-yl)propanoate was reacted with guanidinium carbonate and hydrochloric acid rendering the ring closure reaction to isocytosinyl.[38, 41, 42] The ligand was subsequently coordinated to the already N-metallacycled precursor L-Pt-DMSO in polar organic solvents yielding the desired Pt(II)-complex **L-Pt-Py-iCyt**.

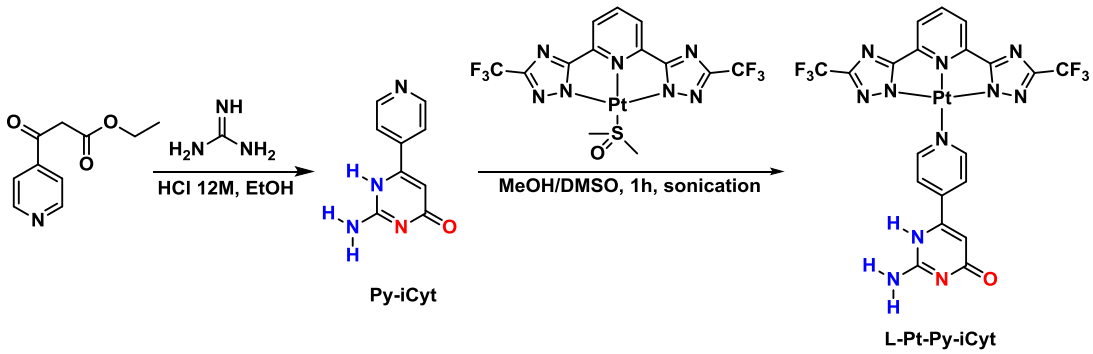

Scheme 4.1: Synthetic route for the synthesis of the molecules **Py-iCyt** and **L-Pt-Py-iCyt** characterized on the solid-liquid interface. Hydrogen-bonding donor and acceptor sites are indicated in blue and red, respectively. **Py-iCyt:** Ethyl 3-oxo-3-(pyridin-4-yl)propanoate, guanidine carbonate, HCl (12M) in EtOH, reflux, 18h, 8%. **L-Pt-Py-iCyt**: Py-iCyt, L-Pt-DMSO in MeOH/DMSO (10:1, *v*,*v*), sonication, 1h, 82%.

Photophysical investigations on L-Pt-Py-iCyt

The photophysical properties of the N-metalacyclic Pt(II)-complex **L-Pt-Py-iCyt** were analyzed in solution and solid state. In a non-polar solvent, *i.e.* THF, in which the compound appears molecularly dissolved, strong absorption bands appear in the UV region (216-300 nm) ascribed to ligand centered transitions (π-π*). The appearance of a weak MLCT band at 415 nm and an absorption onset of 450 nm the UV-Vis absorption spectrum resembles the typical fingerprint of the **L-Pt-Py-**scaffold[13, 43] accompanied by a pronounced band ranging from 335 - 368 nm ascribed to π–π* transitions of the pyridine-isocytosine part. (Figure 4.3 & Table 4.1) At room temperature a weak structured emission (PLQY<1%) peaking at 462 nm with a short excited-state lifetime of 2.3 ns was observed which is ascribed to arise from a ligand-centered state (^{3}LC).

The solid-state (powder) analysis revealed a broad luminescence spectrum centered at 578 nm (Figure 4.3) arising from a metal-metal-to-ligand-charge-transfer state (^{3}MMLCT) with a prolonged excited-state lifetime (Table 4.1). The new lowest excited state emerges from aggregation induced closed-shell Pt•••Pt interactions, which is accompanied by a bathochromically shifted excitation onset of 510 nm.

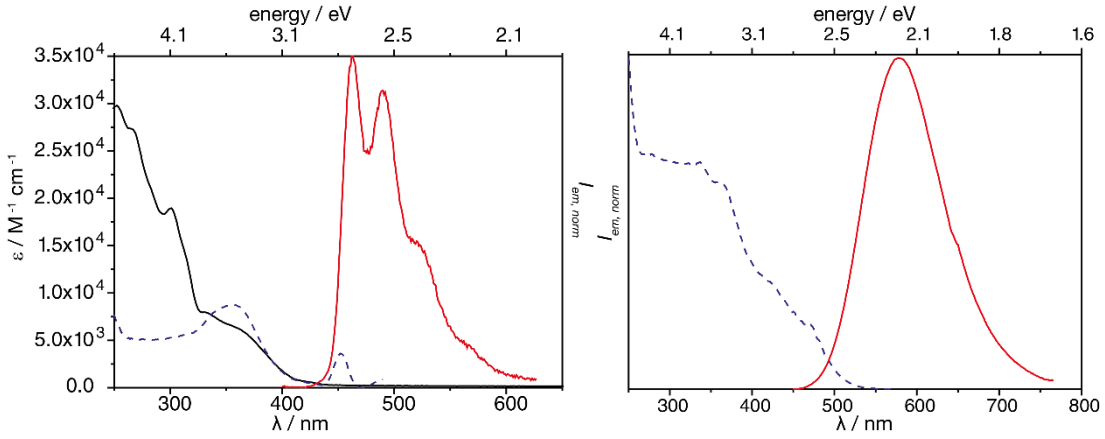

Figure 4.3: left: UV/Vis absorption (solid, black), normalized emission (solid, red, λ_{ex} = 300 nm) and excitation (dashed, blue, λ_{em} = 460 nm) spectra of **L-Pt-Py-iCyt** in aerated THF (10^{-4} M) at ambient conditions. right: Normalized excitation (dashed, blue, λ_{em} = 600 nm) and emission (solid, red, λ_{ex} = 300 nm) spectra of **L-Pt-Py-iCyt**, in solid state (neat film) at ambient conditions.

Unexpectedly, the quantum yield remained very low, which is indicative of a perturbation of the z-directional stacking. The additional rotational axis between the pyridine and the isocytosine moieties as well as the strong intermolecular H-Bond interactions of the latter one may impede the formation of long Pt(II) stacks, namely fibers.[13] This constitution in turn decreases the ridigochromic effect and the shielding from O_2 rendering an efficient quenching of the emissive state.

Another possible explanation is the formation of a strong H-bond network rendering the dissipation of the absorbed light and thus a fast radiationless deactivation of the excited state.

Table 4.1: Summary of the photophysical properties of the complex **L-Pt-Py-iCyt**.

solution				solid state		
λ / nm [a] (ε / $M^{-1}cm^{-1}$)	λ_{em} [a,b] / nm	φ [a,c]	τ / ns [a,d,e]	λ_{em} [b,f] / nm	φ [c,f]	τ / ns [f]
216 (35835), 252 (29758), 267 sh (27243), 300 (18913), 335 (7806), 368 (5714), 415 (785)	462, 489, 517	<1%	2.3	578	<1%	795 (22%), 265 (45%), 46 (33%) [g]

[a] λ_{ex}=300 nm. [b] Average of scanning λ_{ex} = 300 – 400 nm (10 nm interval), [c] λ_{ex} = 375 nm. [d] λ_{em} = 462 nm, [e] λ_{em} = 578 nm

Self-assembly of 4-isoCytosinyl-pyridine (Py-iCyt)

The self-assembly of the ligand **Py-iCyt** was probed at the solid-liquid interface. A drop of a (500 ± 2) μM solution of **Py-iCyt** (Figure 4.4) in 1-phenyloctane was applied to a freshly cleaved graphite surface. The STM characterization revealed that **Py-iCyt** forms a supramolecular ribbon-like motif at the interface between the solution of **Py-iCyt** in 1-phenyloctane and highly oriented pyrolitic graphite (HOPG) (see Figure 4.5).

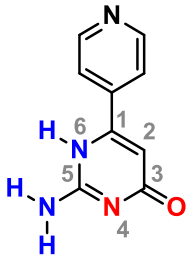

Figure 4.4: Chemical structure of Pyridine-isocytosine (**Py-iCyt**). Hydrogen-bonding donor and acceptor sites are indicated in blue and red, respectively.

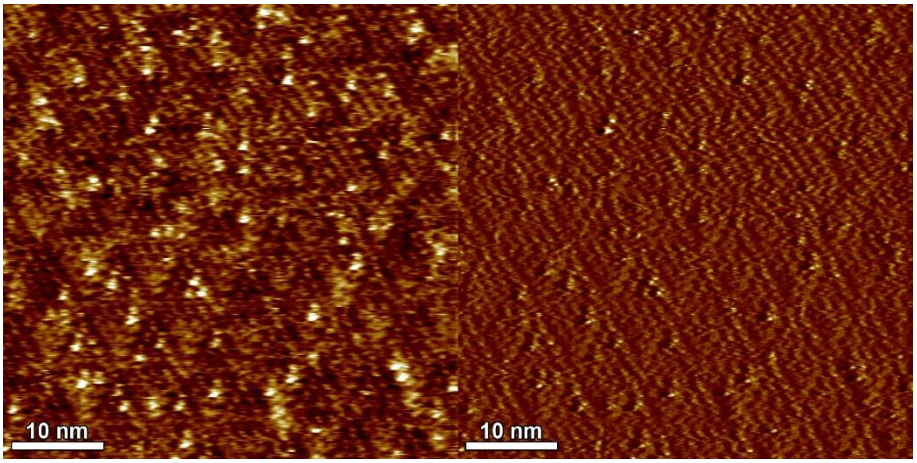

Figure 4.5: Height (a) and current (b) STM image of **Py-iCyt** monolayer at the 1-phenyloctane/HOPG interface. Scanning parameters, average tunneling current (I_t) = 20 pA, tip bias voltage (V_t) = 500 mV.

As shown in Figure 4.6, the network consists of a lamellar pattern that is stable for several hours. The different contrast shown on the STM image of the **Py-iCyt** monolayer is a moiré pattern that is caused by electronic mismatch/interferences of the supramolecular adsorbed lattice and the underlying graphite surface.[44] The pattern reveals 2D polycrystalline structure appearing as a ribbon-like architecture (Figure 4.6). The unit cell parameters are $a = 1.24 \pm 0.1$ nm, $b = 1.68 \pm 0.1$ nm and $\alpha = (60 \pm 2)$ leading to a surface of $A = 1.80 \pm 0.11$ nm^2. The model of the packing within the monolayer is displayed in the Figure 4.6 (center). The structure is stabilized by weak hydrogen bonds occurring between N(4)···H(5) and weak electrostatic interaction formed between O(3), H(5) and H(6) of adjacent molecules (see Figure 4.4 and Figure 4.6 (right)).

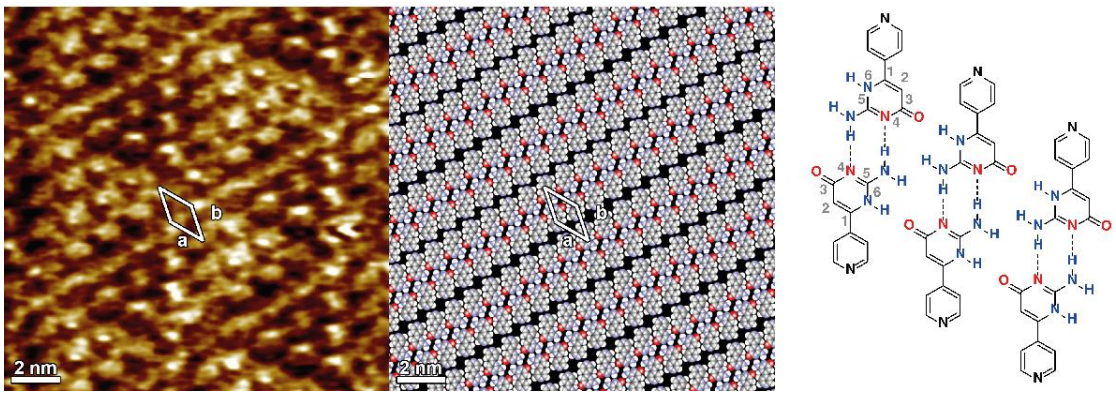

Figure 4.6: left: Zoom-in of STM image showing the structure of **Py-iCyt** self-assembly at the 1-phenyloctane/HOPG interface. Scanning parameters, average tunneling current (I_t) = 20 pA, tip bias voltage (V_t) = 500 mV. center: packing model. right: Schematic representation of the self-assembly motif of **Py-iCyt**.

The observed motif is in a good agreement with previous observations on supramolecular structures of 6-methylisocytosine derivatives,[45, 46] and 6-[4-(octyloxy)phenyl] isocytosine.[38] This finding means that the functionalization of isocytosine with a pyridine unit does not influences its self-assembly behavior at the solid/liquid interface.

Self-assembly of L-Pt-Py-iCyt

The studies were extended to the self-assembly of **L-Pt-Py-iCyt** at surfaces by applying a 4 μL drop of 100 ± 2 μM solution in 1-phenyloctane on a freshly cleaved HOPG substrate. The incorporation of the sterically demanding **L-Pt** moiety (see Figure 4.7) in the scaffold led to a dramatic change in the self-assembly behaviour.

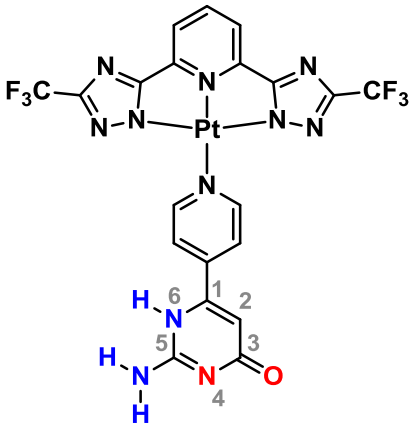

Figure 4.7: Chemical structure of **L-Pt-Py-iCyt**. Hydrogen-bonding donor and acceptor sites are indicated in blue and red, respectively.

The STM image in Figure 4.8 (left) displays discrete supramolecular cyclic architectures. All these cyclic assemblies have been identified, and are portrayed in Figure 4.8 (center): trimers (**iC3**, white), tetramers (**iC4**, blue), pentamers (**iC5**, green), half of hexamer (**½iC6**, red) and hexamers (**iC6**, yellow).

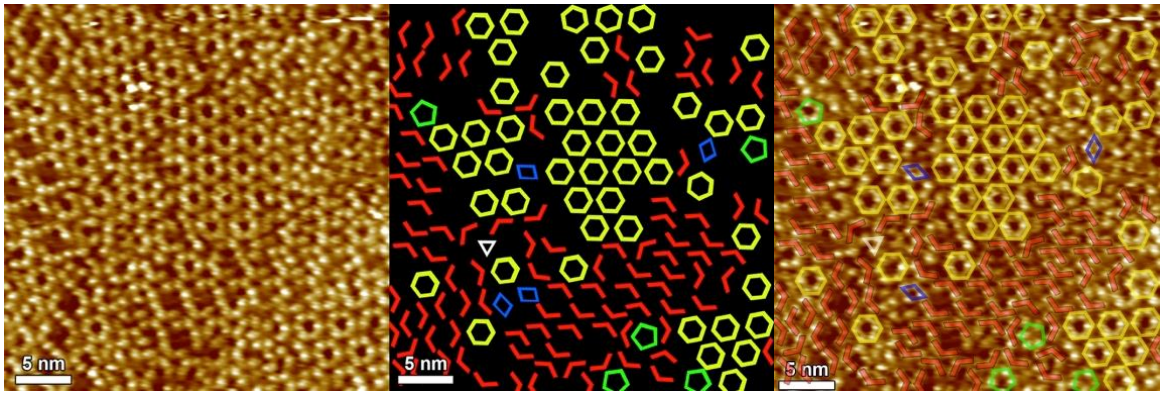

Figure 4.8: left: Height STM image of **L-Pt-Py-iCyt** at solution/HOPG interface. Scanning tunneling parameters: Average tunneling current (It)=25 pA, Tip bias voltage (Vt)=-450 mV. center: Model of different self-assembled molecular motifs. right: merged picture; overlay of models and experimental STM image.

Statistical analysis on these experimentally observed cyclic arrangements was performed on ten independent STM experiments, also by exploring different regions of the samples. Figure 4.9 summarizes the occurrence of each self-assembled discrete motif, which has been monitored and identified. Such an analysis revealed that two supramolecular species dominate, *i.e.* **½iC6** (45%) and **iC6** (35%), suggesting that they are both energetically favoured over the others cyclic motifs, *i.e.* **iC5**, **iC4** and **iC3** assemblies. The analysis of the number of monomers involved in various motifs further

supports this finding. Figure 4.9 shows that > 80% of the adsorbed molecules are involved in the formation of either **iC6** (50%) or **½iC6** (32%) structures.

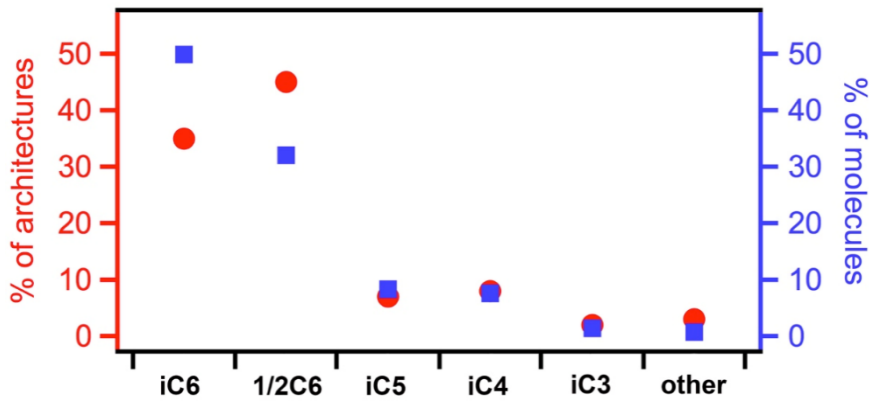

Figure 4.9: The percentage of the different molecular motifs identified on HOPG surface as well as percentage of molecules involved in formation of a given pattern.

The stability of the different supramolecular assemblies and their corresponding electronic structure was computed at the density functional theory (DFT) level of theory with the standard implementation in the CP2K package (for details see Computational details section).

The STM images of ordered molecular motifs (**iC6**, **iC5**, **iC4**, **iC3** and **½iC6**) were simulated and the results are presented in Figure 4.10 and Figure 4.14 (bottom panel). A good agreement is found between the experimental and simulated STM images when the complex is packed onto the graphite in **iC6**, **iC5**, **iC4**, **iC3** and **½iC6** (Figure 4.10). Since the orbitals of major contribution for STM scans are located predominately on (*vide infra*) the L-Pt framework, the STM images show hollow 2D structures in which the bright outer rim is defined by the bulky head group (**L**) and the dark core consists of the hydrogen network formed by isocytosine entities.

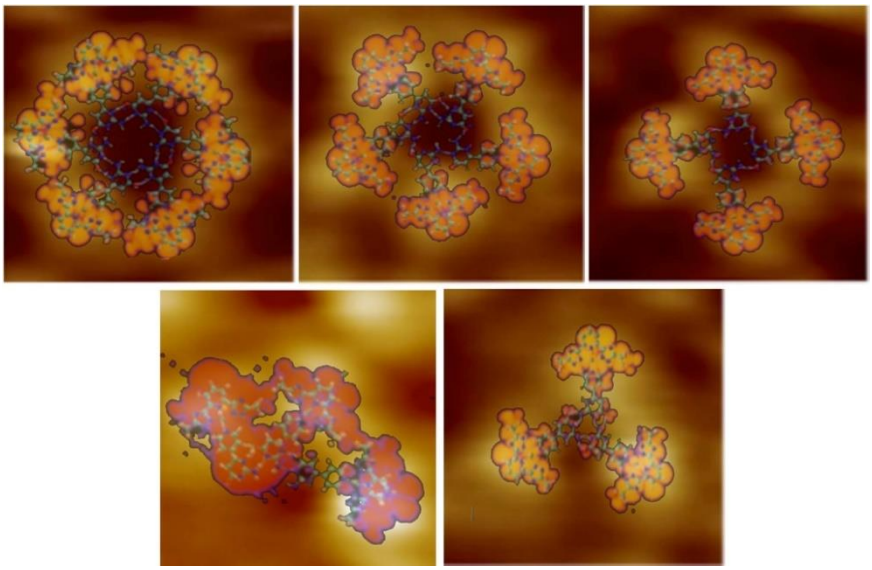

Figure 4.10: Simulated models overlapping the molecular motifs on the STM images. These models fit well the observed motifs.

All molecular motifs are randomly co-existing on HOPG surface. **iC6** and **½iC6**, which are formed respectively by six and three **L-Pt-Py-iCyt**, are stabilized by hydrogen bonding motif of type O(3)···H–N(6) and N(4)···H–N(5), formed between isocytosine groups (Figure 4.7). The H-bond network is exemplified for the case of **iC6** in a schematic representation in Figure 4.11. The self-assembly of the molecular architecture **iC3**, **iC4** and **iC5** can be explained by the formation of hydrogen interaction of O(3)···H–N(6) occurring between the isocytosine groups of adjacent molecules. The fact, that in average two hydrogen bonds per molecule are present displays the thermodynamic stabilization of the self-assemblies **iC6** and **½iC6** over **iC3**, **iC4** and **iC5** for which only one hydrogen bonding per molecule is occurring. The different intermolecular interactions of the polygonal discrete architectures are explicitly illustrated in Figure 4.16.

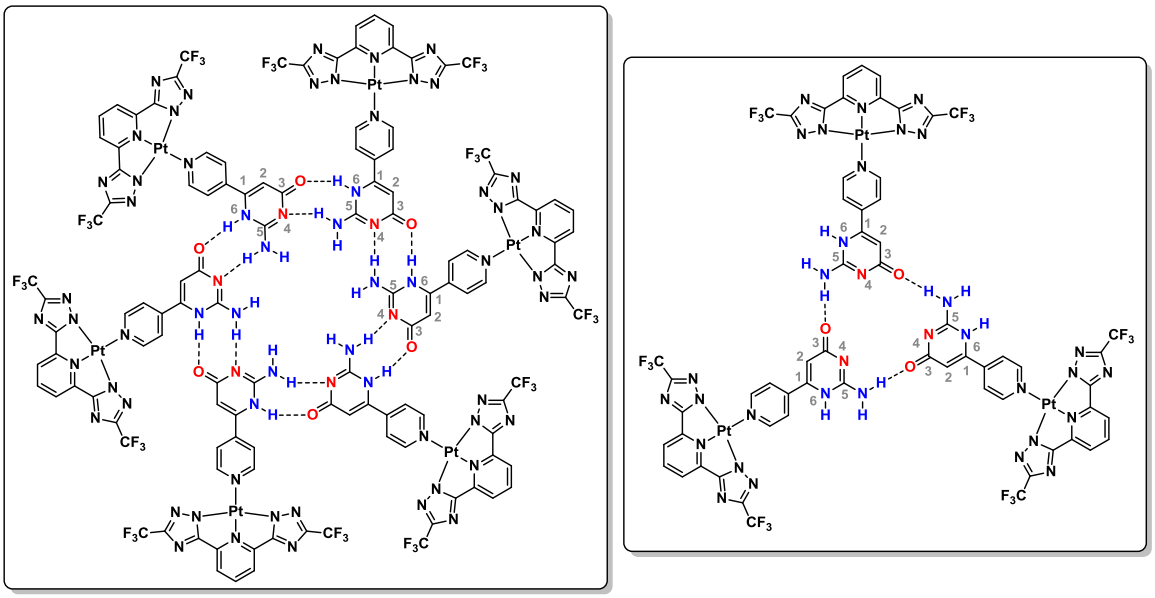

Figure 4.11: Schematic representation of the hydrogen bond network present for **iC6** (left) and **½iC6** as well as present for the self-assemblies of **iC3** (right), **iC4** and **iC5**.

The relevant electronic structural features of the molecular building block (**Pt-Py-iCyt)** are illustrated in Figure 4.12. The 3D representations show the HOMO-1, HOMO and LUMO orbitals of the complex. The gap between the HOMO and HOMO-1 states was computed to be 45 meV. The LUMO level of **L-Pt-Py-iCyt** is spread over the molecular skeleton whereas the HOMO-1 is located only on the fluorinated part (**L-Pt**).

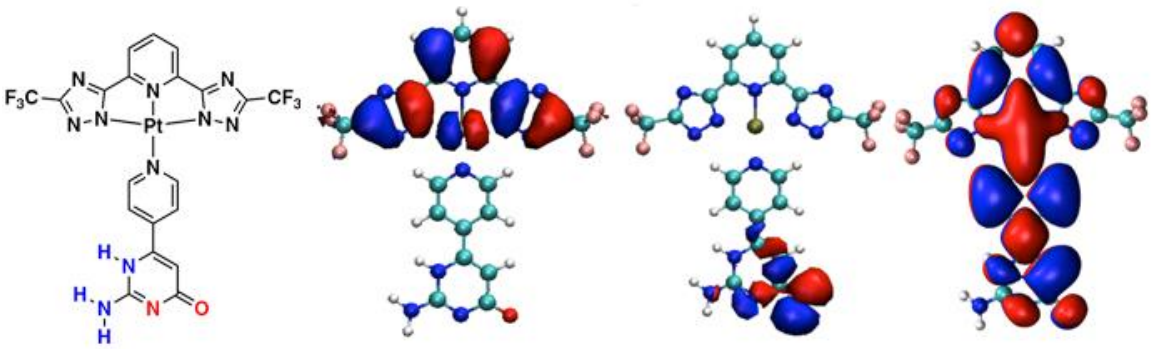

Figure 4.12: far-left: Schematic representation of complex **L-Pt-Py-iCyt**. Ground-state optimized superimposed with particular orbitals. From left to far-right: HOMO-1, HOMO and LUMO orbitals of the iC molecule. The gap between the HOMO and HOMO-1 states was computed to be 45 meV.

The HOMO orbital distributions of the different suggested molecular motifs as well as the ligand ribbons are shown in Figure 4.13. The rather high localization degree of the HOMO orbitals in the different motifs can be understood as follows: Pt has two free

electrons, one in the d-level ($5d^9$) and one free electron in the s-level ($6s^1$). The computed ground-state configuration is of singlet character. Orbital localization is achieved by a hybridization of the *d* free electron of the Pt with the π orbitals generated by the ligand (four nitrogen atoms). Also, the four nitrogen atoms generate an effective crystal field splitting on the Pt and therefore the *d* levels jump to the upper part of the electronic structure and not the *s* levels.

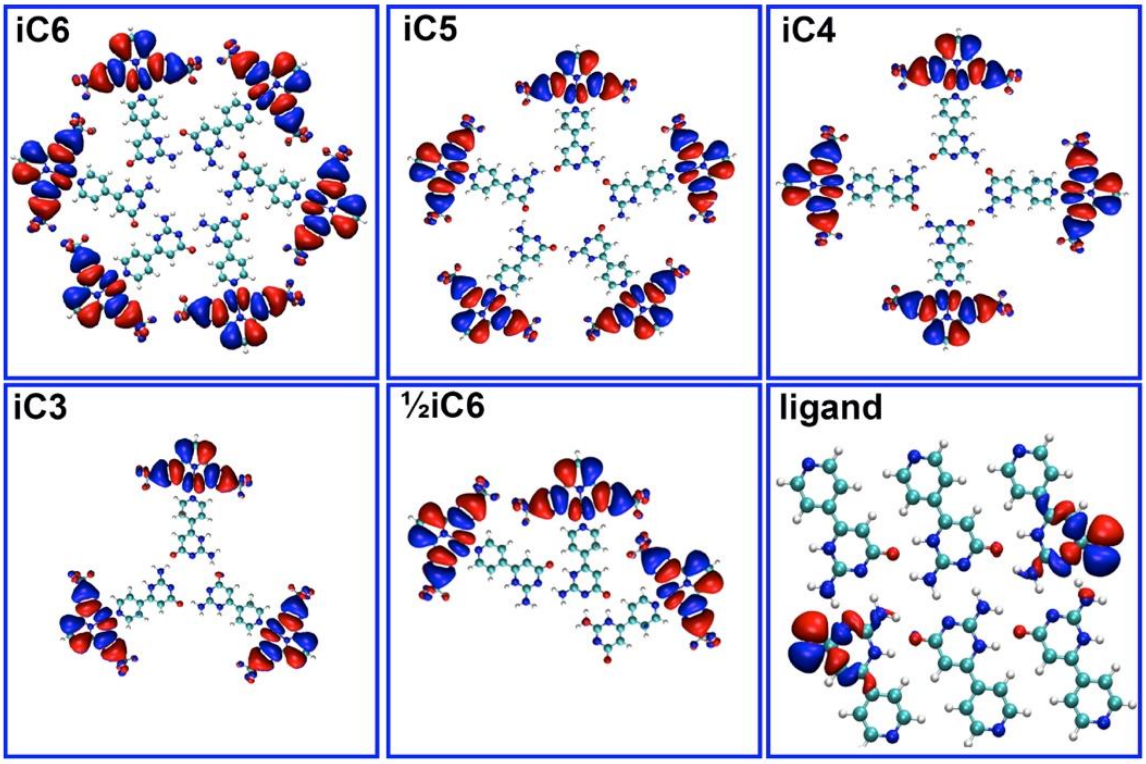

Figure 4.13: Spatial distribution of the HOMO orbitals of different suggested molecular motifs of **L-Pt-Py-iCyt** and a simulation of the ribbon of the ligand **Py-iCyt (**bottom right**)**.

The interpretation of the molecular motifs monitored experimentally by STM is fully consistent with the STM simulations. **iC6** was generated through the formation of hydrogen bonds between isocytosine groups leading to a circular motif (Figure 4.14). The observed contrast of different motifs – for example a dark center and bright contour of **iC6** (Figure 4.14 left) – is due to the HOMO levels of the assembled complexes. For this reason, the STM images are recorded with a negative voltage (scanning the occupied states), each individual **L-Pt-Py-iCyt** complex appears as bright isolated protrusion in different molecular motifs. Three, four, five and six molecules are self-assembled to form respectively **½iC6** or **iC3**, **iC4**, **iC5** and **iC6**.

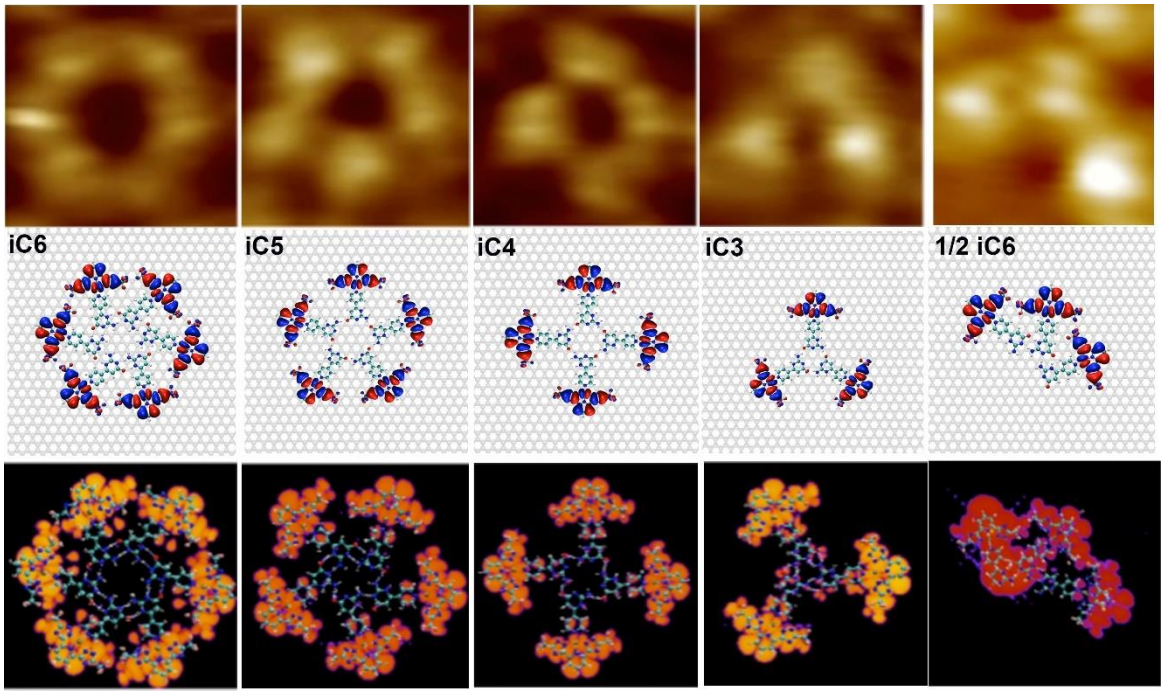

Figure 4.14: top panel: STM images of different **L-Pt-Py-iCyt** motifs. middle panel: simulated structures on graphene. bottom panel: simulated STM images of different motifs.

In order to investigate the mechanical stability of the different motifs, the dissociation energy for each suggested molecular motif was calculated and all are depicted in the middle panel of Figure 4.15. The dissociation energy was defined as follows:

$$E_{diss} = E_N - E_{N-1} - E_{SM} \qquad \text{Eq. 4.1}$$

where *N* denotes the number of molecular units within a given motif, E_N and E_{N-1} are the total energies of a given molecular motif containing N and N-1 molecular units (monomers), respectively, and E_{SM} is the energy of a single isolated monomer. The energy E_{N-1} is computed by first removing a monomer from the motif and subsequently performing a structural relaxation of the system.

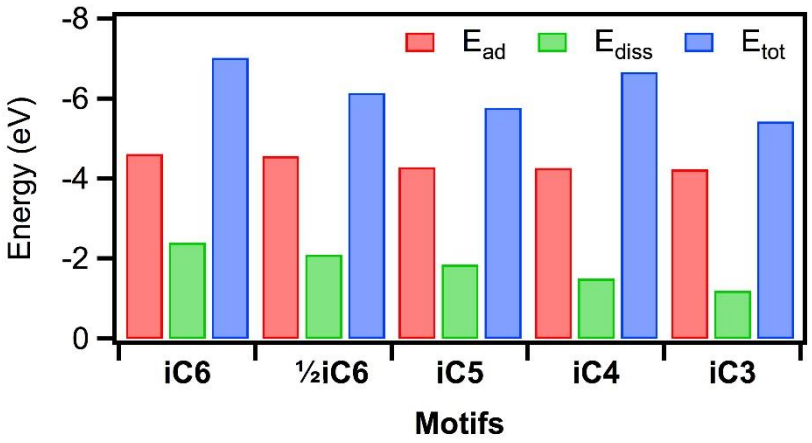

Figure 4.15: Calculated adsorption (E_{ad}, red), dissociation (E_{diss}, green) and the total (E_{tot} = E_{ad} + E_{diss}, blue) energies of the different molecular motifs self-assembled by **L-Pt-Py-iCyt** complex.

Figure 4.15 shows the computed dissociation energies of the molecular motifs. The number of hydrogen bonds, their nature and the degree of molecular packing play a crucial role for the dissociation energy of the molecular motifs. The highest dissociation energies were observed for **iC6** and **½iC6** motifs, both formed through O(3)···H–N(6) and N(4)···H–N(5) hydrogen bonding. Lower E_{diss} was monitored for **iC3-iC5** structures, which are stabilized *via* weaker type of H-bonding, *i.e.* O(3)···H–N(6). The reduction of the total number of H-bonds in the motifs leads to a thermodynamic and kinetic destabilization from **iC5** to **iC3**, which is reflected in the slight decrease of the dissociation energy.

Re-arrangement energies

No structural rearrangement of the motif can take place – such as the transition from the conformation of **iC6** to **iC5** – when only the calculation of the dissociation energies of single supramolecular motifs is considered. The reason for this observation is that structural rearrangement usually occurs through energetic barriers that cannot be overcome by a zero-temperature conjugate gradient relaxation algorithm. Thus, an additional quantity was defined, the rearrangement energy E_{rearr}, given by the relation:

$$E_{rearr} = E_N - E'_{N-1} - E_{SM} \qquad \text{Eq. 4.2}$$

In this expression, E_N refers to the total energy of a motif containing N monomers, while the quantity E'_{N-1} is the total energy of a motif with one monomer less, but also with a different spatial symmetry (compare *e.g.* **iC5** and **iC6** in Figure 4.17) differing by one in the number of molecular units. In this sense, E_{rearr} is a measure of the energy required to reorganize the molecular network, while E_{diss} considers the energy necessary to remove a single monomer without involving a collective rearrangement of the motif, *i.e.* a change of symmetry.

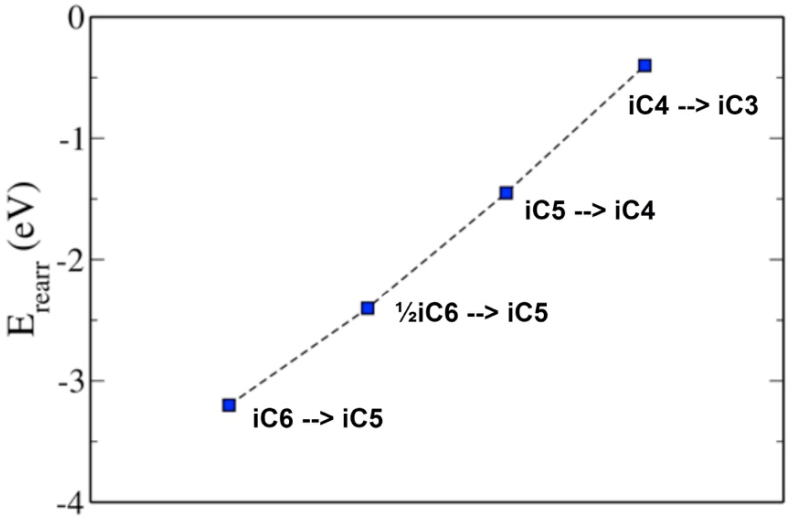

Figure 4.16: Re-arrangement energy of different molecular motifs formed by the Pt(II)-complex. The structures are ranged from **iC6** to **iC3**.

The energy presented in the Figure 4.16 shows the energy consumption of the molecular motifs from **iC6** to **iC3**. In particular, rather large energy of transformation from **iC6** to **iC5** was found on account of the breaking of four H-bonds and rearrangement of the other eight H-bonds. Due to the open structure of **½iC6**, the transformation to **iC5** needs lower energy compared to the close structure of **iC6**. As expected, a rearrangement from one self-assembly to another that possesses the same H-bonding situation such as **iC5→iC4**, **iC4→iC3** (one H-bonds/molecule → one H-bonds/molecule) need less energy than the rearrangement towards a different H-bond situation, namely **iC6→iC5**, **½iC6→iC5** (two H-bonds/molecule → one H-bonds/molecule).

The optimized structures of the different supramolecular motifs on the graphene surface are shown in the Figure 4.14(middle panel). The adsorption energies E_{ad} of these

structures are reported in Figure 4.15. Rather weak yet comparable interaction energies of **L-Pt-Py-iCyt** with the graphene substrate were found for all molecular structures (below 30 meV per atom). The STM analysis of films prepared from **L-Pt-Py-iCyt** solutions revealed the formation of polycrystalline structures dominated by **iC6** and **½iC6** assemblies (ca. 80%; Figure 4.9), which is in a good agreement with the results of the theoretical studies. In particular, both **iC6** and **½iC6** assemblies are being favoured among all **L-Pt-Py-iCyt** structures, a finding, which can be directly correlated to the largest energies of dissociation. While the strength of intermolecular interactions plays a major role in the **L-Pt-Py-iCyt** self-assembly, the impact of the adsorption energies can be neglected, as E_{ad} were found to be comparable among all **L-Pt-Py-iCyt** assemblies.

Conclusion

In summary, STM studies were performed on the formation of different polygonal discrete cyclic supramolecular motifs formed by the isocytosine based Pt(II)-complex **L-Pt-Py-iCyt** at solution/HOPG interface. The results were supported by a comprehensive DFT analysis including the simulation of STM images. The calculation results were in a very good agreement with the experimentally acquired results. Both, the experimental and the theoretical findings, provided unambiguous evidence that the formation of hexameric and half-hexameric motifs of **L-Pt-Py-iCyt** molecules is thermodynamically favoured (82% of all molecules), as ruled by the strength of the association energy. Nevertheless, pentamers, tetramers and trimers are also observed at the solid/liquid interface, but to a minor extent (18% of all molecules). The approach described in this work can be exploited to control the supramolecular structure of Pt(II)-complexes at the surface, and in general for the installation of several entities that can interact intermolecularly. Consequently, a way is demonstrated for tuning the photophysical properties of such organized materials and current studies aiming on multi-layered structures enabling Pt•••Pt interaction are on the way.

Computational details

The calculations were carried out by the group of Gianaurelio Cuniberti including Arezoo Dianat, Alejandro Santana-Bonilla and Rafael Gutierrez at the Technische Universität Dresden who are kindly acknowledged.

The computation of stable molecular conformations and the corresponding electronic structure was carried out at the density functional theory (DFT) level of theory with the standard implementation in the CP2K package. A mixed basis-set approach is used, where the Kohn-Sham orbitals are expanded into linear combinations of contracted Gaussian type orbitals (GTO) and complemented by a plane-wave basis set in order to compute the electronic charge density. In all calculations, the BLYP exchange-correlation functional was used, and its corresponding norm-conserving pseudo-potential GTH (Goedecker, Teter and Hutter). A DZVP (double zeta for valence electrons plus polarization functions) basis set complemented with a plane-wave basis set energy cut-off of 350 Ry. Dispersion corrections were included through the standard D3 Grimme parameterization. The convergence criteria for both geometry and energy calculations were set to 1×10^{-7} Hartree for the SCF energy and 9×10^{-4} (Hartree per Radian). In the case of isolated molecular motifs, calculations were performed with a supercell with box size of $50 \times 50 \times 20$ $Å^3$. These dimensions ensure the avoidance of spurious interactions between neighboring cells when implementing periodic boundary conditions. The different molecular motifs have been constructed partly based on the experimentally observed assemblies visualized with STM, and partly on structural optimization of several additional motifs. In such way, the motifs converged to the supramolecular structures displayed in Figure 4.17.

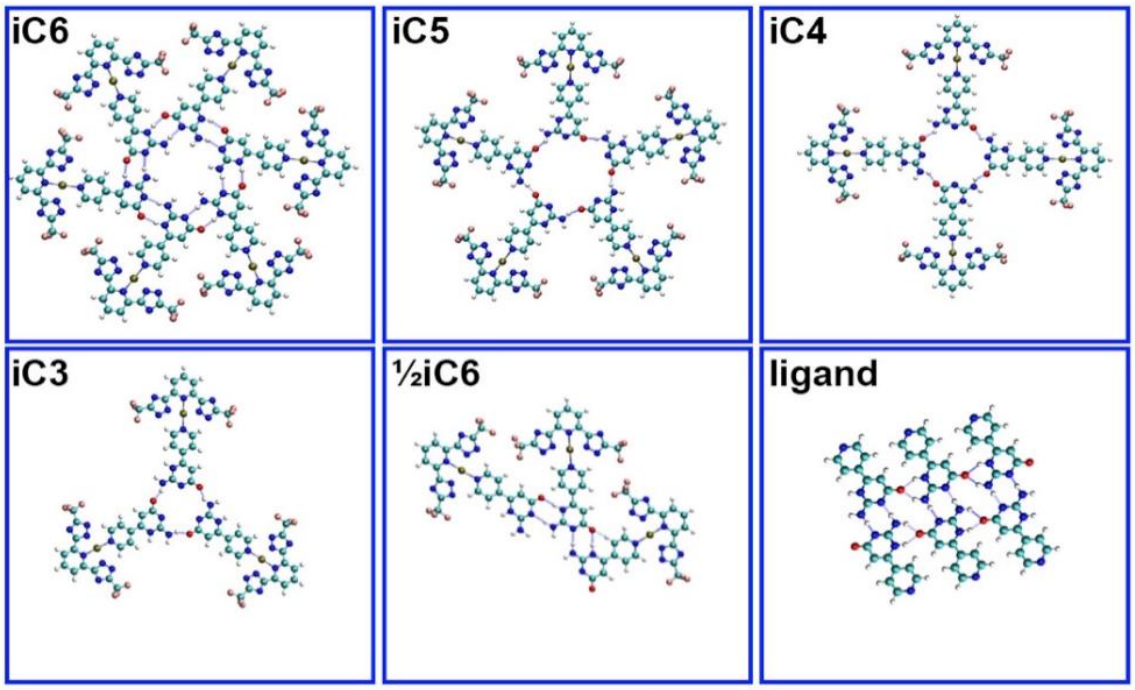

Figure 4.17: Cyclic molecular motifs of **L-Pt-Py-iCyt** and the ligand (**Py-iCyt**) showing the intermolecular interactions.

Experimental part

The scanning tunneling microscope (STM) experiments were conducted in collaboration with Mohamed El Garah and Artur Ciesielski of the group of Paolo Samorí at the Université de Strasbourg who are kindly acknowledged.

Synthesis of 4-isoCytosinyl-pyridine (Py-iCyt)

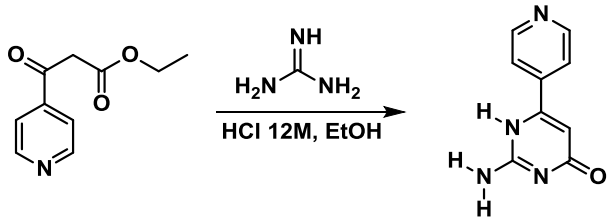

Following the literature in parts,[38, 41, 42] ethyl 3-oxo-3-(pyridin-4-yl)propanoate (707 mg, 3.66 mmol) and guanidinium carbonate (2.4 g, 5.49 mmol) were suspended in absolute ethanol (10 mL) in an inert atmosphere. Subsequently, aqueous HCl (12 M, 110 µL) were added and the reaction mixture heated to reflux for 18 h. The reaction mixture was allowed to cool to room temperature and the precipitate filtered through Buchner filtration. The solid was thoroughly washed with ethanol and diethylether and afterwards

transferred to a round bottom flask and dissolved in aqueous NaOH (1 M, 12 mL). This solution was heated to reflux for 2h and subsequently acidified with glacial acetic acid (3 mL). The resulting precipitate was filtered through a Buchner filtration, washed with distilled water, ethanol, diethylether and subsequently dried under ambient condition to yield a white solid (54 mg, 0.28 mmol, 8%).

^{1}H NMR (400 MHz, DMSO) δ 10.89 (s, 1H), 8.50 (d, *J* = 6.1 Hz, 2H), 7.72 (d, *J* = 6.1 Hz, 2H), 6.59 (s, 2H), 6.12 (s, 1H). HR-ESI-MS (positive scan, *m/z*): $[M+H]^+$ calcd. 189.0771; found 189.0765.

Synthesis of L-Pt-Py-iCyt

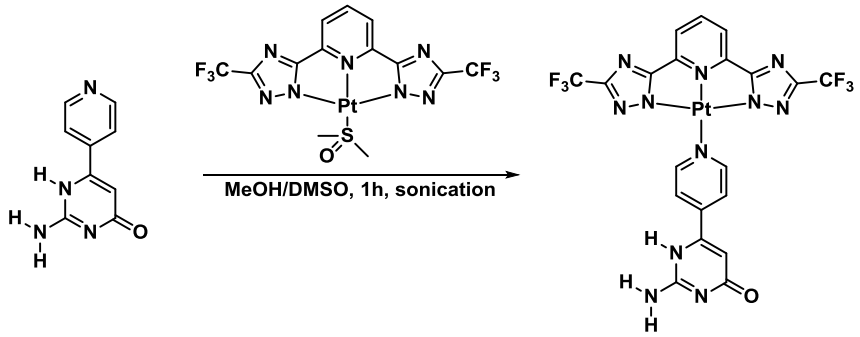

L-Pt-DMSO (6.7 mg, 0.01 mmol) and **Py-iCyt** (2 mg, 0.01 mmol) were dissolved in a mixture of MeOH/DMSO (2 mL, 10:1, *v*,*v*) and sonicated for 1 h in a closed Eppendorf vial leading to the formation of a yellow emissive precipitate. Subsequently, the crude product mixture was centrifuged and the supernatant taken off. The solid was afterwards treated with THF and subsequently again centrifuged to receive the solid. This procedure was repeated with MeOH two times and one time with THF to obtain an orange solid product (8 mg, 0.01 mmol, 82%).

^{1}H NMR (400 MHz, THF, ppm) δ 10.38 (s, 1H), 9.79 (d, *J* = 6.3 Hz, 2H), 8.30 (d, *J* = 6.3 Hz, 2H), 8.25 (t, *J* = 7.6 Hz, 1H), 7.94 (d, *J* = 8.1 Hz, 2H), 6.54 (s, 1H), 6.31 (s, 2H). ^{19}F{^{1}H} NMR (377 MHz, THF, ppm) δ -67.07. HR-ESI-MS (positive scan, *m/z*): $[M+H]^+$ calcd. 731.0773; found 731.1103.

References

1. J. V. Barth, G. Costantini and K. Kern, *Nature*, 2005, **437**, 671-679.
2. M. Stöhr, M. Wahl, C. H. Galka, T. Riehm, T. A. Jung and L. H. Gade, *Angew. Chem. Int. Ed.*, 2005, **44**, 7394-7398.
3. J. A. A. W. Elemans, R. Van Hameren, R. J. M. Nolte and A. E. Rowan, *Adv. Mater.*, 2006, **18**, 1251-1266.
4. G. P. Spada, S. Lena, S. Masiero, S. Pieraccini, M. Surin and P. Samorì, *Adv. Mater.*, 2008, **20**, 2433-2438.
5. T. Kudernac, S. B. Lei, J. A. A. W. Elemans and S. De Feyter, *Chem. Soc. Rev.*, 2009, **38**, 402-421.
6. D. Bonifazi, S. Mohnani and A. Llanes-Pallas, *Chem. Eur. J.*, 2009, **15**, 7004-7025.
7. J. A. G. Williams, in *Top Curr Chem*, eds. V. Balzani and S. Campagna, Springer, Heidelberg, 1st edn., 2007, vol. 281, pp. 205-268.
8. C. A. Strassert, C. H. Chien, M. D. Galvez Lopez, D. Kourkoulos, D. Hertel, K. Meerholz and L. De Cola, *Angew. Chem. Int. Ed.*, 2011, **50**, 946-950.
9. N. K. Allampally, C. A. Strassert and L. De Cola, *Dalton Trans.*, 2012, **41**, 13132-13137.
10. V. M. Miskowski and V. H. Houlding, *Inorg. Chem.*, 1989, **28**, 1529-1533.
11. B. Ma, P. I. Djurovich and M. E. Thompson, *Coord. Chem. Rev.*, 2005, **249**, 1501-1510.
12. M. Mydlak, M. Mauro, F. Polo, M. Felicetti, J. Leonhardt, G. Diener, L. De Cola and C. A. Strassert, *Chem. Mater.*, 2011, **23**, 3659-3667.
13. M. Mauro, A. Aliprandi, C. Cebrian, D. Wang, C. Kübel and L. De Cola, *Chem. Commun.*, 2014, **50**, 7269-7272.
14. B. T. Khan and S. M. Zakeeruddin, *Transition Met. Chem.*, 1991, **16**, 119-121.
15. H. Rauter, I. Mutikainen, M. Blomberg, C. J. L. Lock, P. AmoOchoa, E. Freisinger, L. Randaccio, E. Zangrando, E. Chiarparin and B. Lippert, *Angew. Chem. Int. Ed.*, 1997, **36**, 1296-1301.
16. D. Gupta, M. Huelsekopf, M. M. Cerda, R. Ludwig and B. Lippert, *Inorg. Chem.*, 2004, **43**, 3386-3393.
17. D. Gupta, M. Roitzsch and B. Lippert, *Chemistry A European Journal*, 2005, **11**, 6643-6652.
18. A. G. Quiroga, *J. Inorg. Biochem.*, 2012, **114**, 106-112.
19. X. Wang, X. Wang and Z. Guo, *Account. Chem. Res.*, 2015, **48**, 2622-2631.
20. Z. Xue, M. Lin, J. Zhu, J. Zhang, Y. Li and Z. Guo, *Chem. Commun.*, 2010, **46**, 1212-1214.
21. N. Margiotta, N. Denora, R. Ostuni, V. Laquintana, A. Anderson, S. W. Johnson, G. Trapani and G. Natile, *J. Med. Chem.*, 2010, **53**, 5144-5154.
22. I. Łakomska, *Inorg. Chim. Acta*, 2009, **362**, 669-681.
23. I. Łakomska, E. Szłyk, J. Sitkowski, L. Kozerski, J. Wietrzyk, M. Pełczyńska, A. Nasulewicz and A. Opolski, *J. Inorg. Biochem.*, 2004, **98**, 167-172.
24. F. Rosei, M. Schunack, Y. Naitoh, P. Jiang, A. Gourdon, E. Laegsgaard, I. Stensgaard, C. Joachim and F. Besenbacher, *Progress in Surface Science*, 2003, **71**, 95-146.
25. A. Nickel, R. Ohmann, J. Meyer, M. Grisolia, C. Joachim, F. Moresco and G. Cuniberti, *ACS Nano*, 2013, **7**, 191-197.
26. D. den Boer, M. Li, T. Habets, P. Iavicoli, A. E. Rowan, R. J. M. Nolte, S. Speller, D. B. Amabilino, S. De Feyter and J. A. A. W. Elemans, *Nat. Chem.*, 2013, **5**, 621-627.
27. S. Haq, F. Hanke, J. Sharp, M. Persson, D. B. Amabilino and R. Raval, *ACS Nano*, 2014, **8**, 8856-8870.
28. Y. Yu, J. Lin, Y. Wang, Q. Zeng and S. B. Lei, *Chem. Commun.*, 2016, **52**, 6609-6612.
29. J. Sanning, P. R. Ewen, L. Stegemann, J. Schmidt, C. G. Daniliuc, T. Koch, N. L. Doltsinis, D. Wegner and C. A. Strassert, *Angew. Chem. Int. Ed.*, 2015, **54**, 786-791.
30. M. Lackinger, S. Griessl, W. M. Heckl, M. Hietschold and G. W. Flynn, *Langmuir*, 2005, **21**, 4984-4988.

31. A. Llanes-Pallas, C.-A. Palma, L. Piot, A. Belbakra, A. Listorti, M. Prato, P. Samorì, N. Armaroli and D. Bonifazi, *J. Am. Chem. Soc.*, 2009, **131**, 509-520.
32. J. M. MacLeod, O. Ivasenko, C. Fu, T. Taerum, F. Rosei and D. F. Perepichka, *J. Am. Chem. Soc.*, 2009, **131**, 16844-16850.
33. O. Ivasenko and D. F. Perepichka, *Chem. Soc. Rev.*, 2011, **40**, 191-206.
34. M. El Garah, R. C. Perone, A. S. Bonilla, S. Haar, M. Campitiello, R. Gutierrez, G. Cuniberti, S. Masiero, A. Ciesielski and P. Samorì, *Chem. Commun.*, 2015, **51**, 11677-11680.
35. R. Otero, M. Schock, L. M. Molina, E. Laegsgaard, I. Stensgaard, B. Hammer and F. Besenbacher, *Angew. Chem. Int. Ed.*, 2005, **44**, 2270-2275.
36. W. Xu, R. E. A. Kelly, H. Gersen, E. Laegsgaard, I. Stensgaard, L. N. Kantorovich and F. Besenbacher, *Small*, 2009, **5**, 1952-1956.
37. L. K. Wang, H. H. Kong, C. Zhang, Q. Sun, L. L. Cai, Q. G. Tan, F. Besenbacher and W. Xu, *ACS Nano*, 2014, **8**, 11799-11805.
38. A. Ciesielski, S. Colella, L. Zalewski, B. Bruchmann and P. Samorì, *CrystEngComm*, 2011, **13**, 5535.
39. M. Cai, A. L. Marlow, J. C. Fettinger, D. Fabris, T. J. Haverlock, B. A. Moyer and J. T. Davis, *Angew. Chem. Int. Ed.*, 2000, **39**, 1283-+.
40. K. Li, G. S. Ming Tong, Q. Wan, G. Cheng, W.-Y. Tong, W.-H. Ang, W.-L. Kwong and C.-M. Che, *Chem. Sci.*, 2016, **7**, 1653-1673.
41. J. H. Hirschberg, R. A. Koevoets, R. P. Sijbesma and E. W. Meijer, *Chem. Eur. J.*, 2003, **9**, 4222-4231.
42. F. H. Beijer, R. P. Sijbesma, H. Kooijman, A. L. Spek and E. W. Meijer, *J. Am. Chem. Soc.*, 1998, **120**, 6761-6769.
43. A. Aliprandi, M. Mauro and L. De Cola, *Nat Chem*, 2016, **8**, 10-15.
44. M. Flores, E. Cisternas, J. D. Correa and P. Vargas, *Chem. Phys.*, 2013, **423**, 49-54.
45. L. M. Toledo, K. Musa, J. W. Lauher and F. W. Fowler, *Chem. Mater.*, 1995, **7**, 1639-1647.
46. P. R. Lowe, C. H. Schwalbe and G. J. B. Williams, *Act. Crystallogr. Sect. C: Cryst. Struct. Commun.*, 1987, **43**, 330-333.

Chapter V

Highly Luminescent Virus Like Particles (VLPs) Through the Encapsulation of Pt(II)-Amphiphiles

Abstract

In this chapter, the synthesis and photophysical investigation of water soluble Pt(II)-complexes is reported. The self-assembly and aggregation induced emission properties of these phosphorescent metal complexes were probed. On the basis of excited-state lifetime measurement, a new method for the determination of the critical aggregation concentration for inherently luminescent amphiphiles was established. The encapsulation *via* two different procedures into virus capsids yielded highly emissive virus like particles featuring a drastic quantum yield enhancement by means of rigidochromic effects (Figure 5.1). A negatively charged Pt(II)-complex assembly allowed the reorganization of natively icosahedral CCMV capsid into luminescent cylindrical particles.

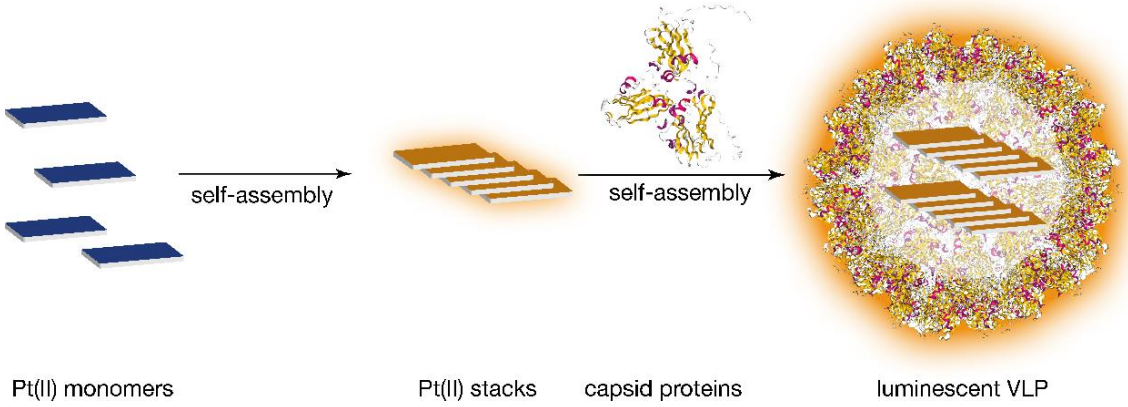

Figure 5.1: Illustration of the formation of the luminescent virus like particles (VLP) by encapsulation of Pt(II) aggregates into self-assembling coat proteins.

Transition metal complexes utilizing for instance Ru(II),[1-7] Os(II),[8] Ir(III),[9-11] Pt(II)[12] show an effective intersystem crossing towards a triplet excited state on account of a strong spin-orbit coupling induced by the heavy atom. In virtue of the spin-conservation rule, the excited state lifetime for these phosphors will be strongly prolonged in contrast to fluorophores up to seconds, resulting in spin-changing emissive relaxation, namely phosphorescence, which is accompanied by a large Stokes shift.

On account of increasing primary and secondary inner filter effects, luminophores in general suffer from self-quenching at higher concentrations, the so-called aggregation-caused quenching (ACQ),[13] resulting in strongly decreasing quantum yields (φ) at high concentrations. Phosphorescent neutral square-planer Pt(II)-complexes, appropriately decorated with chromophoric ligands, exhibit the geometric prerequisite to overcome this problem. In a monomeric form a structured emission peaking in the blue region of the electromagnetic spectrum is observed with a short excited-state lifetime (few nanoseconds) and low quantum yield ($\varphi < 1\%$), while in the aggregated state a featureless bathochromically shifted luminescence occurs exhibiting a prolonged excited-state lifetime (hundreds of nanoseconds) and a strongly increased quantum yield ($\varphi = 65\%$).

The observed effects of prolongation of the excited-state lifetime as well as a strong increase of the quantum yield depending on the self-assembling of the complexes can be assigned as aggregation-induced emission (AIE). Therefore, also high concentrations, global or local, lead to attractive photophysical properties such as excitation and emission in the visible region of the solar spectrum, large Stokes shifts high quantum yield and long excited-state lifetime aiding a facile suppression of possible background fluorescence caused by biological matrices. Furthermore, a change of the nature of the emission from ^{3}LC based to ^{3}MMLCT based occurs already at the formation of dimers rather than supramolecular polymer (see Chapter II, K^+-sensing) and thus possesses a high sensitivity for small molecular changes and the perturbation of the self-assembled structures.

The natively icosahedral virus cowpea chlorotic mottle virus (CCMV) is a potentially interesting natural carrier for a variety of cargos. Due to the facile control of the self-assembly of the virus coat proteins (CPs) *via* pH modulation, not only negatively charged cargos but also neutral ones can be encapsulated. An overview of CCMV in general and encapsulated cargos is given in Chapter I (General Introduction). In this chapter, a more

specified literature review is given for the envisaged encapsulation of Pt(II)-assemblies into CCMV capsids.

The DNA-templated rearrangement of CCMV capsids was achieved by single-stranded (ssDNA) and double-stranded (dsDNA) nucleic acids.[14, 15] Assemblies of chromophors to dsDNA and subsequently templated capsid formation yielded elongated (17 nm diameter) colored VLPs featuring pronounced CD signals.[15]

The encapsulation of metals into confined space is not only of interest for the synthesis of defined nanoparticles[16-18] or mineralization processes, but also for the formation of core-shell nanoconjugates Gold nanoparticles decorated with polyethylene glycol chains enabled the templating of capsid formation of bromo mosaic proteins.[19] Furthermore, gold nanoparticles were successfully used for fluorescence enhancement in spherical VLPs of bacteriophage MS2.[20] The capsid shell was covalently decorated with Alexa Fluor 488 labelled DNA strands (Figure 5.2). With a surfactant support, gold nanoparticles were recently successfully encapsulated into CCMV capsids featuring a high encapsulation efficiency of 99%.[21]

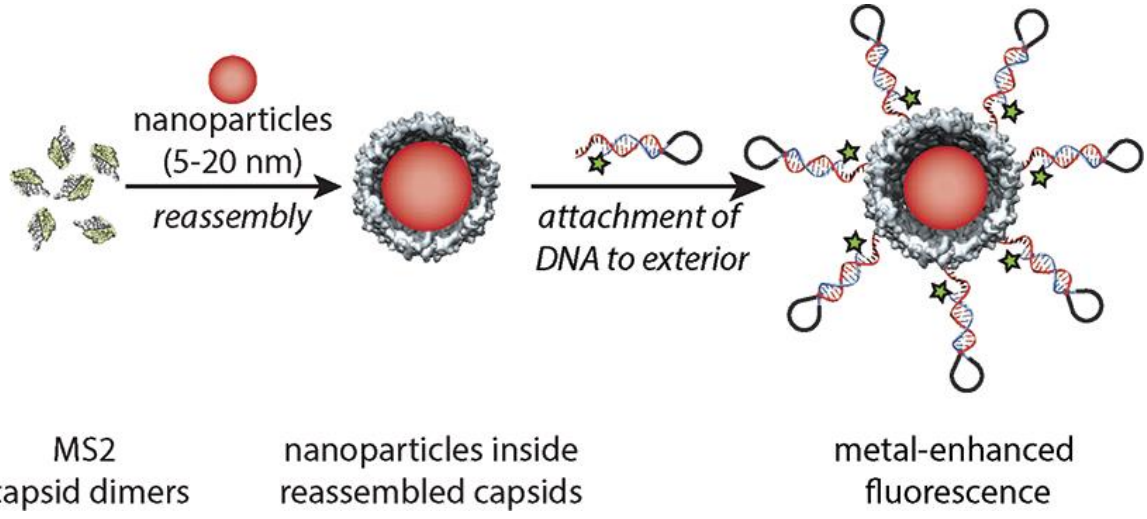

Figure 5.2: Fluorescence enhancement by gold-nanoparticle encapsulation.[20] © 2011 American Chemical Society

That self-assembled molecules can trigger the self-assembly of the CCMV CPs[22] further demonstrated by the usage of an amphiphilic ligand coordinated to Gd(III) resulting in an negatively charged assembly above the critical aggregation concentration in buffered solution.[23] The obtained VLPs displayed a broad size distribution, indicating the formation of T = 2 and T = 3 particles.

An encapsulation of drugs into a natural carrier such as a protein cage is a rational approach for targeted anti-cancer therapy.[24-29] The Pt(II)-complexes cisplatin and carboplatin as efficient cytostatic drugs, which intercalate into the backbone of DNA, were successfully encapsulated into apoferritin.[30] Apoferritin[31] (ferritin lacking Fe) proteins form cages of 12 nm size controlled by pH modulation,[32] which enable the transport of the cytostatic drugs towards cancer cells. Cell viability tests with PC12 cells a significant lowered concentration of the hybrid materials in comparison to other drugs. Preliminary data for the encapsulation of Pt(II)-assemblies into CCMV capsid were obtained in a collaboration between the De Cola and Cornelissen labs.[33, 34]

Water soluble zinc phthalocyanines (ZnPCs) were successfully encapsulated into CCMV capsid by the random and templated encapsulation methods (Figure 5.3).[35] The high local concentration inside the spatially confined protein cage led to the stacking of the ZnPCs inside the VLPs. The obtained icosahedral particles were successfully deployed as photosensitizer in photo dynamic therapy (PDT) due to their efficient single-oxygen production. Fraction of killed cells near unity was reached after only 20 min irradiation.

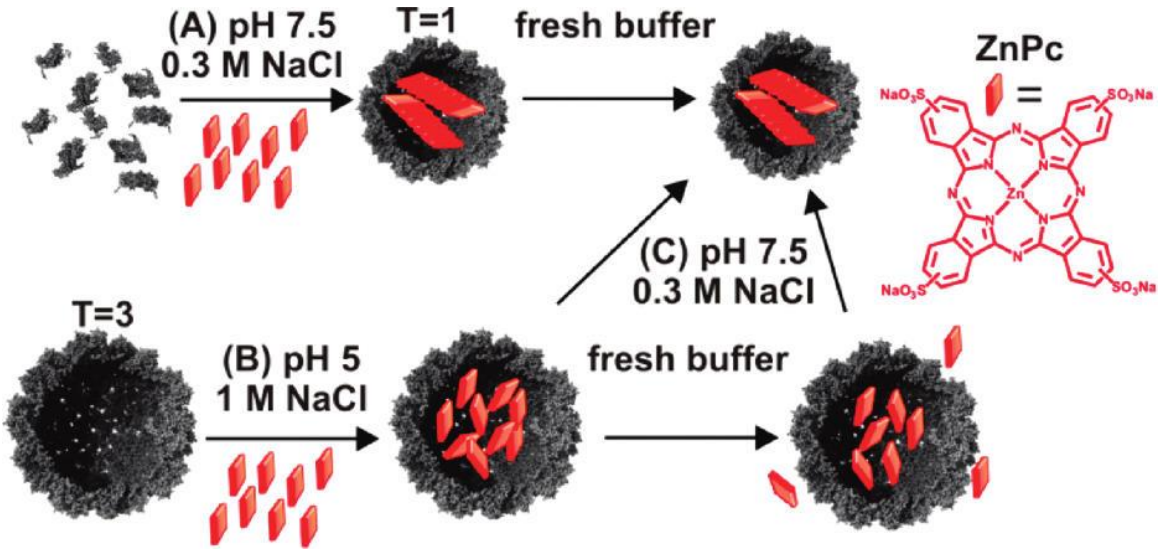

Figure 5.3: Encapsulation of zinc phthalocyanines (ZnPCs) into CCMV.[35] © 2011 American Chemical Society

Emissive CCMV VLPs could be obtained by encapsulation of fluorescent polymers[36]. Fluorescently labeled poly(styrene sulfonate) (PSS) with Rhodamine B was employed to template the self-assembly to emissive T = 1 and T = 2 particles. The aggregation and oxygen independent fluorescently labeled PSSs allows insights into the self-assembly

processes as well as an estimation of loading and local concentrations. (Picture) Furthermore, the covalent and non-covalent loading of teal fluorescent proteins (TFP) into CCMV capsid enables the prediction of the loading through a homo-FRET assay.[37]

As described in Chapter I, for Pt(II)-complex-protein interactions either hydrophobic pockets at the protein are necessary or certain binding motifs such H-bond donor/acceptors or a vacant coordination side are needed. Hydrophobic cavities were so far neither reported for assembled nor for disassembled CCMV coat proteins. The synthesized Pt(II)-amphiphiles are coordinated by a terdentate N-metallacycling ligand and an pyridine, resulting in stable and inert complexes (see Chapter III, exchange reaction experiment).[38] The complexes are decorated with tetra ethylene glycol branches are neutral or negatively charged (Scheme 5.1). Therefore, the predominant supramolecular binding motif will be the electrostatic interactions of the negative cargo and the positive proteins. Furthermore, protein interactions with polyethylene glycol chains were observed for gold nanoparticles in encapsulation experiments with bromomosaic virus (BMV).[19, 39]

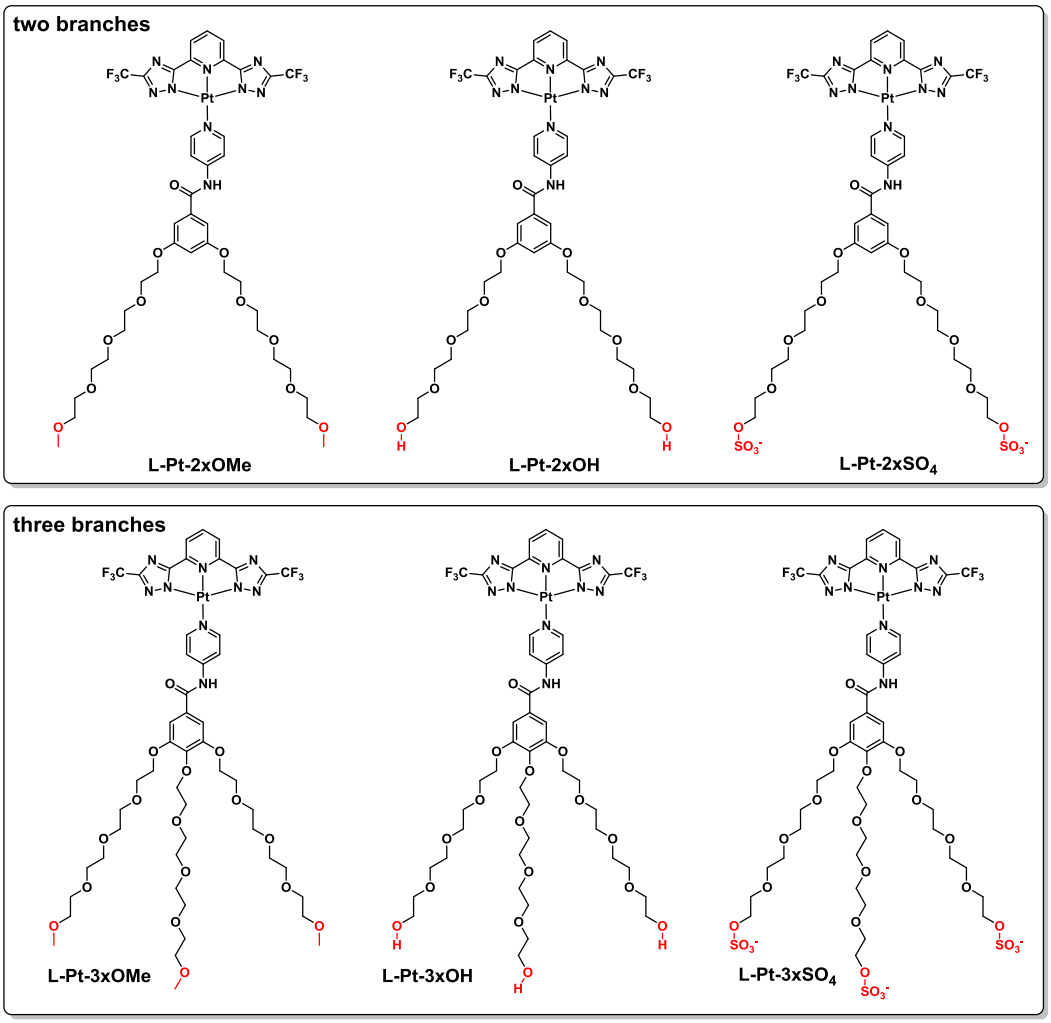

Scheme 5.1: Schematic representation of the synthesized Pt(II)-complexes with two (top) or three (bottom) tetra-ethylene-glycol branches. On the left side of the panels neutral complexes featuring -OMe and -OH end group are depicted. On the right side of the panel the negatively charged complexes carrying sulfite-ester end groups are displayed.

The aim of this work is to combine the beneficial aggregation-induced emission properties of Pt(II)-amphiphiles with the spatial confinement induced by encapsulation into CCMV capsids in order to create novel highly luminescent hybrid functional materials.

Results and discussion

Synthesis of the Pt(II)-amphiphiles

As mentioned before, the Pt(II)-amphiphiles are based on the **L-Pt-Py** framework (hydrophobic part), on account of its advantageous photophysical properties over the bis(tetrazole)-Pt-Py scaffold. The solubility properties were tuned by the ancillary ligand,

namely pyridine derivatives featuring a benzene moiety with branches of tetra ethylene glycol (hydrophilic part). The organic building blocks possess the coordinating pyridine which is amide substituted at position 4. The amide bond links either 3,5-bis(tetraethylene glycolyl) phenyl or 3,4,5-tris (tetraethylene glycolyl) to the pyridine. The terminal oxygens of the ethylene glycol chains are either present as hydroxy groups or substituted with methyl groups or sulfite groups.

First of all, the terminally benzyl (Bnz) or methyl (Me) protected tetra ethylene glycol (TEG) were tosylated with Tosyl chloride (toluenesulfonyl chloride TsCl) by a nucleophilic substitution under basic conditions. The activated glycol chains are then transferred to a methyl hydroxy benzoate (MHB) moiety under basic conditions. The Tosyl moiety is a much better leaving group than the hydroxy group. Either methyl-3,4,5-trihydroxybenzoate (MTB) or methyl-3,5-dihydroxybenzoate (DTB) serve as MHBs to allow either the formation of three arms and two arms branched system, respectively (Scheme 5.2).

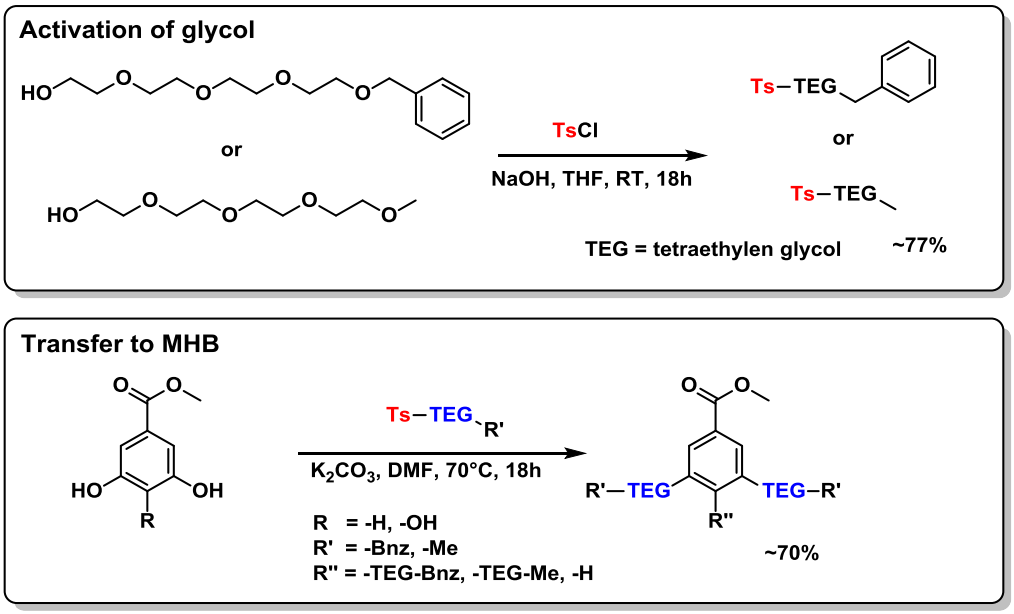

Scheme 5.2: Synthetic route for the activation of the tetra ethylene glycol chains *via* tosylation (top) and the transfer toward the methyl hydroxybenzoate (MHB) moiety to enable a branched system. The average yields for the products are depicted, for synthetic details see Experimental part.

The branched MHB moieties are in a subsequent reaction linked to the coordinative pyridine. The amide formation was performed either in a two or one step synthesis: *i)* a preceding basic saponification of the methyl ester is followed by the amide formation *via*

DCC activation (see Experimental part for details). *ii)* direct conversion of the methyl ester into the amide in technical THF by potassium tertiary butoxide (Scheme 5.3).[40] The latter synthetic route is preferable on account of its velocity, use of ambient condition and high yields observed (see Experimental part for details). For either reaction pathway, the terminal hydroxy groups of the glycol chains need to be protected (Bnz or Me) to avoid undesired side reactions.

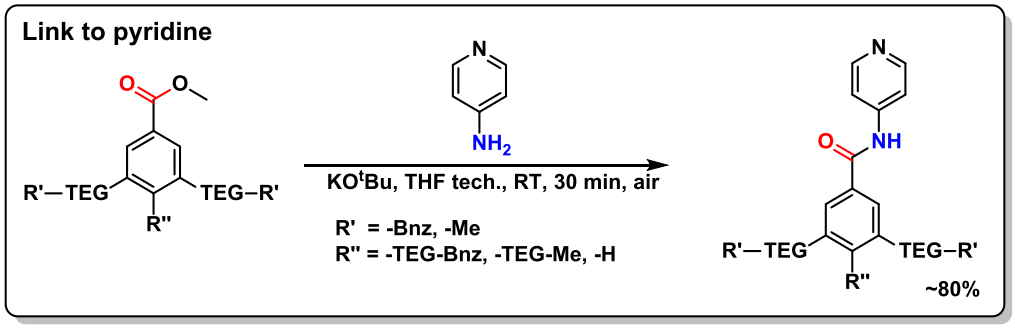

Scheme 5.3: Synthetic route for the formation of the amide bond between the coordinative pyridine and the branching MHB moiety. The average yields for the products are depicted, for synthetic details see Experimental part.

In order to form the ancillary ligands carrying terminal hydroxy (**A-2xOH**, **A-3xOH**) or sulfate groups (**A-2xSO$_4$**, **A-3xSO$_4$**), the benzyl protection group was removed by hydrogenation in the presence of a palladium catalyst (see Experimental part for details).

The final complexation reaction was performed under mild conditions by utilizing the formally introduced highly reactive Pt-precursor L-Pt-DMSO (Scheme 5.4). Due to the preceding N-metallacyclation, bases are omitted and the labile DMSO is rapidly substituted even at room temperature. On account of the high solubility of the obtained complexes, the usually performed separation by filtration was not successful and thus the crude compounds were subjected to a column chromatography for purification.

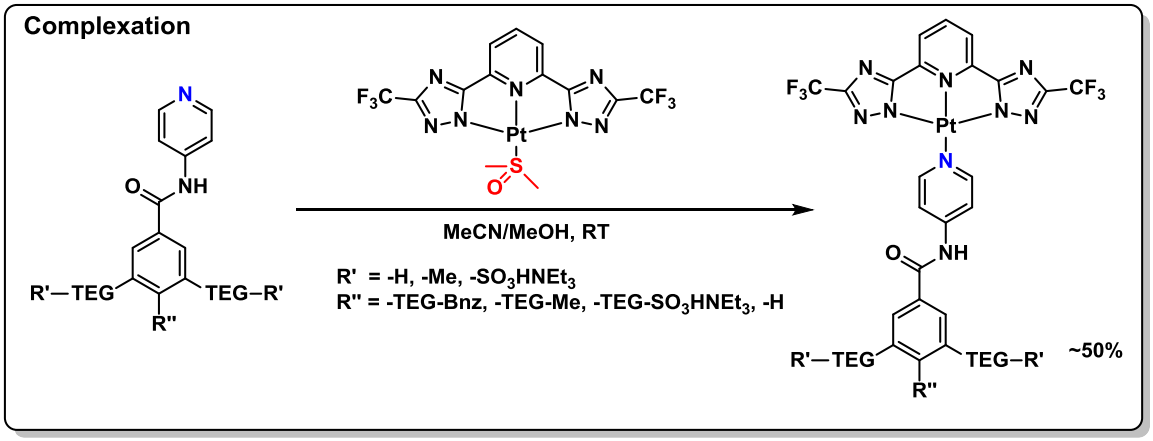

Scheme 5.4: Complexation reaction to obtain the desired Pt(II)-amphiphiles by reacting the ancillary ligand (**A**) with L-Pt-DMSO. The average yields for the products are depicted, for synthetic details see the Experimental part.

In the subsequent sections, the photophysical properties and the self-assembly of the prepared Pt(II)-amphiphiles are comprehensively investigated. From hereafter, the following nomenclature is used. **L-Pt-2xOMe** and **L-Pt-3xOMe** denote the platinum complexes featuring a terminal methoxy group at the two and three ethylene glycol branches, respectively. **L-Pt-2xOH** and **L-Pt-3xOH** denote the platinum complexes featuring a terminal hydroxy group at the two and three ethylene glycol branches, respectively. **L-Pt-2xSO$_4$** and **L-Pt-3xSO$_4$** denote the platinum complexes featuring a terminal sulfate group at the two and three ethylene glycol branches, respectively. **L-Pt-R** refers to a reference compound for initially photophysical investigations in organic solvents and the solid state. **L-Pt-Alkyl-2xSO$_4$** denotes the platinum complex with two alkyl branches and terminal sulfate groups. The reader is referred to the Experimental part for synthesis details of **L-Pt-R** and **L-Pt-Alkyl-2xSO$_4$**.

Photophysics of the Pt-R in organic solvent and the solid state

In Chapter III, it was demonstrated that different ancillary ligands (**A**) at the **L-Pt-A** framework induced distinguishable photophysical properties. The differential photophysics are not only based on the ligands basicity, stereoelectronics, electron-donating and electron-withdrawing abilities, but also their stereochemistry and thus the resulting packing of the Pt(II)-complex. Therefore, prior to the formation of the described amphiphiles a reference compound **L-Pt-R** was synthesized and photophysically investigated. This proceeding allowed the assessment if Pt•••Pt interactions take place

upon aggregation and provided an estimate if desired photophysical properties are achievable. The reference ligand **R** resembles the core structure of the other complexes while avoiding long ethylene glycol branches. The long ethylene glycol branches are expected to adopt a chain-extended conformation in aqueous and organic solution at room temperature and therefore will not contribute to the bulkiness at the **L-Pt-Py** core.[41, 42]

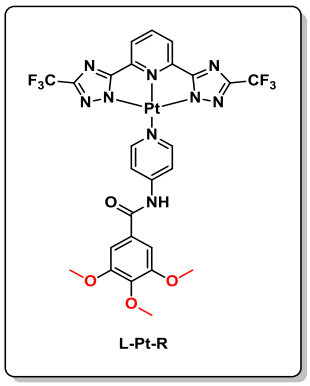

Figure 5.4: Schematic representation of the reference complex **L-Pt-R** without any ethylene glycol branch.

The absorption spectrum in aerated tetrahydrofuran (THF) of the reference complex **L-Pt-R** resembles the one of the parent **L-Pt-Py** complex (see Chapter III for details). The lowest energetic absorption band ($\varepsilon = 800\ M^{-1}cm^{-1}$) in the visible region (450 - 375 nm) is attributable to a metal-to-ligand charge transfer (MLCT) transition (Figure 5.5 left). The absorption bands in the UV region are ascribed as π-π* transitions (335 nm sh, $\varepsilon = 15097\ M^{-1}cm^{-1}$, 303 nm, 49293 $M^{-1}cm^{-1}$, 277 sh, 33406 $M^{-1}cm^{-1}$). On account of the efficient intersystem crossing due to the strong spin orbit, the lowest singlet excited state (^{1}MLCT)[43] is depopulated while the energetic lowest triplet state (^{3}LC) is populated.[44] From this state, a structured emission arises peaking at 462, 489, 519 and 563 nm accompanied by a vibronic progression of 1182 - 1442 cm^{-1} which is attributable to the vibrational modes of the aromatic system of the ligand (C=C, C=N stretch).[45, 46] The excitation spectrum resembles the absorption spectrum. The emission profile and wavelength remain unaffected by the energy of excitation and thus following Kasha's rule.[47] The emission quantum yield (<1%) is very low accompanied by the short lifetime of 1.3 ns (monoexponential decay) at ambient conditions. All detected photophysical parameters and assignments are in agreement with similar complexes described in this thesis and the literature.[43, 48, 49] The photophysical analysis in solution exhibits the absence of Pt•••Pt interactions.

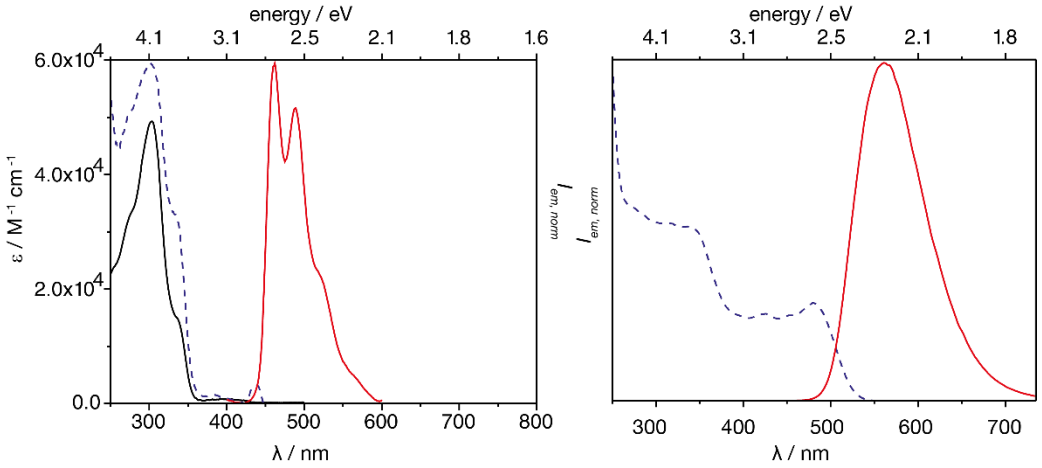

Figure 5.5: left: Absorption (black, solid), normalized emission (red, solid, λ_{ex} = 300 nm) and excitation (blue, dashed, $\lambda_{em} = \lambda_{em,max}$) spectra of complex **L-Pt-R** in aerated THF solution (10^{-4} - 10^{-5}M). right: Normalized emission (red, solid, λ_{ex} = 300 nm) and excitation (blue, dashed, $\lambda_{em} = \lambda_{em,max}$) spectra of complex **L-Pt-R** in solid state (neat film).

The diluted THF solution was subsequently dropcasted onto a quartz substrate to allow for the photophysical analysis of a neat film of **L-Pt-R**. The increase of the concentration during the evaporation of the volatile solvent is accompanied by a self-assembly of the Pt(II)-complexes on account of the high tendency for stacking. In comparison to the solution, the solid-state emission spectrum appears featureless and bathochromically shifted with a maximum at 561 nm. This broad emission is assigned to arise from a triplet metal/metal-to-ligand charge transfer state (^{3}MMLCT) which arises from the Pt•••Pt interactions present in the aggregated state. The excitation spectrum shows intense bands in the visible region (481 - 390 nm) which are attributable to the MMLCT transition with an absorption onset around 507 nm. The intense transitions in the UV region are ascribed to intraligand transitions. In contrast to the findings for molecularly dissolved complexes, the exited-state lifetime of 495 ns (monoexponential decay) of the neat film sample is prolongated and the emission quantum yield (57%) strongly enhanced in the aggregated state. The emissive deactivation of the excited-state of **L-Pt-3xOMe** follows a bi-exponential decay featuring partial lifetimes of 473 ns (84%) and 151 ns (15%), which emerge from arbitrary arrangements of the complexes in solid-state (manifold of polymorphs). For the remainder of the text, the amplitude weighted lifetime (see Instrumentation part for details) are utilized as measure for the average excited-state lifetime, which is recommended on account of the inherent mathematic problem for amplitude weighted lifetime measurements.[50] However, the average excited-state lifetime

is a useful measure for the envisaged purpose of the exclusion of auto fluorescence signals and assessment of lifetime prolongation.

Photophysics of the Pt(II)-amphiphiles in organic and aqueous solution

The results obtained for **L-Pt-R** and the insights from the former chapters suggested that the fundamental scaffold **L-Pt-R** allows for Pt•••Pt interactions to occur. Therefore, upon aggregation an alteration of the nature of the emission, from ^{3}LC to ^{3}MMCLT, is expected. This arrangement allows to utilize the beneficial properties of aggregated Pt(II)-complexes, namely the excitation in the visible region, large Stokes shift, long excited-state lifetime and high quantum yield at ambient conditions. The installation of water soluble TEG branches on the benzene ring follows the principles of phase separation between hydrophobic and hydrophilic entities. When these entities are covalently linked together the phase separation, namely the aggregation of the hydrophobic part (**L-Pt-Py** core) while the hydrophilic part (TEG) are pointing into the surrounding solvent, leads to the formation of supramolecular structures. With this strategy, self-assembled structures such as micelles, bilayers, lamellas or vesicles are formed which realize stable dispersions of supermolecules in an aqueous medium. [51]

The amphiphilic Pt(II)-complexes were therefore analyzed in the organic solvent THF, which serves as solubilizing agent for the hydrophobic and hydrophilic parts and thus avoid a phase separation (no aggregation of the **L-Pt-Py** core). Further analysis took place in the aqueous buffer solution, in which the water molecules expectedly only solubilize the hydrophilic TEG branches whilst the hydrophobic parts aggregate rendering the formation of self-assembled Pt(II)-complexes.

Firstly, the complexes **L-Pt-2xOMe** and **L-Pt-3xOMe** were analyzed more comprehensively including analysis in the solid state and deionized water. A diluted THF solution the absorption spectra of both complexes are similar to each other and resemble the spectrum of the reference compound **L-Pt-R**. The weak MLCT absorption in the visible region (450 - 356 nm ε = 830 $M^{-1}cm^{-1}$ and 340 $M^{-1}cm^{-1}$ for **L-Pt-2xOMe** and **L-Pt-3xOMe**, respectively) is accompanied by pronounced higher energetic transitions in the UV region attributable to intraligand transitions. The room temperature emissions display a structured profile peaking around 461 nm for both complexes. The relatively short excited-state lifetimes of 0.75 ns and 1.58 ns (monoexponential decays) together

with the low quantum yields (<1%) for **L-Pt-2xOMe** and **L-Pt-3xOMe**, respectively, are in agreement with similar compounds including the assignment of a ^{3}LC based emission.[48, 49]

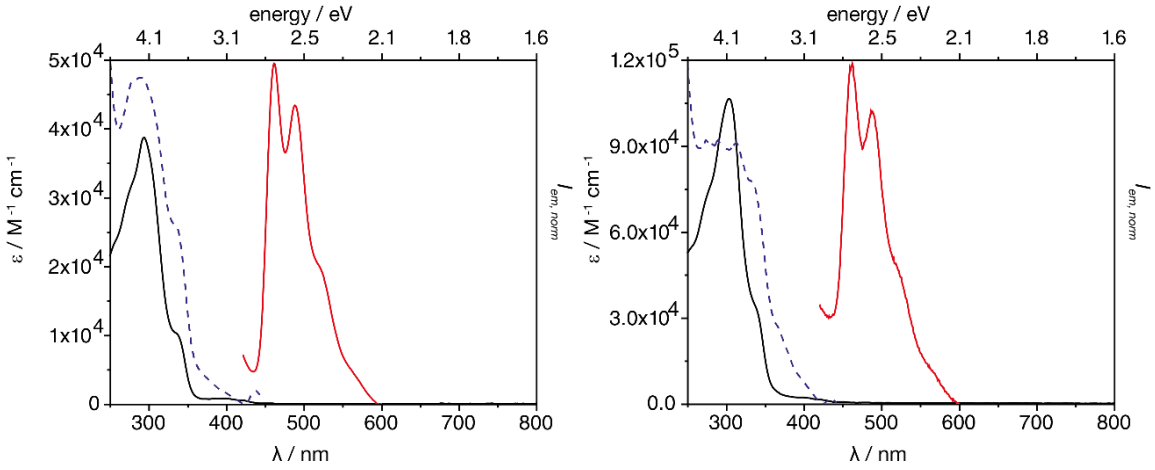

Figure 5.6: Absorption (black, solid), normalized emission (red, solid, λ_{ex} = 300 nm) and excitation (blue, dashed, λ_{em} = 500 nm) spectra of the complexes **L-Pt-2xOMe** (left) and **L-Pt-3xOMe** (right) in aerated THF solution (10^{-4}-10^{-5}M).

The solutions were subsequently dropcasted onto quartz surfaces for solid-state analysis. As also observed for **L-Pt-R**, the nature of the emission changes from ^{3}LC based to ^{3}MMLCT based upon aggregation on the basis of Pt•••Pt interactions. This is reflected by the broad featureless emission profiles peaking at 568 nm and 584 nm of the complexes **L-Pt-2xOMe** and **L-Pt-3xOMe**, respectively. The bathochromic shifts are not only observable in the emission but also in the excitation spectra. The absorption onset for bother complexes appear around 475 nm and intense MMLCT band in the visible region are observed. In comparison to the findings in organic solution, the excited-state lifetime measurements revealed strongly prolongated values of 554 ns (**L-Pt-2xOMe**, monoexponential decay) and 350 ns (**L-Pt-3xOMe**, amplitude weighted lifetime). Furthermore, the photoluminescence quantum yields are enhanced to 59% and 18% for **L-Pt-2xOMe** and **L-Pt-3xOMe**, respectively. The difference in the resulting radiative decay rate of 1.06 10^6 s (**L-Pt-2xOMe**) and 5.14 10^5 s (**L-Pt-3xOMe)** are most likely due to the relatively inhomogeneous dropcasting preparation method. The photophysical parameters are strongly dependent on the arrangement of the complexes, which is hardly controllable in an evaporation process. However, the photophysical results are akin to the

parent **L-Pt-R** complex, allowing for the access to beneficial photophysical properties by Pt•••Pt interactions. The formation of supermolecules by self-assembly can overcome this drawback by means of self-organization avoiding the formation of defects as present in the solid state.[52-54]

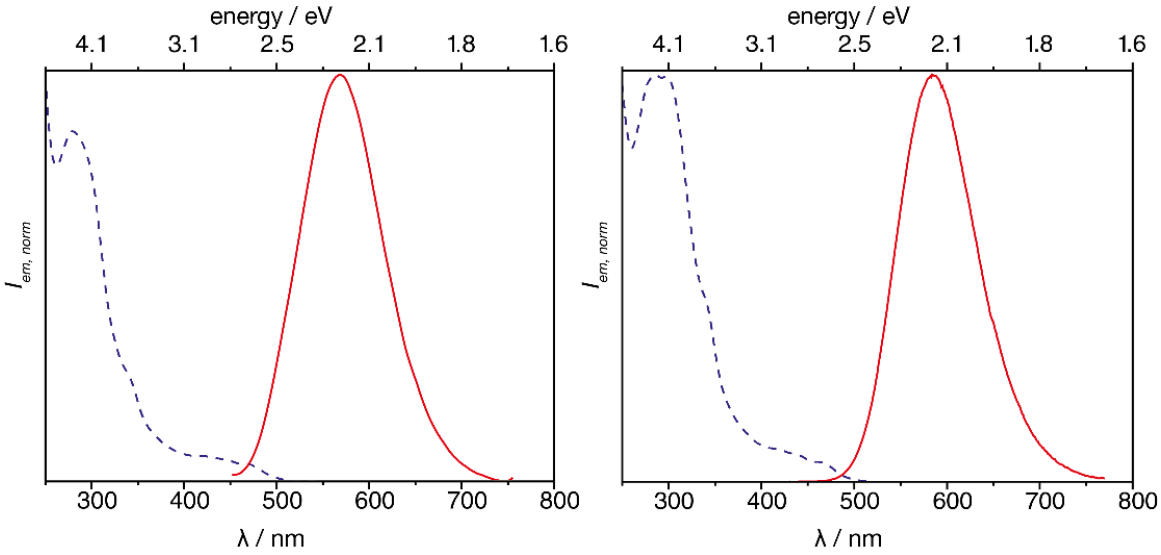

Figure 5.7: Normalized emission (red, solid, λ_{ex} = 300 nm) and excitation (blue, dashed, λ_{em} = $\lambda_{em,max}$) spectra of the complexes **L-Pt-2xOMe** (left) and **L-Pt-3xOMe** (right) in solid state (neat film).

Therefore, the complexes were probed in deionized water. In contrast to complex **L-Pt-3xOMe** which showed very good solubility, complex **L-Pt-2xOMe** was not soluble in water. Therefore, a THF stock solution of **L-Pt-2xOMe** was flash injected into deionized water to enable an analysis.

The absorption spectra of **L-Pt-2xOMe** and **L-Pt-3xOMe** in deionized water display pronounced MMLCT transitions in the visible region (478 - 400 nm, ε = 2872 $M^{-1}cm^{-1}$ and 6864 $M^{-1}cm^{-1}$ for **L-Pt-2xOMe** and **L-Pt-3xOMe**, respectively). In the UV region, an intense band is observed which is assigned to a ligand centered π-π* transition (277 nm, ε = 21132 $M^{-1}cm^{-1}$ and 296 nm, 98887 $M^{-1}cm^{-1}$ for **L-Pt-2xOMe** and **L-Pt-3xOMe**, respectively). The emission and the excitation spectra for both complexes resemble their profiles of the solid-state analysis, which is indicative of Pt•••Pt interaction and thus aggregation formation. The emission profiles are featureless with maxima at 575 nm (**L-Pt-2xOMe**) and 602 nm (**L-Pt-3xOMe**), appearing bathochromically shifted in comparison to the THF solutions. The lower energy of the emission of **L-Pt-3xOMe** is indicative of a shorter Pt-Pt distance (stronger destabilized HOMO, narrower energy gap)

than for **L-Pt-2xOMe**. Although the ethylene glycol chains are remotely attached to the chromophoric system substitution of electron-donating groups such as -OMe may also lead to a bathochromically-shifted emission (see Chapter III). Both excitation spectra resemble the absorption spectra and display a pronounced lowest energy transition at 476 nm ascribed to a MMLCT. In comparison to the organic solvent, in aqueous medium the emission quantum yields are strongly enhanced to 26% (**L-Pt-2xOMe**) and 40% (**L-Pt-3xOMe**). The excited-state lifetime measurements revealed the values of 460 ns for **L-Pt-2xOMe** and 219 ns for **L-Pt-3xOMe**. Although these values strongly differ from each other, which is most likely on account of the differential packing and the concentration dependencies of these parameters (*vide infra*), all measurements are indicative of Pt•••Pt interactions. Thus, the first objective of the transfer of the advantageous (solid-state) photophysical properties into the aqueous phase was fulfilled.

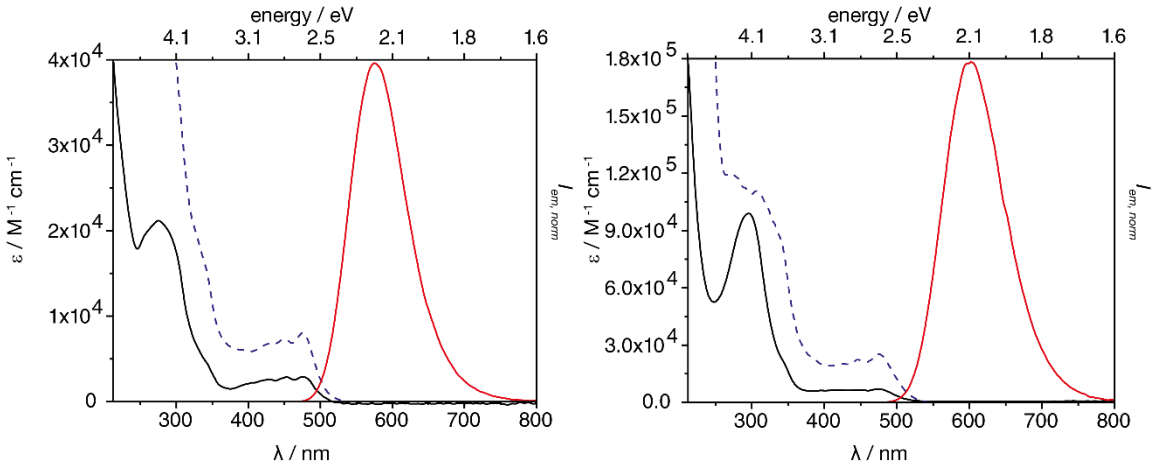

Figure 5.8: Absorption (black, solid), normalized emission (red, solid, λ_{ex} = 405 nm) and excitation (blue, dashed, λ_{em} = $\lambda_{em,max}$) spectra of the complexes **L-Pt-2xOMe** (left) and **L-Pt-3xOMe** (right) in aerated water solution (10^{-4}-10^{-5}M). On account of the insolubility of **L-Pt-2xOMe**, the complex was flash injected from a THF stock solution.

Noteworthy, on account of the low stability of the formed dispersion formed by **L-Pt-2xOMe** and its large particle size and broad size distribution, **L-Pt-2xOMe** was disregarded in the following sections.

The desired nanoconjugate formation with coat proteins is bound to an encapsulation process under pH controlled conditions. Therefore, the complexes were also analysed in buffered media, namely tris(hydroxymethyl)aminomethane (TRIS, pH=7.2) buffer.

Specifically, the utilized buffer solution contained 50 mM TRIS and 10 mM $MgCl_2$, which resembles the conditions as applied for the capsid virus proteins.

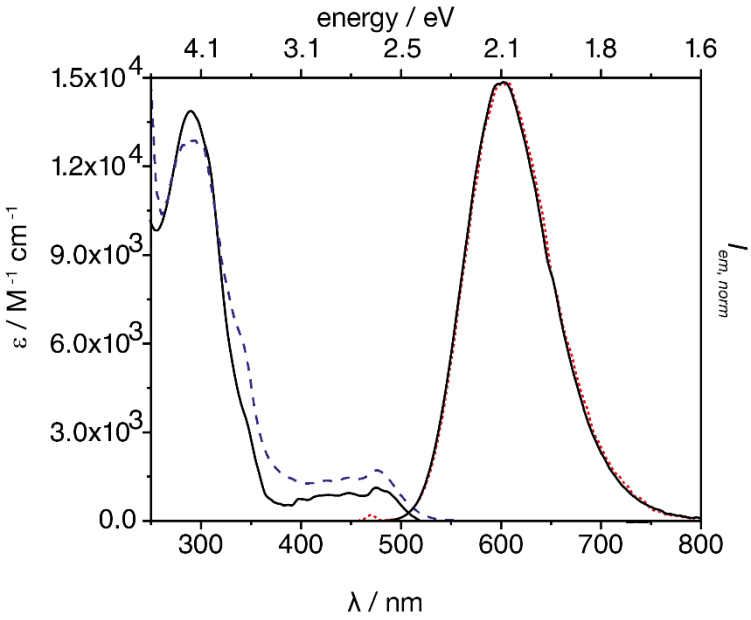

Figure 5.9: Absorption (black, solid), normalized emission (red, solid, λ_{ex} = 405 nm) and excitation (blue, dashed, $\lambda_{em} = \lambda_{em,max}$) spectra of **L-Pt-3xOMe** in aerated buffered TRIS solution (pH=7.2, 10^{-4}-10^{-5}M). The dotted black line represents the emission spectrum of **L-Pt-3xOMe** in water (see Figure 5.8).

The absorption spectrum of **L-Pt-3xOMe** displays (as observed in deionized water) a pronounced MLCT band in the visible region of the spectrum (474 - 380 nm, $\varepsilon = 1066\ M^{-1}cm^{-1}$) (Figure 5.9). The stronger absorptions bands in the UV region are attributable to ligand centered transitions. The obtained broad and featureless emission spectrum is superimposable with the emission spectrum in deionized water (Figure 5.9 dotted black line) peaking at 602 nm. Therefore, the aggregation of the non-ionic Pt(II)-complex **L-Pt-3xOMe** appears to be independent on the ionic strength of the surrounding aqueous medium. The excitation spectrum resembles the absorption spectrum featuring an onset around 500 nm. The excited-state lifetime of 403 ns and 38% quantum yield are as well indicative of Pt•••Pt interaction and are similar to values obtained in deionized water. Therefore, the superior photophysical properties obtained for the amphiphiles in water are retained in a buffer solution with a high ion content and possible quenching entities (sp^3 amine of TRIS).

All complexes were analysed in the organic solvent THF revealing similar photophysical features. A room temperature emission was detected for each complex and

the absorption, emission and excitation spectra as well as excited-state lifetime and quantum yields are akin to the complexes **L-Pt-R**, **L-Pt-2xOMe** and **L-Pt-3xOMe** described above. The spectra are depicted in Figure 5.10 and the photophysical data is summarized in Table 5.1. It can be concluded that Pt•••Pt interactions do not occur for all complexes in the organic solvent THF, and thus that no self-assembly of the Pt(II)-amphiphiles takes place.

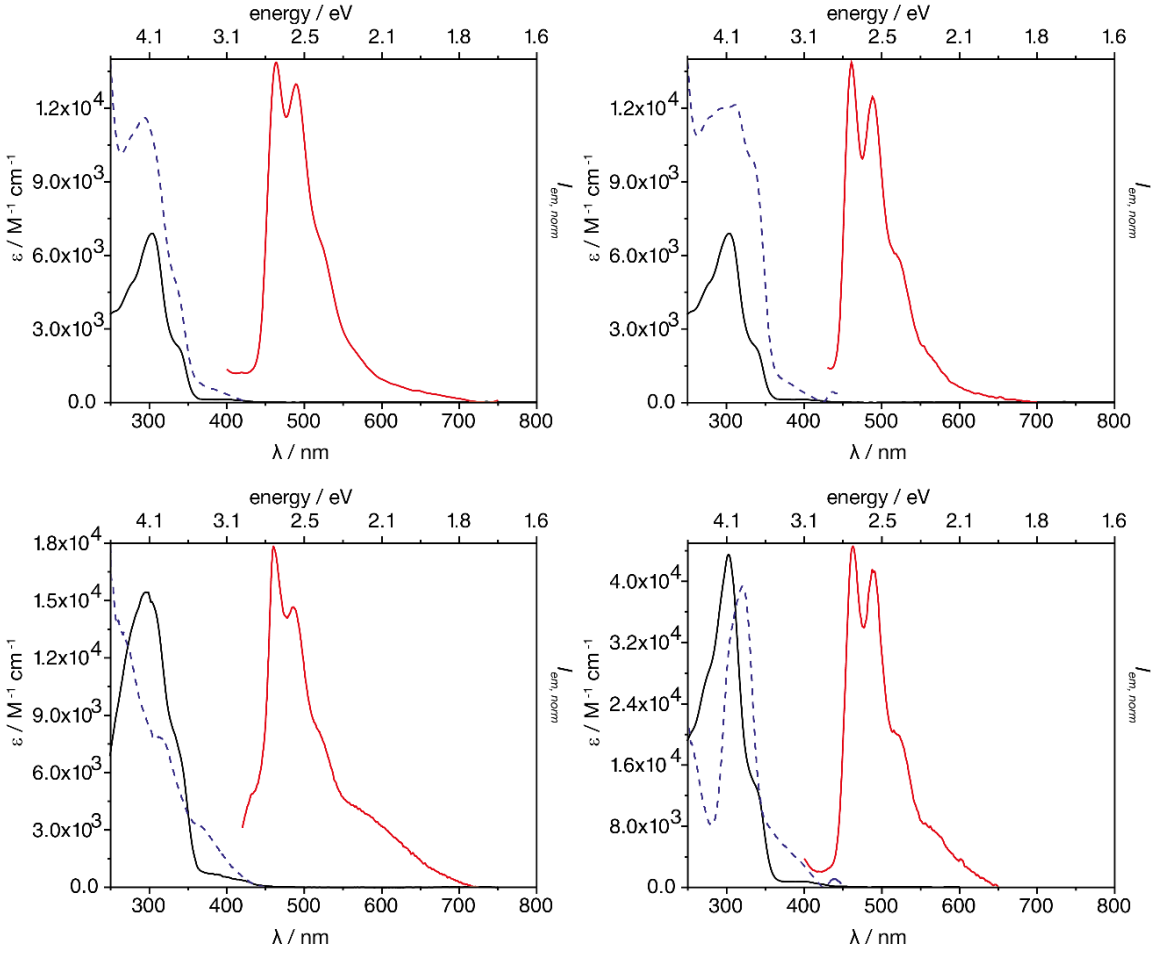

Figure 5.10: Absorption (black, solid), normalized emission (red, solid, λ_{ex} = 300 nm) and excitation (blue, dashed, λ_{em} = 500 nm) spectra of the complexes **L-Pt-2xOH** (top, left), **L-Pt-3xOH** (top, right), **L-Pt-2xSO$_4$** (bottom, left) and **L-Pt-3xSO$_4$** (bottom, right) in aerated THF solution (10^{-4}-10^{-5}M). A solution of THF/MeOH (30%) was utilized for the negatively charged complexes.

Table 5.1: Summary of the photophysical properties of the Pt(II)-amphiphiles in THF.

Complex	λ_{abs} / nm (ε / $M^{-1}cm^{-1}$) [a]	λ_{em} / nm [b]	τ / ns [c]	φ / % [c]
L-Pt-2xOMe	400 (851), 336 (sh, 10229), 294 (38740), 271 (sh, 29640)	461, 488, 520	1.5	<1
L-Pt-3xOMe	400 (2347), 338 (sh, 33607), 303 (106575), 278 (sh, 75445)	462, 486, 518	1.6	<1
L-Pt-2xOH	400 (127), 336 (sh, 2323), 304 (6894), 277 (sh, 4851)	464, 490, 522	1.3	<1
L-Pt-3xOH	400 (127), 338 (sh, 2252), 304 (6894), 279 (sh, 4928)	461, 488, 519	1.7	<1
L-Pt-2xSO_4	400 (530), 335 (sh, 7696), 299 (15413)	460, 490, 519	2.2	<1
L-Pt-3xSO_4	400 (764), 336 (13532), 302 (43479), 276 (sh, 27980)	462, 488, 521	1.5	<1

[a] determined at diluted conditions within the Lambert-Beer regime (pH=7.2, 10^{-4} - 10^{-5} M). [b] λ_{ex} = 300 nm, aerated ambient conditions. [c] λ_{ex} = 375 nm, amplitude weighted average lifetime determined at low concentration, error ~ 1%. [d] determined at low concentration (below CAC), error ~ 5% [e] measured in a mixture of THF/MeOH (30%).

While the complexes remain molecularly dissolved in organic solvents, all compounds aggregate in (buffered) aqueous solution where all complexes show similar features, that are all indicative of Pt•••Pt interactions. The obtained spectra are depicted in Figure 5.11 and the photophysical data is summarized in Table 5.2. **L-Pt-2xOH** displayed the same low solubility such as **L-Pt-2xOMe** and was therefore also excluded from further studies. Nevertheless, a flash injection experiment yielded similar results as obtained for the analogous methylated complex. Therefore, for entirely neutral complexes at least three tetraethylene glycol branches are necessary to ensure sufficient solubility in water for encapsulation experiments.

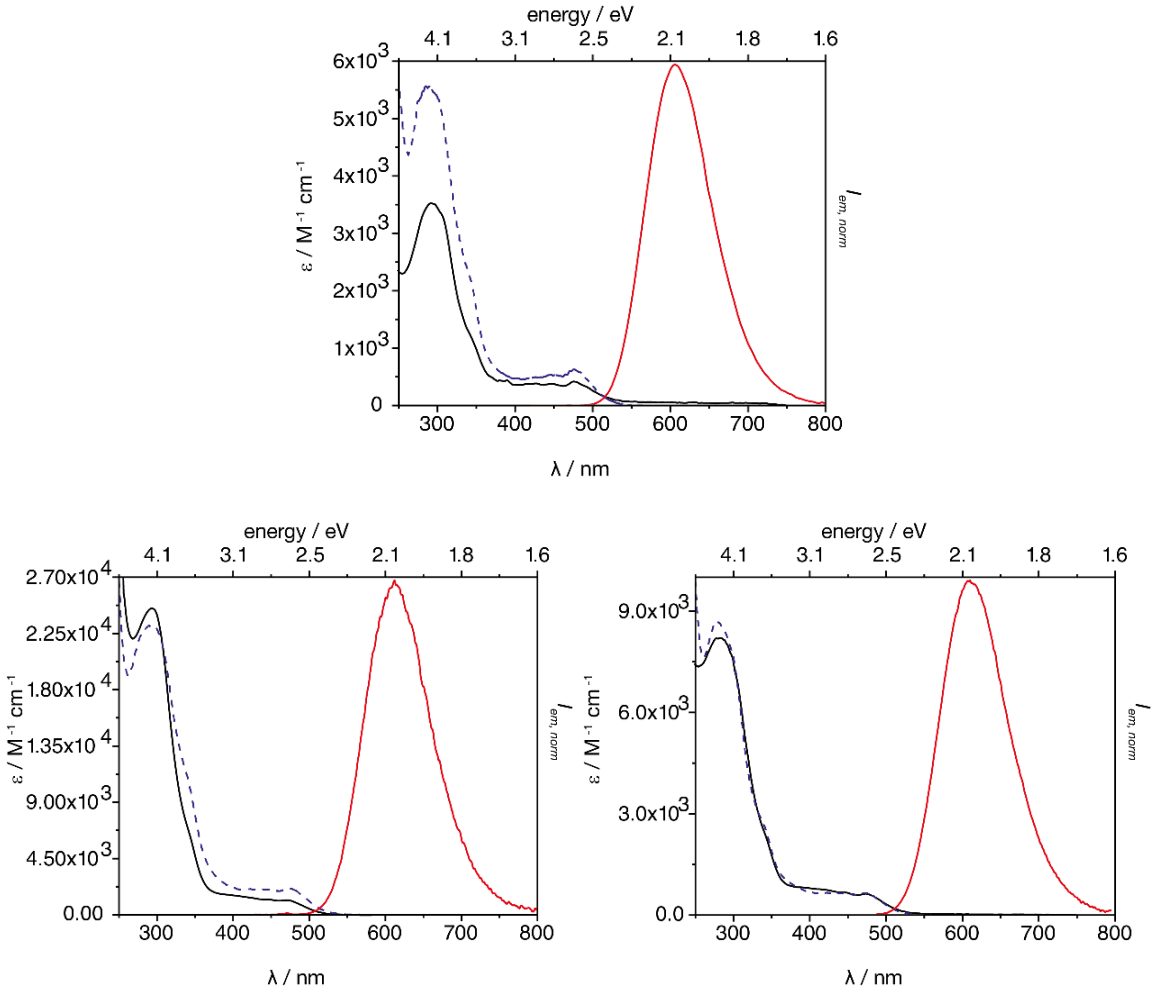

Figure 5.11: Absorption (black, solid), normalized emission (red, solid, λ_{ex} = 300 nm) and excitation (blue, dashed, $\lambda_{em} = \lambda_{em,max}$) spectra of the complexes **L-Pt-3xOH** (top), **L-Pt-3xSO$_4$** (bottom, left)and **L-Pt-2xSO$_4$** (bottom, right) in aerated TRIS buffer solution (pH = 7.2,10^{-4}-10^{-5}M).

The electronic transition spectra of the Pt(II)-amphiphiles are similar to those described for **L-Pt-3xOMe**. Notably, the emission quantum yield for the neutral complexes at ambient conditions ranges from 33 to 36% (3 branches), while the emission negatively charged complexes appears weaker (φ = 6 and 7% for **L-Pt-3xSO$_4$** and **L-Pt-2xSO$_4$**, respectively). As shown in Chapter III, Pt(II) of the same chromophoric framework featuring negatively charged ancillary ligand displayed only a weak emission. Presumably, similar effects are present for the negatively charged amphiphiles as well, but to a lesser extent on account of the remote positioning of the negatively charged sulfate groups.

Table 5.2: Summary of the photophysical properties of the Pt(II)-amphiphiles in TRIS buffer

Complex	λ_{abs} / nm (ε / $M^{-1}cm^{-1}$) [a]	λ_{em} / nm [b]	τ / ns [c]	φ / % [d]
L-Pt-2xOMe	477 (2892), 339 (sh, 4928), 276 (21162) [e]	575	460	26 [e]
L-Pt-3xOMe	475 (1123), 398 (750), 345 (sh, 3445), 290 (13873)	600	367 (443) [f]	36 (52) [f]
L-Pt-2xOH	476 (2642), 339 (sh, 4502), 276 (19332) [e]	592	719	58
L-Pt-3xOH	475 (416), 389 (437), 338 (sh, 1338), 291 (3522)	605	332 (552) [f]	33 (60) [f]
L-Pt-2xSO_4	476 (624), 393 (813), 335 (sh, 2807), 283 (8207)	607	139 (304) [f]	7 (32) [f]
L-Pt-3xSO_4	477 (1099), 402 (1535), 343 (sh, 6368), 294 (24491)	612	45 (171) [f]	6 (14) [f]

[a] determined at diluted conditions within the Lambert-Beer regime (pH=7.2, 10^{-4} - 10^{-5} M). [b] λ_{ex} = 300 nm, aerated ambient conditions. [c] amplitude weighted average lifetime determined at low concentration (below CAC), error ~ 1%. [d] determined at low concentration (below CAC), error ~ 5% [e] flash-injected from THF solution into deionized water (10^{-5} M). [f] measured at high concentration (1 10^{-3} M, above CAC)

All spectra depicted above as well as the obtained photophysical data, summarized in Table 5.1 and Table 5.2, were determined in solution at low concentrations (10^{-4}-10^{-5}M) that follow the lambert beer law. Nevertheless, some photophysical parameters strongly depend on the concentration, namely the excited-state lifetime (τ) and the quantum yield (φ). So, the quantum yields are strongly enhanced at higher concentration accompanied by long excited-state lifetimes. However, the emission profiles and maxima remained unaffected as exemplified for **L-Pt-3xOMe** in Figure 5.12. In the following part, a detailed analysis of the self-assembly of the amphiphiles in TRIS buffer solution is given, also on the basis of τ and φ data.

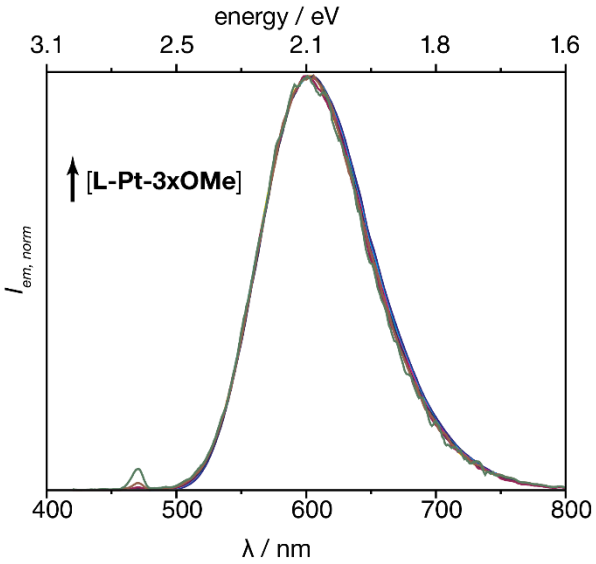

Figure 5.12: Normalized emission spectra of **L-Pt-3xOMe** for different concentrations from 1 10^{-3} - 5 10^{-6} M in TRIS buffer (pH=7.2) at ambient conditions.

Material characterization of the Pt(II)-complexes

A size analysis of the formed supermolecules by dynamic light scattering (DLS) was performed to probe the envisaged interaction with the coat proteins. Typically, a critical concentration is necessary to form stable self-assembled structures such as micelles. This critical micelle concentration (CMC) or more accurate critical aggregation concentration (CAC, because the shape is initially unknown) can be determined by various methods. An established and accessible technique is the determination of the count rate in a DLS measurement by fixed angle and attenuation with varying concentration.[55] Below the CMC, an increase of the amphiphile concentration has only a minor impact on the count rate. Above the CMC, the count rate linearly correlates with the concentration. At the CMC the slope of the plot (count rate vs. concentration) changes drastically its steepness, which can be used to identify the CMC.[55] Further methods were developed in this thesis taking advantageous of the intrinsic luminescence of the amphiphiles.

Methods for the determination of the CMC utilizing a fluorescence probe are established and taking advantage of the fact that the emission properties, namely, the excited-state lifetime and the quantum yield, can be strongly affected by the environment around the fluorophore. Therefore, with a fixed low fluorophore concentration (avoidance of inner filter effects) and upon increasing amphiphile concentration, the increase of the

fluorescence intensity follows two linear functions of different steepness. The crossing point of both linearly approximated functions identifies the CMC.

The necessity of concentration variations of the amphiphile to determine the CAC of the Pt(II)-amphiphiles excludes the above-mentioned technique on the basis of fluorescence spectroscopy, on account of inner filter effect. Primary inner filter effects are defined by the optical density at the excitation wavelength, whereas the secondary inner filter effects are determined by the optical density at the emission wavelength. Due to the large Stokes shift of the assembled Pt(II)-complexes (no reabsorption of emitted light) the secondary inner filter effects are negligible in the investigated system. Nevertheless, the primary inner filter effect would cause a perturbation of the linear dependence between the fluorescence intensity and the concentration, which is basis for the technique described above.

However, the quantum yield and excited-state lifetime of the Pt(II)-amphiphiles are strongly dependent on the environment of the phosphor and therefore can also serve as a read-out for the determination of the CAC. Whereas, the relative quantum yield determination method is limited to systems lacking inner filter effects (low concentration $A<0.1$), an integrating sphere setup can overcome this problem by scanning through several excitation wavelengths. On account of high absorption cross section values for accurate determination of the quantum yield with the integrating sphere, a reliable detection at lower concentrations is critical. Alternatively, excited-state lifetime measurements are known to show a dependency only on secondary inner filter effects, which are negligible for large Stokes shift phosphors such as the Pt(II)-amphiphiles.

Thus, excited-state lifetimes and DLS count rates were determined for a concentration series of each Pt(II)-amphiphile envisaged for the encapsulation into virus capsids, namely **L-Pt-3xOMe**, **L-Pt-3xOH**, **L-Pt-3xSO_4**, **L-Pt-2x-SO_4**. Noteworthy, although the complexes were thoroughly dried *in vacuo* the water might be not entirely removable due to the high ethylene glycol content. Thus, an uncertainty for the weighting and in turn for the actual concentration can arise.

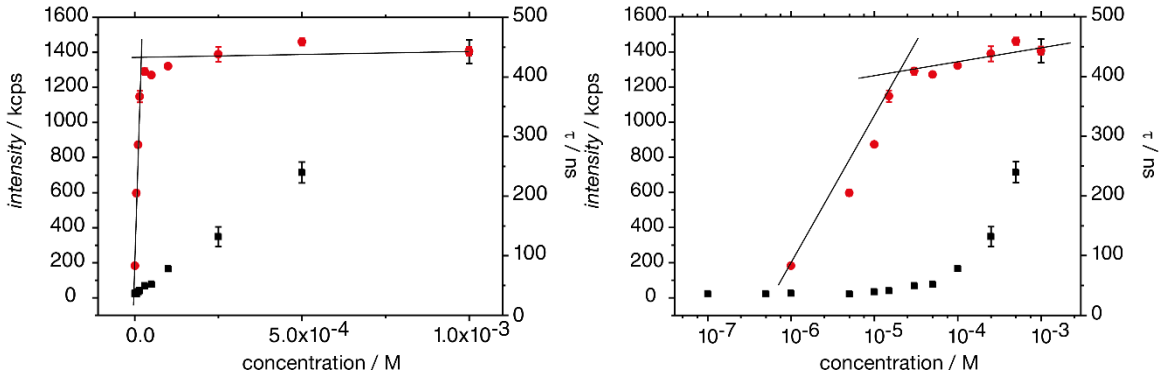

Figure 5.13: Plot of DLS intensity (black squares)/excited state lifetime (red dots) *versus* concentration of **L-Pt-3xOMe** in aqueous TRIS buffer solution (pH = 7.2). left: linear plots; right: semi-logarithmic plot.

As can be seen from Figure 5.13, a linear plot of the DLC intensity and excited-state lifetime against the concentration shows a strong accumulation of data points for low concentrations. This accumulation complicates an assessment of the CAC. In order to spread the data points, a semi-logarithmic plot was chosen. For **L-Pt-3xOMe**, only a minor decrease of the excited-state lifetime (τ) is observed from 1 10^{-3} M to 3 10^{-5} M, while from 1.5 10^{-5} M to 1 10^{-6} M a stronger decline is obtained. Above the CAC, all added molecules (increase of concentration) will form more assemblies with similar photophysical properties, therefore τ does not vary strongly and the DLS count rate increases linearly. These larger assemblies above the CAC most likely preserve their photophysical properties on account of rigidochromic effects. Below the CAC, the DLS count rate remains low independent on the concentration while τ is strongly affected, since only smaller assemblies can be formed (*e.g.* dimers) which are prone to faster deactivation of the excited state.

Linear approximations of the determined data points from 1 10^{-3} M to 3 10^{-5} M and from 1.5 10^{-5} M to 1 10^{-6} M display an apparent difference in steepness. The intercept of the two lines represent the CAC (2.2 10^{-5} M). The analysis for the other complexes are depicted in Figure 5.14 and summarized in Figure 5.14.

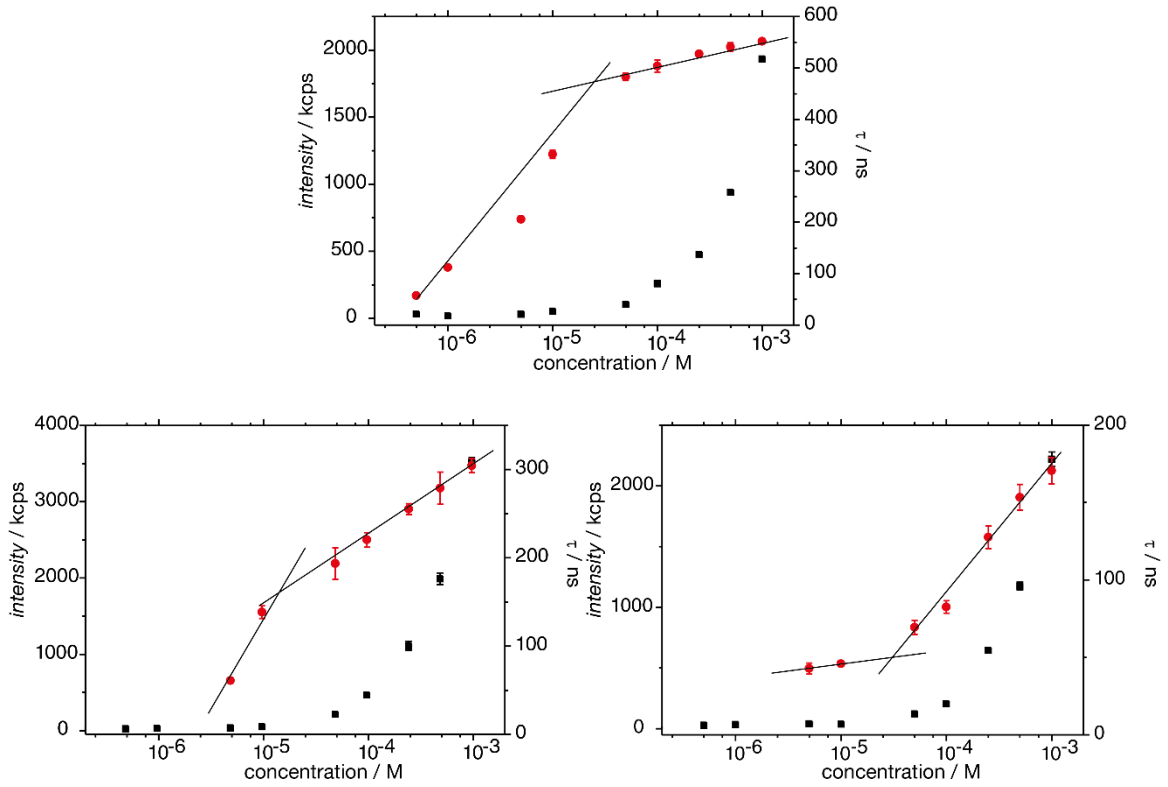

Figure 5.14: Semi-logarithmic plots of DLS intensity (black squares)/excited state lifetime (red dots) *versus* concentration of the Pt complexes in aqueous TRIS buffer solution (pH = 7.2). top: **L-Pt-3xOH**; bottom-left: **L-Pt-3xSO$_4$**; bottom, right: **L-Pt-2x-SO$_4$**.

All complexes exhibit a CAC at low concentration around 10^{-5} M. The novel CAC determination method on the basis of excited-state lifetime is in good agreement with the established DLS count-rate method.

Noteworthy, also at low concentrations (10^{-6} - 10^{-7} M) features indicative for a Pt•••Pt interactions are observed, namely the MMLCT band at 475 nm in absorption/excitation spectrum, broad featureless emission around 600 nm and long excited-state lifetimes. Therefore, even at low concentrations small assemblies are present, presumably dimers.

Table 5.3: Summary of the physical properties of the Pt(II)-amphiphiles in TRIS buffer

Complex	D_{hyd} / nm [a]	CAC-DLS / M [b]	CAC-τ / M [c]
L-Pt-3xOMe	24.2 ± 3.6	$5.3\ 10^{-5}$	$2.2\ 10^{-5}$
L-Pt-3xOH	21.9 ± 3.3	$2.4\ 10^{-5}$	$2.8\ 10^{-5}$
L-Pt-3xSO_4	5.6 ± 1.5	$1.8\ 10^{-5}$	$3.2\ 10^{-5}$
L-Pt-2xSO_4	8.7 ± 2.2	$9.7\ 10^{-6}$	$1.1\ 10^{-5}$

[a] hydrodynamic diameter determined by DLS in aqueous TRIS buffer solution (pH = 7.2) after filtration (syringe filter with pore size ~ 220 nm) [b] determined with DLS at fixed angle and attenuation, CAC error ~ 10%. [c] determined by excited-state lifetime measurements CAC error ~ 10%, λ_{ex} = 405 nm.

The size of the assemblies above the CAC was determined by DLS, which enables the estimation of the hydrodynamic diameter on the basis of the Stokes-Einstein equation approximating a spherical hard particle.[56] Supramolecular assemblies and other materials appear in solution oftentimes non-spherical, dynamic and solvated. Therefore, the diameter derived from the diffusional properties of the sample is indicative of the apparent size of dynamic hydrated particles.[57] The obtained hydrodynamic or Stokes diameter is that of a sphere, which exhibits the same translational diffusion coefficient as the measured particle featuring a surrounding hydration layer. The Stokes diameters of the self-assembled Pt(II)-complexes in TRIS buffer solution (pH = 7.2) are listed in Table 5.3.

The hydrodynamic diameter is around 23 nm for the neutral complexes, while the negatively charged complexes appear smaller featuring a size around 7 nm. Notably, all assemblies are of a similar or smaller size as the interior of a virus coat protein cage being around 10, 15 and 21 nm for T = 1, 2 and 3, respectively.

In order to determine the morphology on the investigated assemblies small-angle X-ray scattering (SAXS) experiments are ongoing. Preliminary Cryo-TEM measurements were carried out as well but did not allow a clear determination of the size and the shape of the assemblies. A current collaboration with Pablo Castro-Hartmann focuses on the assessment of the size and shape of the assemblies by Cryo-TEM measurement.

Encapsulation into CCMV capsids

The growth and purification of the native CCMV virus, the RNA removal and isolation of the coat proteins (CP) were performed by following the literature.[58, 59] The encapsulation into virus coat proteins can be performed in two ways: *i)* tuning the pH value from basic (7.2) to acid (5.1), which allows the CPs to self-assemble and result in a random encapsulation of cargos. This method is based on the protein-protein interactions and yield domains of filled and empty protein cages of native T = 3 state. *ii)* preserving the pH value at basic conditions (7.2) while a negative cargo induces the formation of protein shells. This templating procedure is based on the charge compensation between the positively charged CPs and the negative cargo and result in mostly filled VLPs of a shape also dependent on the cargo.

For the encapsulation of the herein presented Pt(II)-amphiphiles, the method was optimized from literature protocols.[15, 21, 35] A stock solution of CP ($1\ 10^{-4}$ M) in TRIS buffer (50 mM tris, 300 mM NaCl, 10 mM $MgCl_2$) was mixed in a molar ratio of 1:5 with a stock solution of Pt(II)-amphiphile ($1\ 10^{-3}$ M) in TRIS buffer (50 mM tris, 10 mM $MgCl_2$). For the neutral complexes, **L-Pt-3xOMe** and **L-Pt-3xOH**, the pH value was tuned to 5.1 shortly after mixing with a concentrated solution of NaOAc buffer (0.2 M, pH = 5.0). The charged complexes, **L-Pt-3xSO_4**, **L-Pt-2xSO_4**, templated shortly after the mixing the formation of the virus like particles, and thus no additional buffer was necessary. Experiments with a Pt(II)-complex concentration of 1, 2 and $4\ 10^{-3}$ M were conducted. The formed VLPs were subsequently purified by fast protein liquid chromatography by using NaOAc buffer (100 mM NaAc, 150 mM NaCl, pH = 5.0) as eluent.

Material characterization of VLPs

The FLPC not only serves as a preparative method to obtain pure VLPs, but also as an analytical tool. The elution volume provides a measure of the size of the particles and therefore gives insights into the shape if the interactions between particle and column are known (references). FPLC chromatograms of the obtained VLPs, utilizing a standard elution procedure established in the Cornelissen labs, are depicted in Figure 5.15.

Random assemblies of CPs to large, undefined aggregates commonly peak at 7.5 mL. The native CCMV protein cages with T = 3 and an outer diameter of 28 nm and typically

eluent at a volume of 9.5 mL. A shape change, induced for instance by a negative cargo template, to the smaller protein cage with T = 1 is oftentimes observed at 11.5 mL. Smaller particles appear at higher elution volumes *e.g.*, Pt(II)-assemblies (~21 mL) or CP dimers (~17.5 mL). The shape, broadness and position of the peaks depend on the encapsulation method and the cargos.

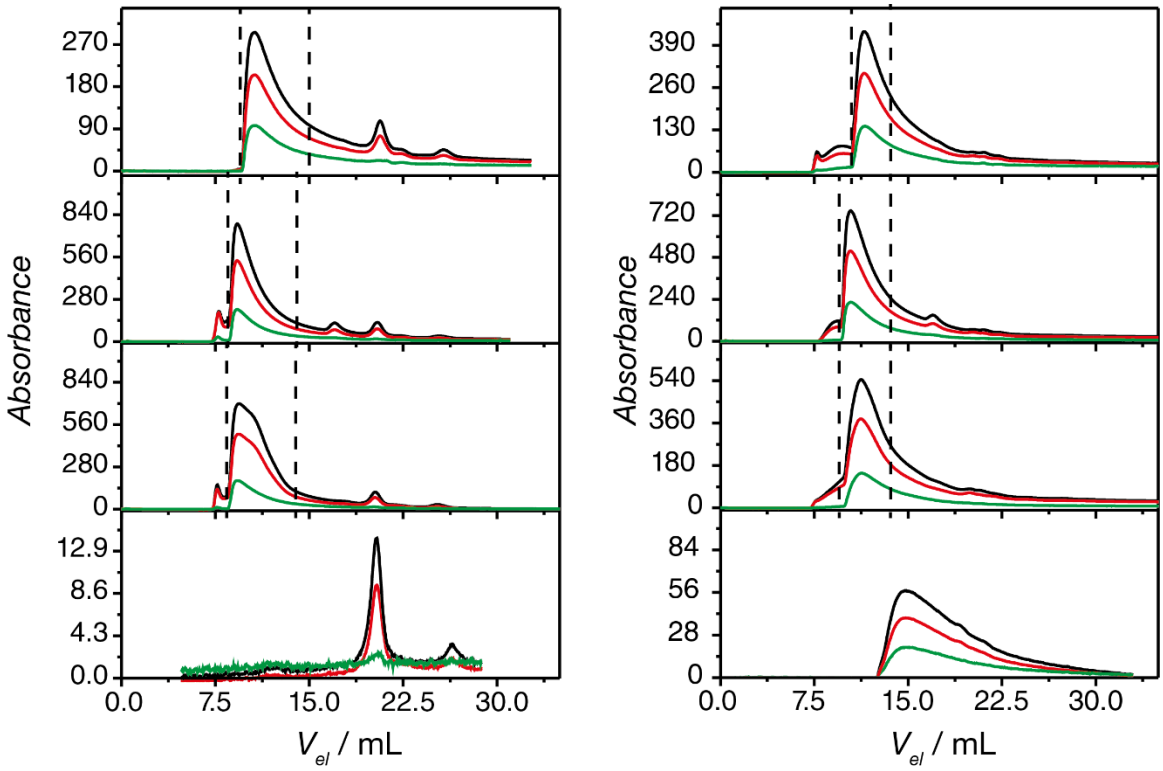

Figure 5.15: FPLC chromatograms of **VLP@3xOMe** (left) and **VLP@3xOH (**right**).** From top to bottom: 1 10^{-3}M, 2 10^{-3}M, 4 10^{-3}M initial Pt concentrations, and pure complex without capsid at 1 10^{-3}M at the bottom: **L-Pt-3xOMe** (left), **L-Pt-3xOH** (right). The vertical dashed lines indicate the isolated fractions for analysis. The colors assign different absorbance wavelength: 260 (black), 280 (red) and 340 nm (green).

FPLC fractions are collected in standard 96 well-plate and thus could be isolated according to the chromatogram. For the VLPs containing neutral Pt(II)-complexes chromatograms peaking between 10.5 and 11.5 mL featuring a tailing at higher volume. The VLPs carrying the Pt(II)-complexes most likely possess different interactions with the column material, which explains the broadness of the observed peaks. Nevertheless, the position of the peaks and the encapsulation method, indicate for T = 3 VLPs. **VLP@3xOMe** could be easily separated from the Pt(II)-amphiphile **L-Pt-3xOMe** on account of the high retention volume of the complex (Figure 5.15, bottom). For

VLP@3xOH the isolated fraction volume was reduced due to the relatively low retention volume of unconverted **L-Pt-3xOH**.

The VLPs of the negatively charged Pt(II)-amphiphiles **VLP@3xSO$_4$** and **VLP@2xSO$_4$** display sharpened peaks in the FPLC chromatograms in comparison to its neutral analogues. The peaks appear around 10.8 mL indicating the formation of T = 3 particles. Presumably, the templating effect defines the formation of the capsids and thus avoiding defects and miss arrangements of CPs.

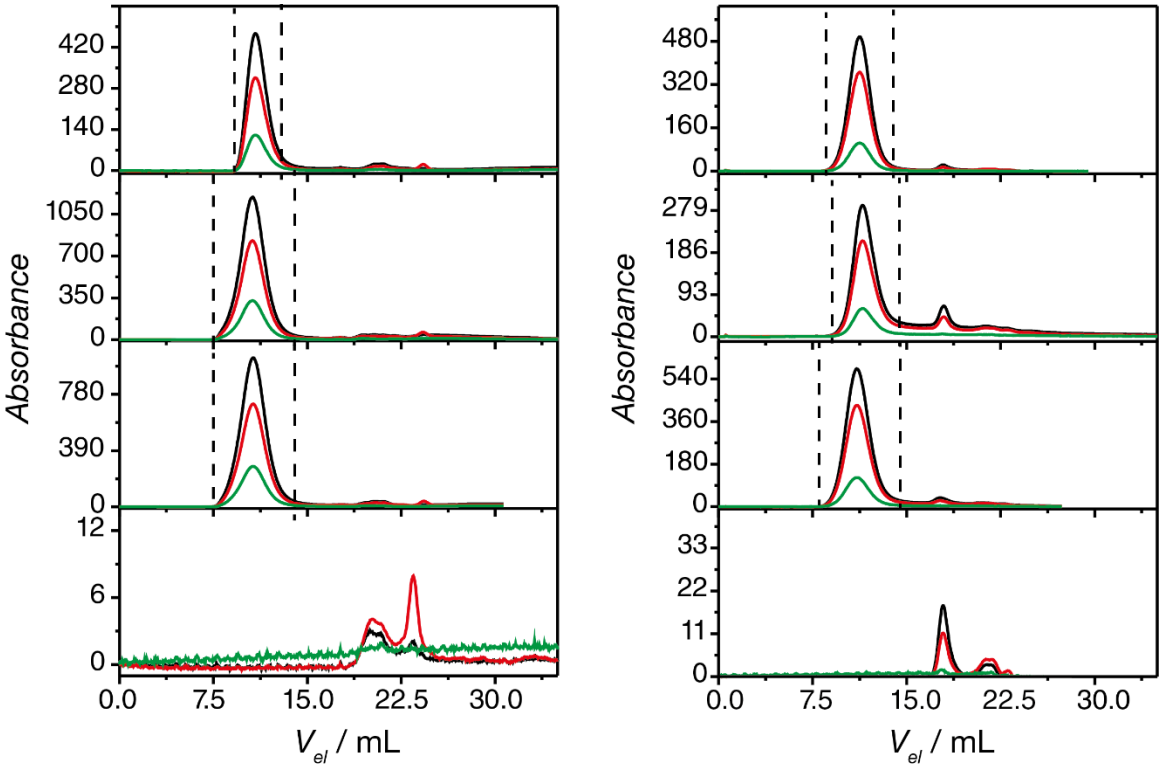

Figure 5.16: FPLC chromatograms of **VLP@3xSO$_4$** (left) and **VLP@2xSO$_4$ (**right**).** From Top to bottom: 1 10^{-3}M, 2 10^{-3}M, 4 10^{-3}M initial Pt concentrations, and pure complexes without capsid at 1 10^{-3}M at the bottom: **L-Pt-3xSO$_4$** (left), **L-Pt-2xSO$_4$** (right) The dashed lines indicate the isolated fractions for analysis. The colors assign different absorbance wavelength: 260 (black), 280 (red) and 340 nm (green).

The collected fractions were analyzed by DLS to estimate the size of the formed protein cages. The DLS measurements are in agreement with the FPLC measurements, indicating the formation of virus like particles featuring a Stokes diameter around 27 nm. The size differences between the possible icosahedral shapes are minor, namely T = 1 (~27 nm), T = 2 (~25 nm), T = 3 (~18 nm). These variations are challenging to estimate from the measurement of the measurement of the hydrodynamic diameter and is should not be over interpreted for the estimation of the shape.

The intensity distributions display clear peaks centered at the hydrodynamic diameter, while no smaller assemblies are detected (Figure 5.13). The FPLC chromatograms and the DLS data confirm the absence of small Pt(II)-assemblies in isolated fractions.

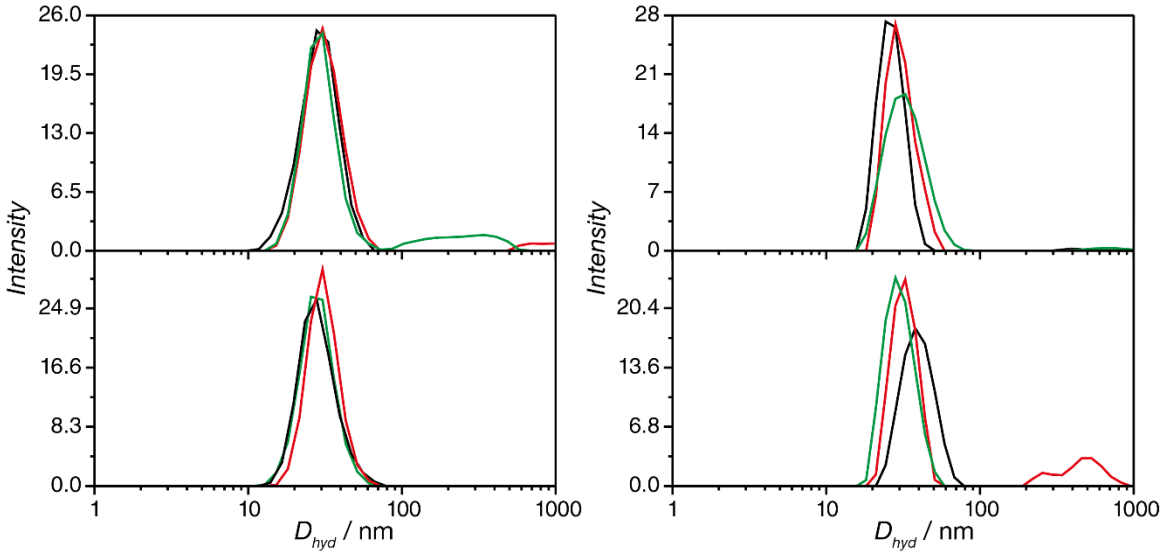

Figure 5.17: DLS intensity distributions of the VLPs **VLP@3xOMe** (left, top), **VLP@3xOH** (left, bottom), **VLP@3xSO$_4$** (right, top), **VLP@2xSO$_4$** (right, bottom). The color of the distribution indicates the applied concentration of the Pt(II)-amphiphiles: 1 10^{-3} M (black), 2 10^{-3} (red), 4 10^{-3} (green).

To further confirm the estimated structures from FPLC and DLS, transmission electron microscopy (TEM) experiments were performed. The TEM samples were stained with uranyl acetate as contrast agent. Filled protein cages appear as spherical particles with an entirely bright contrast, while empty cages appear with a dark contrast in the interior, resembling donuts. Representative TEM images are depicted in Figure 5.18 and Figure 5.19.

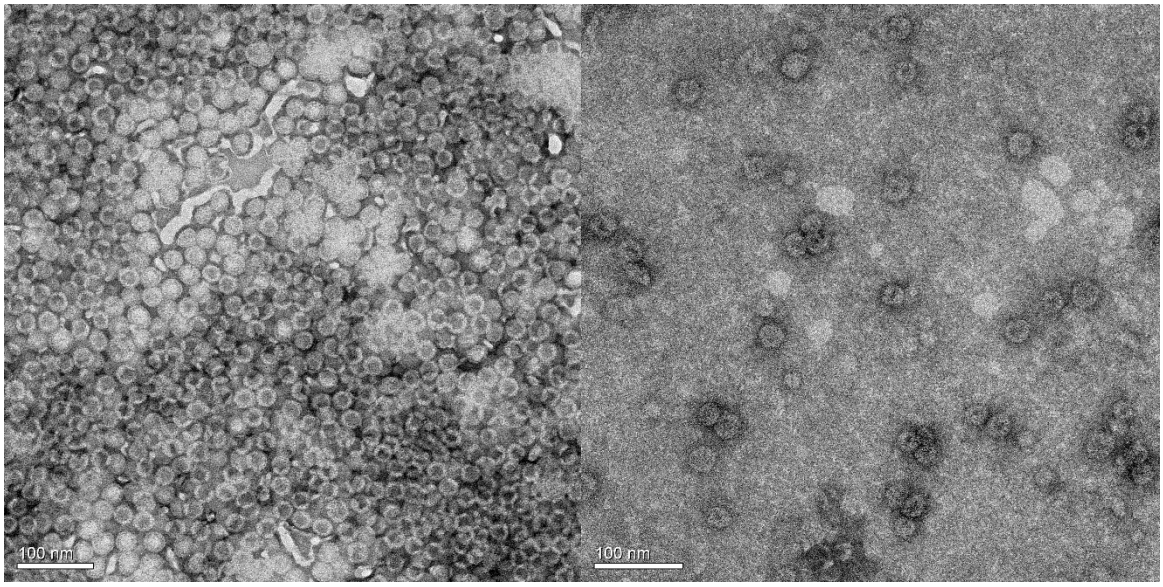

Figure 5.18: Representative TEM images of the VLPs of **VLP@3xOMe** (left) **VLP@3xOH** (right), stained with uranyl acetate. Scale bar: 100 nm.

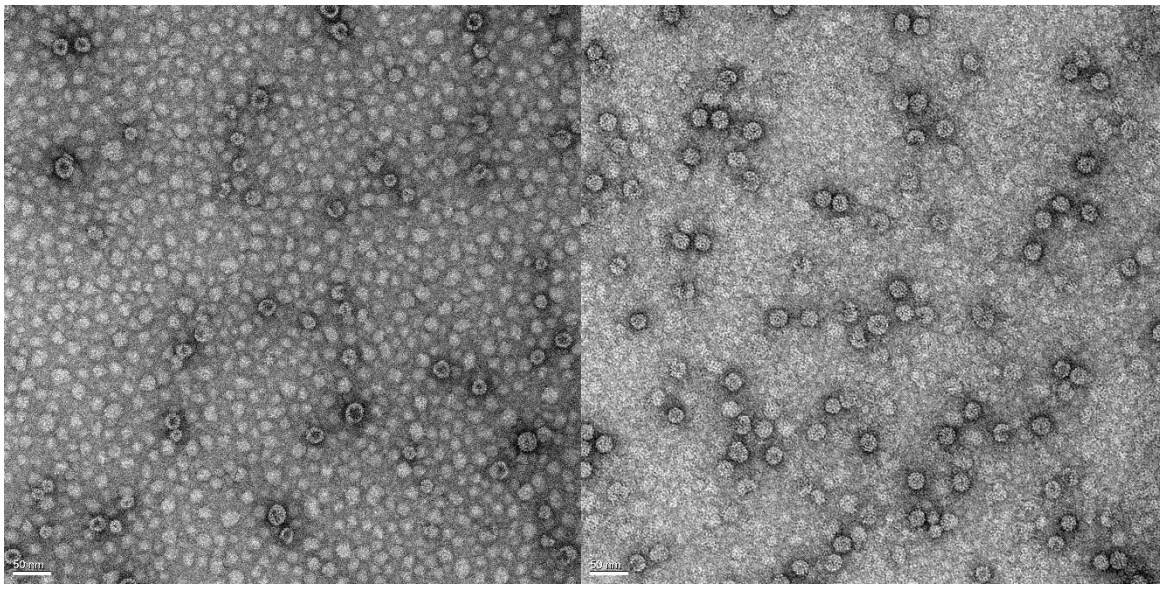

Figure 5.19: Representative TEM images of the VLPs of **VLP@3xSO$_4$** (left) and **VLP@2x-SO$_4$** (right), stained with uranyl acetate. Scale bar: 50 nm.

For the neutral amphiphile VLPs, subsets of filled and empty cages are obtained with a diameter around 28 nm (T = 3). Thus, the random encapsulation method yielded the natively shaped particles. Contrarily, the VLPs templated by the negatively charged amphiphiles display predominantly filled spherical particles with a slightly smaller diameter around 22 nm (T = 2). In all cases, only spherical particles were obtained indicating no disruption of the icosahedral protein arrangement.

For further assessment of the platinum content, high-angle annular dark-field scanning transmission electron microscope (HAADF-STEM) experiments were performed. In such a case, no contrast agent was added, but the heavy metal Pt displays a bright contrast within a low contrast protein (carbon) shell on carbon grids. The presence of Pt was further confirmed by energy dispersive X-ray spectroscopy (EDX). Figure 5.20 depicts the STEM experiments exemplified for **L-Pt-3xOH**.

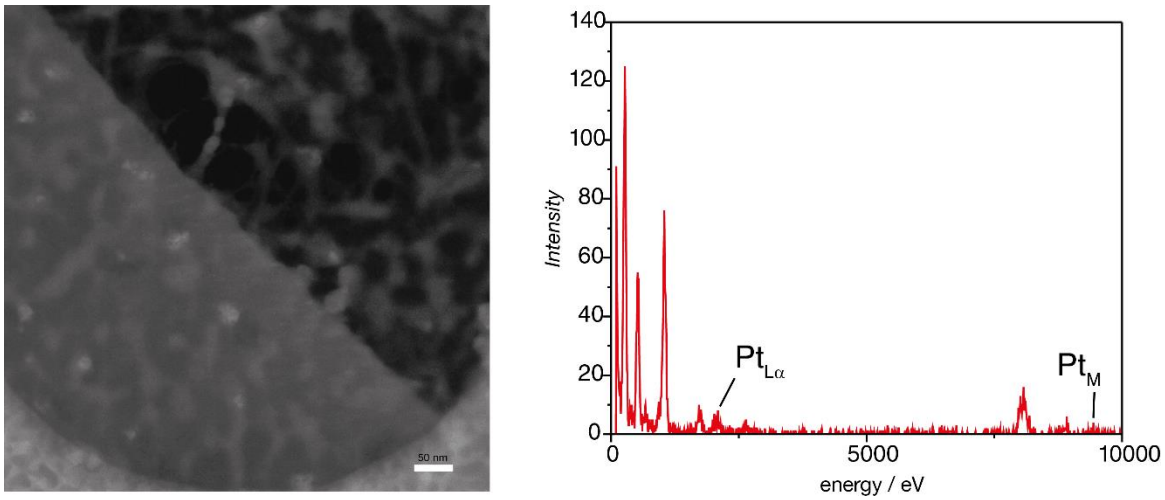

Figure 5.20: left: High-angle annular dark-field imaging scanning transmission electron microscope (HAADF-STEM) image of **L-Pt-3xOH.** right: energy dispersive X-ray spectroscopy (EDX) diagram of the sample.

Photophysics of the VLPs

The obtained VLPs with either neutral or negative Pt(II)-assemblies as cargos display a strong room temperature emission. The VLPs were therefore photophysically investigated, the absorption, excitation and emission spectra for the individual Pt-VLP at different concentration of Pt-amphiphile are depicted in Figure 5.21 and the photophysical information are summarized in Table 5.4.

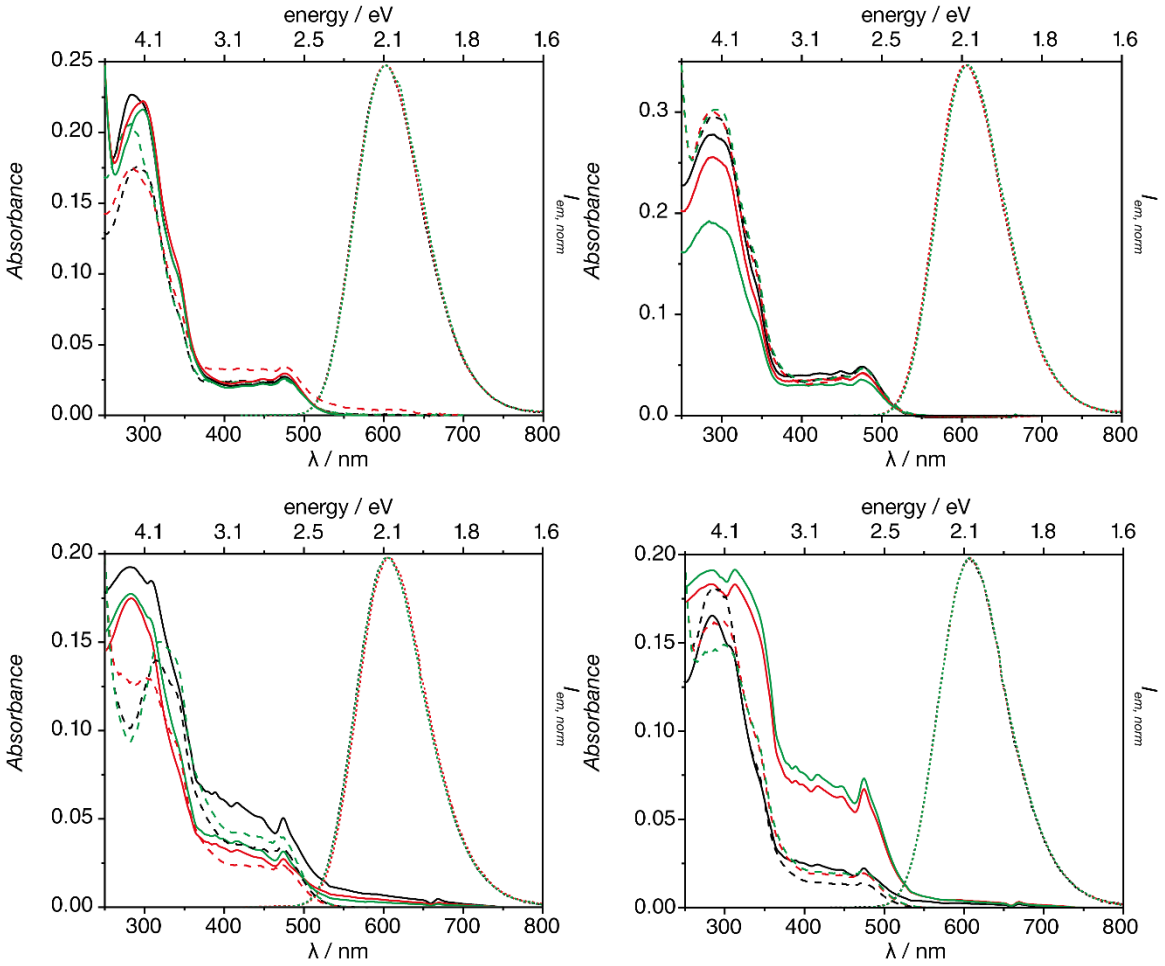

Figure 5.21: Absorption spectra (solid), normalized emission (dotted, λ_{exc} = 405 nm) and excitation (dashed, $\lambda_{em} = \lambda_{em,max}$) spectra of the VLPs containing the Pt(II)-complexes. The color of the spectrum indicates the applied encapsulation concentration: 1 10^{-3}M (black), 2 10^{-3} (red), 4 10^{-3} (green). top, left: **VLP-3xOMe**; top, right: **VLP-3xOH**; bottom, left: **VLP-3xSO$_4$**; bottom, right: **VLP-2xSO$_4$**;

The shape of the absorption, excitation and emission spectra resemble the ones of the Pt amphiphiles in buffered solution. A strong MMLCT transition is observed at 475 nm and the broad emission profiles peak around 600 nm. The emission profiles are independent on the excitation wavelength.

Remarkable quantum yields for all Pt-VLPs of 47 – 59% were obtained. The encapsulation into virus cages enhances the quantum yield (φ, λ_{exc} = 300 - 500 nm) of the Pt(II)-amphiphiles most likely due to rigidochromic effects in the confined space. The enhancement is expressed as the enhancement factor (EF), which is calculated from the ratio of φ of the VLP and φ of the sole Pt(II)-amphiphile at a comparable concentration. As discussed in the previous part, the photophysical properties depend on the aggregation

and thus the concentration of the Pt(II)-complex. The global concentration of Pt(II)-amphiphile in the isolated VLP fraction was estimated from the UV-Vis spectra and listed in Table 5.4. The quantum yield of a comparable concentration in buffered solution was then used to calculate EF. While the enhancement remains modest for the neutral complexes, the negatively charged VLPs reveal superior EFs of up to 13.

Table 5.4: Summary of the photophysical properties of the VLPs

VLP	[Pt] / M [a]	c_{Pt} / M [b]	λ_{em} / nm [c]	τ / ns [d]	φ / % [e]	EF [f]
VLP@3xOMe	$1\ 10^{-3}$	$1.92\ 10^{-5}$	601	467	55	1.5
	$2\ 10^{-3}$	$2.39\ 10^{-5}$	601	469	47	1.3
	$4\ 10^{-3}$	$1.80\ 10^{-5}$	601	487	50	1.4
VLP@3xOH	$1\ 10^{-3}$	$4.66\ 10^{-5}$	605	516	56	1.1
	$2\ 10^{-3}$	$4.08\ 10^{-5}$	605	492	51	1.0
	$4\ 10^{-3}$	$3.53\ 10^{-5}$	605	498	56	1.2
VLP@2xSO$_4$	$1\ 10^{-3}$	$6.61\ 10^{-5}$	604	653	55	4.2
	$2\ 10^{-3}$	$3.55\ 10^{-5}$	604	553	45	4.5
	$4\ 10^{-3}$	$4.47\ 10^{-5}$	604	655	55	5.0
VLP@3xSO$_4$	$1\ 10^{-3}$	$6.3\ 10^{-5}$	607	613	52	13.0
	$2\ 10^{-3}$	$1.0\ 10^{-4}$	607	613	59	9.8
	$4\ 10^{-3}$	$1.1\ 10^{-4}$	607	612	59	9.8

[a] initial Pt(II)-amphiphile concentration for encapsulation. [b] global Pt(II)-complex concentration in analyzed buffer solution after FPLC purification, determined from absorption spectrum [c] λ_{ex} = 405 nm,, aerated ambient conditions. [d] λ_{ex} = 405 nm, amplitude weighted average lifetime, error ~ 1%. [e] error ~ 5% [f] enhancement factor.

The confined cargo interior leads to a high local concentration in the mM range (estimated from UV-Vis)[33, 35], which leads to the strong enhancement of the emission quantum yield. Furthermore, the charge compensation between the negative cargos and the proteins guiding the formation of the cages probably also reduces possible quenching effect from the sulfate groups (*vide supra* and Chapter III).

Initial approaches either with induced pH change (self-assembly of CPs) or in constant low basic conditions (charge compensation between CP and cargo) where conducted following literature procedures.[33, 35] There, the CP stock solutions contained dithiothreitol

(DTT), which is a reducing agent and prevents the oxidization of protein sulfides.[60] This is a common method to preserve proteins over a long time span.

VLPs were obtained with these stock solutions lacking any emission. DTT is a quenching agent not only for fluorescence but also for phosphorescence, presumably by an electron-transfer to the disulfide (after oxidation).[61-63] The omission of DTT enabled the achievement of the phosphorescent VLPs.

Induced Shape Change

From the results obtained so far, it is concluded that a negative charge is necessary to induce a template effect. No template effect was observed for amphiphiles decorated only with TEG branches. The size of the assemblies is in the same range as the interior of the protein cages. Examples, that induced a shape change of the capsids from icosahedral to cylindric structures are based on larger cargo, that are negatively charged.

Therefore, the Pt(II)-complex, **L-Pt-Alkyl-2xSO$_4$**, was synthesized on the basis of preliminary reports[33, 34] that is coordinated by a pyridine ligand with two alkyl branched pyridine featuring sulfate end groups (Scheme 5.5). On account of the increased hydrophobic area, it was supposed that this complex forms larger assemblies. The synthesis is described in detail in the experimental part.

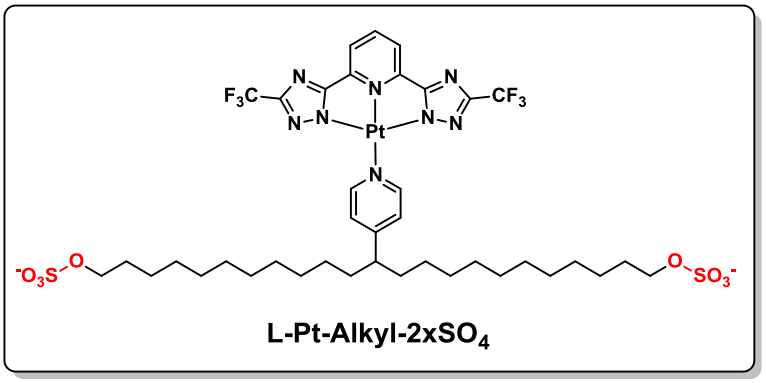

Scheme 5.5: Schematic representation of complex **L-Pt-Alkyl-2xSO$_4$**, which was synthesized on the basis of the obtained results.

The photophysical properties of this complex are fundamentally akin to those of the complexes discussed above and their electronic spectra are similar. However, the assembly properties markedly differ; Specifically, in THF an absorption spectrum with a weak MLCT band around 400 nm and a weak structured emission (^{3}LC based) is

observed. In comparison to the other complexes, the quantum yield ($\varphi = 58.3$) is relatively high in buffered solution also at very low concentrations and a critical aggregation concentration of 1.5 10^{-5} M was determined (DLS and τ method). In buffered solution, the broad emission (^{3}MMLCT based) peaks around 578 nm featuring an excited-state lifetime of 645 ns. DLS measurements reveal contrarily to the other complexes, larger particles featuring a Stokes diameter around 1 μm. The buffered dispersions of this complex are only stable over few hours until a precipitation is observed, in contrast to Pt(II)-amphiphiles **L-Pt-3xSO$_4$** and **L-Pt-2xSO$_4$**.

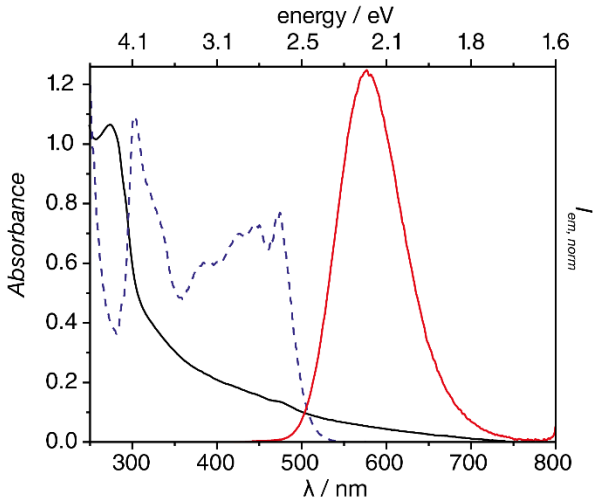

Figure 5.22: Absorption (black, solid), normalized emission (red, solid, $\lambda_{ex} = 405$ nm) and excitation (blue, dashed, $\lambda_{em} = \lambda_{em,max}$) spectra of **VLP@Alkyl-2xSO$_4$**. For encapsulation, the utilized concentration of **L-Pt-Alkyl-2xSO$_4$** was adjusted to 0.5 10^{-3} M due to its low solubility. The molar ratio 5:1 between complex and CPs was preserved.

Complex **L-Pt-Alkyl-2xSO$_4$** was subjected to the encapsulation method as described for the other complexes. The pH value was not tuned, on account of the templating effect of the negatively charged assemblies. The TEM images of the resultant VLP display subsets of spherical and cylindrical (non-icosahedral) particles. Furthermore, the obtained VLP displays room temperature emission peaking at 600 nm with a quantum yield of 23% and an excited-state lifetime of 462 ns, and is excitable in the visible region (Figure 5.22). The reason for the relatively low quantum yield (compared to the other VLPs) is under current investigation.

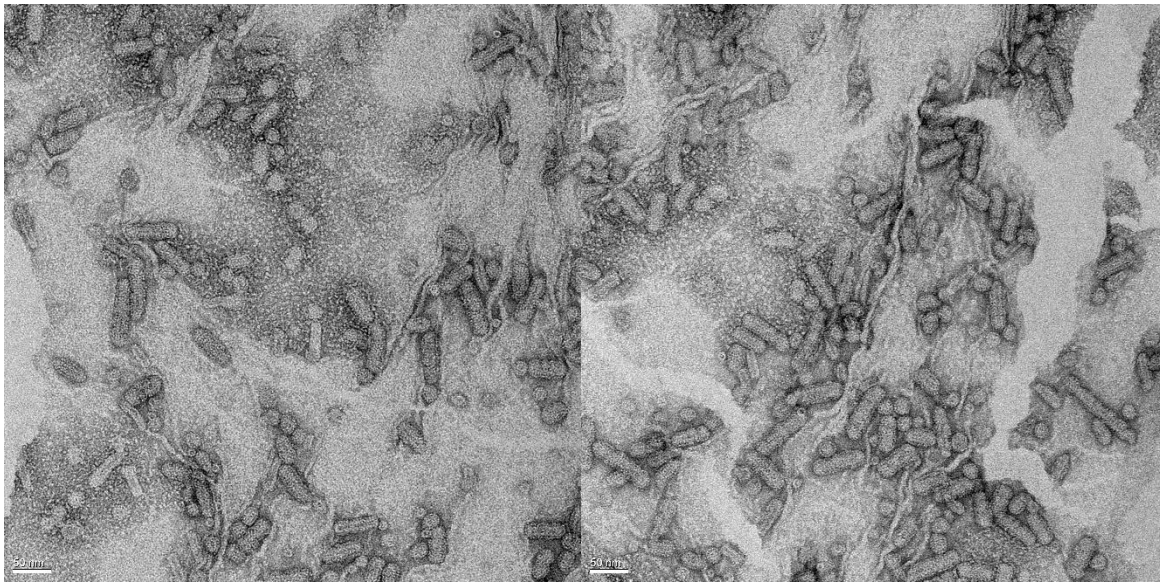

Figure 5.23: TEM images with uranyl acetate staining of **VLP@Alkyl-2xSO_4**.

Conclusion

Pt(II)-amphiphiles decorated with tetraethylene glycol branches and sulfate groups were synthesized and probed for their self-assembly properties. The luminescent Pt(II)-complexes are soluble in organic and aqueous buffered solution. In the latter one, intense room temperature emission was observed also at low concentrations. The photophysical properties are strongly dependent on the aggregation state and therefore the concentration. A novel method for determination of the critical aggregation concentration was established by probing the excited-state lifetime.

The small molecule stacks were encapsulated into CCMV protein cages, yielding luminescent virus like particles. A remarkable enhancement of a factor of 13 was observed for the negatively charged amphiphiles rendering a VLP quantum yield of 59%. Such a strong enhancement upon encapsulation as well as such a high quantum yield for VLPs was so far not reported in the literature.

Furthermore, a Pt(II)-complex was synthesized tethered with sulfated alkyl chains, which rendered the perturbation of the icosahedral capsid structure. This is one of the first examples for the formation of luminescent cylindric VLPs by self-assembled Pt(II)-complexes.

Experimental part

The encapsulation of the Pt(II)-amphiphiles into CCMV coat proteins was performed at the University of Twente under the supervision of Liulin Yang of the group of Prof. Jeroen Cornelissen, who are kindly acknowledged. The STEM experiments were conducted together with Di Wang from the group of Christian Kübel at the Karlsruhe Institute of Technology, who are kindly acknowledged.

The terdentate ligand **L-2H** and the corresponding Pt(II) precursor **L-Pt-DMSO** were synthesized as described in the previous chapters.

Synthesis of Ts-O-TEG-O-Me

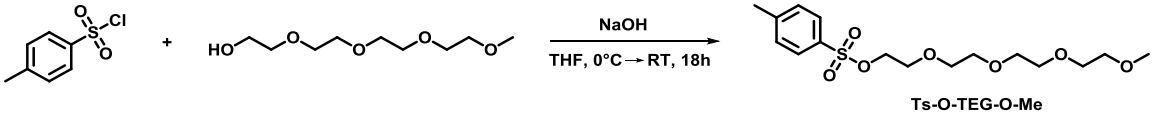

NaOH (3.4 g, 85 mmol) was dissolved in water (10 mL) and cooled to 0°C, and subsequently added to a solution of tetraethylene glycol mono methyl ether (10.4 g, 50 mmol) in THF (50 mL) under constant stirring. The reaction mixture was kept at 0 °C and *p*-toluenesulfonyl chloride (TsCl, 12 g, 62 mmol) dissolved in THF, was carefully added. The reaction mixture was allowed to heat to room temperature and stirred overnight. The crude reaction mixture was concentrated *in vacuo* featuring a water-bath temperature of 30°C and subsequently two times extracted with DCM. The combined organic layers were dried over Na_2SO_4 and all volatiles were evaporated *in vacuo* yielding a pure colorless viscous liquid (15 g, 0.041 mol, 82%).

Synthesis of HO-TEG-O-Bnz

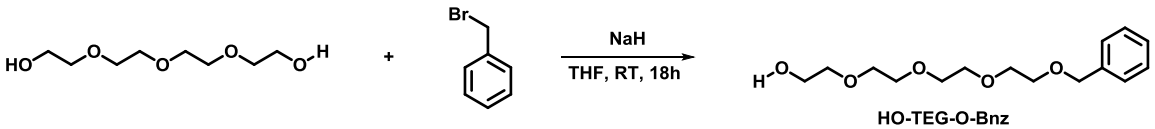

Benzyl bromide (3.47 mL, 5 g, 29 mmol) was added to a mixture of tetraethylene glycol (45 g, 233 mmol) and THF (15 mL). Afterwards, NaH (772 mg, 32 mmol) was added portion-wise and the reaction mixture stirred at ambient temperature overnight. The residual of NaH was quenched with brine and the crude product three times extracted with DCM/brine. The combined organic layers were dried over Na_2SO_4 and all volatiles

were evaporated *in vacuo*. Subsequently, the crude product was subjected to a column chromatography (Silica, EtAc) yielding to a pure colorless viscous liquid (6.4 g, 21 mmol, 72%). HR-ESI-ToF-MS (positive scan, m/z): $[M+Na]^+$ calcd. 307.1516; found 307.1523. HPLC-MS: t_R = 0.99 min.

Synthesis of Ts-O-TEG-O-Bnz

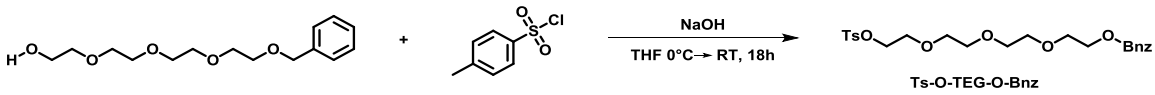

NaOH (1.4 g, 36 mmol) was dissolved in water (10 mL) and cooled to 0°C, and subsequently added to a solution of **HO-TEG-O-Bnz** (6.4 g, 21 mmol) in THF (50 mL) under constant stirring. The reaction mixture was kept at 0°C and *p*-toluenesulfonyl chloride (TsCl, 5.2 g, 27 mmol) dissolved in THF, was carefully added. The reaction mixture was allowed to heat to room temperature and stirred overnight. The crude reaction mixture was concentrated *in vacuo* featuring a water-bath temperature of 30°C and subsequently two times extracted with DCM. The combined organic layers were dried over Na_2SO_4 and all volatiles were evaporated *in vacuo* accomplishing a colorless viscous liquid (7 g, 16 mmol, 76%). HR-ESI-ToF-MS (positive scan, m/z): $[M+Na]^+$ calcd. 461.1537; found 461.1570. HPLC-MS: t_R = 1.76 min.

Synthesis of Py-Alkyl-Br

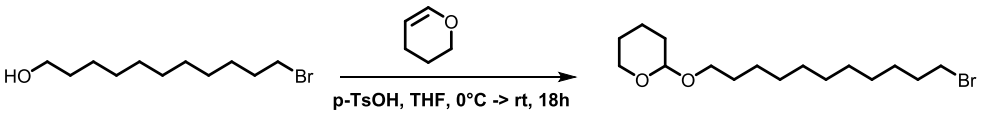

Py-Alkyl-Br

The synthesis was performed as described in the literature.[34] A colorless liquid was obtained (750 mg, 2.23 mmol, 56%).

^{1}H NMR (400 MHz, $CDCl_3$, ppm) δ 4.57 (m, 1H), 3.86 (m, 1H), 3.71 (m, 1H), 3.50 (m, 1H), 3.40 (m, 3H), 1.84 (m, 3H), 1.71 (m, 1H), 1.58 (m, 7H), 1.35 (m, 16H). HR-ESI-ToF-MS (positive scan, m/z): $[M+Na]^+$ calcd. 357.1400; found 357.1386.

Synthesis of PA-2xOMe

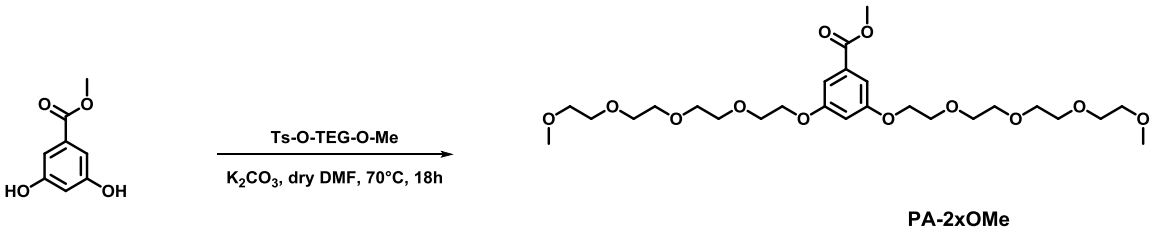

Following the literature in parts,[64] **Ts-O-TEG-O-Me** (3000 mg, 8.28 mmol) was dissolved together with methyl 3,5-dihydroxybenzoate (DTB, 695 mg, 4.14 mmol) and K_2CO_3 (3095 mg, 22.4 mmol) in dry DMF (20 mL) and heated to 70 °C for 18 h under nitrogen atmosphere. The solution displayed an intense brownish color shortly after launch. Water was added and the crude reaction mixture was four times extracted with DCM. The organic layers were combined and washed with water as well as brine and subsequently dried over Na_2SO_4. After evaporation of the solvents, the brown product was used without further purification (1657 mg, 3.02 mmol, 73%) (HPLC-MS analysis confirmed majority of product). HR-ESI-ToF-MS (positive scan, m/z): $[M+Na]^+$ calcd. 571.2725; found 571.2747. HPLC-MS: t_R = 1.21 min.

Synthesis of PA-3xOMe

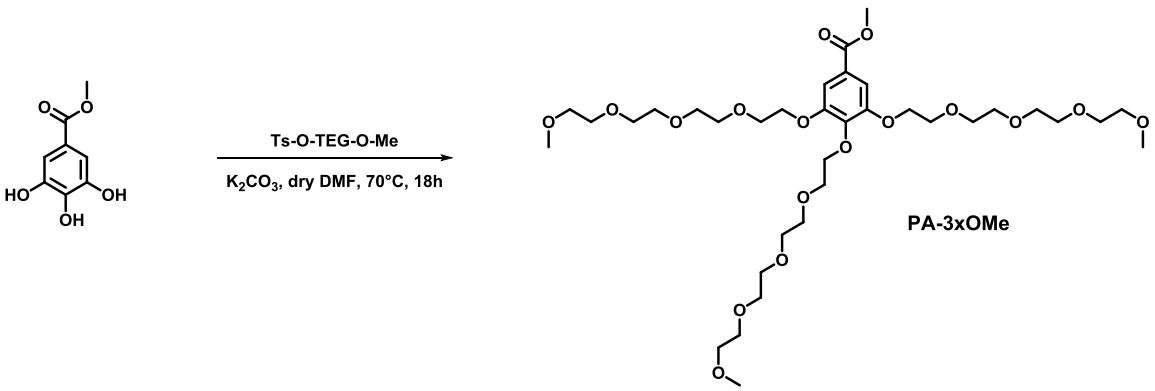

Following the literature in parts,[64] **Ts-O-TEG-O-Me** (1135 mg, 3.26 mmol) was dissolved together with methyl 3,4,5-trihydroxybenzoate (MTB, 200 mg, 1.09 mmol) and K_2CO_3 (811 mg, 5.9 mmol) in dry DMF (20 mL) and heated to 70°C for 18 h in an nitrogen atmosphere. The solution displayed an intense brownish color shortly after launch. Water was added and the crude reaction mixture was four times extracted with DCM. The organic layers were combined and washed with water as well as brine and subsequently dried over Na_2SO_4. After evaporation of the solvents, the brown product was used without further purification (540 mg, 0.71 mmol, 65%) (HPLC-MS analysis

confirmed majority of product). HR-ESI-ToF-MS (positive scan, m/z): $[M+Na]^+$ calcd. 777.3879; found 777.3871. HPLC-MS: t_R = 1.23 min.

Synthesis of P-Alkyl-2

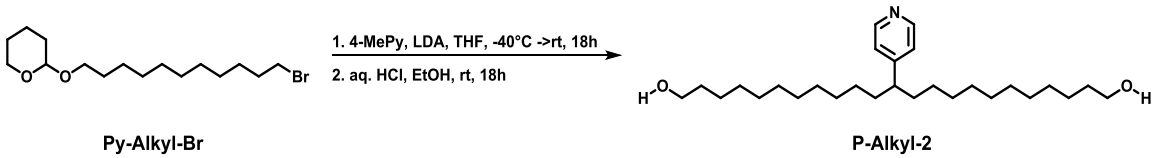

Py-Alkyl-Br **P-Alkyl-2**

Standard Schlenk techniques were applied for the synthesis of **P-Alkyl-2**. 4-methylpyridine (4-MePy, 66 µL, 0.68 mmol) was dissolved in dry THF (5 mL) and the solution was subsequently cooled to -45°C (CO_2 in MeCN) under stirring. A solution of lithium diisoproylamide (LDA) in dry THF/Benzene/Hexane (2 M, 0.99 mL, 1.98 mmol) was dropwise added and the reaction mixture stirred for 1h at -45°C. Then, a solution of **Py-Alkyl-Br** (480 mg, 1.43 mmoL) in dry THF (5 mL) was added slowly and then the mixture was kept at -45°C for 1 h. Afterwards, the reaction mixture was allowed to equilibrate to room temperature and stirred for 18 h. Water was added and the product three times extracted with DCM and the combined organic layers one time washed with brine. The solvents were evaporated *in vacuo* and the resulting crude product dissolved in ethanol.

The pH value was adjusted by concentrated aq. HCl (37%) to 1-2 and the mixture stirred overnight. Na_2CO_3 to neutralize the mixture and the product was extracted three time with DCM and the combined organic layers one time washed with brine. After drying over Na_2SO_4 the volatiles were evaporated *in vacuo* and the crude product subjected to column chromatography (SiO_2, EtAc/MeOH (2%)) yielding a white solid (150 mg, 0.346, 51%). ^{1}H NMR (400 MHz, $CDCl_3$, ppm) δ 8.44 (d, *J* = 6.1 Hz, 2H), 7.05 (d, *J* = 6.1 Hz, 2H), 3.60 (t, *J* = 6.9 Hz, 4H), 2.83 (s, 2H), 2.44 (p, *J* = 9.7, 5.3, 4.8 Hz, 1H), 1.52 (m, 9H), 1.23 (m, 35H). HR-ESI-ToF-MS (positive scan, m/z): $[M+H]^+$ calcd. 434.3993; found 434.4025.

Synthesis of P-2

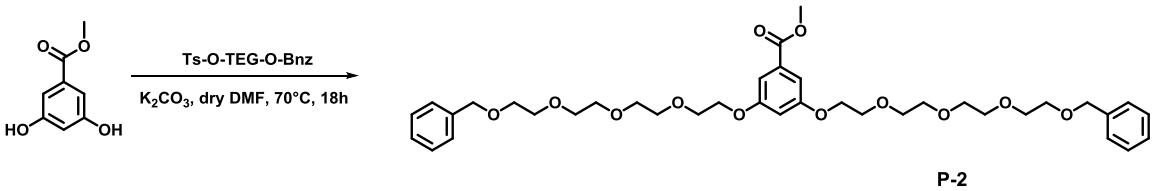

Following the literature in parts,[64] **Ts-O-TEG-O-Bnz** (2 g, 4.56 mmol) was dissolved together with methyl 3,5-dihydroxybenzoate (DTB, 365 mg, 2.17 mmol) and K_2CO_3 (1.6 g, 11.73 mmol) in dry DMF (20 mL) and heated to 70°C for 18 h under nitrogen atmosphere. Water was added and the crude reaction mixture four times extracted with DCM. The organic layers were combined and washed with water and brine, and were subsequently dried over Na_2SO_4. After evaporation of the solvents, the brown product was used without further purification (1.5 g, 2.14 mmol, 98%) (HPLC-MS analysis confirmed majority of product). HR-ESI-ToF-MS (positive scan, m/z): $[M+Na]^+$ calcd. 723.3351; found 723.3312. HPLC-MS: t_R = 1.99 min.

Synthesis of P-3

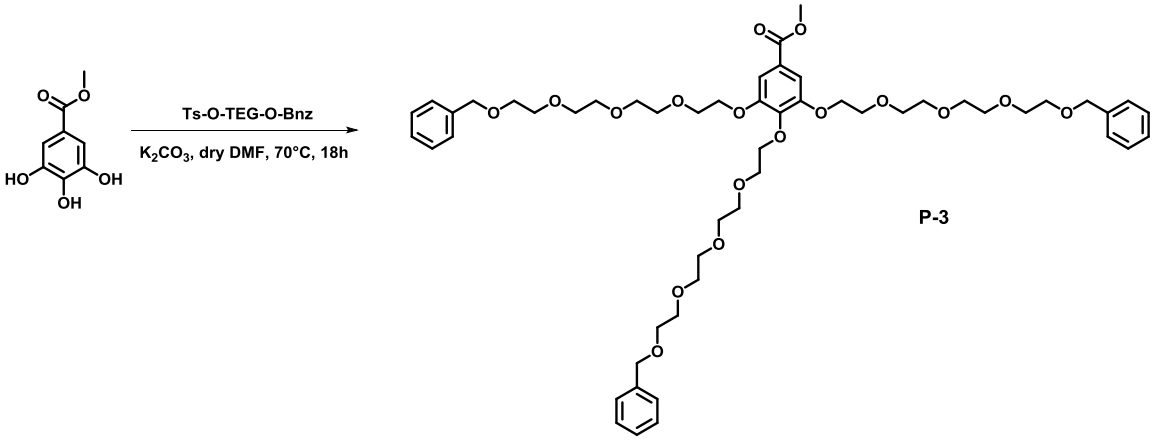

Following the literature in parts,[64] **Ts-O-TEG-O-Bnz** (3 g, 6.84 mmol) was dissolved together with methyl 3,4,5-trihydroxybenzoate (MTB, 400 mg, 2.17 mmol) and K_2CO_3 (1.6 g, 11.7 mmol) in dry DMF (20 mL) and heated to 70°C for 18 h under nitrogen atmosphere. Water was added and the crude reaction mixture four times extracted with DCM. The organic layers were combined and washed with water as well as brine and subsequently dried over Na_2SO_4. After evaporation of the solvents, the brown product was used without further purification (1.2 g, 1.22 mmol, 56%) (HPLC-MS analysis

confirmed majority of product). HR-ESI-ToF-MS (positive scan, m/z): $[M+Na]^+$ calcd. 1005.4818; found 1005.4864. HPLC-MS: t_R = 2.14 min.

Synthesis of AR

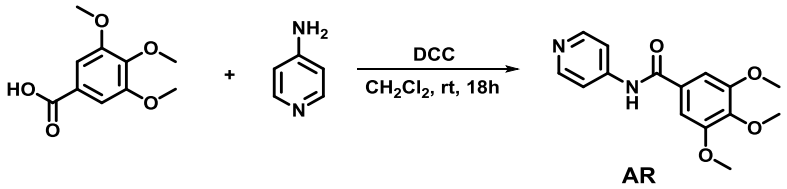

The 3,4,5-trimethoxybenzoic acid (142 mg, 0.67 mmol) was dissolved together with N,N'-dicyclohexylcarbodiimide (DCC, 180 mg, 0.87 mmol) in dry DCM in a one neck round bottom flask under a nitrogen atmosphere. After 5 min at RT temperature, 4-minopyridine (56 mg, 0.60 mmol) was added. The reaction mixture was stirred under a nitrogen atmosphere for 18 h. Subsequently, water was added and the reaction mixture stirred for 2 h to quench the DCC residue. Afterwards, acetone was added to achieve a homogenous solution and the white precipitate was filtered off *via* a folded filter (dicyclohexylurea). The volatiles were evaporated and the crude product subjected to a column chromatography (SiO_2, EtAc/MeOH (1%)) yielding a colorless solid (125 mg, 0.433, 72%). ^{1}H NMR (400 MHz, MeOD, ppm) δ 8.45 (d, *J* = 6.5 Hz, 2H), 7.84 (d, *J* = 6.5 Hz, 2H), 7.32 (s, 2H), 3.94 (s, 6H), 3.84 (s, 3H). HR-ESI-ToF-MS (positive scan, m/z): $[M+H]^+$ calcd. 289.1183; found 289.1180.

Synthesis of PA-2

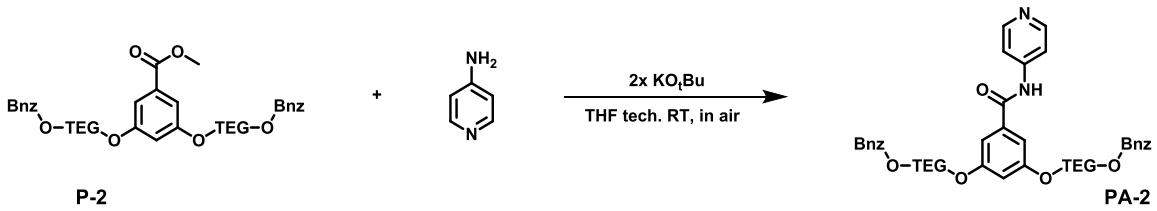

Following the literature in parts,[40] **P-2** (400 mg, 0.57 mmol) was dissolved together with 4-aminopyridine (59 mg, 0.63 mmol) in THF (10 mL, technical grade, stabilizer free). A solution of potassium *tert*-butoxide in THF (2M, 1 mL) was slowly added to the reaction mixture. The mixture was stirred uncapped for 2h, and full conversion was confirmed by HPLC-MS. The solvents were evaporated and the crude product subject to column chromatography (Silica, DCM/MeOH (5%)) yielding a colorless viscous liquid

(320 mg, 0.42 mmol, 73%). HR-ESI-ToF-MS (positive scan, m/z): $[M+H]^+$ calcd. 763.3800; found 763.3803. HPLC-MS: t_R = 1.47 min.

Synthesis of PA-3

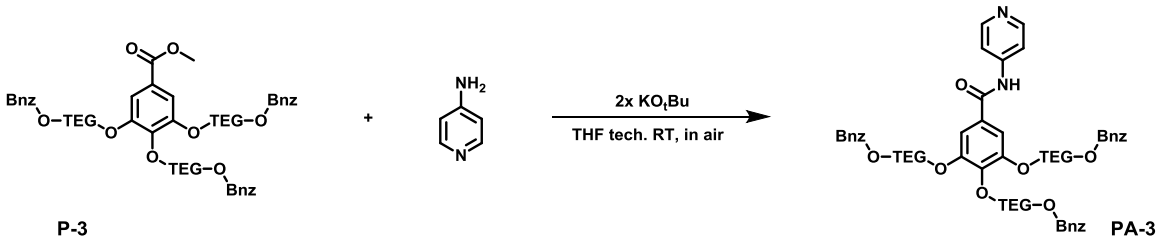

Following the literature in parts,[40] **P-3** (1000 mg, 1.02 mmol) was dissolved together with 4-aminopyridine (105 mg, 1.12 mmol) in THF (20 mL, technical grade, stabilizer free). A solution of potassium *tert*-butoxide in THF (2M, 2 mL) was slowly added to the reaction mixture. The mixture was stirred uncapped for 2h, and full conversion was proven by HPLC-MS. The solvents were evaporated and the crude product subject to column chromatography (Silica, DCM/MeOH (5%)) yielding a colorless viscous liquid (956 mg, 0.915 mmol, 90 %). HR-ESI-ToF-MS (positive scan, m/z): $[M+H]^+$ calcd. 1045.5268; found 1045.5266. HPLC-MS: t_R = 1.61 min.

Synthesis of A-2xOMe

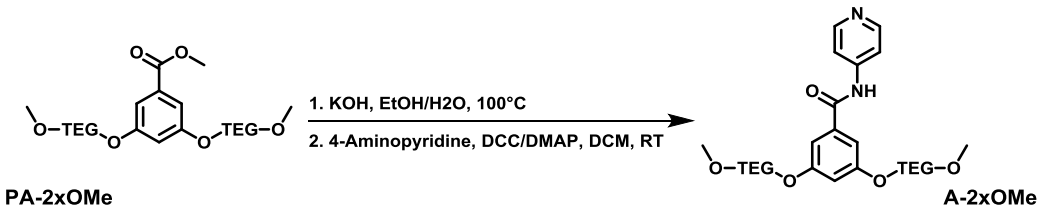

PA-2xOMe (1657 mg, 3.02 mmol) was dissolved together with KOH (800 mg, 14.3 mmol) in 40 mL EtOH/Water (1:1, *v:v*) and heated to 100°C overnight. Full conversion of **PA-2xOMe** was confirmed by HPLC-MS. The reaction mixture was allowed to cool to room temperature and concentrated aq. HCl (37%) was drop wisely added to acidify. The solvents were evaporated *in vacuo* and DCM added and resulting suspension subsequently filtered. The received solution was dried at room temperature resulting in a brown liquid.

Parts of this liquid (105 mg, 0.196 mmol) were dissolved together with N,N'-dicyclohexylcarbodiimide (DCC, 52.7 mg, 0.255 mmol) in DCM (20 mL) and stirred at room temperature in a nitrogen atmosphere. After 5 min, a solution of 4-(dimethyl amino)pyridine (DMAP, 36 mg, 0.295 mmol) in DCM (5 mL) was added. After 5 min stirring at room temperature, a solution of 4-aminopyridine (22 mg, 0.235 mmol) in DCM (5 mL) was added and the reaction mixture stirred for 60h at room temperature. Water was added and the mixture stirred for further 2 h. Subsequently, the product was extracted three times with DCM and the combined organic layers washed with brine (1x). After drying over Na_2SO_4 and evaporation of the volatiles, the crude product was subjected to a column chromatography (Silica, DCM/MeOH (4%)) yielding a colorless viscous liquid (57 mg, 0.09 mmol, 48 %). ^{1}H NMR (400 MHz, $CDCl_3$, ppm) δ 8.87 (s, 1H), 8.53 (s, 2H), 7.71 (s, 2H), 7.06 (d, *J* = 2.2 Hz, 2H), 6.62 (s, 1H), 4.13 (m, 4H), 3.83 (m, 4H), 3.65 (m, 25H), 3.51 (dd, *J* = 5.7, 3.6 Hz, 4H), 3.32 (s, 6H). HR-ESI-ToF-MS (positive scan, m/z): $[M+H]^+$ calcd. 611.3174; found 611.1886. HPLC-MS: t_R = 1.07 min.

Synthesis of A-3xOMe

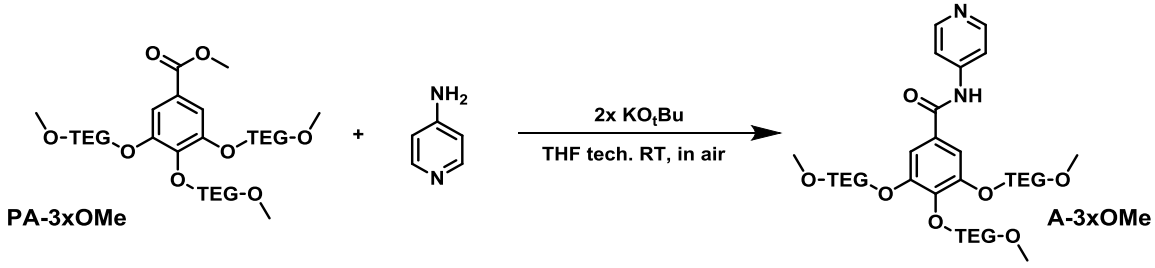

Following the literature in parts,[40] **P-3** (50 mg, 0.051 mmol) was dissolved together with 4-aminopyridine (5.3 mg, 0.056 mmol) in THF (1 mL, technical grade, stabilizer free). A solution of potassium *tert*-butoxide in THF (2M, 0.1 mL) was slowly added to the reaction mixture. The mixture was stirred uncapped for 2 h, and full conversion was proven by HPLC-MS. The solvents were evaporated and the crude product subject to column chromatography (Silica, DCM/MeOH (5%)) yielding a colorless viscous liquid (55 mg, 0.067 mmol, 76%). ^{1}H NMR (400 MHz, CD_2Cl_2, ppm) δ 9.16 (s, 1H), 8.53 (s, 2H), 7.77 (s, 2H), 7.33 (d, *J* = 8.5 Hz, 2H), 4.26 (m, 6H), 3.63 (m, 48H), 3.37 (s, 3H), 3.32 (s, 6H). ^{13}C {^{1}H} NMR (101 MHz, CD_2Cl_2, ppm) δ = 166.52, 153.06, 150.96, 146.40, 142.47, 129.88, 114.74, 108.27, 72.90, 72.41, 72.35, 71.15, 71.09, 71.05, 71.01, 70.94, 70.91, 70.87, 70.84, 70.29, 69.68, 59.16, 59.12. HR-ESI-ToF-MS (positive scan, m/z): $[M+H]^+$ calcd. 817.4329; found 817.4382. HPLC-MS: t_R = 1.03 min.

Synthesis of A-2xOH

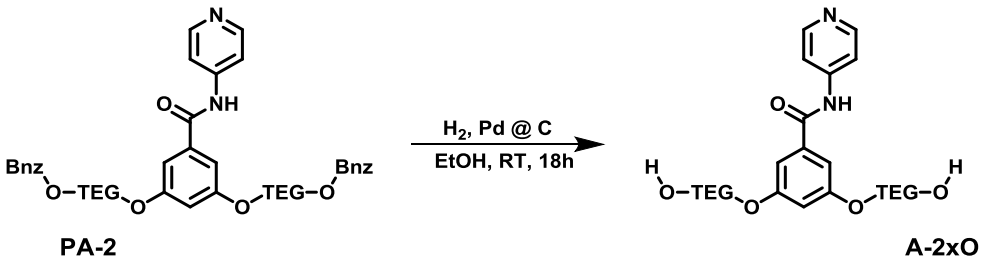

Standard Schlenk techniques were applied for the deprotection of **PA-2**. Compound **PA-2** (320 mg, 0.42 mmol) was dissolved in EtOH (10 mL) with a drop of trifluoro acetic acid (TFA) in a nitrogen atmosphere. Pd@C (10 mg) was added portion-wise in an N_2 stream and the vessel closed. Afterwards, N_2 was exchanged for H_2 and the reaction mixture stirred at room temperature for 18 h. Full conversion was confirmed by HPLC-MS analysis. The crude mixture was filtered through a celite plug and rinsed with EtOH. After evaporation of the solvent *in vacuo*, the product was subjected to a column chromatography (Alox, DCM/MeOH (5%) yielding a colorless viscous liquid (195 mg, 0.36 mmol, 80%). ^{1}H NMR (400 MHz, $CDCl_3$, ppm) δ 8.9 (s, 1H), 8.5 (d, *J* = 5.6 Hz, 2H), 7.7 (d, *J* = 5.6 Hz, 2H), 7.1 (d, *J* = 2.3 Hz, 2H), 6.7 (t, *J* = 2.3 Hz, 1H), 4.2 (m, 4H), 3.9 (m, 4H), 3.7 (m, 25H), 3.6 (m, 4H). ^{13}C {^{1}H} NMR (101 MHz, $CDCl_3$, ppm) δ 166.4, 160.1, 150.9, 145.7, 136.5, 114.2, 106.6, 105.3, 72.6, 70.8, 70.8, 70.7, 70.4, 69.7, 67.9, 61.8. HR-ESI-ToF-MS (positive scan, m/z): $[M+H]^+$ calcd. 583.2861; found 583.2925. HPLC-MS: t_R = 1.18 min.

Synthesis of A-3xOH

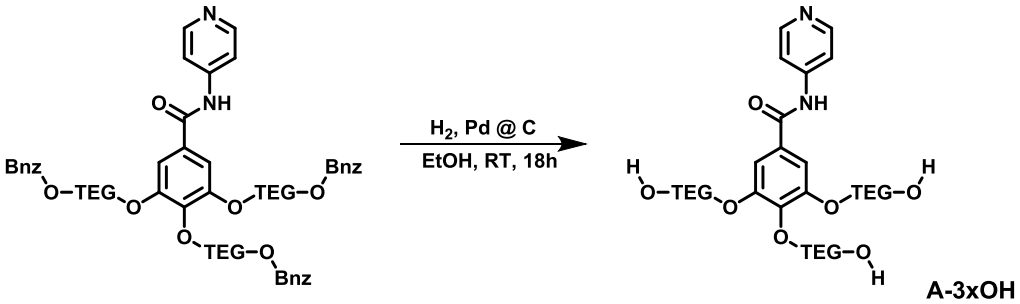

Standard Schlenk techniques were applied for the deprotection of **PA-3**. Compound **PA-3** (250 mg, 0.25 mmol) was dissolved in EtOH (10 mL) with a drop of TFA in a nitrogen atmosphere. Pd@C (10 mg) was added portion-wise in an N_2 stream and the vessel closed. Afterwards, N_2 was exchanged for H_2 and the reaction mixture stirred at

room temperature for 18 h. Full conversion was proven by HPLC-MS analysis. The crude mixture was filtered through a celite plug and rinsed with EtOH. After evaporation of the solvent *in vacuo*, the product was subjected to a column chromatography (Alox, DCM/MeOH (5%) yielding a colorless viscous liquid (128 mg, 0.17 mmol, 65%). ^{1}H NMR (400 MHz, $CDCl_3$, ppm) δ = 9.74 (s, 1H), 8.41 (s, 2H), 7.72 (s, 2H), 7.21 (s, 2H), 4.16 (s, 6H), 3.61 (m, 65H). ^{13}C {^{1}H} NMR (101 MHz, $CDCl_3$, ppm) δ = 166.48, 152.26, 150.23, 141.84, 129.35, 114.52, 108.03, 72.88, 72.72, 72.64, 72.39, 70.66, 70.54, 70.49, 70.45, 70.37, 70.17, 69.99, 69.70, 69.04, 61.50, 61.46, 61.43. HR-ESI-ToF-MS (positive scan, m/z): $[M+H]^+$ calcd. 775.3859; found 775.3939. HPLC-MS: t_R = 0.88 min.

Synthesis of A-2xSO$_4$

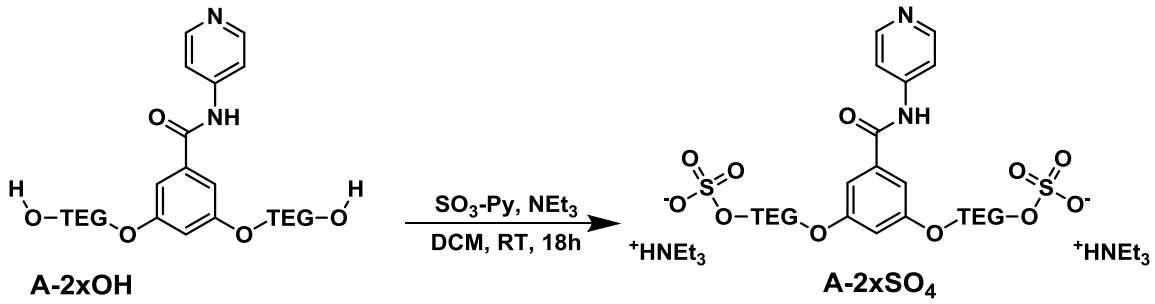

Following the literature in parts,[65] **A-2xOH** (50 mg, 0.086 mmol) was dissolved together with pyridine:trisulfoxide (82 mg, 0.515 mmol) and NEt_3 (95 µL, 0.686 mmol) in DCM and stirred at room temperature for 18 h. The crude mixture tested on complete conversion by TLC of **A-2xOH** and subsequently all volatiles evaporated *in vacuo*. The crude mixure was subjected to column chromatography (SiO_2, DCM, 10% MeOH, 1% NEt_3) (31 mg, 0.028 mmol, 38%). found 842.3092. ^{1}H NMR (400 MHz, MeOD, ppm) δ 8.6 (d, *J* = 6.7 Hz, 2H), 8.3 (d, *J* = 6.7 Hz, 2H), 7.2 (d, *J* = 2.3 Hz, 2H), 6.8 (t, *J* = 2.3 Hz, 1H), 4.2 (m, 4H), 4.1 (m, 4H), 3.9 (m, 4H), 3.7 (m, 17H). ^{13}C {^{1}H} NMR (101 MHz, MeOD, ppm) δ 168.7, 161.7, 153.9, 144.9, 136.6, 116.5, 107.9, 107.3, 71.7, 71.6, 71.6, 71.5, 70.7, 70.7, 69.2, 68.2. ^{19}F {^{1}H} NMR (377 MHz, MeOD) δ -65.42. HR-ESI-ToF-MS (negative scan, m/z): $[M]^{2-}$ calcd. 370.0879; found 370.0912; (negative scan, m/z): $[M+HNEt_3]^{1-}$ calcd. 842.3057.

Synthesis of A-3xSO$_4$

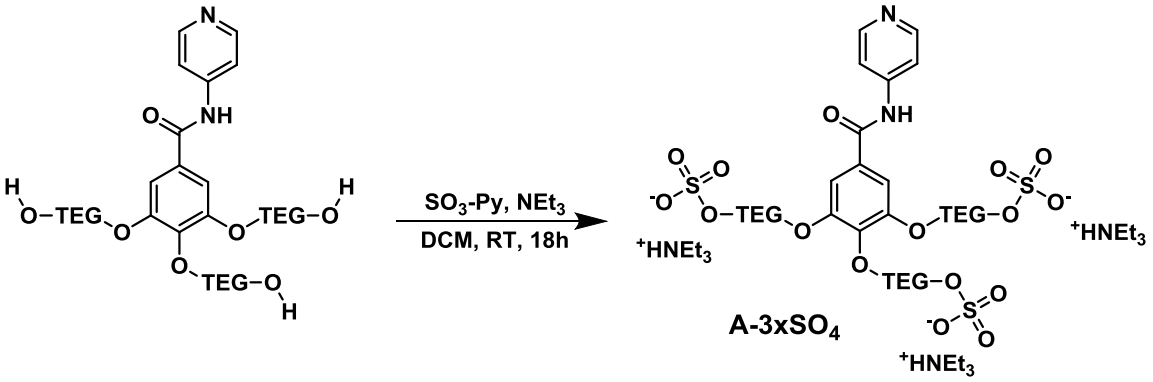

Following the literature in parts,[65] **A-3xOH** (90 mg, 0.116 mmol) was dissolved together with pyridine:trisulfoxide (111 mg, 0.697 mmol) and triethyl amine (NEt_3, 130 µL, 0.929 mmol) in DCM (10 mL) and stirred at room temperature for 18 h. The crude mixture tested on complete conversion of **A-3xOH** by TLC and subsequently all volatiles evaporated *in vacuo*. The crude mixture was subjected to column chromatography (SiO_2, DCM, 10% MeOH, 1% NEt_3) yielding a colorless viscous liquid (120 mg, 0.09 mmol, 76%). ^{1}H NMR (400 MHz, MeOD, ppm) δ 8.89 (s, 1H), 8.54 (d, *J* = 7.3 Hz, 2H), 8.26 (d, *J* = 7.3 Hz, 2H), 7.23 (s, 2H), 4.13 (m, 4H), 4.05 (m, 2H), 3.91 (m, 7H), 3.74 (m, 4H), 3.64 (m, 2H), 3.51 (m, 33H), 3.29 (m, 2H), 3.14 (d, *J* = 6.6 Hz, 2H), 2.87 (m, 1H). ^{13}C {^{1}H} NMR (101 MHz, MeOD, ppm) δ 156.99, 148.46, 123.73, 67.72, 46.56, 45.49, 35.90, 29.28, 29.25, 29.18, 29.08, 28.97, 27.15, 25.52. ^{19}F {^{1}H} NMR (377 MHz, MeOD, ppm) δ -65.31. HR-ESI-ToF-MS (negative scan, m/z): $[M]^{3-}$ calcd. 337.0747; found 337.0750.

Synthesis of A-Alkyl-2xSO$_4$

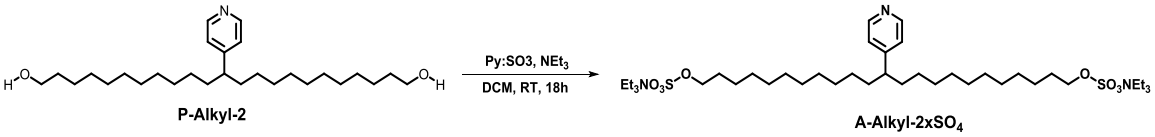

Following the literature in parts,[65] **P-Alkyl-2** (36 mg, 0.083 mmol) was dissolved together with pyridine:trisulfoxide (79 mg, 0.4960 mmol) and triethyl amine (NEt_3, 120 µL, 0.858 mmol) in DCM (10 mL) and stirred at room temperature for 18 h. The crude mixture tested on complete conversion of **P-Alkyl-2** by TLC and subsequently all volatiles evaporated *in vacuo*. The crude mixture was subjected to column chromatography (SiO_2, DCM, 10% MeOH, 1% NEt_3) yielding a colorless viscous liquid

(120 mg, 0.09 mmol, 76%). ^{1}H NMR (400 MHz, MeOD, ppm) δ 8.42 (d, *J* = 6.0 Hz, 2H), 7.27 (d, *J* = 6.4 Hz, 2H), 3.98 (t, *J* = 6.6 Hz, 4H), 3.31 (p, *J* = 1.6 Hz, 1H), 1.64 (m, 9H), 1.30 (m, 58H). HR-ESI-ToF-MS (negative scan, m/z): $[M]^-$ calcd. 592.2983; found 592.2951.

Synthesis of L-Pt-2xOMe

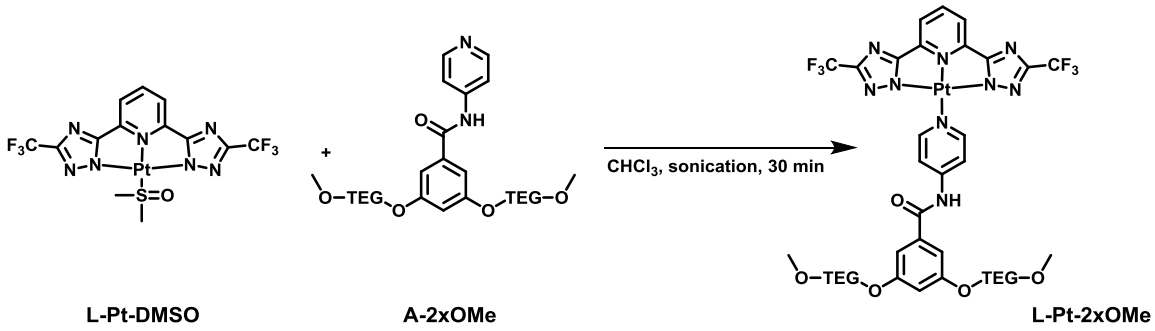

L-Pt-DMSO **A-2xOMe** **L-Pt-2xOMe**

L-Pt-DMSO (5.1 mg, 0.008 mmol) and **A-2xOMe** (5 mg, 0.008 mmol) were dissolved in $CHCl_3$ (1 mL) and MeOH (0.5 mL) and sonicated for 30 minutes. The volatiles were evaporated *in vacuo* and the crude product suspended in DCM. Subsequently, the suspension was subjected to centrifugation and the supernatant was separated. The remaining precipitant was treated two more times with DCM in the same way. The combined organic layers were evaporated and the procedure two times repeated. After evaporation of all volatiles, a pure orange solid was obtained (8.5 mg, 0.007 mmol, 91%). ^{1}H NMR (400 MHz, THF) δ 10.33 (s, 1H), 9.46 (d, *J* = 6.7 Hz, 2H), 8.17 (t, *J* = 7.7 Hz, 1H), 8.03 (d, *J* = 6.7 Hz, 2H), 7.80 (d, *J* = 7.7 Hz, 2H), 7.16 (s, 2H), 6.79 (s, 1H), 4.17 (m, 4H), 3.82 (m, 4H), 3.57 (m, 57H), 3.44 (m, 4H), 3.27 (s, 6H). ^{19}F {^{1}H} NMR (377 MHz, THF, ppm) δ -65.0. HR-ESI-ToF-MS (positive scan, *m/z*): $[M+Na]^+$ calcd. 1175.2998; found 1175.3031.

Synthesis of L-Pt-3xOMe

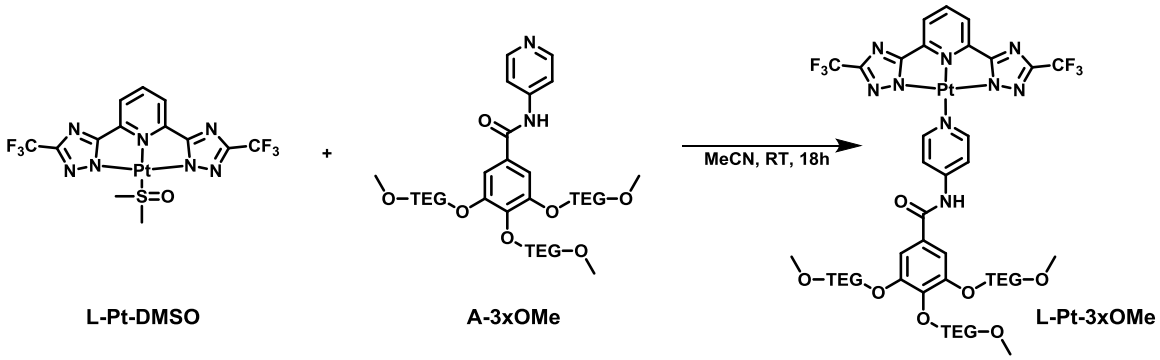

L-Pt-DMSO A-3xOMe L-Pt-3xOMe

L-Pt-DMSO (7.8 mg, 0.012 mmol) and **A-3xOMe** (10 mg, 0.012 mmol) were dissolved in MeCN (1 mL) and DCM (1 mL) and stirred for 18 h at room temperature. The volatiles were evaporated *in vacuo* and the crude product suspended in DCM. Subsequently, the suspension was subjected to centrifugation and the supernatant was separated. The remaining precipitant was treated two more times with DCM in the same way. The combined organic layers were evaporated and the procedure two times repeated. After evaporation of all volatiles, a pure orange solid was obtained (13 mg, 0.01 mmol, 78%).^{1}H NMR (400 MHz, $CDCl_3$, ppm) δ 10.47 (s, 1H), 9.37 (d, *J* = 7.1 Hz, 2H), 8.16 (d, *J* = 7.1 Hz, 2H), 7.96 (t, *J* = 7.8 Hz, 1H), 7.72 (d, *J* = 7.8 Hz, 2H), 7.50 (s, 2H), 7.36 (s, 1H), 4.26 (m, 13H), 3.62 (m, 98H), 3.32 (m, 12H). ^{13}C {^{1}H} NMR (101 MHz, $CDCl_3$, ppm) δ 166.7, 163.9, 153.6, 152.6, 149.3, 149.0, 142.9, 128.6, 121.3, 118.6, 118.3, 116.2, 109.1, 72.5, 72.0, 71.9, 70.8, 70.6, 70.5, 70.5, 70.1, 70.0, 69.4, 59.2, 59.1. ^{19}F {^{1}H} NMR (377 MHz, $CDCl_3$, ppm) δ = -64.11. HR-ESI-ToF-MS (positive scan, *m/z*): $[M+Na]^+$ calcd. 1381.4153; found 1381.4235.

Synthesis of L-Pt-2xOH

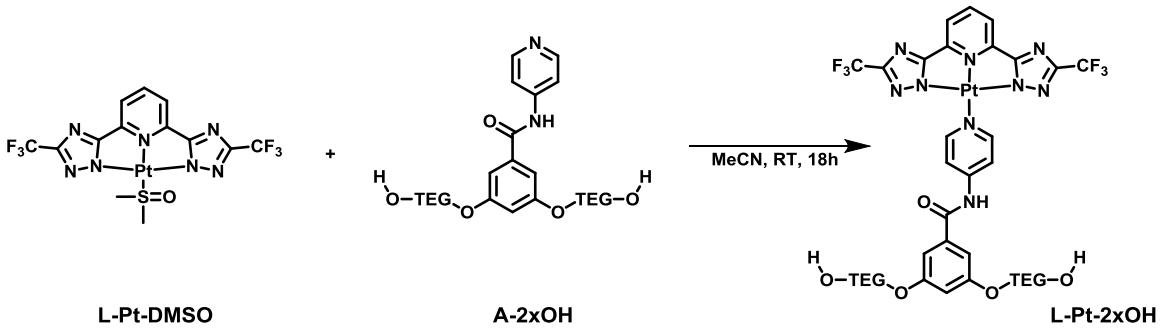

L-Pt-DMSO A-2xOH L-Pt-2xOH

L-Pt-DMSO (15 mg, 0.024 mmol) and **A-2xOH** (17 mg, 0.021 mmol) were dissolved in MeCN (3 mL) and DCM (3 mL) and stirred for 18 h at room temperature. The volatiles were evaporated *in vacuo* and the crude product suspended in DCM. Subsequently, the suspension was subjected to centrifugation and the supernatant was separated. The remaining precipitant was treated two more times with DCM in the same way. The combined organic layers were evaporated and the procedure two times repeated. After evaporation of all volatiles, a column chromatography (Alox, DCM, 2%MeOH) was conducted to obtain a pure product (10 mg, 0.0075 mmol, 34%). ^{1}H NMR (400 MHz, $CDCl_3$, ppm) δ 9.9 (s, 1H), 9.4 (d, *J* = 7.3 Hz, 2H), 8.0 (m, 3H), 7.7 (d, *J* = 7.9 Hz, 2H), 7.1 (d, *J* = 2.1 Hz, 2H), 6.7 (t, *J* = 2.1 Hz, 1H), 4.2 (m, 4H), 3.9 (m, 4H), 3.7 (m, 16H), 3.6 (m, 4H). ^{13}C {^{1}H} NMR (101 MHz, $CDCl_3$, ppm) δ 166.8, 163.7, 160.0, 153.6, 148.9, 148.7, 142.9, 135.7, 129.9, 118.3, 116.0, 107.0, 105.8, 72.6, 70.7, 70.6, 70.3, 69.6, 67.9, 61.7. ^{19}F {^{1}H} NMR (377 MHz, $CDCl_3$, ppm) δ -64.2. HR-ESI-ToF-MS (positive scan, m/z): $[M+H]^+$ calcd. 1339.3684; found 1339.3802.

Synthesis of L-Pt-3xOH

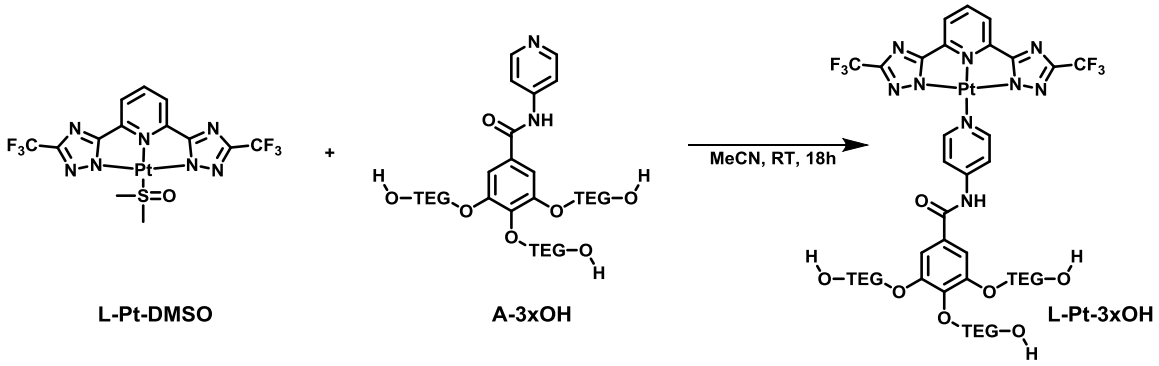

L-Pt-DMSO (15 mg, 0.024 mmol) and **A-3xOH** (17 mg, 0.021 mmol) were dissolved in MeCN (3 mL) and DCM (3 mL) and stirred for 18 h at room temperature. The volatiles were evaporated *in vacuo* and the crude product suspended in DCM. Subsequently, the suspension was subjected to centrifugation and the supernatant was separated. The remaining precipitant was treated two more times with DCM in the same way. The combined organic layers were evaporated and the procedure was twice repeated. After evaporation of all volatiles, a column chromatography (Alox, DCM, 2%MeOH) was conducted to obtain a pure product (10 mg, 0.0075 mmol, 34%). ^{1}H NMR (400 MHz, $CDCl_3$, ppm) δ 9.88 (s, 1H), 9.06 (m, 2H), 7.78 (t, *J* = 7.9 Hz, 1H), 7.74 (d, *J* = 7.0 Hz, 2H), 7.42 (d, *J* = 7.9 Hz, 2H), 7.35 (s, 2H), 4.27 (q, *J* = 4.9, 4.9, 4.9 Hz, 7H), 3.84 (m,

7H), 3.66 (m, 41H), 3.17 (s, 5H). ^{13}C {^{1}H} NMR (101 MHz, $CDCl_3$, ppm) δ 166.6, 163.3, 153.0, 152.6, 148.7, 148.0, 142.8, 142.6, 128.6, 121.1, 118.4, 118.1, 115.9, 108.8, 72.7, 72.6, 70.9, 70.8, 70.7, 70.6, 70.4, 70.4, 69.9, 69.4, 61.7, 61.7. ^{19}F {^{1}H} NMR (377 MHz, $CDCl_3$, ppm) δ -64.09. HR-ESI-ToF-MS (positive scan, m/z): $[M+Na]^+$ calcd. 1339.3684; found 1339.3802.

Synthesis of L-Pt-2xSO₄

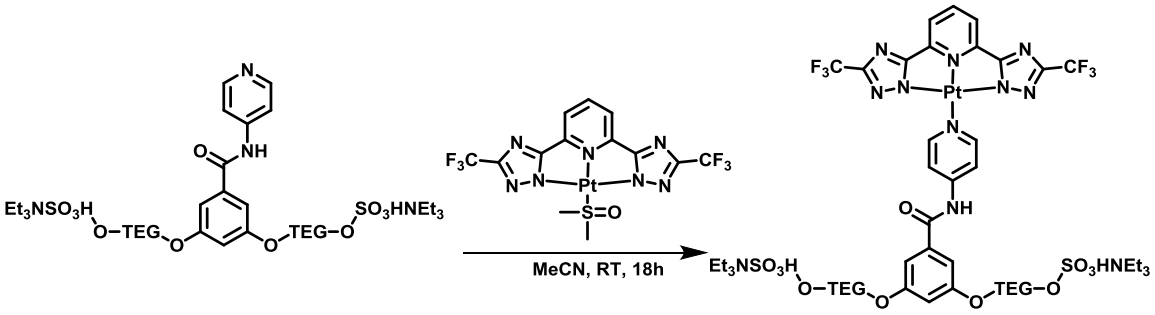

L-Pt-DMSO (13 mg, 0.021 mmol) and **A-2xSO₄** (13 mg, 0.014 mmol) were dissolved in MeCN (5 mL) and MeOH (3 mL) and stirred for 18 h at room temperature. Complete conversion of **A-2xSO₄** was confirmed by TLC. All volatiles were evaporated *in vacuo* and the crude product subjected to column chromatography (SiO_2, DCM, 5% MeOH, 1% NEt_3) yielding a yellow solid (10 mg, 0.01 mmol, 49%). ^{1}H NMR (400 MHz, MeOD) δ 9.0 (d, *J* = 6.4 Hz, 2H), 8.0 (t, *J* = 7.9 Hz, 1H), 7.7 (d, *J* = 6.4 Hz, 2H), 7.5 (d, *J* = 7.9 Hz, 2H), 7.1 (d, *J* = 2.2 Hz, 2H), 6.8 (d, *J* = 2.3 Hz, 1H), 4.2 (t, *J* = 4.6 Hz, 4H), 4.1 (m, 5H), 3.9 (t, *J* = 4.6 Hz, 4H), 3.7 (m, 22H). ^{13}C {^{1}H} NMR (101 MHz, MeOD) δ 161.5, 154.1, 153.4, 146.6, 136.9, 119.8, 116.5, 107.8, 71.8, 71.7, 71.6, 70.8, 70.7, 69.1, 68.3, 64.3, 63.5, 53.6, 9.3, 7.6. ^{19}F {^{1}H} NMR (377 MHz, MeOD) δ -65.4.HR-ESI-ToF-MS (negative scan, *m/z*): $[M]^{2-}$ calcd. 641.0892; found 641.0927

Synthesis of L-Pt-3xSO4

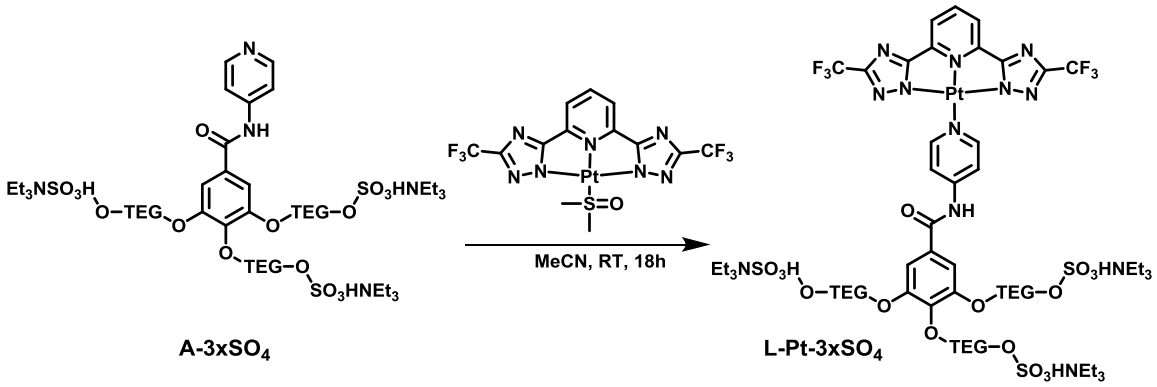

L-Pt-DMSO (17 mg, 0.027 mmol) and **A-3xSO4** (30 mg, 0.023 mmol) were dissolved in MeCN (5 mL) and MeOH (3 mL) and stirred for 18 h at room temperature. Complete conversion of **A-3xSO4** was confirmed by TLC. All volatiles were evaporated *in vacuo* and the crude product subjected to column chromatography (SiO_2, DCM, 10% MeOH, 1% NEt_3) yielding a yellow solid (12 mg, 0.006 mmol, 28%). ^{1}H NMR (400 MHz, MeOD, ppm) δ 8.93 (d, *J* = 6.5 Hz, 2H), 7.93 (s, 1H), 7.70 (m, 2H), 7.38 (d, *J* = 7.8 Hz, 2H), 7.31 (s, 2H), 4.30 (m, 7H), 4.13 (m, 8H), 3.75 (m, 45H), 3.13 (q, *J* = 7.3, 7.3, 7.3 Hz, 26H), 1.29 (t, *J* = 7.3, 7.3 Hz, 40H). ^{13}C {^{1}H} NMR (101 MHz, MeOD, ppm) δ = 166.71, 162.98, 152.53, 152.21, 147.14, 141.03, 120.89, 118.30, 115.11, 106.96, 72.34, 70.18, 70.10, 70.04, 70.02, 69.33, 69.28, 68.59, 66.81. ^{19}F {^{1}H} NMR (377 MHz, MeOD, ppm) δ -65.31. HR-ESI-ToF-MS (negative scan, *m/z*): $[M]^{3-}$ calcd. 517.7415; found 517.7345

Synthesis of L-Pt-Alkyl-2xSO4

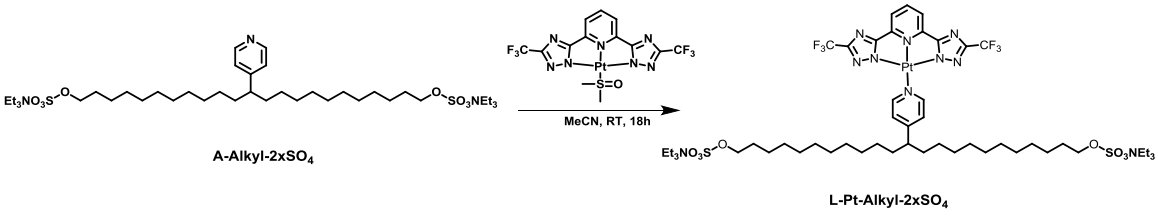

L-Pt-DMSO (16 mg, 0.026 mmol) and **A-Alkyl-2xSO4** (17 mg, 0.021 mmol) were dissolved in MeCN (5 mL) and MeOH (3 mL) and stirred for 18 h at room temperature. Complete conversion of **A-Alkyl-2xSO4** was confirmed by TLC. All volatiles were evaporated *in vacuo* and the crude product subjected to column chromatography (SiO_2, DCM, 5% MeOH, 1% NEt_3) yielding a yellow solid (25 mg, 0.019 mmol, 87%). ^{1}H NMR (400 MHz, MeOD, ppm) δ 8.56 (d, *J* = 4.7 Hz, 2H), 7.81 (t, *J* = 7.8 Hz, 1H), 7.04 (d, *J* =

7.8 Hz, 2H), 6.76 (d, *J* = 4.7 Hz, 2H), 3.99 (m, 4H), 3.52 (q, *J* = 7.3 Hz, 6H), 3.33 (p, *J* = 1.6 Hz, 8H), 1.67 (m, 5H). ^{19}F {^{1}H} NMR (377 MHz, MeOD, ppm) δ -65.27. HR-ESI-ToF-MS (negative scan, *m/z*): $[M]^{2-}$ calcd. 566.6457; found 566.6470.

Synthesis of L-Pt-R

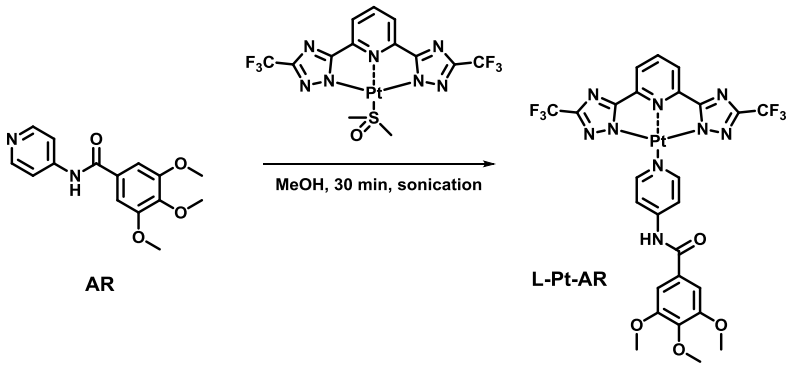

L-Pt-DMSO (19 mg, 0.031 mmol) and **AR** (10 mg, 0.035 mmol) were dissolved in MeOH (3 mL) and sonicated for 30 min. The volatiles were evaporated *in vacuo* and the crude product suspended in DCM. Subsequently, the suspension was subjected to centrifugation and the supernatant was separated. The remaining precipitant was treated twice with DCM in the same way. The combined organic layers were evaporated and the procedure two times repeated. After evaporation of all volatiles, a pure orange solid was obtained (21 mg, 0.025 mmol, 84%).^{1}H NMR (400 MHz, THF) δ 10.24 (s, 1H), 9.50 (d, *J* = 6.5 Hz, 2H), 8.21 (t, *J* = 8.0 Hz, 1H), 8.03 (d, *J* = 6.5 Hz, 2H), 7.87 (d, *J* = 8.0 Hz, 2H), 7.31 (s, 2H), 3.90 (s, 6H), 3.80 (s, 3H). ^{19}F {^{1}H} NMR (377 MHz, THF, ppm) δ -65.09. HR-ESI-ToF-MS (positive scan, m/z): $[M+H]^{+}$ calcd. 831.1186; found 831.1172.

Comment on NMR data: The expected coupling between carbon (^{13}C) and fluorine (^{19}F) is observed for the terdentate ligand **L** in CD_2Cl_2 featuring a quadruplet centered at 119.93 ppm and coupling constants of J_{CF} = 811 Hz and 269 Hz (1:3:3:1). While, for Pt-complexes exhibiting a decent solubility (TEG decorated ones in CDCl3) the coupling is still visible by a splitting into two peaks J_{CF} = 268 Hz, the coupling was not observed for relatively insoluble complexes. The coupling between hydrogen (^{1}H) and platinum (^{195}Pt) was not observed, although relaxation times were strongly prolongated.

References

1. L. J. Charbonnière, R. F. Ziessel, C. A. Sams and A. Harriman, *Inorg. Chem.*, 2003, **42**, 3466-3474.
2. S. A. McFarland and N. S. Finney, *Chem. Commun.*, 2003, 388-389.
3. M. E. Padilla-Tosta, J. M. Lloris, R. Martónez-Máñez, A. Benito, J. Soto, T. Pardo, M. A. Miranda and M. D. Marcos, *Eur. J. Inorg. Chem.*, 2000, **2000**, 741-748.
4. Miguel E. Padilla-Tosta, José M. Lloris, R. Martínez-Máñez, M. D. Marcos, Miguel A. Miranda, T. Pardo, F. Sancenón and J. Soto, *Eur. J. Inorg. Chem.*, 2001, **2001**, 1475-1482.
5. M. Schmittel, H.-W. Lin, E. Thiel, A. J. Meixner and H. Ammon, *Dalton Trans.*, 2006, 4020-4028.
6. R. Y. Lai, M. Chiba, N. Kitamura and A. J. Bard, *Anal. Chem.*, 2002, **74**, 551-553.
7. Subodh K. Dutta, D. Gan and Marc W. Perkovic, *Eur. J. Inorg. Chem.*, 2003, **2003**, 2812-2819.
8. J. V. Ros-Lis, R. Martinez-Manez, J. Soto, C. McDonagh and A. Guckian, *Eur. J. Inorg. Chem.*, 2006, 2647-2655.
9. J. Brandel, M. Sairenji, K. Ichikawa and T. Nabeshima, *Chem. Commun.*, 2010, **46**, 3958-3960.
10. M.-L. Ho, F.-M. Hwang, P.-N. Chen, Y.-H. Hu, Y.-M. Cheng, K.-S. Chen, G.-H. Lee, Y. Chi and P.-T. Chou, *Org. Biomol. Chem.*, 2006, **4**, 98-103.
11. M. Schmittel and H. Lin, *Inorg. Chem.*, 2007, **46**, 9139-9145.
12. V. Balzani and S. Campagna, *Topics in Current Chemistry - Photophysics of Coordination Compounds II*, 2007.
13. X. Ma, R. Sun, J. Cheng, J. Liu, F. Gou, H. Xiang and X. Zhou, *J. Chem. Educ.*, 2016, **93**, 345-350.
14. S. Mukherjee, C. M. Pfeifer, J. M. Johnson, J. Liu and A. Zlotnick, *J. Am. Chem. Soc.*, 2006, **128**, 2538-2539.
15. A. d. l. Escosura, P. G. A. Janssen, A. P. H. J. Schenning, R. J. M. Nolte and J. J. L. M. Cornelissen, *Angew. Chem. Int. Ed.*, 2010, **49**, 5335-5338.
16. H.-A. Hosein, D. R. Strongin, M. Allen and T. Douglas, *Langmuir*, 2004, **20**, 10283-10287.
17. T. Douglas, D. P. E. Dickson, S. Betteridge and J. Charnock, *Science*, 1995, **269**, 54.
18. F. D. Sikkema, M. Comellas-Aragones, R. G. Fokkink, B. J. M. Verduin, J. J. L. M. Cornelissen and R. J. M. Nolte, *Org. Biomol. Chem.*, 2007, **5**, 54-57.
19. J. Sun, C. DuFort, M.-C. Daniel, A. Murali, C. Chen, K. Gopinath, B. Stein, M. De, V. M. Rotello and A. Holzenburg, *PNAS*, 2007, **104**, 1354-1359.
20. S. L. Capehart, M. P. Coyle, J. E. Glasgow and M. B. Francis, *J. Am. Chem. Soc.*, 2013, **135**, 3011-3016.
21. A. Liu, M. Verwegen, M. V. de Ruiter, S. J. Maassen, C. H. H. Traulsen and J. J. L. M. Cornelissen, *J. Phys. Chem. B*, 2016, **120**, 6352-6357.
22. R. M. Putri, J. J. L. M. Cornelissen and M. S. T. Koay, *ChemPhysChem*, 2015, **16**, 911-918.
23. J. G. Millán, M. Brasch, E. Anaya-Plaza, A. de la Escosura, A. H. Velders, D. N. Reinhoudt, T. Torres, M. S. T. Koay and J. J. L. M. Cornelissen, *J. Inorg. Biochem.*, 2014, **136**, 140-146.
24. P. Kopel, D. Wawrzak, A. Moulick, V. Milosavljevic and R. Kizek, *J Metallomics Nanotechnol*, 2015, **2**, 32-38.
25. S. Deshayes and R. Gref, *Nanomedicine*, 2014, **9**, 1545-1564.
26. E. J. Lee, N. K. Lee and I.-S. Kim, *Advanced drug delivery reviews*, 2016, **106, Part A**, 157-171.
27. C. E. Flynn, S.-W. Lee, B. R. Peelle and A. M. Belcher, *Acta Mater.*, 2003, **51**, 5867-5880.

28. S. E. Aniagyei, C. Dufort, C. C. Kao and B. Dragnea, *J Mater Chem*, 2008, **18**, 3763-3774.
29. Y. Ma, R. J. Nolte and J. J. Cornelissen, *Advanced drug delivery reviews*, 2012, **64**, 811-825.
30. Z. Yang, X. Wang, H. Diao, J. Zhang, H. Li, H. Sun and Z. Guo, *Chem. Commun.*, 2007, 3453-3455.
31. C. Sanchez-Cano and M. J. Hannon, *Dalton Trans.*, 2009, 10702-10711.
32. R. Xing, X. Wang, C. Zhang, Y. Zhang, Q. Wang, Z. Yang and Z. Guo, *J. Inorg. Biochem.*, 2009, **103**, 1039-1044.
33. M. Brasch, PhD, University of Twente, 2013.
34. N. K. Allampally.
35. M. Brasch, A. de la Escosura, Y. Ma, C. Uetrecht, A. J. Heck, T. Torres and J. J. Cornelissen, *J. Am. Chem. Soc.*, 2011, **133**, 6878-6881.
36. R. D. Cadena-Nava, Y. Hu, R. F. Garmann, B. Ng, A. N. Zelikin, C. M. Knobler and W. M. Gelbart, *J. Phys. Chem. B*, 2011, **115**, 2386-2391.
37. W. F. Rurup, F. Verbij, M. S. T. Koay, C. Blum, V. Subramaniam and J. J. L. M. Cornelissen, *Biomacromolecules*, 2014, **15**, 558-563.
38. D. Septiadi, A. Aliprandi, M. Mauro and L. De Cola, *RSC Advances*, 2014, **4**, 25709-25718.
39. C. Chen, M. C. Daniel, Z. T. Quinkert, M. De, B. Stein, V. D. Bowman, P. R. Chipman, V. M. Rotello, C. C. Kao and B. Dragnea, *Nano Lett*, 2006, **6**, 611-615.
40. Y.-J. Yoon, J. Park, B. Kim, H.-G. Lee, S.-B. Kang, G. Sung, J.-J. Kim and S.-G. Lee, *Synthesis*, 2012, **44**, 42-50.
41. N. O. B. Lüttschwager, T. N. Wassermann, R. A. Mata and M. A. Suhm, *Angew. Chem. Int. Ed.*, 2013, **52**, 463-466.
42. J. N. Byrd, R. J. Bartlett and J. A. Montgomery Jr, *J. Phys. Chem. A*, 2014, **118**, 1706-1712.
43. C. Cornioley-Deuschel and A. Von Zelewsky, *Inorg. Chem.*, 1987, **26**, 3354-3358.
44. J. DePriest, G. Y. Zheng, N. Goswami, D. M. Eichhorn, C. Woods and D. P. Rillema, *Inorg. Chem.*, 2000, **39**, 1955-1963.
45. S. Ghammamy and S. Narimany, *Global Journal of Pharmacology*, 2013, **7**, 187-191.
46. M. Mauro, A. Aliprandi, C. Cebrian, D. Wang, C. Kübel and L. De Cola, *Chem. Commun.*, 2014, **50**, 7269-7272.
47. M. Kasha, *Discuss. Faraday Soc.*, 1950, **9**, 14-19.
48. A. Galstyan, A. R. Naziruddin, C. Cebrián, A. Iordache, C. G. Daniliuc, L. De Cola and C. A. Strassert, *Eur. J. Inorg. Chem.*, 2015, **2015**, 5822-5831.
49. M. Mydlak, M. Mauro, F. Polo, M. Felicetti, J. Leonhardt, G. Diener, L. De Cola and C. A. Strassert, *Chem. Mater.*, 2011, **23**, 3659-3667.
50. J. R. Lakowicz, *Principles of Fluorescence Spectroscopy*, Springer, 3rd edn., 2007.
51. J. N. Israelachvili, *Intermolecular and surface forces*, Academic Press, Elsevier, Third edn., 2011.
52. E. Mattia and S. Otto, *Nat Nano*, 2015, **10**, 111-119.
53. G. M. Whitesides and B. Grzybowski, *Science*, 2002, **295**, 2418-2421.
54. J. M. Lehn, *Science*, 2002, **295**, 2400-2403.
55. M. I. Limited, Surfactant micelle characterization using dynamic light scattering, http://www.malvern.com/en/support/resource-center/application-notes/AN101104SurfactantMicelleCharacterization.aspx).
56. A. Einstein, *Annalen der Physik*, 1906, **324**, 371-381.
57. M. I. Limited, DYNAMIC LIGHT SCATTERING COMMON TERMS DEFINED, http://www.malvern.com/en/support/resource-center/Whitepapers/WP111214DLSTermsDefined.aspx).
58. B. J. M. Verduin, *FEBS Lett.*, 1974, **45**, 50-54.
59. M. Comellas-Aragones, H. Engelkamp, V. I. Claessen, N. A. Sommerdijk, A. E. Rowan, P. C. Christianen, J. C. Maan, B. J. Verduin, J. J. Cornelissen and R. J. Nolte, *Nature nanotechnology*, 2007, **2**, 635-639.

60. W. W. Cleland, *Biochemistry*, 1964, **3**, 480-482.
61. D. V. Bent and E. Hayon, *J. Am. Chem. Soc.*, 1975, **97**, 2599-2606.
62. D. V. Bent and E. Hayon, *J. Am. Chem. Soc.*, 1975, **97**, 2612-2619.
63. G. Sanyal, E. Kim, F. M. Thompson and E. K. Brady, *Biochem. Biophys. Res. Commun.*, 1989, **165**, 772-781.
64. M. K. Muller and L. Brunsveld, *Angew. Chem. Int. Ed.*, 2009, **48**, 2921-2924.
65. M. Mauro, G. De Paoli, M. Otter, D. Donghi, G. D'Alfonso and L. De Cola, *Dalton Trans.*, 2011, **40**, 12106-12116.

Instrumentation

The experimental part of this work was executed at the Université de Strasbourg, France and in parts at the University of Twente, Netherlands.

All solvents were used as received from Aldrich or Fluka without any further purification. All chemicals were purchased and used as received. The compounds were purified by column chromatography using silica gel 60 (230–400 mesh, Merck Millipore) as the stationary phase.

^{1}H, ^{13}C and ^{19}F NMR spectra were recorded on a Bruker Avance 400 spectrometer. The ^{1}H NMR chemical shifts (δ) are given in ppm and refer to residual protons on the corresponding deuterated solvent. All deuterated solvents were used as received without any further purification. All coupling constants (*J*) are given in Hertz (Hz). HRMS experiments were performed on a Bruker Daltonics microTOF spectrometer (Bruker Daltonik GmbH, Bremen, Germany) equipped with an orthogonal electrospray (ESI) interface. Calibration for mass analysis was performed using Tunning mix (Agilent Technologies). Sample solutions were introduced into the spectrometer source with a syringe pump (Harvard type 55 1111: Harvard Apparatus Inc., South Natick, MA, USA) with a flow rate of 5 $\mu L.min^{-1}$. HPLC-MS measurements were carried out on a Thermo Scientific Accela LC system.

For spectroscopy analysis in quartz cuvettes, suprasil (type 111-QS) emission cuvettes with a light path of 10x10 mm from Hellma-Analytics were utilized. For routine spectroscopic analysis, single-use polymethylmethacrylate (PMMA) cuvettes from Carl Roth (NK50.1) were utilized.

Absorption spectra were measured on a Shimadzu UV-3600 spectrophotometer double-beam UV–VIS–NIR spectrometer and baseline corrected. Steady-state emission spectra were recorded on a Horiba Jobin−Yvon IBH FL-322 Fluorolog 3 spectrometer equipped with a 450 W xenon arc lamp, double-grating excitation, emission monochromators (2.1 nm mm^{-1} of dispersion; 1200 grooves mm^{-1}) and a TBX-04 single photoncounting detector. Emission and excitation spectra were corrected for source intensity (lamp and grating) and the emission spectral response (detector and grating) by standard correction curves.

The absolute photoluminescence quantum yields (PLQY) were measured on a Hamamatsu Quantaurus-QY integrating sphere in air-equilibrated condition using an empty quartz tube as a reference. The measurements were conducted in scan mode with typical excitation wavelengths 250 - 550 nm with a 10 nm increment. The PLQY values were considered in regard of the absorption cross-section value and their standard deviation.

Time resolved measurements were performed using either the time-correlated single-photon counting (TCSPC) electronics PicoHarp300 or the Multi-Channel Scaling (MCS) electronics NanoHarp 250 of the PicoQuant FluoTime 300 (PicoQuant GmbH, Germany), equipped with a PDL 820 laser pulse driver. Pulsed laser diodes LDH-P-C-375 (λ = 375 nm, pulse FWHM <70 ps, repetition rate 50 kHz - 40 MHz) and LDH-P-C-405 (λ = 405 nm, pulse FWHM <70 ps, repetition rate 50 kHz - 40 MHz) were used to excite the sample and mounted directly on the sample chamber at 90°. The photons were collected by a PMA-C-192 photomultiplier (PMT) single-photon-counting detector. The data was acquired by using the commercially available software EasyTau (PicoQuant GmbH, Germany), while data analysis was performed using the commercially available software FluoFit (PicoQuant GmbH, Germany).

For the labelling process (Chapter III), a New Brunswick Scientific Excella E24 Incubator Shaker Series was utilized enabling control over temperature, time and rotations per minute (rpm). A filter based PerkinElmer VICTOR X5 multilabel plater reader was used for micro-well analysis in 96 standard micro-well plates using the bandpass filters 355 nm and 535 nm for excitation and emission, respectively.

Analyte stock solutions either in an aqueous PBS (pH=7.4) or ethanol were prepared. These solutions were mixed with the Pt-DMSO stock solution in a 3 mL PBS P123 (0.5 wt%) solution to result a concentration of 33.4 μM and 100 μM concentration of the L-Pt-DMSO and the analyte, respectively. In order to also enable a sufficient complex formation within 3 h of shaking (100 rpm) of analytes with sluggish kinetics, the temperature was raised to 37°C. In order to show this proof-of-principle for a broad scope of analytes, the optimized conditions for pyridine were kept for all analytes. All spectra were recorded by utilizing disposable PMMA cuvettes, if not mentioned otherwise.

Dynamic light scattering measurements were conducted on a Delsa Nano C Particle Analyzer (Beckman Coulter, Brea, CA, USA; operative wavelength 655 nm, Chapter III)

and on a Zetasizer Nano S (Malvern Instruments, He-Ne laser 633nm, Chapter IV). All DLS measurements of the were conducted in aqueous buffer solutions; PBS (pH = 7.4, Chapter III) or TRIS (50 mM, 20 mM $MgCl_2$, pH = 7.2). The Contin algorithm was used to supply the hydrodynamic diameters as intensity and volume distributions.

Scanning Tunneling Microscopy (STM) measurements were carried out by using a Veeco scanning Tunneling microscope (multimode Nanoscope III, Veeco) at the interface between a highly oriented pyrolitic graphite (HOPG) substrate and a supernatant solution, thereby mapping a maximum area of 1 µm × 1 µm. Solution of molecules were applied to the basal plane of the surface. For STM measurements, the substrates were glued to a magnetic disk and an electric contact was made with silver paint (Aldrich Chemicals). The STM tips were mechanically cut from a Pt/Ir wire (90/10, diameter 0.25 mm). The raw STM data were processed through the application of background flattening and the drift was corrected using the underlying graphite lattice as a reference. The lattice was visualized by lowering the bias voltage to 20 mV and raising the current up to 65 pA. STM imaging was carried out in constant height mode without turning off the feedback loop, to avoid tip crashes.

Fast-protein liquid chromatography (FPLC) was performed using the following buffers: 100 mM NaOAc, 150 mM NaCl (pH 5.0) and the GE Healthcare FPLC Akta purifier 900 combined with fraction collector Frac-950. Samples were injected into a 500 µL injection loop and purified over a column Superose 6 10/300 GL (GE Healthecare Life Sciences) with a 24 mL bed volume.

Transmission electron microscopy (TEM) samples were examined using an analytical FEG-TEM (Philips CM3000ST) operated at 300 kV acceleration voltage. For sample preparation, 5 µL of sample solution was applied onto carbon coated grids. The sample was left to incubate for 1 min before removing the excess liquid using a piece of filter paper. The sample was then stained by Uranyl acetate solution (5 µL, 0.5% w/v) for 30 s, then the excess liquid was removed. The grid was left to dry for 2 h at room temperature.

If not stated differently in the respective chapters, density functional theory (DFT) calculations were carried out utilizing the parameter-free hybrid functional Perdew-Burke-Ernzerhof PBE0[1-3] with the standard valence basis set 6-31G(d,p) for C,H,N,O and F.[4] The Stuttgart-Dresden effective core potential[5, 6] along with its corresponding basis set was employed for Pt. The found stationary points possessed no imaginary frequencies

(checked by frequency analysis) and therefore assumed to be true minima. All calculations were performed and visualized with the Gaussian09 program package.[7]

Electronic absorption spectroscopy

In order to measure the electronic absorption behavior of sample, a double-beam UV-Vis spectrophotometer was used. A monochromator selects a certain wavelength from the polychromatic light source and a beam splitter render two parallel beams of the same wavelength. One beam is guided through a reference cell (I_0), while the other is transmitted through the sample (I_S). The relationship between I_0 and I_S reveals the absorbance by the following equation:

$$A = \log(\frac{I_0}{I_S})$$

Usually sample holders made of transparent and chemical inert material are used such as quartz cuvettes.

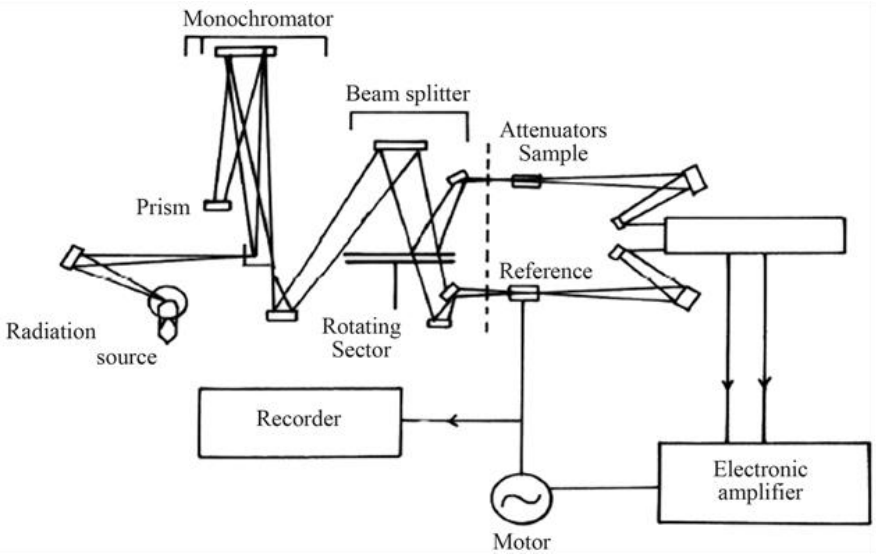

Figure Instr.1: Schematic representation of a double-beam spectrophotometer.[8] © 2014 Scientific Research

If one considers a thin layer of a sample solution of a thickness *dx* which contains *n* light absorbing molecules/cm^3 and σ is the effective cross-section for absorption in cm^2, then the light intensity *dI* per thickness of layer *dx* is proportional to the incident light intensity *I*:

$$\frac{dI}{dx} = I\sigma n$$

Together with the conditions limitations $I = I_0$ at $x = 0$, integration leads to the Bouguer-Lambert-Beer law[9-11], which is often depicted as follows:

$$A = -\log(T) = \varepsilon cd$$

where T denotes the transmittance as the ratio between I_S and I_0, ε the molar extinction coefficient in L mol cm^{-1}, c the concentration of the sample in mol L^{-1} and d the thickness of the cell in cm. The equation displays a direct correlation between the absorbance and the concentration of the sample. This relationship remains valid, when no interactions between the molecules are present, and thus only at diluted conditions. Supramolecular interactions can therefore lead to a perturbation of the linearity between absorbance and concentration. Furthermore, larger aggregates, large particles or dust scatter light stronger than molecular dissolved species. The effects observed in an absorption spectrum caused by the Rayleigh scattering,[12, 13] which is dependent on the wavelength of the incident light ($I_R \sim \lambda^{-4}$). Therefore, Rayleigh scattering is reflected as an increasing absorbance upon decreasing wavelength (often hyperbolic shape with large particles). A synonym for the absorbance is the optical density.

Fluorescence spectroscopy

Upon excitation by a photon to its excited state, a molecule can relax to its ground state by emitting a photon *via* fluorescence or phosphorescence. The direction of propagation of the emitted light is isotropic around the center of emission, and can therefore be estimated as a sphere around the center of excitation. In contrast to the linear arrangement of an absorption spectrophotometer, a fluorescence spectrophotometer is setup in perpendicular arrangement to avoid most of the incident light reaching the detector (Figure Instr.2). The emission spectrum is collected by fixing the excitation wavelength while the emission wavelength is varied. The resulting plot wavelength vs. emission intensity represents the emission profile/spectrum. The excitation is obtained by fixation of the emission wavelength, while the excitation wavelength is varied. To realize steady-state emission experiments, a polychromatic light source (Xe lamp) emits photons passing the excitation monochromator for the selection of a single wavelength. The

monochromatic light beam excites the sample, solid or solution (quartz cuvettes), in the sample compartment.

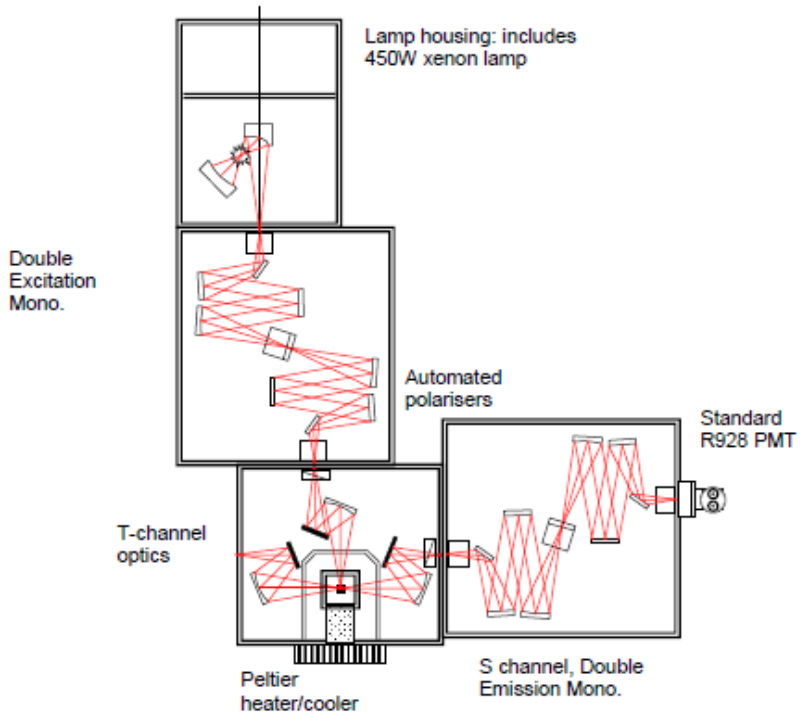

Figure Instr.2: Schematic representation of the setup of the Horiba Jobin−Yvon IBH FL-322 Fluorolog 3 spectrometer.[14] © Horiba

The polychromatic (spectrum) emitted light from the luminescent sample is guided through the emission monochromator after which a detector converts the photons into electrical signals. For high sensitivity, usually a photomultiplier tube (PMT) is used, which is commonly color-blind. In the utilized fluorescence spectrometer, the monochromator are gratings based in a Czerny-Turner arrangement.[15]

In contrast to the double-beam spectrophotometer described above, which avoid many artefacts, up-to-date fluorescence spectrometer do not yield true excitation and emission spectra. The spectral output of the light sources and the wavelength dependent efficiency of the monochromators as well as the detectors are sourced, that need to be corrected by reasonable calibrations. Furthermore, polarization of the emitted light from the sample is accompanied by errors due to anisotropic efficiencies of the monochromators. Thus, emission spectra can differ from one instrument to another.

In this thesis, all presented steady-state emission and excitation spectra are measured on the Horiba Jobin−Yvon IBH FL-322 Fluorolog 3 spectrometer, if not stated

differently. The spectra are corrected for the light source and the gratings. Optical filters are used to avoid undesired artefacts such as Raman scattering, second-order diffraction and stray light.

Time correlated single photon counting

Excited-state lifetime measurements were conducted by time-correlated single photon counting (TCSPC) on a fluorescence spectrometer (Figure Instr.3). In order to gain insights into the transient excited state, a pulsed light source (laser, diode, flash lamp) excited the sample molecules and transmits a signal to the electronics. The accurate measurement of the arrival time of the pulse is ensured by a constant function discriminator (CFD).[16] The signal is passed to a time-to-amplitude converter (TAC) that initialized the charging of a capacitor by generating a voltage ramp. This voltage increases linearly with time at the nanosecond scale. A single detected photon signal is again subjected to a CFD and stops the voltage ramp. Therefore, the voltage of the capacitor is now a read-out for the time from excitation to emission. This process is repeated several times, since luminescence is a random event. Each time is stored in a histogram, in which the abscissa refers to a certain time bin (time interval) and the ordinate to the number of counts for each time interval. Usually, most of the photons are emitted shortly after excitation. On account of the dead-time of the electronics and to avoid a piling-up of the histogram at shorter times, the pile-up rate (counts per seconds/repetition rate) should not exceed 1-2%. The physical meaning of this low pile-up rate is that 100 excitations lead to a single emission event. The application of this statistic is crucial for short excited-state lifetimes in the regime of a few nanoseconds. For longer excited-state lifetimes of hundreds of nanoseconds, a multi-scalar card accessory was utilized in order to reduce the measurement time drastically.[16]

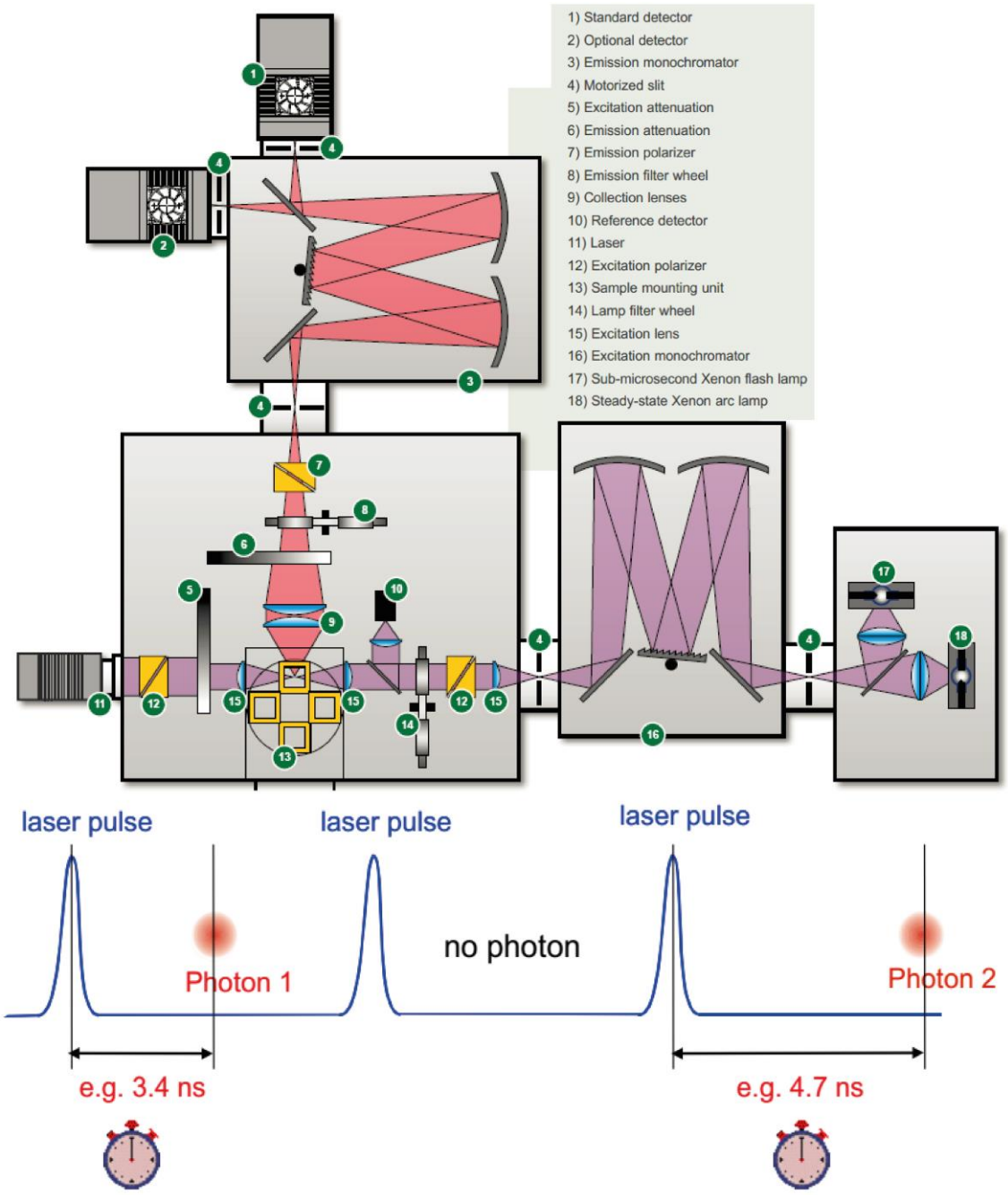

Figure Instr.3: Schematic representation of the setup the PicoQuant FluoTime 300 together with the principle for TCSPC. © PicoQuant GmbH, Germany

In any case, the histogram, so the intensity (*I*, counts) vs. time (*t*, time-bins) are fitted by the following equation covering also multiexponential decay forms as a sum of single exponential decay:

$$I(t) = \sum_{i=1}^{n} A_i e^{\frac{t}{\tau_i}}$$

The obtained excited-state lifetime (τ_i) can be correlated with their amplitudes (A_i) to identify several emissive deactivation processes.[16] Nevertheless, the mathematical fundament of this equation easily represents inaccurate percentages (amplitudes) for each lifetime. Therefore, in many cases is more reasonable to use the amplitude weighted excite-state lifetime which allows an estimation of the average excite-state lifetime:

$$< \tau > = \frac{\sum_i^n A_i \tau_i}{\sum_i^n A_i}$$

Photoluminescence quantum yield

The photoluminescence quantum yield is defined as the ratio between emitted and absorbed photons and is thus a measure for the efficiency of the radiative decay. The quantum yield of a compound in solution is dependent on the experimental conditions, namely the solvent, concentration of the sample, oxygen concentration, temperature and excitation wavelength (rare cases). Furthermore, certain experimental specification regarding effect referred to the refractive indices, polarization, inter reflection, reabsorption/reemission and the spectral sensitivity of the detection system.[17-19] The quantum yield can be determined *via* relative or absolute methods.

In the relative method, the quantum yield of a sample solution is obtained by a comparison of its integrated fluorescence intensity with the integrated fluorescence intensity of a standard solution of known quantum yield at identical conditions. There, it is crucial to correct for the spectral sensitivity of the instrument, namely for the excitation and emission wavelength. The quantum yield of the sample (φ_s) can be obtained from the following equation[16]:

$$\varphi_S = \varphi_R \frac{\int_{\lambda_i}^{\lambda_m} I_s(\lambda) d\lambda \; OD_R \; n_S^2}{\int_{\lambda_i}^{\lambda_m} I_R(\lambda) d\lambda \; OD_S \; n_R^2}$$

where φ_R denotes the known quantum yield of the reference, $I_S(\lambda)$ and $I_R(\lambda)$ the emission intensity at wavelength λ, OD_S and OD_R the optical densities at excitation wavelength and n_S and n_R the refractive indices of the sample and the reference, respectively.

Various methods for the determination of absolute quantum yields were developed such as the Teale and Weber technique (scattering solution as standard)[20]. Calorimetric

methods or photoacoustic (optoacoustic) techniques determine the fractional energetic loss by non-radiative processes. An integrating sphere equipped with a calibrated photodiode was used in this thesis for the detection of absolute photoluminescence quantum yields in solution and solid state (Figure Instr.4).[19] With this measurement method, effects of polarization, scattering and refractive indices are directly eliminated.

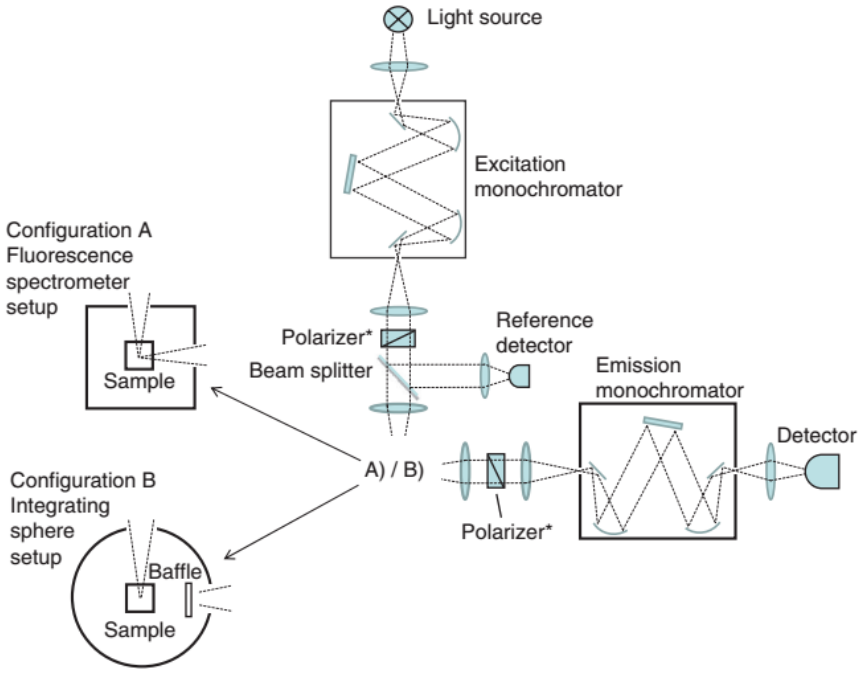

Figure Instr.4: Schematic representation of the setup of fluorescence spectrometer (A) and an integrating sphere (B) for the determination of the photoluminescence quantum yield.[19] © 2013 Nature

In the used instrument, Hamamatsu Quantaurus-QY, polychromatic light from the light source (Xe lamp) is monochromatized by an optical prism and guided by optical fibers into the integrating sphere. The emitted light passes another optical fiber and is detected by a multichannel spectroscope. The measurement is repeated for the reference (blank quartz cell). The absolute quantum yield is calculated with the following equations:

$$F = \int_{\lambda_{em}} \frac{I_s(\lambda_{em}) - I_B(\lambda_{em})}{s(\lambda_{em})} \lambda_{em} d\lambda_{em}$$

$$F_{abs} = \int_{\lambda_{em}} \frac{I_B(\lambda_{exc}) - I_S(\lambda_{exc})}{s(\lambda_{exc})} \lambda_{exc} d\lambda_{exc}$$

$$\varphi_S = \frac{F}{F_{abs}}$$

where F denotes the emitted photon flux and F_{abs} the absorbed photon flux. I refers to the intensities at the emission (λ_{em}) and excitation (λ_{exc}) wavelength, s is a wavelength correction factor, S and B represent the indices for sample and blank, respectively.

Dynamic light scattering

Dynamic light scattering (DLS) is a non-invasive, widespread photon-correlation technique for the measurement of the size and size distribution of small particles (<μM). Due to random collisions with solvent molecules, suspended particles follow the Brownian motion.[21] The Stokes-Einstein equation describes the solvent viscosity (η_0), the hydrodynamic diameter (D_{hyd}, corresponding to the particle size in a solvent) and the diffusion coefficient (D) of these randomly moving particles:

$$D = \frac{k_B T}{3\pi\eta_0 D_{hyd}}$$

In the Stokes-Einstein equation, k_B refers to the Boltzmann constant and T denotes the temperature. Therefore, the diffusion decreases for increasing particle size (hydrodynamic diameter), which in turn mean that larger particle move slower than smaller ones. Therefore, the observation of the motion of the particles in a liquid medium can be utilized to derive information about the particle size. The Stokes-Einstein equation takes only spherical particle into account, and thus the derived information about size and distribution are strictly speaking only valid for spherical particles.[21]

Particles in solution scatter the monochromatic beam from the light source (often a laser). The observed scattered light at a charge-coupled device (CCD) detector is emanated from a collection of scattering elements. Therefore, the observed intensity of scattered light at any instant is a result of the interference of scattered light by each element. Thus, the observed intensity depends on the relative positions of the elements. On account of the Brownian motion of the particles, the relative positions of the particles change in time resulting in random intensity fluctuations of the scattered light (Figure Instr.5). The smaller the particle size, the faster the fluctuations.

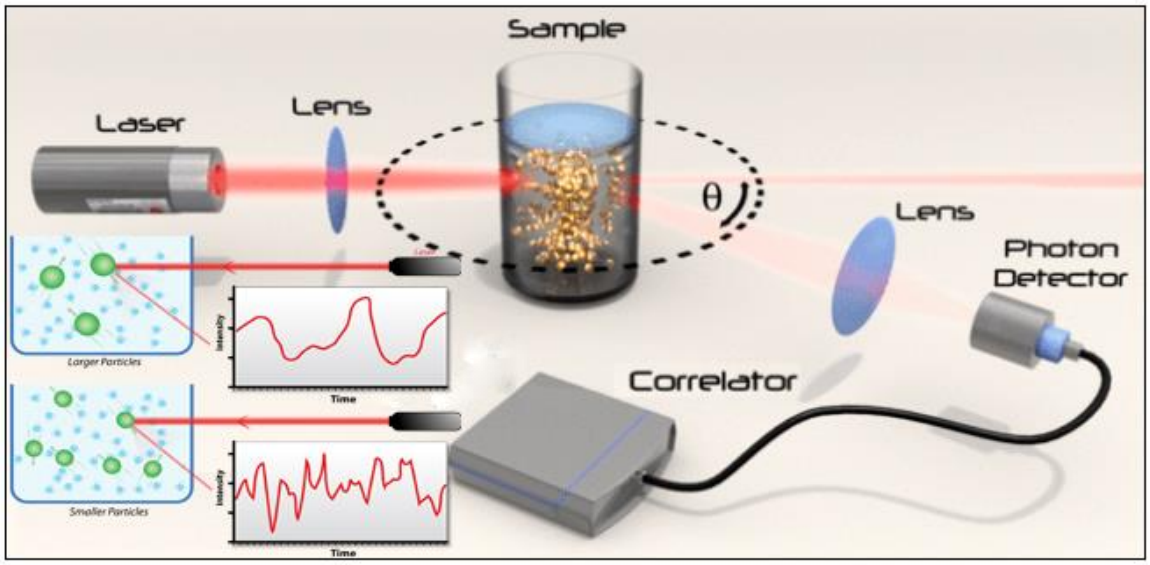

Figure Instr.5: Schematic representation of the measurement principle of a dynamic light scattering (DLS) instrument.[22] © LS instruments; The inset displays the random intensity fluctuations of scattered light over time either for smaller or larger particles.[23] © Quantachrome

An autocorrelation function (ACF) is used to analyze the fluctuations of the scattered light. Small particles featuring a rapid motion and intensity fluctuations result in an autocorrelation function that decays rapidly as an exponential function with a large decay constant. For larger particles, the decay constant will be smaller. Therefore, a fitting of the ACF enables the calculation of the diffusion coefficient and particle size/distribution.

The particle size is usually shown as a statistical (Gauss profile) distribution of scattering intensity, volume or number of particles. The intensity distribution is the directly measured result and is the most common way to depict DLS plots. Volume and number distributions are calculated on the basis of the intensity distribution by the usage of the Mie theory.[24]

The volume distribution describes the relative proportion of several components within the sample based on their volume. The number distribution assigns a size value to each inspected particle. In general, volume and number distributions, which are deduced from the intensity distribution, are best used for comparative purposes.

Scanning tunneling microscopy

The quantum tunneling effect describes the phenomenon that a quantum mechanical particle such as an electron or an atom is able to surmount a finite potential barrier, which

it could not overcome in classical physics. Therefore, although the potential energy of an electron is not high enough to surmount a potential barrier between two electrodes, a low probability exists that the electron can tunnel through the barrier.[25-27] This phenomenon is exploited in scanning tunneling microscopy, in which a fine metal tip moves over a conductive surface covered with a few layers of atoms (Figure Instr.6).[28, 29] A bias is applied between the surface and the metal tip, which are brought to close proximity (3 - 10 Å). At a certain distance the electrons start to tunnel through the adsorbed material on the surface to the tip, which is reflected in the appearance of a tunneling current. The movement of the tip (controlled by piezoelectronics) can be performed in two methods: *i)* constant current mode: The tip is vertically adjusted to ensure a constant tunneling current. The current is dependent on the local density of states and thus a topographic image of the sample is recorded. *ii)* constant height mode: The vertical position of the tip is kept constant and the obtained contrast of the surface images are caused by changes in the electron density. The latter mode can be performed at high scanning frequencies (10 kHz), but is limited to monolayers to avoid collisions between the tip and the surface. Scanning tunneling microscopes are able to render a lateral resolution of 0.1 nm and a depth resolution of 0.01 nm.

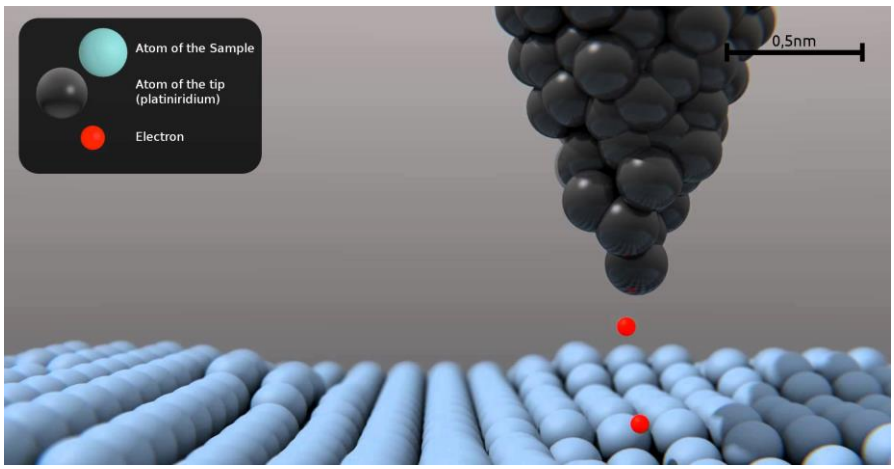

Figure Instr.6: Illustration of the principle of a scanning tunneling microscope. Black spheres represent the atoms of the tip, sky-blue sphere represent the atoms of the scanned layer and red spheres represent the electrons tunneling from the surface to the tip. © 2012 Johanneum

References

1. C. Adamo and V. Barone, *J. Chem. Phys.*, 1999, **110**, 6158-6170.
2. J. P. Perdew, K. Burke and M. Ernzerhof, *Phys. Rev. Lett.*, 1997, **78**, 1396-1396.
3. J. P. Perdew, K. Burke and M. Ernzerhof, *Phys. Rev. Lett.*, 1996, **77**, 3865-3868.
4. M. M. Francl, W. J. Pietro, W. J. Hehre, J. S. Binkley, M. S. Gordon, D. J. DeFrees and J. A. Pople, *J. Chem. Phys.*, 1982, **77**, 3654-3665.
5. M. Dolg, U. Wedig, H. Stoll and H. Preuss, *J. Chem. Phys.*, 1987, **86**, 866-872.
6. D. Andrae, U. Häußermann, M. Dolg, H. Stoll and H. Preuß, *Theoret. Chim. Acta*, 1990, **77**, 123-141.
7. M. J. Frisch, G. W. Trucks, H. B. Schlegel, G. E. Scuseria, M. A. Robb, J. R. Cheeseman, G. Scalmani, V. Barone, B. Mennucci, G. A. Petersson, H. Nakatsuji, M. Caricato, X. Li, H. P. Hratchian, A. F. Izmaylov, J. Bloino, G. Zheng, J. L. Sonnenberg, M. Hada, M. Ehara, K. Toyota, R. Fukuda, J. Hasegawa, M. Ishida, T. Nakajima, Y. Honda, O. Kitao, H. Nakai, T. Vreven, J. A. Montgomery Jr., J. E. Peralta, F. Ogliaro, M. J. Bearpark, J. Heyd, E. N. Brothers, K. N. Kudin, V. N. Staroverov, R. Kobayashi, J. Normand, K. Raghavachari, A. P. Rendell, J. C. Burant, S. S. Iyengar, J. Tomasi, M. Cossi, N. Rega, N. J. Millam, M. Klene, J. E. Knox, J. B. Cross, V. Bakken, C. Adamo, J. Jaramillo, R. Gomperts, R. E. Stratmann, O. Yazyev, A. J. Austin, R. Cammi, C. Pomelli, J. W. Ochterski, R. L. Martin, K. Morokuma, V. G. Zakrzewski, G. A. Voth, P. Salvador, J. J. Dannenberg, S. Dapprich, A. D. Daniels, Ö. Farkas, J. B. Foresman, J. V. Ortiz, J. Cioslowski and D. J. Fox, *Journal*, 2009.
8. S. Sagadevan and P. Murugasen, *Journal of Crystallization Process and Technology*, 2014, **2014**.
9. A. Beer, *Annalen der Physik und Chemie*, 1852, **162**, 78-88.
10. P. Bouguer, *Essai d'optique sur la gradation de la lumière*, C. Jombert, 1729.
11. J. H. Lambert, *J. H. Lambert,... Photometria, sive de Mensura et gradibus luminis, colorum et umbrae*, sumptibus viduae E. Klett, 1760.
12. A. T. Young, *Appl. Opt.*, 1981, **20**, 533-535.
13. J. W. Strutt, *The London, Edinburgh, and Dublin Philosophical Magazine and Journal of Science*, 1871, **41**, 447-454.
14. Horiba, http://www.horiba.com/scientific/products/fluorescence-spectroscopy/application-notes/).
15. M. Czerny and A. F. Turner, *Zeitschrift für Physik*, 1930, **61**, 792-797.
16. J. R. Lakowicz, *Principles of Fluorescence Spectroscopy*, Springer, 3rd edn., 2007.
17. G. A. Crosby and J. N. Demas, *J. Phys. Chem.*, 1971, **75**, 991-1024.
18. D. F. Eaton, *Pure Appl. Chem.*, 1988, **60**, 1107-1114.
19. C. Würth, M. Grabolle, J. Pauli, M. Spieles and U. Resch-Genger, *Nat. Protocols*, 2013, **8**, 1535-1550.
20. G. Weber and F. W. J. Teale, *Transactions of the Faraday Society*, 1957, **53**, 646-655.
21. A. Einstein, *Annalen der Physik*, 1906, **324**, 371-381.
22. L. instruments, www.lsinstruments.ch/technology/dynamic_light_scattering_dls/).
23. Quantachrome, http://www.quantachrome.co.uk/en/particle-size/dynamic-light-scattering.asp).
24. G. Mie, *Annalen der Physik*, 1908, **330**, 377-445.
25. G. Wentzel, *Zeitschrift für Physik*, 1926, **38**, 518-529.
26. H. A. Kramers, *Zeitschrift für Physik*, 1926, **39**, 828-840.
27. L. Brillouin, *CR Acad. Sci*, 1926, **183**, 24-26.
28. G. Binnig, H. Rohrer, C. Gerber and E. Weibel, *Phys. Rev. Lett.*, 1982, **49**, 57-61.
29. H. Rohrer, *PNAS*, 1987, **84**, 4666-4666.

Appendix

Table Appendix 1: Crystal data and structure refinement for **Py_2-18C4**	
Empirical formula	$C_{28}H_{36}N_4O_6$
Formula weight	524.61
Temperature/K	179.95(10)
Crystal system	monoclinic
Space group	$P2_1/n$
a/Å	24.4000(8)
b/Å	10.41201(19)
c/Å	24.5180(8)
α/°	90
β/°	117.630(4)
γ/°	90
Volume/Å^3	5518.5(3)
Z	8
ρ_{calc}g/cm^3	1.263
μ/mm^{-1}	0.733
F(000)	2240.0
Crystal size/mm^3	0.7685 × 0.5031 × 0.363
Radiation	CuKα (λ = 1.54184)
2Θ range for data	7.252 to 145.322
Index ranges	-29 ≤ h ≤ 30, -12 ≤ k ≤ 12, -30 ≤ l ≤
Reflections collected	38359
Independent reflections	10795 [R_{int} = 0.0483, R_{sigma} =
Data/restraints/parameters	10795/4/702
Goodness-of-fit on F^2	1.081
Final R indexes [I>=2σ (I)]	R_1 = 0.0660, wR_2 = 0.1552
Final R indexes [all data]	R_1 = 0.0680, wR_2 = 0.1565
Largest diff. peak/hole / e	0.54/-0.30

Table Appendix 2: Crystal data and structure refinement for **Py_2-18C6**	
Empirical formula	C33H42N4O9
Formula weight	638.70
Temperature/K	180.15
Crystal system	monoclinic
Space group	P21/n
a/Å	10.43180(15)
b/Å	18.5656(3)
c/Å	17.6555(3)
α/°	90
β/°	90.8170(13)
γ/°	90
Volume/Å3	3419.05(8)
Z	4
ρcalcmg/mm3	1.241
m/mm-1	0.751
F(000)	1360.0
Crystal size/mm3	0.8092 × 0.4242 × 0.1313
Radiation	CuKα (λ = 1.54184)
2Θ range for data	6.91 to 145.074°
Index ranges	-12 ≤ h ≤ 8, -15 ≤ k ≤ 22, -21 ≤ l ≤
Reflections collected	13891
Independent reflections	6622 [Rint = 0.0162, Rsigma =
Data/restraints/parameters	6622/299/521
Goodness-of-fit on F2	1.106
Final R indexes [I>=2σ (I)]	R1 = 0.0377, wR2 = 0.1295
Final R indexes [all data]	R1 = 0.0426, wR2 = 0.1370
Largest diff. peak/hole / e	0.23/-0.17

Table Appendix 3: Crystal data and structure refinement for **L-2H**	
Empirical formula	$C_{14}H_{11}F_6N_7O$
Formula weight	407.30
Temperature/K	173(2)
Crystal system	monoclinic
Space group	$P2_1/c$
a/Å	9.8584(4)
b/Å	11.7351(5)
c/Å	15.5995(6)
α/°	90
β/°	106.0420(10)
γ/°	90
Volume/Å^3	1734.42(12)
Z	4
ρ_{calc}g/cm^3	1.560
μ/mm^{-1}	0.149
F(000)	824.0
Crystal size/mm^3	0.350 × 0.300 × 0.250
Radiation	MoKα (λ = 0.71073)
2Θ range for data	4.3 to 60.034
Index ranges	-13 ≤ h ≤ 13, -16 ≤ k ≤ 16, -21 ≤ l ≤
Reflections collected	20636
Independent reflections	5050 [R_{int} = 0.0251, R_{sigma} =
Data/restraints/parameters	5050/0/263
Goodness-of-fit on F^2	1.038
Final R indexes [I>=2σ (I)]	R_1 = 0.0419, wR_2 = 0.1042
Final R indexes [all data]	R_1 = 0.0576, wR_2 = 0.1140
Largest diff. peak/hole / e	0.39/-0.22

Table 3.4: Summary of the photophysical data collected for all analyzed compounds.

Index	λ_{max} /cm^{-1}	$\lambda_{exc,onset}$ / cm^{-1}	Int	τ /ns	*SiNo*
1	17421.60279	20428.23880	478.23317	440	21.84567
1	17543.85965	20419.00159	427.11935	426	20.64266
1	17543.85965	20386.84861	352.08994	454	18.73739
2	18315.01832	20761.19812	60.73321	95	7.72873
2	18518.51852	20770.33992	161.3627	86	12.66344
2	18214.93625	20828.63431	42.53858	93	6.44504
3	17452.00698	20034.16707	360.09823	556	18.94989
3	17574.69244	19958.65883	204.2387	542	14.25618
3	17513.13485	19884.26483	186.57369	497	13.62254
4	17574.69244	20429.60267	240.79801	259	15.48541
4	17574.69244	20417.40318	191.71802	284	13.81007
4	17543.85965	20402.03017	285.14527	267	16.85661
5	17271.15717	20258.88833	412.71126	321	20.29067
5	17301.03806	20260.35365	473.18001	337	21.7297
5	17271.15717	20312.27152	306.1892	347	17.46967
6	17513.13485	19763.37313	263.20316	366	16.19269
6	17605.63380	19810.32643	184.82609	274	13.55825
6	17543.85965	19810.13844	109.41781	437	10.41239
7	18083.18264	20566.48575	371.7198	299	19.25409
7	18050.54152	20471.68775	371.75431	293	19.25498
7	18050.54152	20450.71411	506.79636	306	22.48992
8	17825.31194	21095.84787	164.13552	383	12.77245
8	17825.31194	21093.91259	193.82316	417	13.88608
8	17857.14286	21094.12127	181.78135	353	13.4455
9	17985.61151	20624.85813	329.74981	194	19.26124
9	17953.32136	20634.43969	339.30065	196	21.08032
9	18083.18264	20622.51665	376.07492	207	21.33847
10	18416.20626	20865.62767	265.05347	192	16.24972
10	18416.20626	20865.36253	221.01039	159	14.83275
10	18115.94203	20876.84982	247.3472	174	15.69545
11	17271.15717	20183.71215	604.93887	530	24.57517
11	17301.03806	20209.20120	461.12619	532	21.45055
11	17331.02253	20236.02326	709.7613	565	26.62257
12	21691.97397	26335.41005	15.82871	57	3.85081
12	21598.27214	25975.82944	14.89902	56	3.72814
12	21691.97397	26035.06230	19.94665	54	4.35278
13	18975.33207	21215.84575	371.45597	230	19.24723
13	18939.39394	21206.71556	418.79151	218	20.43995

Table 3.4: Summary of the photophysical data collected for all analyzed compounds.

Index	λ_{max} /cm^{-1}	$\lambda_{exc,onset}$ / cm^{-1}	Int	τ /ns	*SiNo*
13	18796.99248	21223.71978	408.05017	235	20.17548
14	18656.71642	21026.13378	403.51995	260	20.0629
14	18726.59176	21112.47990	460.86282	276	21.44441
14	18832.39171	21100.44118	350.54969	243	18.69625
15	17793.59431	20423.06794	584.64638	473	24.15877
15	17182.13058	20490.87153	397.36645	482	19.90895
15	17793.59431	20483.62074	315.84359	405	17.74383
16	21413.27623	26874.73661	25.10686	131	4.90987
16	21413.27623	26872.99971	37.11229	161	6.00935
16	21459.22747	26875.37726	33.82777	130	5.72955
17	16694.49082	19439.37390	82.02124	181	9.00118
17	16556.29139	19455.39032	73.05665	324	8.48862
17	16638.93511	19387.43837	97.94025	325	9.84582
18	21367.52137	23392.21231	12.50236	34	3.39151
18	21367.52137	25943.94717	12.78055	39	3.43228
18	21276.59574	23456.85502	4.79337	20	1.94766
19	17953.32136	21157.97603	860.62731	615	29.3194
19	18518.51852	21039.86149	897.76944	649	29.94611
19	17793.59431	21172.50226	909.24892	667	30.13717
20	20202.02020	26306.31228	3.99145	12	1.72958
20	20920.50209	26772.82986	5.08784	26	2.02184
20	20161.29032	26312.15563	3.82736	12	1.68148
21	21551.72414	23028.27903	59.08571	1717	7.6214
21	21551.72414	23029.69078	66.31427	2327	8.08172
21	21551.72414	23039.24452	50.64828	1834	7.04615
22	16977.92869	20506.63950	86.32565	289	9.23719
22	17182.13058	20514.07913	76.81274	294	8.70705
22	16920.47377	20500.68579	93.95944	306	9.64155
23	17543.85965	21450.30258	41.48788	335	6.7678
23	17543.85965	21424.54453	47.47511	340	7.83057
23	17482.51748	21441.17041	48.43223	339	7.60051
blank	18518.51852	25582.12902	1	3	0
blank	18518.51852	25605.36328	1	3	0
blank	18518.51852	25548.02885	1	2	0
Sample X	21551.72414	23020.42582	58.25299	2101	7.56657

Sample X denotes the average of a triple replica experiment of an unknown sample. For analyte names indicated by the indices see Scheme 3.2 and Table 3.4.

Curriculum Vitae

Personal information

Name	Stephan Sinn
Date of Birth	22 March 1988
Nationality	German
Address	10 Rue de la Broque, 67000 Strasbourg, France
E-mail	sinn@unistra.fr; stephan.sinn.edu@gmail.com

Education

2013 – 2017	PhD thesis at the Université de Strasbourg, France (Prof. De Cola)
2007 – 2012	University studies and diploma thesis in chemistry at the Friedrich-Schiller-Universität Jena, Germany (Prof. Schubert)
2006 – 2007	Civilian service: Asklepios Kliniken, Bad Salzungen, Germany
1998 – 2006	Grammar school: Dr.-Sulzberger-Gymnasium, Bad Salzungen, Germany
1994 – 1998	Elementary school: Krayenberg Schule, Tiefenort, Germany

Scientific publications

- *Platinum Complex Assemblies as Luminescent Probes and Tags for Drugs and Toxins in Water;* S. Sinn, F. Biedermann, L. De Cola, Chem. Eur. J. 2016, 2017, **23**, 1965-1971.
- *Stabilisation effects of phosphane ligands in the homogeneous approach of sunlight induced hydrogen production;* C. Strabler, S. Sinn, R. Pehn, J. Pann, J. Dutzler, W. Viertl, J. Prock, K. Ehrmann, A. Weninger, H. Kopacka, L. De Cola and P. Brueggeller, Faraday Discuss., 2016. DOI: 10.1039/C6FD00210B
- *Discrete polygonal supramolecular architectures of isocytosine-based Pt(ii) complexes at the solution/graphite interface;* M. El Garah, S. Sinn, A. Dianat, A. Santana-Bonilla, R. Gutierrez, L. De Cola, G. Cuniberti, A. Ciesielski and P. Samori, Chem. Commun., 2016, **52**, 11163-11166.
- *A Ratiometric Luminescent Switch Based on Platinum Complexes Tethered to a Crown-Ether Scaffold*; S. Sinn, F. Biedermann, M. Vishe, A. Aliprandi, C. Besnard, J. Lacour and L. De Cola, *ChemPhysChem*, 2016, **17**, 1829-1834.
- *A heteroleptic bis(tridentate) ruthenium(II) platform featuring an anionic 1,2,3-triazolate-based ligand for application in the dye-sensitized solar cell;* S. Sinn, B. Schulze, C. Friebe, D. G. Brown, M. Jager, J. Kubel, B. Dietzek, C. P. Berlinguette and U. S. Schubert, Inorg. Chem., 2014, **53**, 1637-1645.
- *Physicochemical Analysis of Ruthenium(II) Sensitizers of 1,2,3-Triazole-Derived Mesoionic Carbene and Cyclometalating Ligands;* S. Sinn, B. Schulze, C. Friebe, D. G. Brown, M. Jager, E. Altuntas, J. Kubel, O. Guntner, C. P. Berlinguette, B. Dietzek and U. S. Schubert, Inorg. Chem., 2014, **53**, 2083-2095.
- *Ruthenium(II) photosensitizers of tridentate click-derived cyclometalating ligands: a joint experimental and computational study;* B. Schulze, D. Escudero, C. Friebe, R. Siebert, H. Gorls, S. Sinn, M. Thomas, S. Mai, J. Popp, B. Dietzek, L. Gonzalez and U. S. Schubert, Chem. Eur. J., 2012, **18**, 4010-4025.
- *Highly Luminescent Virus Like Particles (VLPs) Through the Encapsulation of Pt(II)-Amphiphiles;* S. Sinn, Liulin Yang, F. Biedermann, Jeroen Cornelissen and L. De Cola, manuscript in preparation.

Oral presentations

Highly luminescent Virus Like Particles (VLPs) through the encapsulation of Pt(II) amphiphiles

SupraChem, **2017**, Aachen

Strongly Emissive Platinum(II)-Complexes as Platforms for Different Types of Sensing

Young Scientist Seminar, **2016**, Strasbourg

Aggregation properties and gas-phase analysis of luminescent self-assembling dinuclear cyclometalated Pt(II) crown ether complexes

Young's Forum on Supramolecular and Materials Chemistry, **2014**, Padova

Poster presentations

Sensing of Drugs and Toxins in Water by *in situ* Formation of Emissive Platinum-complexes

International Symposium on Macrocyclic and Supramolecular Chemistry, **2016**, Seoul

Pt(II) complexes as sensors for detection of alkali and alkaline earth metals

Faraday Discussions on Supramolecular Photochemistry, **2015**, Cambridge

Highly emissive liquid crystaline Pt(II) complexes

International Conference on Molecular Electronics, **2014**, Strasbourg

Photophysics and Electrochemistry of Pt(II) and Ir(III) complexes

Strasbourg-Groningen Symposium, **2014**, Strasbourg

Pt(II) complexes of ditopic crown ethers

European-Winter School on Physical Organic Chemistry, **2014**, Bressanone

Acknowledgment

I would like to thank Prof. Luisa De Cola and Prof. Jean-Marie Lehn for the supervision and co-direction of my thesis, respectively. In particular, I am very grateful to Prof. Luisa De Cola for the opportunity to work in her laboratories at the Université de Strasbourg and her continuous support. The entire De Cola group welcomed me very warmly. Not only the scientific level but also the very important social aspects allowed me to work in a very motivating and convenient environment.

I am grateful to Prof. Jereon Cornelissen for letting me stay in his group for a short period to learn and carry out my experiments at the University of Twente.

I wish to thank Frank Biedermann, who did not only support me at any stage of my thesis, but also became a friend. I am betting on more scientific bets in the future.

My limited English is not good enough to express my thankfulness to Youssef Atoini, who helped me with an endless number of things, particularly, to survive the French bureaucracy. Merci mon pote, c'était toujours un plaisir pour moi.

For his teaching and continuous knowledge exchange also over longer distances, I am very grateful to Liulin Yang.

I thank the Stéphanie for the ESI-ToF MS measurements and Corrine from the X-ray diffractometry service. Jean-Louis Schmitt is kindly acknowledged for his maintenance of literally every common instrument in ISIS.

I am very grateful to Ines Below, who was always a perfect lab mate and an advisor for all things in life. I would like to thank Claire Menouna-Ekani for all organizations and help with so many things.

I wish to thank Leana Travaglini for her suggestions in DLS, knowledge exchange for particle analysis and all the tea I stole from her. Simone Silvestrini is kindly acknowledged for the training in particle analysis as well as fruitful discussions about statistics (and his clementines). I thank Mike Dentinger for his help with the confocal microscope and the SEM. Dedy Septiadi is kindly acknowledged for confocal and cell training. I am grateful to John Ddungu for his remote support for chemical management

and TEM organization. Christoph Strabler from the group of Peter Brüggeler is kindly acknowledged for the collaboration on Co(III)-complexes.

I wish to thank Amparo for the scientific discussions and all the great moment inside and outside the lab. For all their scientific support and funny moment Ingrid, Ondrey, Elena Longhi, Ale Sorenti, Thomas, Federica, Laura, Chien-Wei, Damiano, Ricardo, Becky and Eko are kindly acknowledged.

I am grateful to the BASF group of ISIS, Elena Wolf, Paul and Jan, for letting me occupy their DLS machine for several months and the nice dejeuners. I would like to acknowledge the football crew Youssef, Ricardo, Hadus, Jorge, Aki, Thibault, Seb, Ousama, Dedy (the lazy Chita) and Bertu for all the funny afternoons.

My greatest gratitude goes to my family. My beautiful wife Elisabeth, who is always my greatest motivation and the biggest pillar to hide in the storm. Elisabeth, du warst die beste Entscheidung in meinem Leben. My son Tristan, who is simply a gift. My mother Doris and brother Bastian, who defined me and my life in a way that this work I carried out is also partially theirs. My mother in law Isolde, who helps wherever she can.

I would like to thank all my colleagues within the De Cola group and inside the ISIS for their support and friendship. Finally, I would like to thank all my friends, old and new ones that I found.

UNIVERSITÉ DE STRASBOURG

Stephan Sinn

Complexes de platine (II) comme ossatures dans les assemblages supramoléculaires

Résumé

Cette thèse se concentre sur la synthèse et l'analyse photophysique de complexes de Pt(II) luminescents and leur assemblage après agrégation. Multiples motifs supramoléculaires ont été utilisé pour acquérir un contrôle sur l'assemblage de ces complexes plan-carrés.

Des ossatures de type couronne-éther furent attachés à des complexes métalliques phosphorescents pour donner un bouton supramoléculaire qui peut être actionné par des cations potassium. De plus, l'altération de l'arrangement de l'empilage des Pt(II) après coordination d'un ligand fut exploité pour la réalisation d'un senseur chimique qui peut être utilisé pour la détection différentielle d'aza-hétérocylces. L'agrégation induite par l'analyte a permis non seulement la détection à base concentration mais aussi la discrimination de drogues et toxines en appliquant une analyse de données multivariée. Par ailleurs, l'installation d'un motif pont hydrogène, isocytosine, à un complexe de Pt(II) luminescent fut établie, donnant un composé ayant un organisation 2D sur graphène. Les motifs pont hydrogène et les superstructures résultantes furent résolues par microscopie à effet tunnel and simulées par DFT. Finalement, des complexes de Pt(II) amphiphiles qui s'auto-assemblent en solution aqueuse dans des agrégats hautement luminescents furent synthétisés. La série de complexes soluble dans l'eau, chargés négativement ou neutres furent caractérisés par rapport à leurs paramètres photophysiques et leurs interactions avec des protéines capsides virales. L'encapsulation dans des capsides CCMV via contrôle du pH donna des particules pseudo-virales hautement luminescentes, prouvant la formation de matériaux hybrides fonctionnels basés sur des protéines naturelles.

Mots-clés : Complexes de Pt(II); senseurs chimiques; phosphorescence; particules pseudo-virales; matériaux hybrides fonctionnels

Résumé en anglais

The presented thesis focused on the synthesis and photophysical investigation of luminescent Pt(II)-complexes and their resulting assemblies that form upon aggregation. Multiple supramolecular motifs were utilized in order to gain control over the assembling behavior of the square-planar complexes.

Crown-ether scaffolds were tethered with the phosphorescent metal complexes rendering a supramolecular switch that can be triggered by potassium cations. Moreover, alteration of the Pt(II)-stacking arrangement upon ligand coordination was exploited to realize a chemosensor that can be employed for of differential detection of aza-heterocycles. The analyte-induced aggregation allowed for both low concentration detection and discrimination of drugs and toxins by applying multivariate data analyses. Furthermore, the installation of the H-bond motif, isocytosine, to a luminescent Pt(II)-complex was established, which resulted in a compound forming a two-dimensional organization on graphene. The H-bonding motifs and the resulting superstructures were resolved by scanning tunneling microscopy and simulated by density functional theory. Finally, amphiphilic Pt(II)-complexes were synthesized that self-assemble into highly luminescent aggregates in aqueous solutions. The series of water soluble neutral and negatively charged metal complexes were characterized with respect to their photophysical parameters and their interactions with virus coat proteins. The encapsulation into CCMV capsids *via* pH control yielded highly luminescent virus like particles, demonstrating the formation of hybrid functional materials based on natural proteins.

Keywords: Pt(II) complexes; chemosensors; phosphorescence; virus like particles; hybrid functional materials